

NNT : 2017SACLC028

THESE DE DOCTORAT  
DE  
L'UNIVERSITE PARIS-SACLAY  
PRÉPARÉE À  
CENTRALESUPELEC

ECOLE DOCTORALE N° 579  
SMEMAG

Spécialité de doctorat Mécanique des Fluides

Par

**Pablo AGUADO LOPEZ**

Titre de la these

Numerical study of nozzle geometry impact on  
in-nozzle flow and primary breakup

**Thèse présentée et soutenue à Rueil-Malmaison le 22 Mai 2017**

**Composition du Jury :**

Hasse, Christian  
Saurel, Richard  
Lai, Ming-Chia  
Allaire, Grégoire  
Guerrassi, Noureddine  
Shi, Junmei  
Angelberger, Christian  
Jay, Stéphane

Professeur, TU Bergakademie Freiberg, Germany  
Professeur, Aix-Marseille Université, France  
Professeur, Wayne State University, USA  
Professeur, Ecole Polytechnique, France  
Docteur, Delphi Automotive Systems, Luxembourg  
Docteur, Delphi Automotive Systems, Luxembourg  
Docteur, IFP Energies Nouvelles, France  
Docteur, IFP Energies Nouvelles, France

Rapporteur  
Rapporteur  
Examinateur  
Président du jury  
Examinateur  
Examinateur  
Examinateur  
Directeur de thèse





---

# Abstract

---

A numerical study of nozzle flow and primary breakup in Diesel injection is conducted in order to understand the link between injector geometry and fuel atomization. Owing to the complex physical processes involved, flow compressibility effects are studied separately from turbulence and vortex dynamics.

In a first part, a 5-Equation model for two-phase, two-species flows is developed and implemented in the IFP-C3D code to analyze the flow behavior under compressibility effects. It is intended for liquid-gas mixtures where the gas phase is composed of two species, vapor and noncondensable gas. It is the result of a reduction of a 7-Equation model, assuming instantaneous velocity and pressure equilibrium. Heat and mass transfer are taken into account by assuming temperature and Gibbs free energy equilibrium.

The model is validated against three well-known test cases: shock tube, water cavitation tube and two-phase expansion tube. The results show its ability to capture phase transition subject to strong expansion waves. Furthermore, its accuracy is comparable to that of a 7-Equation model, while allowing to reduce the computational cost by as much as 20%. Finally, the 5-Equation model is applied to a single hole injector in order to validate its ability to deal with cavitating flows and non-condensable gas expansion. The results are compared with available experimental and numerical data, showing that it is able to successfully predict vapor formation and air expansion. The proposed 5-Equation model is ready to be used for investigating nozzle flow under real operating conditions, provided that it is coupled with a turbulence model.

In a second part, the impact of nozzle geometry on turbulence generation, vortex dynamics and primary breakup is studied assuming incompressible flow. Large-Eddy Simulation is used to simulate the flow inside the nozzle and close to its exit. The investigation strategy consists of comparing different geometries with contrasting design parameters, isolating their impact on the flow behavior. In some cases, qualitative correlations between numerical results and X-ray images of the near-nozzle spray are proposed.

The results show that fuel atomization in the primary breakup region is driven by vortex dynamics. More specifically, there are two events that play a key role in liquid ligament formation and breakup: a high frequency event triggered by shed vortices generated at the nozzle inlet, and a low frequency event caused by large string vortices formed in the sac as a consequence of flow recirculation. The complex interaction between shed vortices and string vortices determines not only the breakup pattern and the spray stability, but also the size of ligaments and droplets. In view of the results, it is concluded that acting on these two structures makes it possible to control the dynamics of the spray to some extent, enhancing atomization and increasing spray stability.

As a future perspective, research work aimed at finding quantitative correlations between vortices generated inside the nozzle and droplet size distribution in the spray could contribute increasing the predictivity of reactive spray simulations.



*A mis padres...*



---

# Acknowledgments

---

Completing this thesis has been possible thanks to the support of many people. I would like to acknowledge especially those whose contribution has been key to the success of this work.

First of all, I would like to thank my jury members Prof. Christian Hasse, Prof. Richard Saurel and Prof. Grégoire Allaire for their time and interest in reading my thesis.

I would like to thank Dr. Gavin Dober and Dr. Nouredine Guerrassi for their immense support and valuable advice. My most sincere gratitude to Dr. Junmei Shi for his guidance throughout the whole PhD. His great knowledge, enthusiasm and admirable dedication encouraged me to put in my best efforts.

I am very grateful to Dr. Stéphane Jay for his help during the development of the multiphase model at IFP. I appreciate his clever advice and our always productive discussions. A huge thank you goes to Dr. Christian Angelberger for his great support and kindness, especially during the writing process. I am greatly indebted to him for his efforts reading my thesis over and over again, never complaining and always providing constructive feedback.

The numerical results presented in this thesis would not have been obtained without the simulation tools provided by ANSYS. I express my most sincere gratitude to Dr. Wolfgang Bauer, who always trusted in the value of this work and genuinely offered his unconditional support. As for the experimental data, I would like to give considerable thanks to Prof. Ming-Chia Lai for his collaboration and for sharing his impressive results. Finally, I want to thank the FNR for funding my PhD project (number 588638).

During the last three years I have been very lucky to meet people from different cultures and backgrounds that have made of this PhD a unique experience. I will never forget the moments shared with Eduardo, Kristijan, Harun, Kevin, Davide, Benedikt, Francesco and Rafael, who are now among my dearest friends. I also owe a big thank you to the people from the Advanced Injection and Combustion Center at Delphi and the people from IFP Energies Nouvelles for their help throughout the project.

On a more personal note, I would like to thank my whole family for their love and support to the very last day of the PhD. To my parents, who suffered with me the joys and pains of this adventure and to my sister, whose immense kindness was a continuous source of inspiration.

Finally, my most sincere thank you goes to my dear partner Francesca, for her love and trust and for always motivating me in every challenge I took. Although being more than a thousand kilometers apart has been the hardest part of this adventure, I learned to value every moment we shared. I am thrilled to look ahead to the future and think of the new experiences we will live together.

Pablo Aguado



---

# Contents

---

<b>List of Figures</b>	<b>v</b>
<b>List of Tables</b>	<b>ix</b>
<b>Nomenclature</b>	<b>xi</b>
<b>I Context and objectives</b>	<b>1</b>
<b>1 Introduction</b>	<b>3</b>
1.1 Research context . . . . .	3
1.2 Motivations . . . . .	5
1.3 Objectives and approach . . . . .	7
1.4 Structure of the thesis . . . . .	8
<b>2 Literature review</b>	<b>11</b>
2.1 Introduction . . . . .	11
2.2 Physical processes in nozzle and near-nozzle flows . . . . .	12
2.2.1 Nozzle flows . . . . .	12
2.2.2 Near-nozzle flows . . . . .	17
2.3 Mathematical and numerical models for nozzle flow and primary breakup . . .	21
2.3.1 Models for in-nozzle flows . . . . .	22
2.3.2 Models for near-nozzle flows . . . . .	24
2.3.3 Turbulence models . . . . .	29
2.4 Analysis methods . . . . .	33
2.4.1 Vortex identification . . . . .	33
2.4.2 Flow pattern characterization . . . . .	35
2.5 Conclusions . . . . .	36
<b>II Development of a multiphase model for compressible flows</b>	<b>37</b>
<b>3 5-Equation model for compressible, two-phase, two-species flows</b>	<b>39</b>
3.1 Introduction . . . . .	39
3.2 5-Equation reduced model . . . . .	39
3.3 5-Equation model formulation . . . . .	43
3.3.1 Thermodynamic closure . . . . .	44

3.3.2	Mixture temperature . . . . .	45
3.3.3	Heat transfer . . . . .	47
3.3.4	Mass transfer . . . . .	48
3.4	Numerical Method . . . . .	55
3.4.1	Phase-Splitting method . . . . .	55
3.4.2	Implicit calculation of diffusion terms . . . . .	57
3.4.3	Explicit calculation of convective terms . . . . .	64
3.4.3.1	Interface reconstruction . . . . .	65
3.4.4	Calculation of heat transfer . . . . .	67
3.4.5	Calculation of mass transfer . . . . .	67
3.4.6	Calculation of thermodynamic variables using the EOS . . . . .	68
3.5	Conclusions . . . . .	69
<b>4</b>	<b>5-Equation model validation</b>	<b>71</b>
4.1	Introduction . . . . .	71
4.2	Shock tube . . . . .	72
4.2.1	Computational performance . . . . .	74
4.3	Water cavitation tube . . . . .	75
4.4	Two-phase expansion tube . . . . .	77
4.5	Single hole injector . . . . .	79
4.5.1	Problem set-up . . . . .	79
4.5.2	Analysis of results . . . . .	82
4.6	Conclusions . . . . .	86
<b>III</b>	<b>Exploring nozzle geometry impact on internal nozzle flow and primary breakup</b>	<b>89</b>
<b>5</b>	<b>Investigation strategy and simulation methodology</b>	<b>91</b>
5.1	Investigation strategy . . . . .	91
5.2	X-ray image processing . . . . .	94
5.3	LES of in-nozzle flow . . . . .	98
5.3.1	Model setup . . . . .	98
5.3.2	Mesh generation and boundary conditions . . . . .	98
5.3.3	Numerical setup, flow initialization and workflow . . . . .	102
5.3.4	Verification of mesh resolution for LES . . . . .	104
5.3.5	Cavitation model evaluation . . . . .	106
5.4	LES of in-nozzle and near-nozzle flow . . . . .	108
5.4.1	Computational domain and mesh generation . . . . .	109
5.4.2	Model setup and verification of mesh resolution for LES . . . . .	110



<b>6</b>	<b>Analysis of LES of in-nozzle flow</b>	<b>113</b>
6.1	Introduction . . . . .	113
6.2	Needle lift effect . . . . .	114
6.2.1	LES of in-nozzle flow . . . . .	114
6.2.2	Correlation between LES of in-nozzle flow and X-ray images of near-nozzle flow . . . . .	118
6.3	Hole inlet rounding effect . . . . .	121
6.3.1	LES of in-nozzle flow . . . . .	121
6.3.1.1	High frequency event . . . . .	125
6.3.1.2	Low frequency event . . . . .	127
6.3.2	Correlation between LES of in-nozzle flow and X-ray images of near-nozzle flow . . . . .	129
6.4	Hole length effect . . . . .	133
6.5	Hole number effect . . . . .	138
6.6	Hole taper effect . . . . .	142
6.7	Conclusions . . . . .	147
<b>7</b>	<b>Analysis of LES of in-nozzle and near-nozzle flow</b>	<b>151</b>
7.1	Introduction . . . . .	151
7.2	Link between vortex dynamics and liquid-gas interface . . . . .	151
7.3	Correlation between LES results and X-ray images . . . . .	158
7.4	Conclusions . . . . .	164
<b>IV</b>	<b>Conclusions</b>	<b>167</b>
<b>8</b>	<b>Conclusions and future research</b>	<b>169</b>
8.1	General conclusions . . . . .	169
8.2	Recommendation for future work . . . . .	172
	<b>Bibliography</b>	<b>175</b>
<b>A</b>	<b>Calculation of SG-EOS parameters</b>	<b>191</b>
<b>B</b>	<b>Derivation of the mixture energy equation coefficients</b>	<b>195</b>
<b>C</b>	<b>IFP-C3D solver</b>	<b>199</b>
<b>D</b>	<b>Mathematical model and numerical method for LES of in-nozzle flow</b>	<b>201</b>
D.1	Mixture model . . . . .	201
D.2	LES model . . . . .	203
D.3	Numerical method . . . . .	206
D.3.1	Interface reconstruction . . . . .	208

<b>E</b>	<b>Impact of URANS-LES interface on turbulence and vortex generation</b>	<b>209</b>
E.1	Turbulence generation method at the interface . . . . .	209
E.2	Interface position . . . . .	212
<b>F</b>	<b>Implementation of Proper Orthogonal Decomposition (POD)</b>	<b>215</b>

---

# List of Figures

---

1.1	Influence of injector design on pollutant emissions and nozzle efficiency . . . . .	4
1.2	Example of Diesel injector compared to a conventional pen . . . . .	5
1.3	Schematic representation of injection and combustion processes . . . . .	5
1.4	Physical processes in the nozzle and spray . . . . .	6
2.1	Sequence of nozzle flow images after start of injection . . . . .	13
2.2	High resolution CCD camera visualization of transparent nozzle . . . . .	14
2.3	X-ray micro-CT of single-hole nozzle . . . . .	14
2.4	X-ray radiography of single hole nozzle . . . . .	15
2.5	Experimental and numerical results of 5-hole cylindrical nozzle . . . . .	16
2.6	Visualization of in-nozzle and near-nozzle flows during full needle lift . . . . .	18
2.7	Long-distance microscopy of VCO nozzle . . . . .	19
2.8	Ballistic Imaging of single hole nozzle . . . . .	19
2.9	Near-nozzle jet morphology characterization using X-ray PCI . . . . .	21
2.10	Primary breakup regimes . . . . .	26
2.11	Schematic representation of the turbulent kinetic energy spectrum . . . . .	31
2.12	Vortex structures predicted by different turbulence models . . . . .	33
2.13	Vortex structure visualization in isotropic turbulence decay . . . . .	34
2.14	Comparison between POD and DMD methods for subsonic gas jet . . . . .	36
3.1	Internal energy of the mixture per unit volume vs temperature of the mixture .	46
3.2	Flow-tracking control volume in the phase-splitting technique . . . . .	56
3.3	Phase-splitting strategy . . . . .	58
3.4	Definition of volume swept between stages B and C . . . . .	65
3.5	Representation of cell face normal and sign criterion for the volume swept . . .	66
4.1	Initial conditions and dimensions of the shock tube test case . . . . .	72
4.2	Shock tube test case results at $t = 5.10^{-4}s$ . . . . .	73
4.3	Shock tube test case results at $t = 5.10^{-4}s$ with increased dissolved phase . . .	74
4.4	Initial conditions and dimensions of the water cavitation tube test case . . . .	75
4.5	Water cavitation tube without mass transfer at $t = 3.2ms$ . . . . .	76
4.6	Water cavitation tube with mass transfer enabled at $t = 3.2ms$ . . . . .	77
4.7	Initial conditions and dimensions of the two-phase expansion tube . . . . .	78
4.8	Two-phase expansion tube tests using the 5-Equation model . . . . .	78

4.9	Vaporization front velocity for different initial liquid temperatures . . . . .	79
4.10	Single hole injector geometry and experimental test conditions . . . . .	80
4.11	Single hole injector mesh and boundary conditions . . . . .	80
4.12	Void fraction integrated along the transverse direction . . . . .	83
4.13	Close-up view of the 5-Equation model void fraction . . . . .	83
4.14	Pressure and axial velocity color iso-levels obtained with 5-Equation model . .	84
4.15	Pressure distribution along nozzle hole centerline . . . . .	84
4.16	Comparison of gas, vapor and air color iso-levels on the mid-cut plane . . . . .	85
5.1	Nozzle designs considered . . . . .	92
5.2	X-ray PCI images of near-nozzle flow . . . . .	93
5.3	2D FFT image processing of the Sharp edge nozzle . . . . .	96
5.4	1D-directional FFT of the Sharp edge nozzle . . . . .	97
5.5	Reference nozzle geometry . . . . .	99
5.6	Computational mesh of Reference nozzle . . . . .	100
5.7	Boundary conditions and internal interfaces . . . . .	102
5.8	Simulation strategy . . . . .	103
5.9	Mass flow rate convergence history . . . . .	104
5.10	$y^+$ color iso-levels on the housing and hole. Reference nozzle . . . . .	104
5.11	SGS viscosity ratio and cell-based CFL number. Reference nozzle . . . . .	105
5.12	Velocity, volume fraction and TKE for different cavitation model coefficients . .	107
5.13	Vortex and cavitation structures for different cavitation model settings . . . . .	108
5.14	Mesh definition of the coupled internal nozzle - spray simulation . . . . .	109
5.15	SGS viscosity ratio and CFL number. LES of in-nozzle and near-nozzle flow . .	111
5.16	Sketch of 2D interface smearing due to numerical diffusion . . . . .	112
5.17	Estimation of droplet size based $d_{1\%}$ criterion . . . . .	112
6.1	Vortex and cavitation structures. Needle lift effect . . . . .	114
6.2	Average velocity and resolved turbulent kinetic energy. Needle lift effect . . . .	115
6.3	Instantaneous turbulent kinetic energy and volume fraction. Needle lift effect .	116
6.4	POD at the hole exit plane. Needle lift effect . . . . .	117
6.5	POD modal energy and accumulated energy. Needle lift effect . . . . .	118
6.6	Correlation between LES results and X-ray images. Needle lift effect . . . . .	119
6.7	Correlation between string vortex and breakup initiation. Needle lift effect . . .	120
6.8	Average velocity and resolved TKE. Hole inlet rounding effect . . . . .	121
6.9	Vortex and cavitation structures. Hole inlet rounding effect . . . . .	122
6.10	Instantaneous TKE and vapor volume fraction. Hole inlet rounding effect . . .	123

6.11	Mass flow rate at the hole outlet and its FFT. Hole inlet rounding effect . . . .	124
6.12	High frequency event in the Sharp edge nozzle . . . . .	125
6.13	Shed vortex dynamics. Hole inlet rounding effect . . . . .	126
6.14	Low frequency event in the Rounded nozzle . . . . .	128
6.15	Correlation between LES results and X-ray images. Hole inlet rounding effect .	130
6.16	Characteristic length scale of interface structures. Hole inlet rounding effect . .	131
6.17	Link between shed vortices and interface structures. Hole inlet rounding effect	132
6.18	Average velocity and resolved turbulent kinetic energy. Hole length effect . . .	133
6.19	Vortex and cavitation structures. Hole length effect . . . . .	134
6.20	Instantaneous TKE and vapor volume fraction. Hole length effect . . . . .	135
6.21	Link between MFR and vortex dynamics in the Short hole nozzle . . . . .	136
6.22	POD at the hole exit plane. Hole length effect . . . . .	138
6.23	POD modal energy and accumulated energy. Hole length effect . . . . .	138
6.24	Average velocity and resolved turbulent kinetic energy. Hole length effect . . .	139
6.25	Vortex and cavitation structures. Hole number effect . . . . .	140
6.26	Mass flow rate and FFT. 6-Hole nozzle . . . . .	141
6.27	Average velocity and resolved turbulent kinetic energy. Hole taper effect . . . .	142
6.28	Vortex and cavitation structures. Hole taper effect . . . . .	143
6.29	Instantaneous resolved TKE and vapor volume fraction. Hole taper effect . . .	144
6.30	Low frequency event in the HP hole nozzle . . . . .	146
6.31	Vortex shedding phenomenon. Hole taper effect . . . . .	147
7.1	Correlation between shed vortices, surface vortices and ligament breakup . . .	152
7.2	Vortex driven atomization process . . . . .	153
7.3	Quantitative correlation of in-nozzle and near-nozzle vortices . . . . .	154
7.4	In-nozzle - near-nozzle vortex and liquid-gas interface correlation. Front view .	155
7.5	In-nozzle - near-nozzle vortex and liquid-gas interface correlation. Bottom view	157
7.6	Liquid-gas interface deformation caused by secondary vortices . . . . .	158
7.7	Correlation between liquid-gas interface predicted by LES and X-ray images. Instant 1 . . . . .	159
7.8	Correlation between liquid-gas interface predicted by LES and X-ray images. Instant 2 . . . . .	160
7.9	Probability density function of characteristic length scale. HP hole nozzle . . .	161
7.10	Correlation between liquid-gas interface predicted by LES and X-ray images. Instant 3 . . . . .	162
7.11	Correlation between liquid-gas interface predicted by LES and X-ray images. Instant 4 . . . . .	163
7.12	Correlation between liquid-gas interface predicted by LES and X-ray images. Instant 5 . . . . .	164

A.1	Experimental and approximated curves of specific enthalpy of Viscor 16BR . . .	192
A.2	Experimental and approximated curves of specific volume at saturation conditions of Viscor 16BR . . . . .	193
C.1	IFP-C3D solver flowchart . . . . .	200
D.1	Solver flow chart . . . . .	208
E.1	Computational domain for turbulence generation method evaluation . . . . .	210
E.2	Average velocity and TKE using the initial mesh . . . . .	211
E.3	Instantaneous Q-criterion iso-surfaces. Synthetic turbulence and vortex generation methods . . . . .	212
E.4	Mesh used for URANS-LES interface position evaluation. Reference nozzle . .	213
E.5	Instantaneous Q-criterion iso-surfaces. Initial and extended URANS-LES interface postion . . . . .	213
F.1	Example of POD . . . . .	216

---

# List of Tables

---

3.1	Differences between one-species and two-species models in the mass transfer process . . . . .	54
4.1	Computational efficiency of the 5-Equation model compared with the 7-Equation model implemented in IFP-C3D . . . . .	75
4.2	Initial liquid temperature and pressure and vaporization front velocities . . . .	79
4.3	Summary of simulation settings . . . . .	81
5.1	Summary of experimental data available and numerical simulations conducted .	94
5.2	1D FFT setup parameters . . . . .	98
6.1	Comparison between shed vortex length scale (LES) and interface structure length scale (X-ray). Hole inlet rounding effect . . . . .	131





---

# Nomenclature

---

## Roman Symbols

A	Area [ $m^2$ ]
$C_d$	Discharge coefficient $[-]$
$C_v$	Specific heat capacity at constant volume [ $J.kg^{-1}.K^{-1}$ ]
$C_p$	Specific heat capacity at constant pressure [ $J.kg^{-1}.K^{-1}$ ]
D	Species diffusion coefficient [ $m^2.s^{-1}$ ]
E	Specific total energy [ $J.kg^{-1}$ ]
$e$	Specific internal energy [ $J.kg^{-1}$ ]
$g$	Specific Gibbs free energy [ $J.kg^{-1}$ ]
$h$	Specific enthalpy [ $J.kg^{-1}$ ]
$k$	Turbulent kinetic energy [ $m^2.s^{-2}$ ]
K	Thermal conductivity [ $J.K^{-1}.m^{-1}.s^{-1}$ ]
M	Molar weight [ $mol$ ]
$p$	Pressure [ $Pa$ ]
Q	Heat transfer per unit volume [ $J.s^{-1}.m^{-3}$ ]
R	Ideal gas constant [ $kg.mol^{-1}.K^{-1}$ ]
$s$	Specific entropy [ $J.K^{-1}.kg^{-1}$ ]
t	Time [ $s$ ]
$T$	Temperature [ $K$ ]
$u$	Velocity [ $m.s^{-1}$ ]
V	Volume [ $m^3$ ]
Y	Mass fraction $[-]$

## Greek Symbols

$\alpha$	Volume fraction $[-]$
$\gamma$	Specific heat capacity ratio $[-]$
$\varepsilon$	Internal energy per unit volume [ $J.m^{-3}$ ] / Turbulence dissipation rate [ $m^2.s^{-3}$ ]

$\eta$	Kolmogorov length scale $[m]$
$\kappa$	Temperature relaxation coefficient $[J.m^{-3}]$
$\lambda$	Velocity relaxation coefficient $[kg.m^{-3}.s^{-1}]$
$\mu$	Dynamic viscosity $[kg.m^{-1}s^{-1}]$
$\nu$	Kinematic viscosity $[m^2s^{-1}]$
$\rho$	Density $[kg.m^{-3}]$
$\sigma$	Surface tension $[J.m^{-2}]$
$\omega$	Specific dissipation rate $[s^{-1}]$

## Dimensionless numbers

$CN$	Cavitation number
$Oh$	Ohnesorge number
$Re$	Reynolds number
$St$	Strouhal number
$We$	Weber number

## Acronyms

AKE	Axial Kinetic Energy
BI	Ballistic Imaging
CCD	Charge-Coupled Device
CFL	Courant-Friedrich-Levy
CICSAM	Compressive Interface Capturing Scheme for Arbitrary Meshes
CLSVOF	Combined Level Set Volume of Fluid
CT	Computed Tomography
DMD	Dynamic Mode Decomposition
DNS	Direct Numerical Simulation
EGR	Exhaust Gas Recirculation
ELSA	Eulerian-Lagrangian Spray Atomization
EOS	Equation of State
FFT	Fast Fourier Transform

GDI	Gasoline Direct Injection
GERM	Gibbs Energy Relaxation Model
HEM	Homogeneous Equilibrium Model
HLLC	Harten-Lax-van Leer-Contact
HRM	Homogeneous Relaxation Model
HT	Heat Transfer
LES	Large-Eddy Simulation
MFR	Mass Flow Rate
MOF	Moment-of-Fluid
MT	Mass Transfer
NAKE	Non-Axial Kinetic Energy
PCI	Phase-Contrast Imaging
POD	Proper Orthogonal Decomposition
PRESTO	Pressure Staggering Option
QSOU	Quasi-Second-Order Upwind
RANS	Reynolds-Averaged Navier Stokes
ROI	Region of Interest
RSM	Reynolds Stress Model
SAS	Scale-Adaptive Simulation
SG	Stiffened Gas
SGS	Sub-Grid Scale
SIMPLEC	Semi-Implicit Method for Pressure Linked Equations-Consistent
SLIPI	Structured Laser Illumination Planar Imaging
SRS	Scale-Resolving Simulation
SST	Shear Stress Transport
TAB	Taylor Analogy Breakup
TKE	Turbulent Kinetic Energy
URANS	Unsteady Reynolds-Averaged Navier Stokes
VCO	Valve Covered Orifice
V-LES	Very Large-Eddy Simulation
VOF	Volume of Fluid
VD	Viscous Dissipation
WALE	Wall-Adapting Local Eddy-Viscosity



## Part I

# Context and objectives



# Chapter 1

---

## Introduction

---

### 1.1 Research context

The increasingly restrictive emission regulations for Diesel engines and the need for higher fuel economy have fostered the development of new technologies for fuel injection and combustion systems. Reducing the levels of exhausted species such as carbon dioxide (CO<sub>2</sub>), nitrogen oxides (NO<sub>x</sub>), unburned hydrocarbons (HC), carbon monoxide (CO) and particulates (PM) entails optimizing each component as part of the whole system, taking into account the interaction between different elements. This interdependence, together with the broad range of operating points, makes it very challenging to come up with a single design that satisfies all the requirements under real operating conditions.

The influence of fuel injection on combustion efficiency and pollutant emissions has been intensively investigated over the last decades, aiming at understanding the link between injector design, spray atomization, mixture formation and combustion performance. It is known that the injector geometry has a strong impact on emissions, as the flow developed inside the injector directly affects the atomization and mixing mechanisms leading to combustion. This is illustrated in Figure 1.1 showing the potential reduction of CO<sub>2</sub>, NO<sub>x</sub> and PM that can be obtained by modifying the injector hole geometry. Increasing the hole conicity (higher taper) can reduce the PM by 45% or the NO<sub>x</sub> by 20% with exhaust gas recirculation (EGR), determining whether the emissions are compliant with the legislation or not. As illustrated in Figure 1.1b, the hole geometry can also affect the injector efficiency, measured in terms of the discharge coefficient  $C_d$  as the actual mass flow rate relative to the ideal mass flow rate (based on isentropic evolution). Additionally, Figure 1.1c shows the correlation between smoke and  $C_d$  under different operating conditions, suggesting that smoke is very sensitive to  $C_d$ .

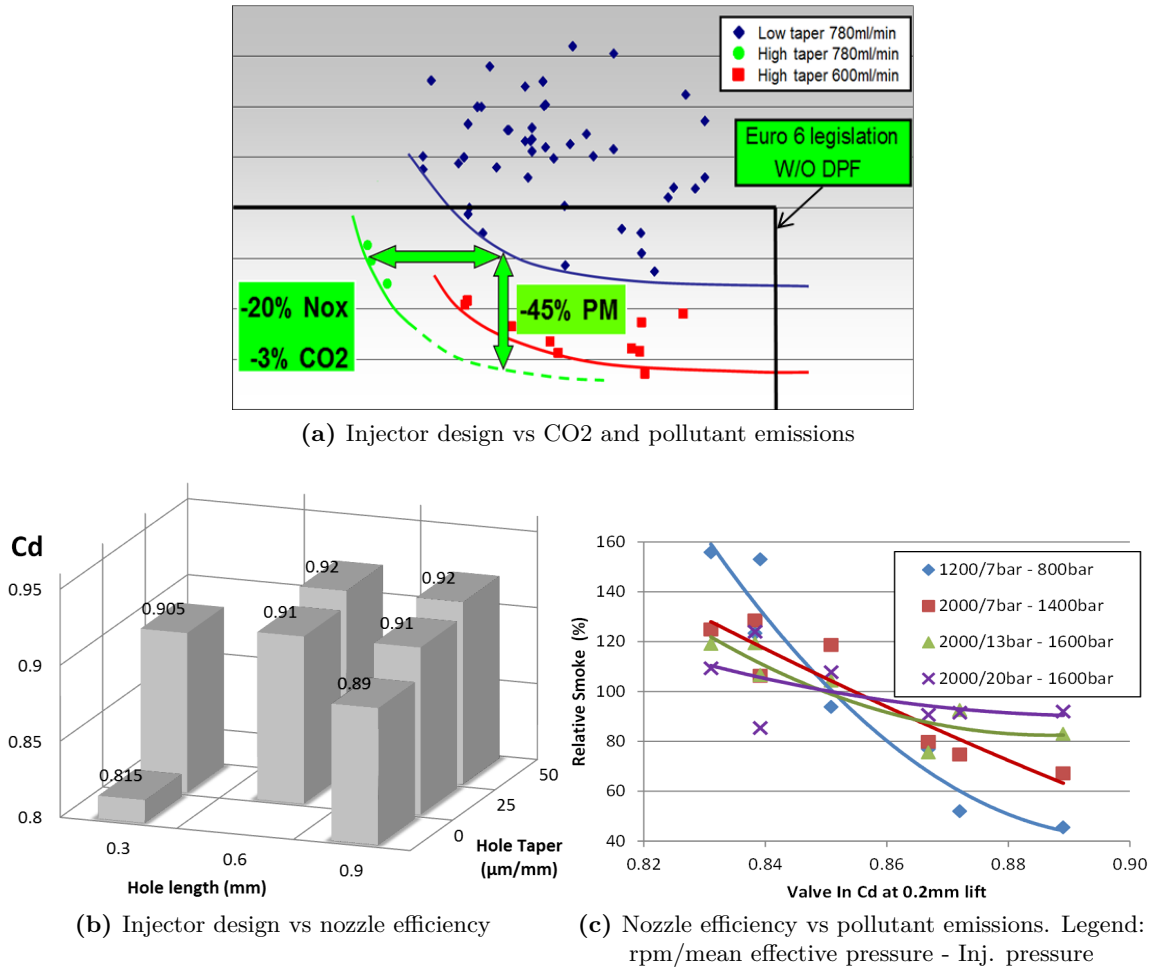


**Figure 1.1:** Influence of injector design on pollutant emissions and nozzle efficiency. Delphi internal report

There is a general lack of sufficiently detailed knowledge of how the flow features generated inside the injector propagate outside and affect the atomization and mixing processes. Many empirical correlations have been proposed in order to link injection design parameters and operating conditions (i.e. injection pressure, injection orifice diameter, etc.) to spray features such as droplet size distribution, spray angle and liquid penetration length. Although these correlations can be used as a first approximation to the problem, they are unable to predict the intricate relationship between injector design and atomization, especially for the increasingly complex injector geometries. Understanding this link requires identifying and characterizing the physical processes inside the injector, determining how they affect the atomization mechanisms. Unfortunately, these processes remain largely unknown due to their complexity and to the limited experimental accessibility resulting from the combination of high injection pressures and micro-scale injectors.



## 1.2 Motivations

Knowledge-based injector design is of great interest for the industry as it would allow predicting the performance of a certain injector in early design stages. To acquire the necessary knowledge, a detailed understanding of how the physical processes developing inside and outside the injector interact is essential. On the one hand, the experimental studies characterizing the flow inside the injector, or simply in-nozzle flow, are limited by the small diameters of nozzle holes of the order of few micro-meters (Figure 1.2) and very high injection pressures above 2000 bar. Optical access cannot be easily achieved due to the very small spatial scales and extreme thermodynamic conditions, preventing optical diagnostic techniques from characterizing the nozzle flow. Hence, experimental studies are very scarce and are typically restricted to large-scale nozzles under lower operating pressures. Moreover, owing to significantly different thermodynamic conditions and length-scales between in-nozzle, primary breakup, secondary breakup and combustion (Figure 1.3), they often neglect the flow field outside the injector and do not provide information about how the internal features affect the spray. On the other hand, the experimental and numerical investigations focusing on atomization, evaporation, mixing and combustion, generally provide little or no information about the in-nozzle flow, preventing the full interpretation of the atomization mechanisms. Linking the in-nozzle flow and spray is therefore of great interest for the industry to better predict the injector design impact on combustion performance and to support the development of more accurate numerical models.

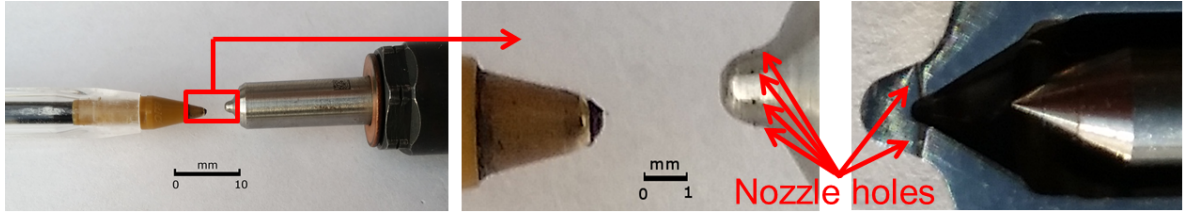


**Figure 1.2:** Example of Diesel injector compared to a conventional pen

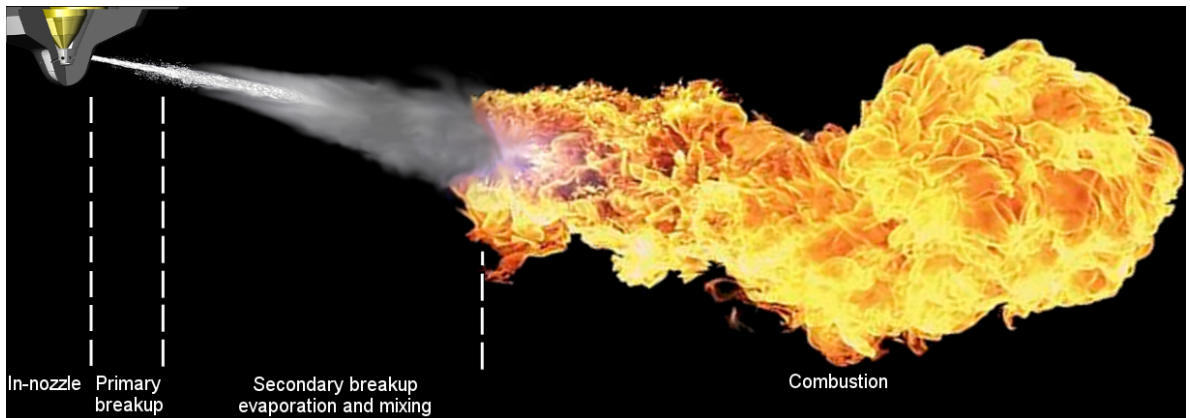


**Figure 1.3:** Schematic representation of injection and combustion processes

The diversity of physical processes associated with in-nozzle flow and spray in Diesel engines holds great complexity. At high pressures the in-nozzle flow is subject to strong acceleration and pressure gradients, leading to compressibility effects, heat and mass transfer, and intense

turbulence generation. The resulting fluid is a mixture of liquid, vapor and non-condensable gases (i.e. air) with strong density and viscosity variation. As sketched in Figure 1.4, the problem involves multiple flow scales where cavitation and turbulence play a very important role. Outside the nozzle, the liquid-gas mixture undergoes strong aerodynamic effects, breaking up into ligaments and droplets (primary breakup). Subsequently, these droplets collide, collapse and undergo further atomization, forming a dense cloud around the spray axis (secondary breakup) that evaporates and mixes with the air before combustion.

If the atomization mechanisms are identified and linked to the main geometric features, it would be easier to select the configuration that leads to a specific spray pattern. Understanding this link requires combining experimental measurements whenever possible and numerical methods in those regions where experimental accessibility is poor or cannot provide the desired information. The most advanced experimental techniques allow measuring the flow field very close to the injector holes, providing useful information about the primary breakup of real-size nozzles under high injection pressures. Unfortunately, they cannot easily penetrate the metal housing, especially when the experiment relies on low frequency radiation such as visible light. As a result of this limitation, numerical modeling stands as the best option to “see” inside the injector in real-size nozzles.

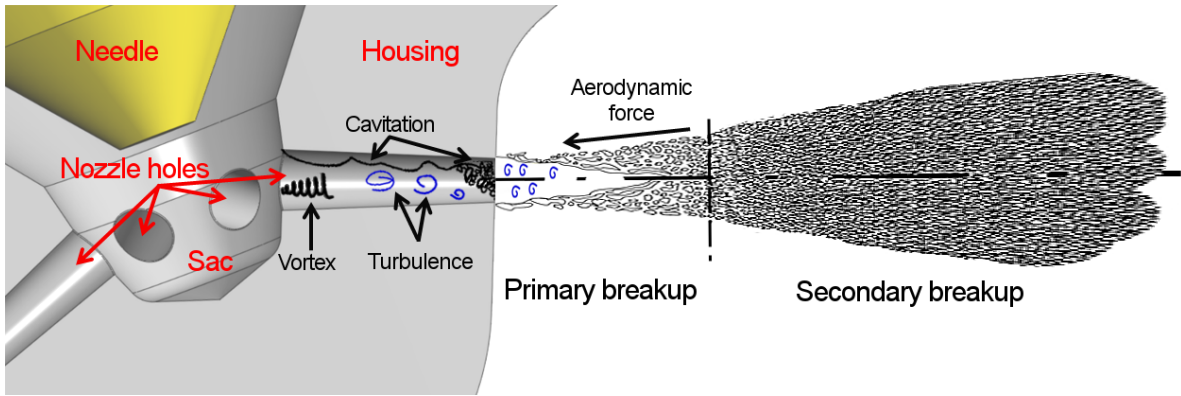


**Figure 1.4:** Physical processes in the nozzle and spray

From a numerical standpoint, modeling the in-nozzle flow is an arduous task. First, accounting for the liquid compressibility requires resolving the pressure wave propagation at very high speed, establishing restrictive numerical stability conditions. Additionally, modeling cavitation and heat transfer increases the complexity as well as the computational cost of the simulations, introducing their own stability requirements. Finally, the turbulence structures and vortex dynamics can only be accurately resolved using very fine computational grids, which in turn affect the numerical stability. Owing to these difficulties, it is often necessary to investigate the aforementioned effects separately as far as possible, notwithstanding the fact that all cited phenomena are interdependent.

The present technological trend in Diesel engines is towards multiple-injection patterns where the main injection event is followed or preceded by shorter pilot injections. During these pilots, aimed at favoring evaporation and combustion of fuel issued during the main injection, the needle describes a ballistic motion where highly compressible phenomena associated with needle opening and closing dominate the flow. Examples of these are the air compressibility during sac filling, the shock and expansion waves triggered in the near-nozzle region around

### 1.3 Objectives and approach

---

the liquid jet, and the pressure waves generated by cavitation bubble expansion and collapse (closely related to erosion damage). Apart from the pilot injection, extremely high operating pressures can eventually induce supercritical conditions. In this state, the liquid and gas phases are no longer defined and the resulting fluid shares properties of both phases with strong changes in viscosity and surface tension. To account for supercritical fluids the models have to be equipped with sophisticated equations of state, adding more complexity to the numerical approach.

Flows developing under lower injection pressures (i.e 800 bar) are less affected by compressibility and more affected by turbulence and vortex structures, which depend largely on the nozzle geometry. These structures develop inside the injector and spread to the spray, contributing to the atomization process. To resolve the multiple-scale problem originated, it is necessary to use millions of computational cells and high-order numerical schemes with low discretization errors, leading to expensive simulations. Resolving these scales is essential to accurately capture vortex dynamics and turbulence generation, which are key to understand the influence of nozzle geometry on primary breakup.

Numerical tools able to predict the influence of injector design on spray atomization are of great interest to industry, especially if they are accessible at low cost. However, the need for quick answers and the limitations in computational power make it very difficult to resolve all phenomena simultaneously. For this reason, and considering the lower impact of flow compressibility compared with vortex dynamics and turbulence at lower injection pressures, it is reasonable to study both phenomena separately based on this parameter. This allows providing an interpretation of their influence on the in-nozzle flow and spray atomization.

### 1.3 Objectives and approach

The present work aims at contributing to the understanding of in-nozzle flow dynamics and primary breakup. Accordingly, the following research question are posed:

- What are the main processes developing inside the nozzle?
- How are these processes linked to nozzle geometry and primary breakup?

The following objectives have been identified to answer these questions:

- Establish the equations and associated thermodynamic closure relations for the investigation of in-nozzle flow under cavitating conditions including compressibility and thermal effects
- Investigate the impact of nozzle geometry on turbulence, vortex dynamics and primary breakup using high fidelity simulations of incompressible flow and experimental results

Flow compressibility, heat transfer and the effect of non-condensable gases are addressed via the formulation of a fully compressible multiphase, multispecies model and its implementation in the IFP-C3D code [1, 2]. The model assumes thermodynamic equilibrium, including heat and mass transfer based on temperature and Gibbs free energy equilibrium. It is validated

against well-known one-dimensional test cases and is finally applied to a single hole injector under cavitating conditions.

Complementary to the model development work, the effect of vortex dynamics and turbulence are investigated using Large-Eddy Simulation (LES) of different nozzle layouts at low injection pressure of 800 bar. The multiphase flow is considered incompressible and isothermal, but enables mass transfer between the liquid and the incompressible vapor. Although these assumptions simplify the model considerably, they are deemed sufficient to capture the dominant flow structures qualitatively. To understand how different injector design parameters affect the flow dynamics, a systematic approach including a number of typical designs with extreme features is applied. Once the dominant processes are identified in each design, they are correlated with experimental X-ray Phase Contrast Imaging (PCI) visualizations of the near-nozzle spray. Under non-cavitating conditions, it is possible to simulate the near-nozzle flow using interface-tracking methods. A non-cavitating case is selected and simulated, comparing the liquid-gas interface predicted with the structures observed in X-ray images.

The approach followed to accomplish the objectives can be summarized as follows

- Development and validation of a compressible, two-phase, two-species 5-Equation model to provide a computationally efficient and robust numerical framework to assess the impact of compressibility and heat transfer on the in-nozzle flow
  - Validation against well-known one-dimensional test cases
  - Application to single-hole injector under cavitating conditions, comparing the results with experimental visualizations
- Development of a simulation methodology to investigate vortex dynamics and turbulence generation using LES, assessing their impact on spray atomization
  - Systematic evaluation of the impact of contrasting design parameters on vortex dynamics inside the nozzle
  - Identification of possible links between LES results inside the nozzle and X-ray images outside the nozzle
  - Simulation of coupled LES of in-nozzle and near-nozzle flow for non-cavitating nozzle, comparing the predicted liquid-gas interface with X-ray visualizations

## 1.4 Structure of the thesis

This manuscript comprises three main parts:

The first Part reviews physical processes in nozzle and near-nozzle flows and numerical methods for multiphase flows, primary breakup, cavitation and turbulence (Chapter 2). The literature survey includes a review of analysis methods for vortex identification and flow pattern characterization in the context of LES.

In the second Part, the proposed 5-Equation multispecies model for compressible flows is described, as well as the numerical method used (Chapter 3). Validation is carried out

## 1.4 Structure of the thesis

---

using a number test cases (Chapter 4), namely the shock tube problem, water cavitation tube problem, two-phase expansion tube. Finally, the model is applied to a single hole injector under cavitating conditions with heat transfer, comparing the results with available experimental data and other similar models for cavitating flows.

The third Part is dedicated to the investigation of nozzle design impact on vortex dynamics and primary breakup using LES. The simulation and analysis methodology are presented in Chapter 5, detailing the problem setup (mesh generation, boundary conditions, flow initialization) and post-processing tools. The results concerning LES of in-nozzle flow are reported in Chapter 6, comparing several nozzle geometries in order to evaluate different effects such as needle lift, hole inlet rounding, hole tapering, hole length and hole number. Chapter 6 also includes qualitative correlation between LES of in-nozzle flow and X-ray images of near-nozzle flow. Finally, Chapter 7 provides direct comparison between LES results and X-ray images by simulating in-nozzle and near-nozzle flow simultaneously under non-cavitating conditions.

The last Part of the thesis is dedicated to the conclusions and recommendations for further work, which are discussed in Chapter 8.



## Chapter 2

---

# Literature review

---

---

### 2.1 Introduction

In-nozzle flows and sprays are paramount for the performance of internal combustion engines. They are responsible for providing an adequate mixture for the combustion to be carried out in an efficient and stable way. In Diesel engine injection systems in particular, the flow is subject to a wide range of thermodynamic conditions inducing very different physical sub-processes. For instance, an injected fluid particle initially stored at very high pressure ( $>2000$  bar), is strongly accelerated up to more than  $600$  m/s before being separated from the liquid core. Subsequently, it evaporates due to high temperatures in the combustion chamber, burns as part of the air-fuel mixture, and exits the chamber as exhaust gas.

Owing to different thermodynamic conditions and characteristic space and time scales, the study of Diesel injection has been traditionally separated into in-nozzle flow, primary breakup and secondary breakup. This separation is justified from a phenomenological perspective as long as the physical processes taking place inside the nozzle are very different from those developing outside. Whereas the in-nozzle flow is subject to very high pressure, the liquid core in the near-nozzle region undergoes strong aerodynamic interaction leading to surface distortion and ligament detachment. These aerodynamic effects become even more important further downstream, where the ligaments break up into smaller droplets that collide and coalesce. From a numerical standpoint, modeling all these phenomena is very challenging, since turbulence, flow compressibility, mass transfer and liquid-gas interaction can be very different inside and outside the nozzle. As a consequence, different numerical methods are required to successfully resolve the flow behavior in both regions.

This Chapter presents a literature survey focusing on nozzle flows and primary breakup in Diesel engine injection. First, Section 2.2 addresses the physical phenomena. Next, mathematical and numerical models for nozzle flow and near-nozzle atomization are reviewed in Section 2.3. Finally, Section 2.4 provides insight into analysis tools for turbulence and

vortex characterization.

## 2.2 Physical processes in nozzle and near-nozzle flows

### 2.2.1 Nozzle flows

For years, investigation of nozzle flow in Diesel engine injection has relied on non-invasive imaging techniques based on light absorption. Owing to the combination of very small geometries of the order of a few  $\mu\text{m}$  and injection pressures above 2000 bar, the need for using dense materials with limited optical accessibility has hampered their study. Physical processes developing inside the nozzle such as flow separation and recirculation, turbulence generation or cavitation are still far from being understood. However, the combination of recently developed experimental techniques and high-resolution numerical methods enables their detailed investigation, which is the first step towards linking them to spray atomization and mixture formation.

Experimental methods based on light absorption have been extensively used to characterize cavitation structures developing inside the nozzle. These structures are regarded as important phenomena contributing to in-nozzle flow mixing [3, 4, 5]. Owing to high injection pressures and small geometries of real-size injectors, most experimental studies focus on cavitation visualization using either scaled-up nozzles or low injection pressures. A very illustrative study of in-nozzle flow dynamics is found in Mitroglou et al. [6], who conducted a series of experimental visualizations in real-size, 6-hole, cylindrical, transparent nozzles (hole diameter 0.160 mm) operating at 300 bar to 1 bar back pressure. Their visualizations during a single injection event are reproduced in Figure 2.1, showing important phenomena associated with in-nozzle flows. At the beginning of the injection ( $t = 0$  ms), the nozzle is filled with stagnant bubbles that are evacuated immediately after needle opening. At low needle lift ( $t = 0.04$  ms), needle truncation leads to local flow separation and pressure drop, triggering cavitation at the needle seat sealing. Next, the flow is partially diverted directly into the holes and partially forced to recirculate in the sac, generating large vortices and cavitation onset in the low pressure vortex core ( $t = 0.66$  ms,  $t = 0.85$  ms). The cavitation string enters the hole with the recirculating flow moving all over the nozzle. This unstable behavior is clearly observed at time instants 0.66 ms and 0.85 ms, where the string appears near the upper inlet edge and in the center of the hole respectively. At 2.27 ms, cavitation forms on the upper side due to flow separation (geometric cavitation) and the string cavitation enters the hole from the lower side. Strong interaction between geometric and string cavitation structures results from the unstable behavior of the string. Finally, the low sac pressure after needle closing triggers air suction into the sac, yielding the dense cloud observed at 2.61 ms.

String cavitation not only affects the flow inside the nozzle hole but also the flow between adjacent holes (hole-to-hole interaction). Figure 2.2 reproduces the experimental results obtained by Arcoumanis et al. [7] using high resolution CCD camera visualizations of a transparent nozzle. Geometric cavitation onset on the upper side and the cavitation string entering the hole on the lower side are clearly distinguishable in the real-size nozzle shown in Figure 2.2a. The authors also used the large-scale nozzle reproduced in Figure 2.2b to get better resolution of the hole-to-hole interaction. The cavitation strings are connected inside



## 2.2 Physical processes in nozzle and near-nozzle flows

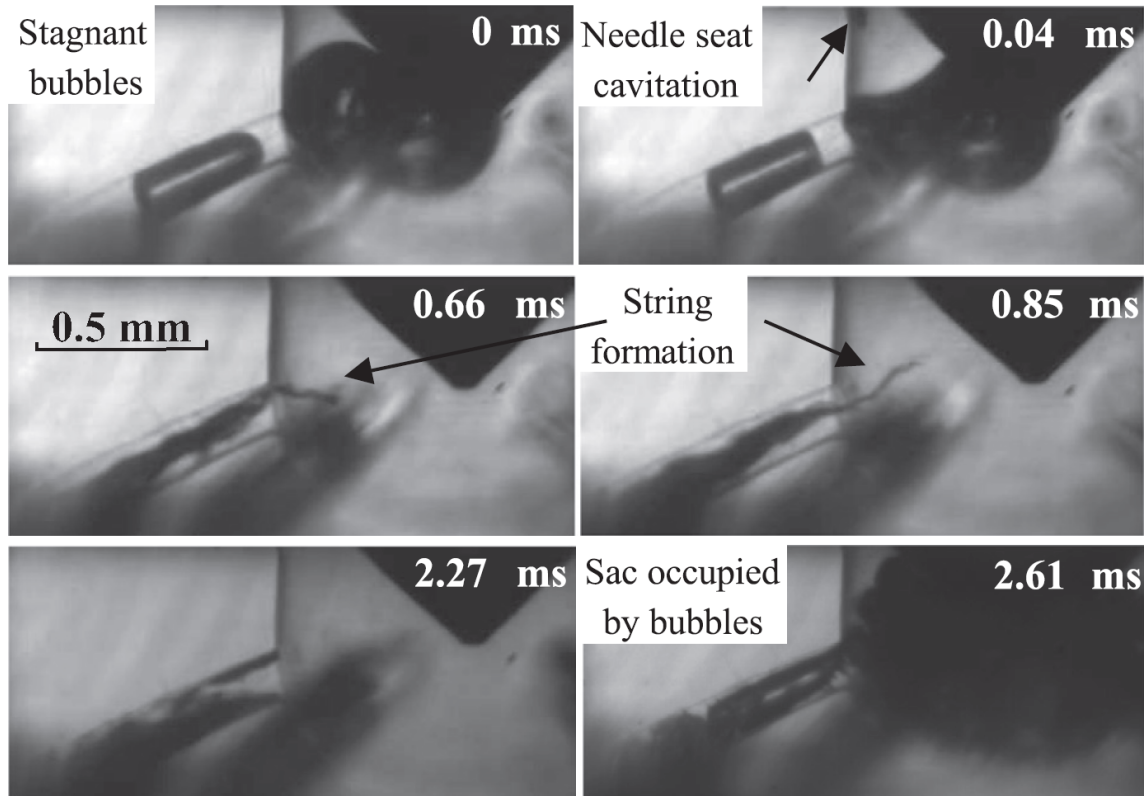


**Figure 2.1:** Sequence of representative side view images after start of injection. Injection pressure 300 bar, back pressure 1 bar. 6-hole cylindrical nozzle. Nozzle hole diameter 0.160 mm. Reproduced from Mitroglou et al. [6]

the sac forming a thread between the holes. This thread can break up if pressure in the core of the string increases, introducing strong perturbations in the flow.

Cavitation structures generated inside the nozzle hole cannot be accurately quantified using conventional imaging methods. Recent developments in X-ray technology have enabled quantification of these structures formed under very high pressures and small geometries. Mitroglou et al. [8] utilized X-ray micro-computed tomography (CT) to provide a three-dimensional reconstruction of the high-speed cavitating Diesel fuel flow in a single-hole nozzle. Figure 2.3 illustrates an instantaneous flow shadowgraphy and different views of the reconstructed liquid volume fraction yielded by the X-ray micro-CT. From the shadowgraphy in Figure 2.3a, it seems that the entire nozzle is blocked by cavitation structures in the first quarter of the hole. However, the X-ray CT corrects this wrong perception, demonstrating that while the lower side is indeed occupied by vapor volume fraction, a large amount of liquid is allowed through the upper side of the hole.

Despite the ability of X-ray CT to provide three-dimensional reconstruction of the cavitating flow, it presents some problems when applied to real-size nozzles where small cavitation structures are scattered all over the nozzle hole [8]. As suggested by Duke et al. [9], this shortcoming is not present in X-ray radiography, which uses highly collimated synchrotron X-rays beams to enable high temporal and spatial resolution at the same time. In [9] the authors applied this technique to a single hole injector under low injection pressure conditions in order to characterize cavitation formation inside the nozzle. Figure 2.4 reproduces part of their results, which include quantification of void fraction along line-of-sight beams

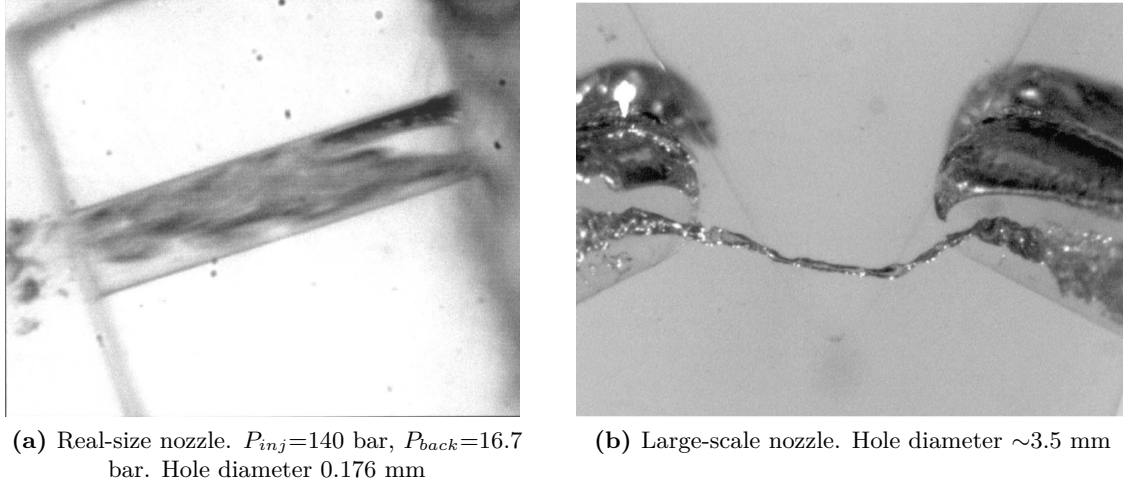


**Figure 2.2:** High resolution CCD camera visualization of transparent nozzle. Reproduced from Arcoumanis et al. [7]

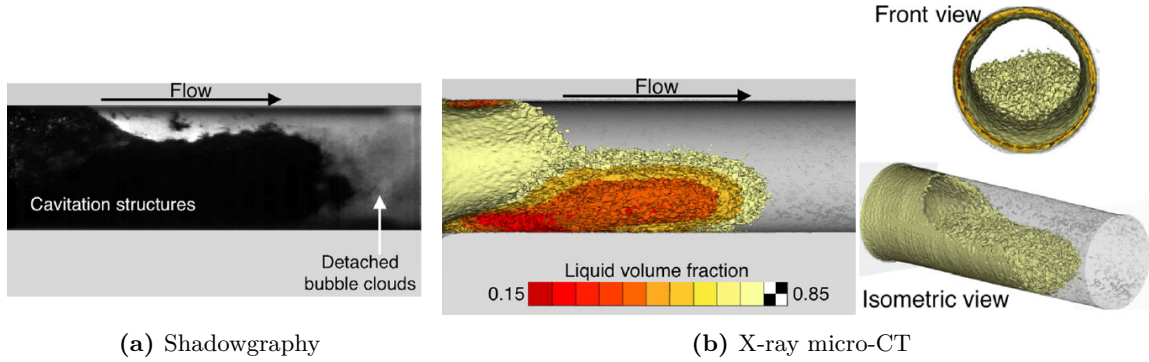


**Figure 2.3:** X-ray micro-CT of single-hole nozzle with diameter 3 mm. Reproduced from Mitroglou et al. [8]

perpendicular to the hole axis. The projected void fraction can be vapor, non-condensable gas or a combination of both, since the X-ray radiography is unable to discern between gas species. Despite this limitation, the authors experimented with different levels of degassification to conclude that while vapor is triggered near the inlet walls, the large gas structure along the center line of the nozzle stems from non-condensable gas expansion. This last phenomenon is regarded as very important in nozzle flows, as it can reduce significantly the effective hole area and thus the nozzle efficiency. Furthermore, since it does not only occur when cavitation conditions are reached but whenever pressure drops significantly, non-condensable gas expansion can appear in many regions of the nozzle where cavitation is not expected.

The aforementioned experimental techniques focus on cavitation visualization but none on vortex and turbulence characterization. The intricacies of vortex dynamics together with the need for non-intrusive flow tracers prevent the use of most experimental methods. Although Laser Doppler Velocimetry and Particle Image Velocimetry have been applied to characterize flow turbulence in a real-size nozzle [10], the length scales resolved are still much larger than the microscopic length scales developing inside the nozzle hole. This limits the information that can be obtained from experiments, especially compared to increasingly accurate numerical

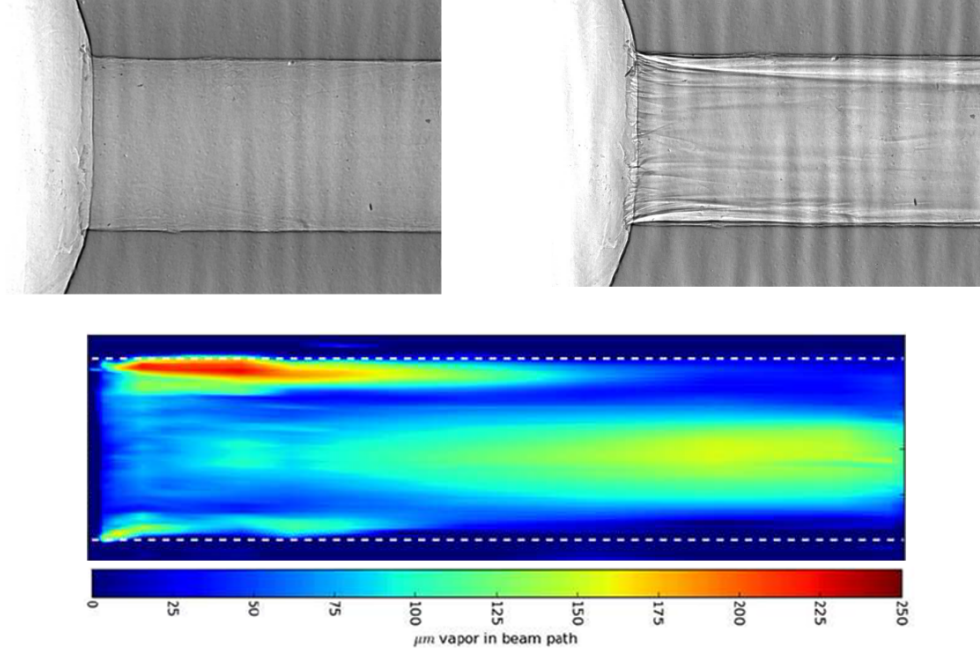


**Figure 2.4:** X-ray radiography. No cavitating nozzle (top-left), cavitating nozzle (top-right), interpolated contour plots of time-average, projected void fraction. Nozzle diameter 0.5 mm. Injection pressure 10.6 bar, back pressure 0.87 bar. Reproduced from Duke et al. [9]

methods. Hence, a combination of experimental methods and numerical simulations seems to be a good strategy to investigate the link between turbulence and cavitation and their effects on the in-nozzle flow. Mitroglou et al. [11] followed this strategy to investigate a 5-hole cylindrical nozzle with orifice diameter 2.1 mm operating under different injection and back pressures in the range 5-15 bar and 0.7-1 bar respectively. They aimed at keeping the cavitation number (CN)

$$CN = \frac{P_{inj} - P_{back}}{P_{back} - P_v}$$

within the range 5-21 ( $P_{inj}$  is injection pressure,  $P_{back}$  is back pressure and  $P_v$  is vapor pressure). As shown in Figure 2.5 the numerical results predict a large recirculation zone in the sac where the string cavitation forms as a consequence of low pressure in the vortex core. The string is driven by the vortices developing inside the sac and can collapse if the vortices dissipate. The dynamic behavior of the string vortices is transferred to the cavitation structures, resulting in a cloud of droplets entering the hole.

A combination of experimental measurements and numerical simulations has also been used to investigate cavitation formation and turbulence generation during needle opening and closing [12, 13] and their link to bubble collapse leading to erosion damage [14, 15]. The implosion of cavitation bubbles generates local pressure waves that erode the material surface, which deforms and can release material particles. This in turn alters the original geometry, affecting the in-nozzle flow behavior and reducing the injector durability. The importance of flow compressibility in this process is highlighted in [15], showing that turbulence, cavitation and compressibility effects need to be taken into account in order to identify the causes of erosion. A good example is the recent work of Orley et al. [16], who provided detailed understanding of these effects during a full injection event. They simulate a 9-hole solenoid Diesel injector

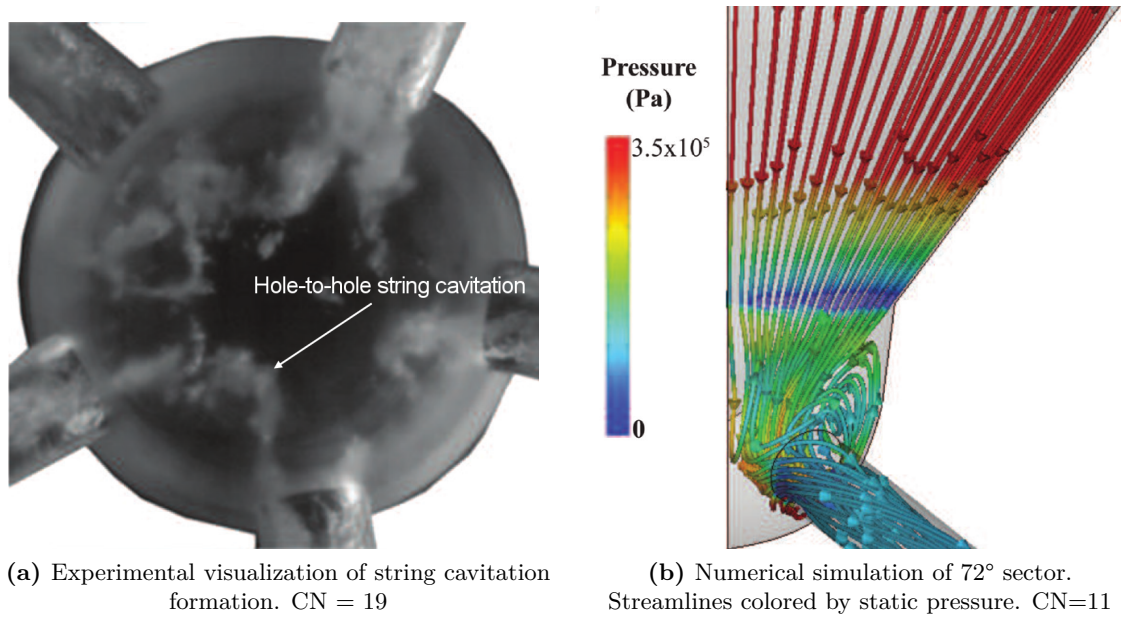


**Figure 2.5:** Experimental and numerical results of 5-hole cylindrical nozzle. Exit orifice diameter 2.1 mm. Reproduced from [11]

operating at 1500 bar injection pressure to 10 bar back pressure. During the needle closing, they observe the formation of large vortex-induced cavitation structures at the nozzle hole inlet. Immediately after needle closing, strong collapse of vapor structures triggers violent shock waves propagating to the needle seat, sac and hole. The entire flow field is affected by these events, including turbulence structures and cavitation pockets. The authors conclude that fully compressible models are key to understand the causes of erosion damage during needle transients. This is especially important in light of the current technological trend toward multiple injection patterns with short pilot injections, where the needle opening and closing stages occupy most of the injection event.

In-nozzle flow dynamics are significantly affected by fuel property variation induced by strong pressure gradients. At injection pressures of 2000 bar, fuel viscosity can increase 7 times and density by 10% [17], causing turbulence decay and viscous dissipation as the Reynolds number decreases. As a consequence, heat transfer increases and thermal effects become important, inducing changes in other fuel properties such as surface tension, thermal conductivity and heat capacity at constant pressure. As suggested in [18], these variations have a strong impact on turbulence generation and cavitation formation and can decrease significantly the nozzle efficiency. For instance, Shi et al. [19] found that cavitation formation is particularly sensitive to density and viscosity variation. Further implications of fuel property variation were reported in [20, 21], extending the investigation to spray tip penetration and droplet size distribution.

With extremely high injection pressures, i. e. above 3000 bar, the liquid fuel can reach supercritical conditions, leading to strong fluctuations of thermodynamic properties [22]. In this state the phases do not behave as interpenetrating continua and the fuel injected does not evaporate but rather shows transition to a supercritical state with a disappearing border [23]. Under such conditions, the classical understanding of fuel evaporation does not apply and the concept of atomization needs to be redefined. Although supercritical flows have been

## 2.2 Physical processes in nozzle and near-nozzle flows

---

deeply studied in other fields (i.e. liquid propellant in rocket engines), little is known about their behavior in Diesel atomization. Thus, further work on this topic is required in order to identify and better clarify their advantages and disadvantages in fuel injection systems.

### 2.2.2 Near-nozzle flows

While optical accessibility to the near-nozzle region is better than to the in-nozzle flow, it is still limited by the dense spray. Simultaneous visualization of in-nozzle and near-nozzle flow has been used in some studies to investigate the impact of cavitation structures on primary breakup. If the pressure in the nozzle hole is sufficiently low, cavitation bubbles can exit the nozzle, enhancing primary breakup and spray dispersion [24]. Large cavitation pockets generated at the hole inlet (i.e. geometric cavitation) can also propagate outside the nozzle, promoting breakup on one side of the spray and leading to a certain level of spray asymmetry. This effect is particularly important in nozzles where flow turning at the hole inlet is intense, as in Valve-Covered Orifice (VCO) nozzles [25].

Cavitation strings have a very strong influence on primary breakup and spray dynamics. Andriotis et al. [26] performed a series of experimental visualizations and numerical simulations that, although they were based on a two-hole scaled up nozzle, they are particularly illustrative of the impact of string vortex dynamics on primary breakup. Figure 2.6 reproduces three instantaneous visualizations taken during full needle lift. It also includes volume fraction distribution at the hole exit plane predicted with the cavitation model of Giannadakis et al. [27]. As can be seen, even at constant needle lift the spray is very dynamic, shifting from a relatively concentrated jet to a wide spray. The absence of cavitation string at the hole outlet (a) results in a concentrated jet with poor atomization. When the string is located at the top of the nozzle (b), the interaction with geometric cavitation is stronger and atomization is clearly promoted on the upper side of the spray. Alternatively, when the string is located at the bottom (c), both sides of the spray are perturbed either by geometric cavitation or by string cavitation, leading to a smaller and relatively symmetric dispersion angle. These observations suggest that string cavitation is largely responsible for the spray instability and primary breakup pattern.

Simultaneous visualizations of in-nozzle and near-nozzle flows in real-size nozzles are scarce and generally restricted to low injection pressures. For this reason, the impact of cavitation and vortex dynamics on primary breakup in real Diesel injection is still not well understood. Advanced imaging techniques enabling visualizations of the near-nozzle flow at high injection pressures are essential to understand the main atomization mechanisms. Figure 2.7 reproduces the results obtained by Heimgartner et al. [28] using long-distance microscopy applied to a VCO nozzle. The images show surface waves developing on the boundary of the spray caused by aerodynamic effects. With the help of Mie scattering [29], the authors attempted to correlate the amplitude  $h$  and the wavelength  $\lambda$  of these waves to the size of eventual ligament and droplets detaching from the liquid core. They concluded that for the VCO nozzle and injection pressure 800 bar, more than 75% of the droplets have diameters within 2-5  $\mu\text{m}$ . On the other hand, they applied the same investigation strategy to a mini sac nozzle at the same injection pressure, showing that 75% of the droplets have diameters between 2-10  $\mu\text{m}$ .



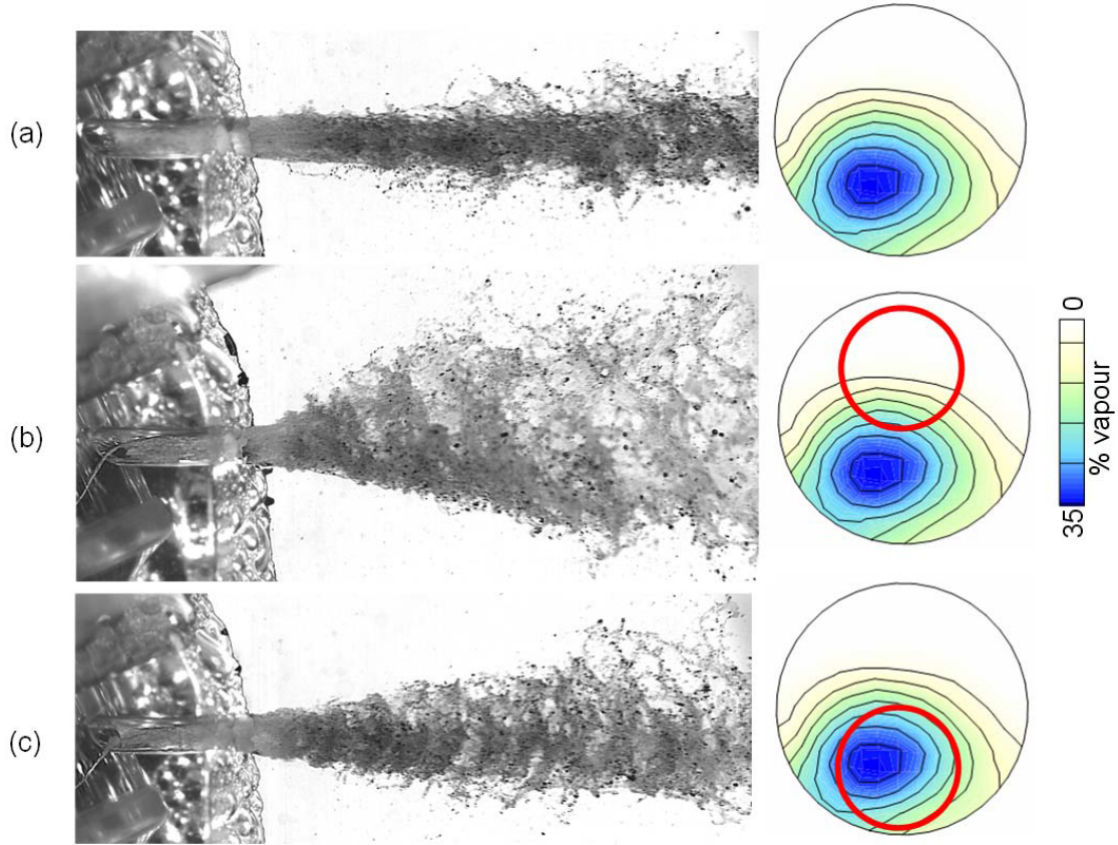


**Figure 2.6:** Instantaneous visualizations of in-nozzle and near-nozzle flows during full needle lift (left); vapor volume fraction distribution at the hole exit predicted numerically (right), using red circles to mark the position of the cavitation string. Two-hole cylindrical nozzle (hole diameter 1.5 mm). Needle lift  $\sim 3$  mm.  $CN = 2$ ,  $Re = 48300$ . Reproduced from [26]

Characterizing the liquid core near the nozzle is a complicated task as it involves identifying and removing ligaments and droplets from the spray visualization. However, this is a necessary step in the three-dimensional reconstruction of primary breakup, which is arguably one of the most ambitious objectives associated with spray atomization. Berrocal et al. [30] used Structured Laser Illumination Planar Imaging (SLIPI) in order to isolate ligaments and droplets from the liquid core. They effectively measured droplet size distribution and droplet dynamics in diluted areas of the spray but were unable to characterize the liquid core of dense sprays. Moreover, the artifacts caused by multiple light scattering led to blurring effects in the images.

Another technique attempting to remove small ligaments and droplets from the liquid core is Ballistic Imaging (BI) [31, 32], which has reached a good level of maturity to be used in Diesel injection. BI isolates the liquid core by segregating the photons emitted by the light source and passing through the spray. While some of the photons are not scattered, the vast majority of them are scattered when they pass through ligaments and droplets. Undisturbed photons are the first to cross the spray and are used together with slightly scattered photons to compose the images. Alternatively, photons that are scattered multiple times take longer to cross the spray and exit with a high diffraction angle. These photons are not included in the image in order to remove light-diffuse effects associated with ligaments and droplets. Figure 2.8 reproduces four images obtained with BI at different injection times. During the steady

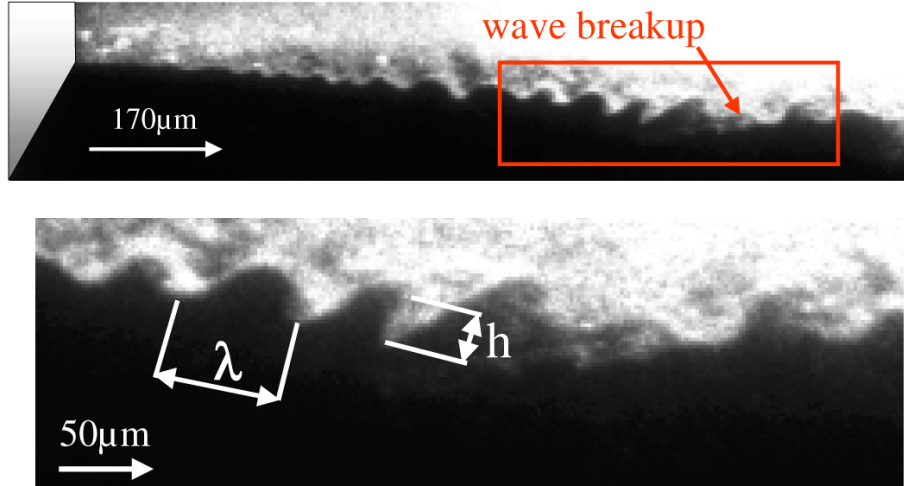


**Figure 2.7:** Long-distance microscopy visualizing surface waves at the spray boundaries. Injection pressure 300 bar, back pressure 2 bar. VCO nozzle. Reproduced from [28]

spray, cases a and b, the liquid-gas structures appear as dark black, light black and white areas interspersed all over the spray, suggesting that the liquid core is formed by liquid and void structures even at the nozzle exit. These results contradict to some extent the classical understanding of liquid core, assumed to be a dense column of liquid fuel extruding from the nozzle hole. Finally, at the end of injection, cases c and d, disconnected regions of what seems to be ligament structures propagate along the spray axis.

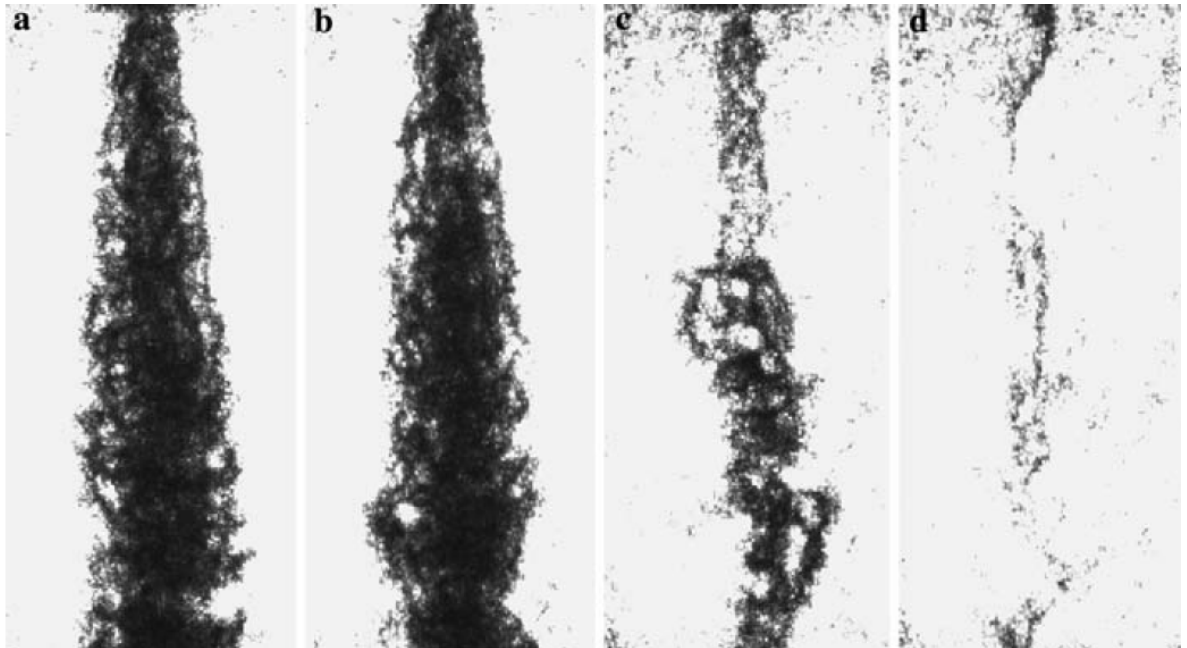


**Figure 2.8:** Ballistic Imaging. Injection pressure 1000 bar to atmospheric pressure. Single-hole nozzle, orifice diameter 0.155 mm. Images during steady spray; **a** 1.99 ms, **b** 2.01 ms after start of injection. Images at end of injection; **c** 0.02 ms and **d** 0.001 ms before end of injection. Reproduced from Linne et al. [32])

Despite BI avoids polluting the liquid core visualization with misleading effects triggered by light scattering, the liquid-gas interface structures are difficult to interpret. This is particularly critical whenever BI is compared with numerical results, since modeling the

scattering effect is extremely difficult. In this context, experimental visualizations based on line-of-sight measurements are more intuitive and much easier to reproduce numerically, including the effect of surrounding droplets and ligaments. Near-nozzle flow characterization using line-of-sight measurement techniques requires high penetrating power of the illuminating beams and negligible light scattering. This can be attained with high-intensity X-ray, which enables accurate quantitative measurements of the mass flow injected and of the dense spray propagation over time [33].

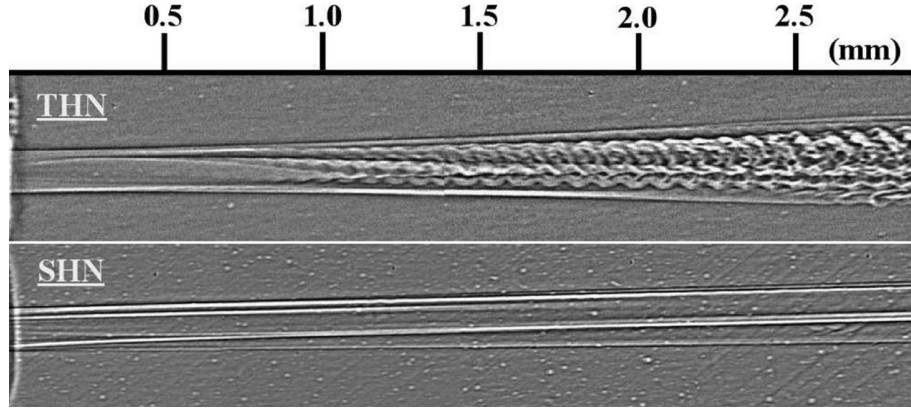
Generalization of X-ray technology for near-nozzle spray visualization has fostered intensive research of the liquid-gas interface structures developing very close to the nozzle ( $< 2.5$  mm). Lai et al. [34] produced high resolution images in time (150 ps) and space (1  $\mu\text{m}$ ) by applying X-ray Phase Contrast Imaging (X-ray PCI) to two-hole and single-hole nozzles. Figure 2.9a reproduces their experimental results at 300 bar. In the two-hole nozzle case, the image shows a longitudinal distribution of coherent helical structures (waves) occupying most of the spray width. Further from the nozzle exit, the intensity of these waves grows subject to aerodynamic interaction until they smear after 2.5 mm. Conversely, the single-hole nozzle has a completely different atomization pattern with absence of waves. By using different injection pressures, the authors found that higher pressures lead to shorter wavelengths and higher wave amplitudes, enhancing atomization. The authors concluded that aerodynamic forces are responsible for the amplitude variation, and noted that the periodic excitation determining the characteristic wavelength is originated inside the injector. They suggested the string vortices as a plausible cause of the characteristic wavelength but did not identify the physical processes involved. The two-hole nozzle results evidence a very different breakup pattern at injection pressure 1000 bar, Figure 2.9b. The liquid-gas interface distortion appears within the first 0.5 mm yielding small, relatively isotropic structures. Breakup initiation occurs on the upper side first, where the instabilities are stronger due to in-nozzle perturbations (i.e. separated flow and geometric cavitation). For the same reason, the structures developed further downstream are finer on this side than on the lower side of the spray. After approximately 1 mm, the small scales are well distributed all over the spray and become larger further downstream.

More recently, a study of the characteristic breakup structures and their link to the in-nozzle flow was conducted by Lai et al. [36] using injection pressures up to 1200 bar. They combined X-ray PCI visualizations of the near-nozzle flow with numerical simulations of the in-nozzle flow in order to correlate “atomization energy” (sum of non-axial kinetic energy, turbulent kinetic energy and cavitation energy) with variations in spray morphology. After investigating different nozzle geometries, they concluded that higher atomization energy leads to a more repeatable atomization pattern with relatively constant spray dispersion angle. Moreover, they found a clear correlation between turbulence generation and atomization, stating that in multi-hole nozzles at full needle lift “the turbulent kinetic energy is the main mechanism driving atomization for Diesel nozzles”.

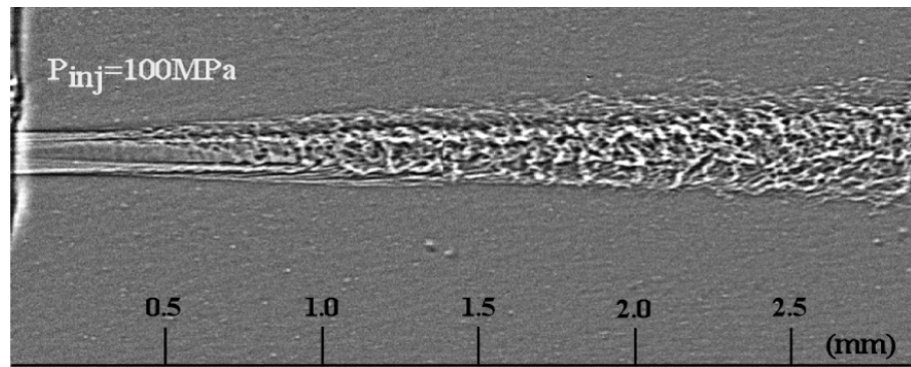
As noted by Linne et al. [37], one of the major shortcomings of X-ray PCI is the inability to reconstruct the internal spray structure, as the resulting images are two-dimensional projections of the liquid phase. X-ray images cannot distinguish between droplets and ligaments around the liquid core. Notwithstanding, it provides a unique representation of the liquid-gas interface structures, whatever they represent, which are very useful to characterize the spray morphology and can easily be replicated numerically. Consequently, X-ray PCI is very attractive to investigate the influence of nozzle design on the primary breakup pattern.



### 2.3 Mathematical and numerical models for nozzle flow and primary breakup



(a) Two-hole cylindrical nozzle (THN) and single-hole cylindrical nozzle (SHN), injection pressure 300 bar. Reproduced from [34]



(b) Two-hole cylindrical nozzle, injection pressure 1000 bar. Reproduced from [35]

**Figure 2.9:** X-ray Phase Contrast Imaging of near-nozzle flow. Fuel: Biodiesel. Back pressure 1 bar

Apart from the very different single-hole and two-hole primary breakup patterns shown in Figure 2.9, many other spray morphologies can appear depending on the nozzle geometry, injection pressure and exit conditions. The relative importance of these parameters is strongly case dependent, as higher back pressure and density would enhance aerodynamic effects at the expense of cavitation and vice-versa. Nevertheless, it is widely accepted that in-nozzle flow perturbations propagate to the near-nozzle flow and influence the primary breakup mechanisms.

### 2.3 Mathematical and numerical models for nozzle flow and primary breakup

Owing to the diverse phenomena associated with Diesel injection, modeling the resulting multiphase flow is an arduous task that requires sophisticated mathematical models and numerical methods. Inside the nozzle, a two-phase flow mixture of liquid and gas subject to compressibility and thermal effects undergoes cavitation and non-condensable gas expansion. The flow is generally described using an Eulerian-Eulerian approach where each phase is considered a continuous medium. Outside the nozzle the liquid-gas interface distorts and breaks up, eventually becoming a discrete distribution of ligaments and droplets. In this case, the phases can be described using Eulerian-Eulerian or Lagrangian-Eulerian formalism, where

the gas is treated as continuous medium and the liquid droplets as discrete particles.

This Section reviews relevant models for in-nozzle and near-nozzle flows, with special attention to two-phase models used within the Eulerian-Eulerian framework. At the end of the Section, a review of turbulence models for both in-nozzle and near-nozzle flows is provided.

### 2.3.1 Models for in-nozzle flows

In the context of Eulerian-Eulerian flow, the work of Baer and Nunziato [38] pioneered the description of two-phase compressible mixtures in reactive granular materials. They proposed a 7-Equation model composed of two sets of conservation equations, one for each phase including continuity, momentum and energy, plus an evolution equation for the volume fraction. The model allows for unequal phase velocities and pressures at the interface, and includes source terms for drag and compaction that strive to erase velocity and pressure disequilibria. Their work inspired the development of new models based on interface equilibrium or disequilibrium: Saurel et al. [39, 40] generalized the 7-Equation model to an arbitrary number of fluids, including mass and energy transfer through relaxation mechanisms; Abgrall [41] proposed a quasi-conservative scheme to avoid spurious pressure oscillations arising from the pressure discontinuity at the interface, and Zein et al. [42] devised a mass transfer mechanism based upon full thermodynamic equilibrium. Although the 7-Equation model is unconditionally hyperbolic, it involves conservative and non-conservative terms and equations, posing several difficulties when solved numerically [43].

Allowing for different interfacial pressures, velocities and temperatures is a characteristic feature of the 7-Equation model. Although it works well when both phases coexist in non-equilibrium, it can trigger numerical instabilities when thermodynamic equilibrium is reached very fast. The relaxation processes by which the phase velocities, pressures and temperatures tend to equilibrium at the interface have diverse time-scales and are enhanced or detracted by different factors. In particular, mechanical equilibrium, including velocity and pressure relaxation, is generally faster than thermal and chemical equilibrium. Hence, it is reasonable to use different mathematical treatments for each process. Saurel et al. [44] developed a 6-Equation model assuming instantaneous velocity relaxation, solving the conservation equations with a single velocity. This approach enables two interfacial pressures, mitigating the numerical difficulties associated with the non-monotonic behavior of the sound speed, which arises from instantaneous pressure relaxation. Pelanti et al. [45] applied a variant of the 6-Equation model to fluids with interface, cavitation and evaporation waves using a high-resolution wave propagation method based on the HLLC and Roe Riemann solvers [46, 47, 48]. More recently, Bore [49] conducted a detailed analysis of the 6-Equation model, proposing small modifications to the ASY-method [50] for the calculation of mass relaxation.

Whenever mechanical and thermal equilibrium at the interface are very fast, the reduction of the 7-Equation model to a 5-Equation model is justified. In this case, only one set of conservation equations are used, including: one continuity equation for each phase, one momentum equation for the mixture, one energy equation for the mixture, and one additional equation for the volume fraction evolution. The 5-Equation reduced model developed by Kapila et al. [51] aimed at avoiding the numerical stiffness associated with the 7-Equation

### 2.3 Mathematical and numerical models for nozzle flow and primary breakup

---

model due to small time-scales of the relaxation processes. However, although the 5-Equation system is hyperbolic and mathematically consistent with its 7-Equation counterpart, it cannot be expressed in conservation form, leading to problems at the interface and to non-monotonic behavior of the sound speed. To overcome this, they eliminated the excess of dissipation far away from the interface by using a regularization of the model [52].

The 5-Equation model is very attractive owing to its enhanced robustness and reduced computational cost. However, ill-posed formulations can easily lead to loss of hyperbolicity and numerical stability. Allaire et al. [53] studied the mathematical properties of the model, proposing two different closures: isobaric and isothermal. They concluded that isobaric closure performs better with respect to numerical diffusion at the interface, which is inherent in conservative schemes. The same study demonstrates that the well-posedness of the hyperbolic system is respected by a well-defined speed of sound. Related to this work, the equation of state (EOS) used to close the mathematical problem under mass transfer conditions has been further developed in [54, 55, 56], preserving the hyperbolicity of the overall problem. Finally, the authors successfully applied the model to boiling phenomena in two dimensions, reproducing nucleation mechanisms which are essential to describe bubble dynamics. The calculation of phase transition in metastable liquids using a 5-Equation model was also carried out in [57], assuming different phase temperatures and entropies under non-equilibrium conditions.

In some particular cases, the continuity equations of both phases together with the momentum equation of the mixture become redundant, thus enabling 5-Equation model reduction to a 4-Equation model. For instance, if the phases are two immiscible perfect gases, the characteristic EOS suffices to close the mathematical problem using one continuity equation for the mixture density, one momentum equation for the mixture and one energy equation for the mixture, in addition to the equation for the volume fraction evolution. Karni [58] investigated the dynamics of inviscid multicomponent fluids, proposing a 4-Equation model that suppresses the unwanted numerical oscillations at interfaces. More recently, Morin et al. [59] derived a 4-Equation model with infinitely fast heat and mass relaxation, showing that the effect of relaxation on sound speed is independent of the order in which the thermodynamic variables are relaxed. Although numerical solutions based on 4-Equation models are attractive from a computational cost standpoint, they are restricted to phases modeled with very specific EOS. This is the case of perfect gases, which allow defining a general EOS for the mixture. Unfortunately, 4-Equation models are not compatible with real gases and liquids present in many engineering applications.

In two-phase flows, heat and mass transfer between phases last until temperature and chemical equilibria are reached at the liquid-gas interface. Based on the type of mass transfer model, two groups can be identified: thermodynamic equilibrium models and bubble dynamic models. In the first group, the models can be classified as Homogeneous Equilibrium Model (HEM) if liquid and vapor are in thermal equilibrium [60], or as Homogeneous Relaxation Model (HRM) if liquid and vapor are in thermal non-equilibrium [61]. HRM is intended for metastable fluids where the temperature equilibrium is not fully reached during the mass transfer process, as it occurs in flash boiling. The HRM was applied to the study of wave propagation [62] and choking [63], obtaining good agreement with mass flow rate and pressure measurements. The HEM was used by Ning et al. [64] to simulate cavitating flows within injector nozzle passages, focusing on the effect of nozzle length, nozzle inlet radius and hole tapering effects

on cavitation formation. They successfully linked these parameters to the amount of cavitation generated and to the nozzle efficiency.

The underlying assumptions of HRM and HEM are substantiated in experimental observations. In particular, the concept of different relaxation time-scales is supported by the work of Guillard et al. [65], who found that the mechanical properties relaxed much faster than the thermal properties and these ones much faster than the chemical ones for a wide range of experiments. As noted by Chawki [66], one of the major drawbacks of HEM is that during phase changes it ignores the thermodynamic processes at the liquid-gas interface, which are particularly important under non-equilibrium conditions. To overcome these limitations, he proposed a cavitation model based on Gibbs Free Energy relaxation (GERM), allowing different velocities, pressures and temperatures across the liquid-gas interface. GERM was applied to a transparent single-hole nozzle, predicting both cavitation and non-condensable gas expansion.

Regarding the second group of mass transfer models, bubble dynamic based models can be used for cavitating flows. They entail resolving the bubble dynamics, accounting for bubble growth and collapse as well as bubble-to-bubble interaction. Although many versions have been proposed over the years, they generally use the Rayleigh-Plesset equation [67, 68, 69] as a starting point to describe the bubble behavior. They treat cavitation as a mechanically driven phenomenon initiated by the presence of nuclei, which grow subject to pressure difference between the inner bubble and the surrounding liquid. The complexity of bubble dynamic based models has increased with the development of more sophisticated descriptions of the cavitation process, including bubble inertia, surface tension and viscous effects [70], turbulence effects [71, 72] and bubble-to-bubble interaction effects on the momentum exchange during bubble growth and collapse [73]. The work of Giannadakis et al. [74] is illustrative of the numerous efforts to unveil the dominant mechanisms governing cavitation. More recently, Koukouvini et al. [75] simulated bubble collapse subject to gravity, obtaining good agreement between their numerical results and high-speed camera images.

Thermodynamic equilibrium and bubble dynamic based models have been extensively compared in terms of accuracy, robustness and ability to deal with cavitation processes in compressible mixtures. For internal nozzle flows in particular, Battistoni et al. [76] concluded that the bubble dynamic model is able to discern between cavitation and gas expansion better than the HRM. However, it also overpredicts bubble collapse, yielding less accuracy in terms of the amount of gas phase produced. They also found that the HRM model predicts less cavitation in the separated flow, promoting gas expansion along the centerline of the nozzle hole. Overall, all the models were found to perform similarly compared with experimental measurements of void fraction, with the bubble dynamic model being slightly superior.

### 2.3.2 Models for near-nozzle flows

Historically, numerical models for primary breakup have assumed that the main atomization mechanisms are controlled by aerodynamic forces competing with cohesion forces, leading to liquid-gas interface distortion. In the primary breakup region, Kelvin-Helmholtz and Rayleigh-Taylor instabilities develop at the liquid-gas interface [77, 78], triggering different breakup regimes. There are three non-dimensional numbers allowing to differentiate these

## 2.3 Mathematical and numerical models for nozzle flow and primary breakup

regimes:

- Reynolds number, which quantifies the ratio between convection and viscous forces

$$Re = \frac{\rho_l u d}{\mu_l} \quad (2.1)$$

- Ohnesorge number, which quantifies the ratio between viscous and surface tension forces

$$Oh = \frac{\mu_l}{\sqrt{\sigma_l \rho_l d}} \quad (2.2)$$

- Weber number, which quantifies the ratio between convection and surface tension forces

$$We = \frac{u \rho_g d}{\sigma_l} \quad (2.3)$$

where  $\rho_l$ ,  $\rho_g$  are liquid and gas densities,  $\sigma_l$  is surface tension of the liquid,  $\mu_l$  is liquid viscosity,  $d$  is nozzle exit diameter and  $u$  is flow velocity. Although the Weber number is more relevant during secondary breakup of the discrete spray, it can also be used to identify ligament and droplet breakup regimes in the near-nozzle flow.

Figure 2.10a illustrates different primary breakup regimes for non-turbulent flows proposed in [77], ordered by increasing flow rate, and Figure 2.10b classifies them as a function of  $Re$  and  $Oh$ . The author identified four different regimes: Rayleigh, first wind-induced, second wind-induced and atomization. Rayleigh breakup involves strong interaction between liquid inertia and surface tension. Droplets detaching from the liquid core are somewhat larger than the nozzle hole diameter and the liquid core penetration length increases with mass flow rate. This mode only occurs for low  $Re$  when the surface tension forces are comparatively large. First wind-induced is caused by twisting or helical instabilities of the liquid column as a whole, yielding droplets with diameters of the order of the nozzle diameter. In the second wind-induced regime, surface instabilities add to the helical instabilities of the liquid column, leading to local distortion and breakup of the liquid-gas interface. As a consequence, liquid structures of multiple scales detach from the liquid core yielding a wide range of drop and ligament sizes. Opposite to the Rayleigh regime, the liquid core penetration length decreases with higher mass flow rate in both first wind-induced and second-wind induced breakup modes. Atomization breakup occurs when the inertial and aerodynamic forces exceed viscous and surface tension forces. In this case breakup occurs very close to the nozzle, yielding ligaments and droplets that can be orders of magnitude smaller than the nozzle diameter. In Diesel engine injection typical values of  $Re$  and  $Oh$  are  $Re \sim 40,000$  and  $Oh \sim 0.03$ . Looking at Figure 2.10b, it is clear that these values lie within the atomization regime.

Identifying the breakup regime is the first step to decide which numerical approach would be appropriate for each injection conditions. Simple numerical models incorporate experimental correlations to account for primary breakup in the atomization regime. These models correlate injection parameters such as injection pressure, back pressure, fuel properties or nozzle hole diameter with different spray features such as liquid core penetration length [79] or spray dispersion angle [80, 81, 82], taking into account cavitation [83], heat transfer [84] and turbulence [85]. Most of these models are purely phenomenological and their validity is limited to a specific range of operating conditions and nozzle designs. Furthermore, they are

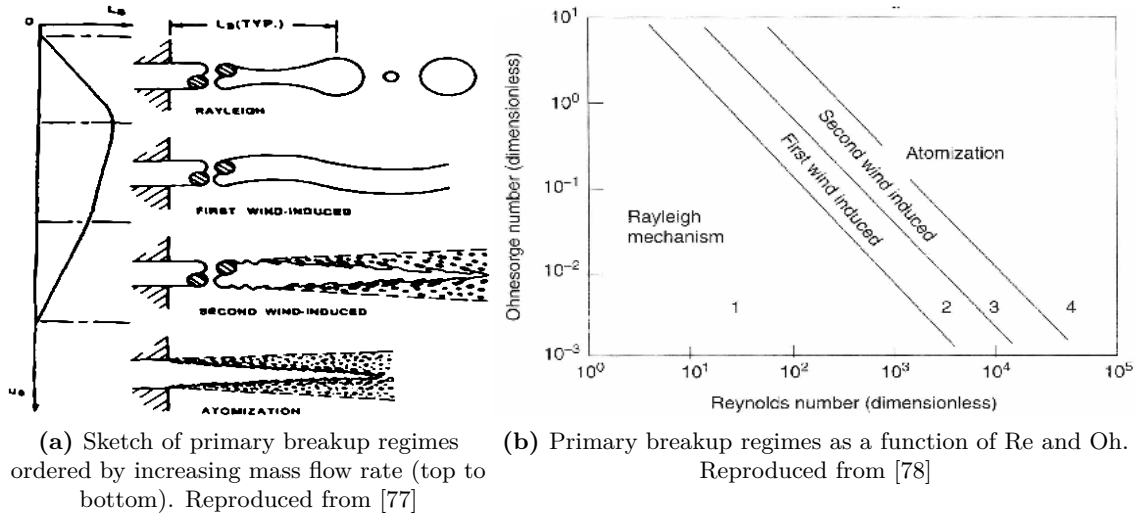


Figure 2.10: Primary breakup regimes

not suitable for complex injector geometries where the physical processes developing inside the nozzle have a strong influence on primary breakup. Hence, they are suitable for very specific problems typically involving single hole injectors.

Efforts to model atomization in the primary breakup region have lead to simple but robust and computationally efficient numerical models. One of them is the “Wave” model [86], based on the assumption that the primary breakup can be effectively represented by discontinuous spherical droplets or “blobs” with diameter equal to the nozzle exit. The “Wave” model relies on wave stability theory to estimate unstable growth of Kelvin-Helmholtz instabilities at the liquid-gas interface, offering a reasonable description of low-speed liquid jets. For high-speed jets, further developments include the effects of cavitation [87], turbulence [88] and liquid distribution over the nozzle exit [89]. However, the intricate interaction between vortex structures, cavitation, turbulence and liquid-gas interface is still unresolved. This is a major limitation of the Wave model, especially with increasingly complex nozzle geometries and injection conditions.

Another model for ligament and droplet breakup is the so-called Taylor Analogy Breakup (TAB) model [90] based upon Taylor’s analogy [91] between a spring mass system and an oscillating-distorting droplet. The analogy associates the restoring force of the spring with surface tension forces, the external force with droplet drag forces and the damping force with droplet viscosity forces. The resulting equations determine the droplet dynamics at any time, including oscillation and distortion. Whenever droplet deformation exceeds a given threshold, the “parent” droplet breaks up into smaller “child” droplets with different aerodynamic coefficients. The breakup process goes on with former “child” droplets treated as “parent” droplets until the cohesion forces exceed the distorting ones. The TAB model works well in low Weber number atomization problems but is unable to accurately predict intense droplet deformation and shattering observed in high velocity jets.

The limitations associated with simple models have encouraged more sophisticated approaches aimed at resolving the three-dimensional flow evolution in the primary breakup region. To resolve interface distortion and ligament separation, different numerical strategies must be

### 2.3 Mathematical and numerical models for nozzle flow and primary breakup

---

deployed in combination with the two-phase flow description. One of the possible techniques is the so-called Eulerian-Lagrangian Spray Atomization (ELSA), originally proposed by Vallet et al. [92, 93] and intended for primary breakup of flows with high Weber and Reynolds numbers. In addition to the conserved variables, ELSA transports the surface density  $\Sigma$ , defined as

$$\Sigma = \frac{S_l}{Vol} \quad (2.4)$$

where  $S_l$  is the liquid surface in a given volume  $Vol$ . The surface density is transported taking into account production and destruction effects such as evaporation, turbulence, droplet collision and breakup. Variants of the ELSA model can be found in [94], where the concept of dense and dilute region is introduced, and in [95], where the model is extended for Large-Eddy Simulation. One of the main advantages of ELSA is that it provides information about the surface density, which is very useful for blending the Eulerian-Eulerian description with Lagrangian-Eulerian description of the discrete spray. Moreover, droplet size distribution can be easily linked to the in-nozzle flow features, which allows assessing the influence of cavitation and turbulence. This link has been extensively investigated [96, 97, 64] in the context of high pressure Diesel injection. On the downside, the ELSA model assumptions regarding interface distortion lead to calibration parameters that are relatively case dependent, making difficult their generalization to different geometries and operating conditions.

The Volume Of Fluid (VOF) method is another technique suitable for primary breakup modeling. This approach entails reconstructing the liquid-gas interface by means of numerical algorithms with low numerical diffusion. The aim is to redefine the interface at the end of each calculation step, yielding a sharp interface between the interpenetrating phases. The algorithm can be built upon multi-fluid or mixture models such as the 7-Equation or 5-Equation models, integrating the interface reconstruction via low-diffusive interpolation. Youngs [98] initially proposed a piecewise-linear scheme to perform a geometric reconstruction of the interface during VOF calculation. This approach assumes that the interface has a linear slope within each cell and uses this shape to calculate the advection through the cell faces. Although the interface interpolation of Youngs is numerically robust and only requires local information, it only produces first order results. A second order method was developed by Pilliod et al. [99] using local and neighbor volume fraction gradients near the interface. They obtained good results at corners and in regions with discontinuous derivatives. To preserve the second order approximation while removing the dependency on neighboring cells, Dyadechko et al. [100] presented the moment-of-fluid method (MOF), reconstructing the interface from the volumes and centroids of the cell fractions occupied by different phases. Other methods are the Donor-Acceptor scheme [101] and the Compressive Interface Capturing Scheme for Arbitrary Meshes (CICSAM) [102]. With the Donor-Acceptor scheme the amount of fluid transferred from the “donor” cell to the “acceptor” cell is controlled, reducing numerical diffusion. Alternatively, the CICSAM method utilizes a high-resolution differencing scheme at the interface, particularly suitable for flows with high viscosity ratios between phases.

The conservative nature of VOF is largely appreciated in two-phase flow calculations. However, the excess of numerical diffusion can smear the interface out of the acceptable limits. To overcome this, additional methods have been developed, minimizing the numerical diffusion near discontinuities while maintaining the accuracy in smooth regions. The Level Set method [103] defines a smooth function that varies linearly with the distance to the interface, where

it becomes 0. The level-set function is convected with the flow, indicating the exact position of the interface in the fluid domain. Owing to its differentiability, the sharp gradients can be accurately calculated, yielding a precise reconstruction of the liquid-gas interface. Level Set is generally used for incompressible flows with high density and viscosity ratios, stiff surface tension and curvature effects. Sussman et al. [104, 105] coupled Level Set with an adaptive projection method to achieve higher resolution of the interface with a minimum increase of computational cost. They also improved the accuracy of the level set function formulation and the accuracy of the advection scheme, validating their results against flows involving air bubbles and water drops. Their simulations successfully predicted complex phenomena such as arbitrary merging and breakup of droplets and bubbles, impact of drops on liquid surfaces and air bubble entrainment in the liquid core.

The major drawback of the Level Set method is the inability to preserve volume conservation [106]. This shortcoming has raised the interest of many researchers over the years. Enright et al. [107] proposed a novel numerical method based on Lagrangian marker particles to rebuild the level set function. This model is suitable for flows undergoing stretching and tearing, and performs very well in terms of mass conservation as compared with classical VOF. The coupling between Level Set and VOF, known as Combined Level Set VOF (CLSVOF), is the cornerstone of many recent studies that try to harness the conservative capabilities of VOF while minimizing interface smearing. This method, initially proposed in [108], uses the volume fraction to reconstruct the interface and to solve the VOF equations before calculating the level set function from the reconstructed interface. The CLSVOF has been applied to the simulation of primary breakup of a liquid jet [109], to Large-Eddy Simulation of GDI single hole [110] and to multi-hole nozzle sprays [111], yielding excellent results in terms of interface resolution and mass conservation.

Apart from VOF and Level Set, other alternatives have been developed to deal with liquid-gas interfaces. The Lagrangian Particle method [112, 113] represents the liquid-gas interface using marker particles that give information about the curvatures and normals on the interface. This approach is useful for highly-distorted interfaces but it is computationally expensive. Conversely, the Front Tracking method [114] uses an auxiliary surface grid to mark the interface between phases, leading to relatively inexpensive calculations. A disadvantage of Lagrangian Particle and Front Tracking methods is that both are non-conservative, posing the same problems as the Level Set method. A conservative interface reconstruction can be achieved by tracking interface deformation with the computational mesh [115, 116, 117]. Although this method gives very good results in terms of mass conservation and resolution, their applicability is restricted to small degrees of interface distortion.

Downstream of the nozzle exit (but still in the near-nozzle region), small ligaments and droplets originate and interact. From a computational standpoint, modeling their dynamics using the Eulerian-Eulerian approach can be extremely expensive and unfeasible in most of the cases. Instead, the Lagrangian-Eulerian approach (LE) is generally selected. LE represents the spray by a finite number of Lagrangian “parcels” containing droplets with same properties (i.e. velocity, size, etc.). The dynamics of these parcels are resolved using models that account for droplet breakup [86, 90], droplet coalescence [118], droplet collision [119, 120] and wall impingement [121, 122]. Although LE provides a reasonably complete description of droplet dynamics, the maximum numerical resolution is limited to ensure statistical significance of the population of droplets contained in each parcel. This is particularly problematic when using



## 2.3 Mathematical and numerical models for nozzle flow and primary breakup

---

high resolution methods with small cells sized for the Eulerian phase in the near-nozzle region, since a given cell could contain parcels with only a few droplets. For such cases, improved stochastic models are required, minimizing the number of droplets needed to ensure statistical significance of the results.

LE provides a good description of droplet dynamics in regions where the Eulerian-Eulerian approach is completely unfeasible. Despite the fact that the increasing computational power is enabling extremely expensive Eulerian-Eulerian simulations of the near-nozzle region, complete substitution of LE is difficult due to higher injection and in-cylinder pressures leading to smaller ligaments and droplets.

### 2.3.3 Turbulence models

Turbulence and vortex structures developing inside the nozzle have a strong influence on internal flow dynamics and primary atomization. Strong velocity and pressure gradients, flow turning and recirculation trigger complex turbulence phenomena both inside and outside the nozzle. The amount of turbulence strongly depends on the geometry and operating conditions, leading to a wide range of scales distributed all over the fluid domain.

As reviewed in Section 2.2.1, flow recirculation in multi-hole nozzles with micro sac generates large counter-rotating vortices that enter the sac and interact with separated flow from the inlet edges. Additionally, the needle induces both large and small flow scales transported by the main flow into the nozzle hole. Strong shear layers promote local onset of very small turbulent scales and cavitation pockets. These structures interplay with the large scales and break them up into smaller scales. Despite the high Reynolds number ( $\sim 40,000$ ), turbulence decay and even certain level of relaminarization can be locally attained due to the intense flow stretching entering the nozzle. Moreover, the high pressure leads to 700% viscosity increase [17], which has a direct impact on the Reynolds number. To account for all these phenomena advanced modeling is essential, including turbulence generation at the boundaries and shear layers, laminar-to-turbulent transition and turbulence decay.

From a numerical standpoint, turbulence models are generally separated into Reynolds Averaged-Navier-Stokes (RANS) and Scale-Resolving Simulation (SRS). In the RANS approach the conservation equations are time-averaged, turbulence being only addressed based on their statistical effects. The resulting formulation involves the so-called Reynolds stress tensor arising from the nonlinear terms of the underlying Navier-Stokes equations [123]. The Reynolds stress tensor is unknown, so it must be modeled in order to close the mathematical problem. The role of the RANS model is therefore to provide the link between the Reynolds stress tensor and the averaged velocity field, which is effectively calculated. On the other hand, SRS involves spatial filtering of the governing equations [124], resolving the flow scales larger than the filter size. This approach also requires modeling the contribution of unresolved sub-filter scales. The size of flow scales resolved can range from very large (Very Large-Eddy Simulation, V-LES) to very small (Direct Numerical Simulation, DNS) where viscosity dissipates turbulence into heat. Although SRS provides an instantaneous resolution of the turbulence field, its computational cost is typically several orders of magnitude higher than that of RANS. For the particular case of DNS it scales with  $Re^3$ , limiting its applicability to problems with very low Reynolds numbers.

Owing to the relatively small computational cost, RANS has been the preferred option for many industrial problems, especially when accuracy can be sacrificed at the expense of complexity. However, the problem-dependent nature of turbulence forced the development of different models, optimized for different conditions and flow regimes. The RANS models can be classified as algebraic [125, 126], one-equation [127, 128], two-equation [129, 130, 131] and nonlinear [132] models. Algebraic (or zero-equation) models do not require the solution of any additional transport equation, yielding the turbulent viscosity as a function of the time-averaged velocity field. One-equation models solve one additional transport equation, usually for the turbulent kinetic energy. Although these models perform well in wall-bounded, high-speed aerodynamic flows, they cannot be relied on to predict turbulence decay. This prevents them from being used for high pressure fuel injection, where turbulence decay must be captured along with turbulence transition. Two-equation models overcome this limitation by adding two transport equations to the conservation equations, one to determine the energy in the turbulence (usually turbulent kinetic energy) and the other to determine the scale of the turbulence (length scale or time scale). These models are suitable for high pressure fuel injection, since they allow independent evolution of turbulent velocity and length scales. Other turbulence models are the Reynolds Stress Model (RSM) [133], which resolves a full set of transport equations for the Reynolds stress tensor and non-linear models [134], which propose expansions of the Boussinesq hypothesis [71] to link the Reynolds stress tensor to the turbulent viscosity. Although these models can be very accurate, they are computationally expensive.

Two-equation models, particularly  $k - \varepsilon$  and  $k - \omega$ , have been widely used in high pressure fuel injection [135, 136, 137]. Both models transport the turbulent kinetic energy  $k$  and either the turbulent dissipation  $\varepsilon$  or the specific dissipation rate  $\omega$ , which can be thought as the ratio of  $\varepsilon$  to  $k$ . While the  $k - \varepsilon$  is generally applied in combination with wall functions, the  $k - \omega$  model offers a more accurate and robust modeling framework for boundary layers [138]. The  $k - \varepsilon$  model works very well with freestream flows and shear layers, but has a strong tendency to under-predict separation caused by inaccurate resolution of the viscous sub-layer. Conversely, the  $k - \omega$  model performs well near the wall but is very sensitive to freestream values of  $\omega$ , especially at the boundary layer edge [139]. In order to harness the accuracy of the  $k - \omega$  model near the wall while taking full advantage of the  $k - \varepsilon$  model far away from it, Menter [140] proposed the Shear Stress Transport (SST) model, which binds the  $k - \omega$  near the wall with the  $k - \varepsilon$  in the freestream region. This model is well-suited for laminar-turbulent transition in wall-bounded flows [141] appearing in fuel injection problems.

$k - \varepsilon$  models perform well when applied to cavitating flows [142]. They have been used to study cavitation in multi-hole Diesel engine injectors [143] and the effect of valve covered orifice hydro-grinding on the internal nozzle flow [144]. More recently, the improvements in turbulence modeling have increased the popularity of the  $k - \omega$  model to deal with mixture and cavitating flows in high pressure fuel injection. Shi et al. [145] employed the  $k - \omega$  SST turbulence model to investigate the dominant mechanisms of spray formation and breakup using a wide range of injection pressures, varying from 100 bar to 2000 bar. They paid special attention to the turbulent kinetic energy distribution at the outlet, which was used to correct the velocity components when coupling the in-nozzle flow with spray simulations.

Although RANS modeling is very useful, especially for nozzle design exploration with dozens of simulation cases, it is unable to capture the local flow instabilities developed inside the injector.

### 2.3 Mathematical and numerical models for nozzle flow and primary breakup

RANS successfully predicts global instabilities, such as those introduced by transient motion of statistically repeatable integral vortices, but cannot reproduce the disturbances triggered by local phenomena. These local perturbations grow and diffuse to other parts of the nozzle, promoting mixing and controlling the spray stability to a large extent. Recent experimental measurements [146] show strong temporal spray pattern variation in the primary breakup region even with constant needle lift and absence of external perturbations, highlighting the impact of local instabilities on primary atomization.

Increasingly higher computational power enables the use of high-resolution SRS to investigate the most important mechanisms governing the atomization process. Generally, the elevated cost of such simulations limits its application to the analysis of very specific features. The ability to accurately render the impact of instantaneous flow features is dependent on the achievable resolved scale. As inferred from the turbulent kinetic energy spectrum shown in Figure 2.11, the characteristic cell size of the computational mesh determines how much of the spectrum of flow scales (and their effects) can be resolved and how much must be modeled. In high pressure Diesel injection the small scales play an important role in flow mixing and cannot be neglected. Hence, very fine meshes are required to accurately predict the main mixing processes.

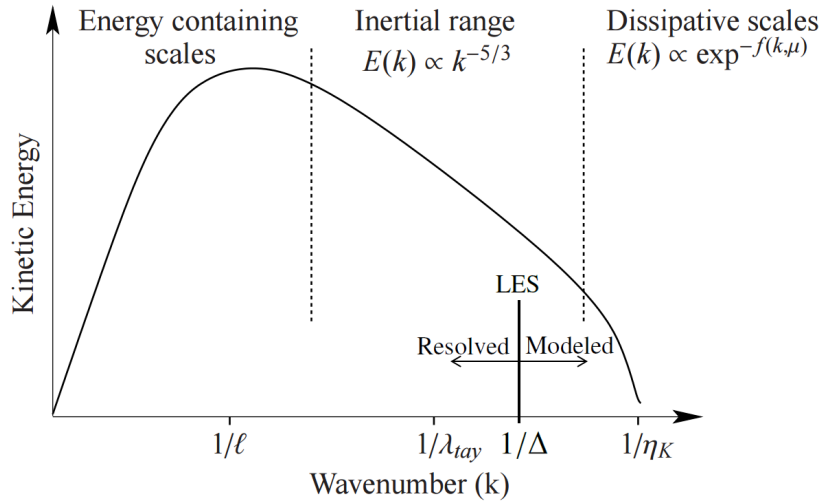


**Figure 2.11:** Schematic representation of the turbulent kinetic energy spectrum.  $\lambda_{tay}$  and  $\eta_K$  are Taylor and Kolmogorov scales respectively.  $\Delta$  is LES filter size (i.e. cell size). Reproduced from [147]

Among the SRS methods, Large-Eddy Simulation (LES) stands as one of the most popular choices due to its ability to resolve a wide range of turbulence scales with a reasonable computational cost. LES is based on the idea that while the largest scales are problem-dependent, the smallest scales are relatively universal and can be modeled using a Sub-grid scale model (SGS). Thus, the impact of the SGS on the solution depends on the amount of flow scales modeled. If the spectrum is resolved up to the Kolmogorov scale, no turbulence modeling is needed and DNS is performed.

Over the last decades, a number of SGS models have been proposed in the context of LES. The Smagorinsky-Lilly model [124] assumes that the SGS eddy viscosity is proportional to the filtered rate-of-strain tensor and to the mixing length squared, which in turn is proportional to the filter size. This model is very attractive due to its simplicity, but it

does not behave well near walls or in regions where turbulence decay and laminar-turbulent transition occurs. For such cases, Germano et al. [148] and Lilly [149] proposed the Dynamic Smagorinsky-Lilly model, where the coefficient of proportionality between the mixing length and filter size is adapted dynamically. Although the calculation of turbulence decay is significantly improved, the conventional Dynamic Smagorinsky-Lilly model yields an inaccurate resolution of near-wall turbulence decay.

In order to predict the correct behavior near the wall, Nicoud et al. [150] proposed the Wall-Adapting Local Eddy-Viscosity (WALE) Model, expressing the SGS eddy viscosity as an elaborated function of the symmetric and antisymmetric parts of the velocity gradient tensor. The WALE model not only yields an accurate decay of turbulence close to walls but also takes into account the contributions of both rate-of-strain and flow rotation, which are necessary to predict partial laminarization, turbulence inception and transition [151]. The WALE model is suitable for high pressure injection flows since the computational cost does not increase significantly with respect to other SGS models. Kim et al. [152] proposed the so-called Dynamic Kinetic Energy SGS, solving a complete transport equation for the sub-grid scale turbulent kinetic energy. While this model can yield accurate results, the computational cost and the requirements to ensure numerical stability increase significantly.

As it occurs in other industrial problems involving high Reynolds numbers, application of LES and DNS to high pressure fuel injection is limited by high mesh resolution requirements near the walls. To relax these requirements, Strelets [153] and Spalart et al. [154] proposed Detach Eddy Simulation (DES), switching between RANS and LES based on the grid resolution provided. In DES, the wall boundary layers are solved using RANS formulation and the free-shear flow is computed using LES. Similarly, Menter et al. [155] formulated Scale-Adaptive Simulation (SAS) based on the introduction of the von Karman length scale in the turbulence model. This length scale is naturally adjusted to resolved structures if the grid resolution permits, producing similar results to LES. If the mesh is excessively coarse, the von Karman length scale adapts to the new condition, leading to RANS-like results. Despite the advantages of DES and SAS with respect to full LES in terms of computational cost, both methods inherit the most common inaccuracies of RANS modeling.

Figure 2.12 illustrates the impact of the turbulence model on the numerical solution by comparing the vortex structures predicted by RANS, SAS and LES in three different fuel injection simulations. As can be observed, the RANS model only predicts the statistically repeatable scales that extend from the nozzle inlet to the nozzle outlet. Alternatively, the SAS model allows capturing a part of the range of turbulent scales originated at the nozzle hole inlet. This model shows a very active turbulence field where the smallest scales interact with the largest ones. Finally, LES resolves multiple scales growing from the nozzle inlet down to the primary breakup region.

There is no universal turbulence model for fuel injection applications. For each case, a preliminary assessment must be carried out in order to select the option that can best suit the problem conditions. Nevertheless, even if the choice is correct it can lead to a completely erroneous solution if not applied correctly (i.e. mesh resolution, calibration of coefficients, etc.). It seems that owing to the continuous increase of computational power more and more studies focus on resolving turbulence instead of modeling it. However, the higher injection pressures foreseen in the forthcoming years will prevent the use of high-resolution LES or

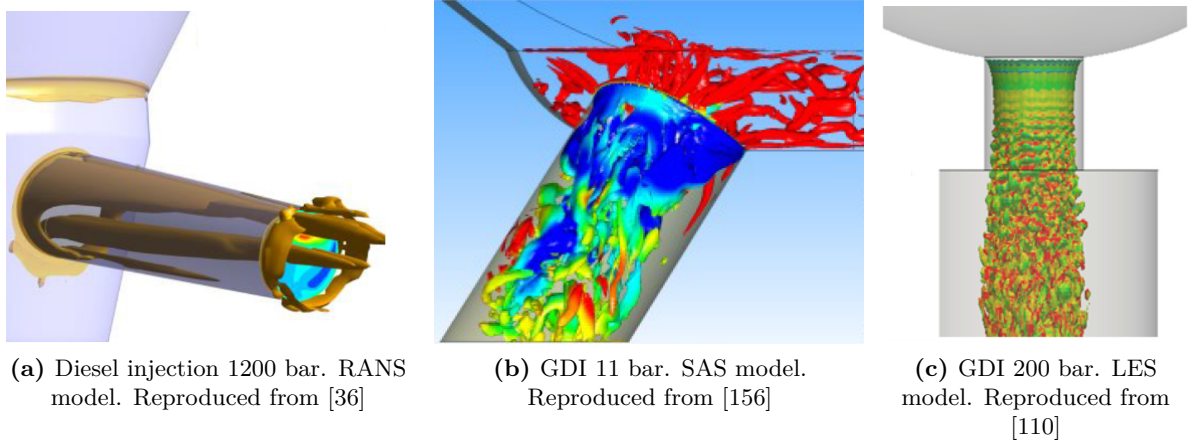


**Figure 2.12:** Vortex structures predicted by different turbulence models in three different fuel injection problems

DNS for systematic studies and design optimization.

## 2.4 Analysis methods

Obtaining relevant information about vortex dynamics is key to understand the link between in-nozzle flow and primary breakup. For this reason, the choice of adequate analysis tools is a very important step. This Section reviews some of the existing analysis methods for vortex and flow pattern characterization in the context of LES.

### 2.4.1 Vortex identification

Vortex identification methods aim at isolating the vortices from the surrounding flow. Most of them are substantiated in the velocity gradient tensor, which is decomposed into its symmetric and anti-symmetric parts in order to account for the rate-of-strain and rotation. The Q-criterion [157, 158] defines a vortex as a connected fluid region with a positive second invariant of the velocity gradient tensor. In practice, this means that the Q-criterion “sees” the vortices as regions where the vorticity magnitude is greater than the rate-of-strain. The presence of the rate-of-strain tensor in the mathematical description allows capturing not only rotating vortices, but also vortices originated in shear layers. The  $\Delta$ -criterion [159] defines vortices as regions in which the eigenvalues of the velocity gradient tensor are complex and the streamline pattern is spiraling or closed. According to Chakraborty et al. [160], the  $\Delta$ -criterion is less restrictive than the Q-criterion, which filters out scales with weaker vorticity and rate-of-strain. The  $\lambda_2$ -criterion [161] assumes that a vortex is characterized by a local pressure minimum, neglecting the viscous effects on the rate-of-strain. Overall, this method produces similar vortex structures to the Q-criterion in a wide range of flows. The Swirling Strength criterion [162] seeks for coherent vortices as a function of the swirling strength  $\lambda_{ci}^2$ , which is calculated from complex eigenvalues of the velocity gradient tensor. These eigenvalues are also used in the Enhanced Swirling Strength criterion [160] to form the inverse spiraling compactness, defined as the ratio  $\lambda_{cr}/\lambda_{ci}$ , where  $\lambda_{cr}$  is the real part and  $\lambda_{ci}$

the imaginary part. The inverse spiraling compactness refines the definition of a vortex core given by the Swirling Strength criterion.

A comparison between some vortex identification criteria can be found in [160] regarding isotropic turbulence decay. Figure 2.13 reproduces their results for the Swirling Strength criterion, Q-criterion,  $\Delta$ -criterion and  $\lambda_2$ -criterion. The authors showed that all of them can be linked through the inverse spiraling compactness, leading to very similar structures. As can be seen in all cases, the differences are negligible in terms of vortex size and distribution. The only difference seems to be the  $\Delta$ -criterion, which appears to be noisy in some regions of the flow (black circles in Figure 2.13c).

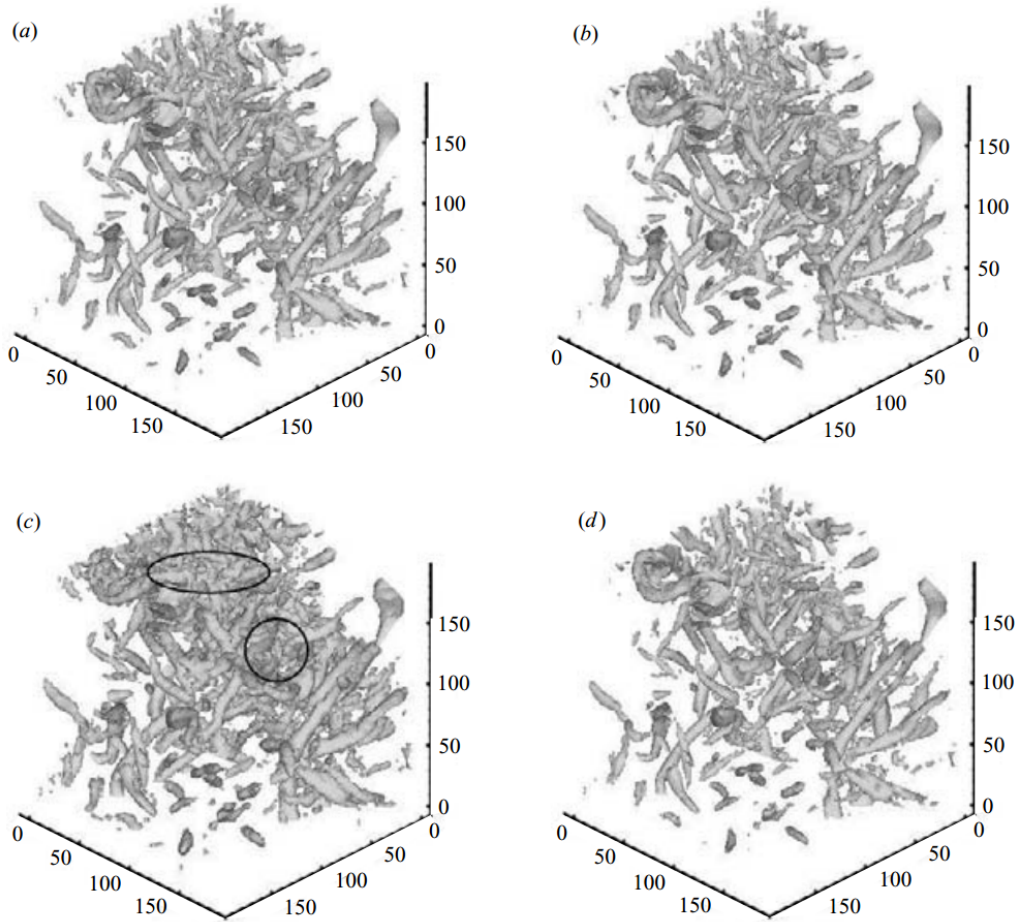


**Figure 2.13:** Comparison of vortex identification criteria in isotropic turbulence decay: Swirling Strength criterion (a), Q-criterion (b),  $\Delta$ -criterion (c) and  $\lambda_2$ -criterion (d). Reproduced from [160]

The aforementioned criteria belong to the so-called Eulerian methods, which capture similar structures and share similar disadvantages. In particular, vortex identification relies on a user-defined threshold, filtering out the scales lying outside of it. This lends subjectivity to the definition of vortex size, which becomes dependent on the criterion and threshold selected. To overcome this limitation, Lagrangian methods track the fluid particle trajectory, quantifying the deviation from the “expected” path. For instance, the Direct Lyapunov Exponent [163] method measures the rate of separation of neighboring particles initially located at the same point. This information is used to calculate an expansion coefficient, which highlights areas of maximum stretching and shear. Alternatively, the Mz-criterion [164]

## 2.4 Analysis methods

---

describes vortices through the stability of fluid trajectories, defining them as material regions where the long-term evolution of a fluid element does not follow the trend expected from the instantaneous rate-of-strain tensor. Despite the advantages associated with an objective definition of vortex size, Lagrangian methods are typically more expensive than Eulerian methods, which enable relatively fast identification of vortex structures for a given threshold.

### 2.4.2 Flow pattern characterization

Energy-carrying structures developing inside the nozzle have a strong influence on primary breakup. Their characterization and quantification can help understand how they are linked to the main atomization mechanisms. Among the available methods, Dynamic mode decomposition (DMD) and proper orthogonal decomposition (POD) have gained wide popularity due to their ability to identify coherent patterns in an overall chaotic flow field.

Both DMD and POD decompose the motion (generally velocity or vorticity fields) into a finite number of “instantaneous states” sampled over time. These states define a linear space composed of basis vectors or “modes”, which are spatial fields that identify coherent structures in the flow. In the case of POD [165], this can be seen as the linearization of a non-linear problem; the flow motion can be approximated by linear combination of a finite number of modes equal to the number of instantaneous states sampled over time. When the number of samples tends to infinity, this approximation tends asymptotically to the exact solution with an infinite number of modes. One of the main advantages of POD is that it offers an optimal decomposition of the fluid states, classifying the modes by increasing kinetic energy if applied to the velocity field. Unfortunately, this decomposition does not retain information about the temporal evolution, which is a clear disadvantage in problems where this information needs to be preserved (i.e. combustion processes).

As opposed to POD, the modal decomposition yielded by DMD [166, 167] is non-linear, preventing the reconstruction of the original data. In fact, it has been demonstrated that DMD modes may be reconstructed from POD modes [168]. On the other hand, DMD retains information about the temporal evolution by defining growth and decay rates as well as oscillation frequencies for each mode. Furthermore, it discriminates between structures associated with different characteristic frequencies, classifying the modes by increasing frequency. Although this is a great advantage during transient injection events, it becomes less important during constant needle lift injections.

Application of POD and DMD to in-nozzle flow is seldom, but they have been extensively used for spray pattern characterization [169, 170] and for internal combustion engine data processing [171, 172]. Tirunagari et al. [173] applied both methods to their LES results in the context of subsonic gas jets with Reynolds number 10,000. The first 4 modes of gas concentration field are shown in Figure 2.14. The characteristic Kelvin-Helmholtz instabilities generated at both sides of the jet are well captured in mode 1 of DMD and mode 2 of POD. However, modes 2, 3, and 4 of DMD are very similar and do not add significant information. On the contrary, the fact that these instabilities appear in mode 2 of POD suggests that they are not dominant with respect to the pattern shown in mode 1.

Whenever the coherent structures can be hierarchically ordered in terms of the energy, POD

maximizes the flow energy captured with a minimum number of modes. However, if the energy content is not sufficient to describe the dynamic behavior, additional information about the temporal evolution is required. Such information is provided by DMD, classifying the most unstable modes in terms of the frequency distribution. Although DMD enables detailed characterization of the flow motion, POD generally offers more flexibility and robustness. Hence, the choice of POD or DMD for fuel injection applications will primarily depend on the nature of the problem addressed.

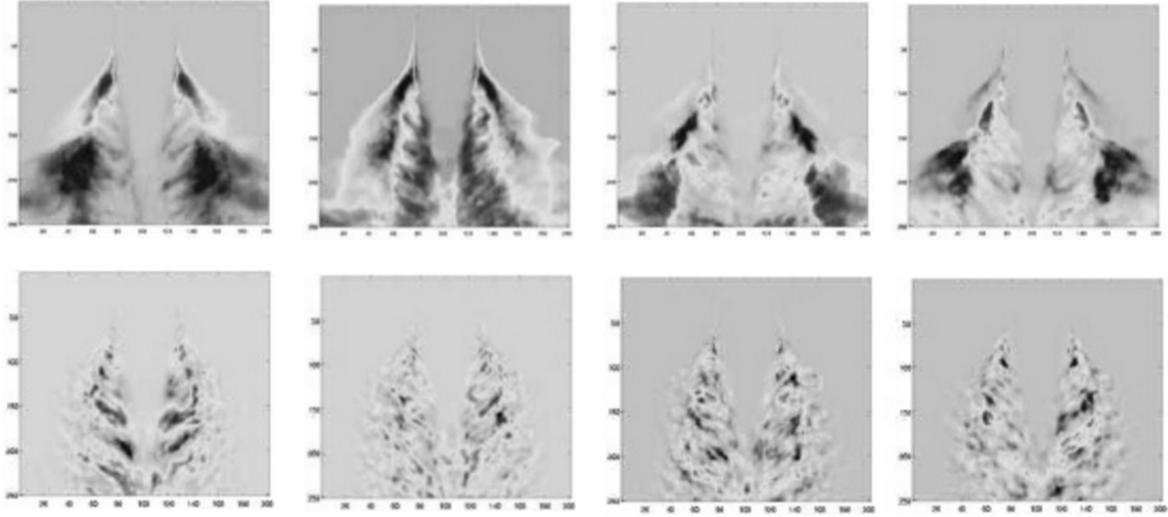


**Figure 2.14:** Comparison of first 4 POD modes (top row) and DMD modes (bottom row) for gas jet concentration field. Modes are ordered 1 to 4 from left to right. Reproduced from [173]

## 2.5 Conclusions

This Chapter presented a critical review of the available understanding of in-nozzle flows and primary breakup. Limited optical accessibility to the in-nozzle and near-nozzle regions has hampered the investigation of complex phenomena such as turbulence, vortex dynamics, cavitation, heat transfer and flow compressibility. Some experimental studies utilized scale-up nozzles or low injection pressures to link different flow structures developing inside and outside the nozzle. In real Diesel injection, however, this link remains far from understood, since non-invasive experimental techniques cannot characterize most of the flow scales. A combination of experimental measurements and high resolution numerical simulations is therefore necessary to answer the research questions posed in Section 1.3.

The Chapter also provided an overview of numerical models and analysis methods suitable for investigating in-nozzle and near-nozzle flows. The review showed that, owing to very different time scales, resolving the multiple flow scales while accounting for compressibility and thermal effects is generally not possible. Hence, it is necessary to separate their study using on the one hand models for compressible flows, and on the other hand models for turbulence and vortex dynamics. These models, together with suitable analysis tools, can be useful to understand the nozzle geometry impact on in-nozzle flow and primary breakup.



## Part II

# Development of a multiphase model for compressible flows



## Chapter 3

---

# 5-Equation model for compressible, two-phase, two-species flows

---

### 3.1 Introduction

In Diesel engine injection, high pressure ( $>2000\text{bar}$ ) induces strong compressibility effects in both gas and liquid phases. Furthermore, flow decompression leads to vapor cavitation and the so-called “gaseous cavitation”, when dissolved, non-condensable gas present in the fuel expands under low pressures (Himmelblau [174], Baur et al. [175] or Arcoumanis et al. [176]). Aiming at analyzing these phenomena, a 5-Equation model for compressible, two-phase, two-species model is proposed and validated. Heat and mass transfer are accounted by assuming full thermodynamic equilibrium, which is attained through temperature and Gibbs free energy relaxation. Validation of the model is carried out using four different cases: shock tube, water cavitation tube, two-phase expansion tube and single hole injector.

The chapter is organized as follows. First, the 5-Equation model is derived from a 7-Equation multifluid model, describing the thermodynamic closure and detailing the models for heat and mass transfer. Second, the numerical method is described, including the solution strategy and numerical schemes. Third, the four validation cases are compared with experimental and numerical data available in the literature. Finally, the last Section is dedicated to the conclusion of the Chapter.

### 3.2 5-Equation reduced model

The multifluid description of multiphase flows consists of a full set of conservation equations applied to each fluid phase, plus a volume fraction relation per phase [38, 40, 177]. For two-phase problems, the system is defined by seven equations, the so-called 7-Equation

model. For simplicity, the subsequent description is particularized for the hyperbolic liquid-gas system:

- Volume Fraction

$$\frac{\partial \alpha_l}{\partial t} + \mathbf{u}^I \cdot \nabla \alpha_l = \mu_c (p_l - p_g) \quad (3.1)$$

- Gas phase

$$\frac{\partial (\alpha_g \rho_g)}{\partial t} + \nabla \cdot (\alpha_g \rho_g \mathbf{u}_g) = 0 \quad (3.2)$$

$$\frac{\partial (\alpha_g \rho_g \mathbf{u}_g)}{\partial t} + \nabla \cdot (\alpha_g \rho_g \mathbf{u}_g \mathbf{u}_g) + \nabla (\alpha_g p_g) = p^I \nabla \alpha_g + \lambda (\mathbf{u}_l - \mathbf{u}_g) \quad (3.3)$$

$$\frac{\partial (\alpha_g \rho_g E_g)}{\partial t} + \nabla \cdot [(\alpha_g \rho_g E_g + \alpha_g p_g) \mathbf{u}_g] = p^I \frac{\partial \alpha_l}{\partial t} + \lambda \mathbf{u}^I (\mathbf{u}_l - \mathbf{u}_g) \quad (3.4)$$

- Liquid phase

$$\frac{\partial (\alpha_l \rho_l)}{\partial t} + \nabla \cdot (\alpha_l \rho_l \mathbf{u}_l) = 0 \quad (3.5)$$

$$\frac{\partial (\alpha_l \rho_l \mathbf{u}_l)}{\partial t} + \nabla \cdot (\alpha_l \rho_l \mathbf{u}_l \mathbf{u}_l) + \nabla (\alpha_l p_l) = p^I \nabla \alpha_l + \lambda (\mathbf{u}_g - \mathbf{u}_l) \quad (3.6)$$

$$\frac{\partial (\alpha_l \rho_l E_l)}{\partial t} + \nabla \cdot [(\alpha_l \rho_l E_l + \alpha_l p_l) \mathbf{u}_l] = p^I \frac{\partial \alpha_g}{\partial t} + \lambda \mathbf{u}^I (\mathbf{u}_g - \mathbf{u}_l) \quad (3.7)$$

where  $\alpha_l$ ,  $\rho_l$ ,  $\mathbf{u}_l$ ,  $p_l$ ,  $E_l$ ;  $\alpha_g$ ,  $\rho_g$ ,  $\mathbf{u}_g$ ,  $p_g$ ,  $E_g$  are volume fraction, density, velocity, pressure and total energy of the liquid and gas phases respectively,  $p^I$  and  $\mathbf{u}^I$  are interfacial pressure and velocity,  $\lambda$  is the velocity relaxation factor and  $\mu_c$  the compressibility factor. As shown in Saurel et al. [178],  $p^I$  and  $\mathbf{u}^I$  are the pressure and velocity at the liquid-gas interface that arise from the integral averaging process over the control volume, which is omitted here for simplicity. The relaxation factors  $\lambda$  and  $\mu_c$  are parameters that determine the stiffness of the system (3.1)-(3.7) towards mechanical equilibrium, achieved when  $p_l = p_g$ ,  $\mathbf{u}_l = \mathbf{u}_g$ . If  $\lambda \rightarrow 0$ ,  $\mu_c \rightarrow 0$ , both liquid and gas phases can coexist in non-equilibrium for unlimited time and  $p_l \neq p_g \neq p^I$ ,  $\mathbf{u}_l \neq \mathbf{u}_g \neq \mathbf{u}^I \forall t$ . If  $\lambda \rightarrow \infty$ ,  $\mu_c \rightarrow \infty$ , the equilibrium is achieved instantaneously and  $p_l = p_g = p^I$ ,  $\mathbf{u}_l = \mathbf{u}_g = \mathbf{u}^I \forall t$ . If  $\lambda > 0$  and  $\mu_c > 0$  are finite, there is a relaxation period where the phase pressures and velocities converge at the interface. Extensive work has been conducted in the literature to characterize and measure the values of  $\lambda$  and  $\mu_c$  for real materials (see for example the work of Baer [179] using polyurethane foam). In many physical situations, the inertia of one of the phases is negligible compared to the inertia of other phase (i. e. dissolved gas bubbles in a liquid medium, porous materials, etc.). In such cases, it is reasonable to assume an instantaneous mechanical equilibrium,  $\lambda \rightarrow \infty$ ,  $\mu_c \rightarrow \infty$ . In the context of nozzle flows in Diesel injection, the assumption of a low inertia gas phase embedded in a high inertia liquid phase is reasonable, and is therefore applied throughout the present work. The system (3.1)-(3.7) can be recast using primitive variables as

- Volume Fraction

$$\frac{\partial \alpha_l}{\partial t} + \mathbf{u}^I \cdot \nabla \alpha_l = \mu_c (p_l - p_g) \quad (3.8)$$

### 3.2 5-Equation reduced model

- Gas phase

$$\frac{\partial \rho_g}{\partial t} + \mathbf{u}_g \cdot \nabla \rho_g = -\rho_g \nabla \cdot \mathbf{u}_g + \frac{\rho_g}{\alpha_g} (\mathbf{u}^I - \mathbf{u}_g) \cdot \nabla \alpha_g + \rho_g \mu_c (p_l - p_g) \quad (3.9)$$

$$\frac{\partial \mathbf{u}_g}{\partial t} + \mathbf{u}_g \cdot \nabla \mathbf{u}_g = -\frac{1}{\rho_g} \nabla p_g + \frac{1}{\alpha_g \rho_g} (p^I - p_g) \nabla \alpha_g + \frac{\lambda}{\alpha_g \rho_g} (\mathbf{u}_l - \mathbf{u}_g) \quad (3.10)$$

$$\begin{aligned} \frac{\partial p_g}{\partial t} + \mathbf{u}_g \cdot \nabla p_g + \rho_g c_g^2 \nabla \cdot \mathbf{u}_g &= \frac{\rho_g c_g^2}{\alpha_g} (\mathbf{u}^I - \mathbf{u}_g) \cdot \nabla \alpha_g + \frac{\rho_g c_g^2 \mu_c}{\alpha_g} (p_l - p_g) \\ &+ \frac{\lambda}{\alpha_g \rho_g \varepsilon_{p_g}} (\mathbf{u}^I - \mathbf{u}_g) (\mathbf{u}_l - \mathbf{u}_g) \end{aligned} \quad (3.11)$$

- Liquid phase

$$\frac{\partial \rho_l}{\partial t} + \mathbf{u}_l \cdot \nabla \rho_l = -\rho_l \nabla \cdot \mathbf{u}_l + \frac{\rho_l}{\alpha_l} (\mathbf{u}^I - \mathbf{u}_l) \cdot \nabla \alpha_l + \rho_l \mu_c (p_g - p_l) \quad (3.12)$$

$$\frac{\partial \mathbf{u}_l}{\partial t} + \mathbf{u}_l \cdot \nabla \mathbf{u}_l = -\frac{1}{\rho_l} \nabla p_l + \frac{1}{\alpha_l \rho_l} (p^I - p_l) \nabla \alpha_l + \frac{\lambda}{\alpha_l \rho_l} (\mathbf{u}_g - \mathbf{u}_l) \quad (3.13)$$

$$\begin{aligned} \frac{\partial p_l}{\partial t} + \mathbf{u}_l \cdot \nabla p_l + \rho_l c_l^2 \nabla \cdot \mathbf{u}_l &= \frac{\rho_l c_l^2}{\alpha_l} (\mathbf{u}^I - \mathbf{u}_l) \cdot \nabla \alpha_l + \frac{\rho_l c_l^2 \mu_c}{\alpha_l} (p_g - p_l) \\ &+ \frac{\lambda}{\alpha_l \rho_l \varepsilon_{p_l}} (\mathbf{u}^I - \mathbf{u}_l) (\mathbf{u}_g - \mathbf{u}_l) \end{aligned} \quad (3.14)$$

$$c_g^2 = \frac{\frac{p_g}{\rho_g^2} - \varepsilon_{p_g}}{\varepsilon_{p_g}} ; c_l^2 = \frac{\frac{p_l}{\rho_l^2} - \varepsilon_{p_l}}{\varepsilon_{p_l}} ; \varepsilon_{p_g} = \left. \frac{\partial e_g}{\partial \rho_g} \right|_{p_g} ; \varepsilon_{p_l} = \left. \frac{\partial e_l}{\partial \rho_l} \right|_{p_l} \quad (3.15)$$

$e_g, e_l$  are the specific internal energies and  $c_l, c_g$  the speed of sound. The 7-Equation system (3.8)-(3.14) can be reduced to a 5-Equation formulation using the method of perturbations. A first order approximation to the phase pressures and velocities near the liquid-gas interface yields

$$\left. \begin{aligned} p_g &= p^I - \frac{1}{2} p_0 \frac{\mu_c^*}{\mu_c} & p_l &= p^I + \frac{1}{2} p_0 \frac{\mu_c^*}{\mu_c} \\ \mathbf{u}_g &= \mathbf{u}^I - \frac{1}{2} \mathbf{u}_0 \frac{\lambda^*}{\lambda} & \mathbf{u}_l &= \mathbf{u}^I + \frac{1}{2} \mathbf{u}_0 \frac{\lambda^*}{\lambda} \end{aligned} \right\} \Rightarrow \begin{aligned} p_l - p_g &= p_0 \frac{\mu_c^*}{\mu_c} \\ \mathbf{u}_l - \mathbf{u}_g &= \mathbf{u}_0 \frac{\lambda^*}{\lambda} \end{aligned} \quad (3.16)$$

$p_0, \mathbf{u}_0$  are reference values and  $\mu_c^*, \lambda^*$  are introduced to ensure consistency in the physical dimensions. Neglecting terms  $o(\frac{1}{\lambda}), o(\frac{1}{\mu_c})$ , renaming  $p = p_g = p_l = p^I$  as the pressure of the mixture,  $\mathbf{u} = \mathbf{u}_g = \mathbf{u}_l = \mathbf{u}^I$  the velocity of the mixture, and doing eq. (3.11) - eq. (3.14), one arrives to

$$0 = - \left( \frac{\rho_g c_g^2}{\alpha_g} + \frac{\rho_l c_l^2}{\alpha_l} \right) p_0 \mu_c^* + (\rho_g c_g^2 - \rho_l c_l^2) \nabla \cdot \mathbf{u} \Rightarrow p_0 \mu_c^* = \frac{\rho_g c_g^2 - \rho_l c_l^2}{\frac{\rho_g c_g^2}{\alpha_g} + \frac{\rho_l c_l^2}{\alpha_l}} \nabla \cdot \mathbf{u} \quad (3.17)$$

With  $p_0\mu_c^*$  defined, the 5-Equation reduced model can be obtained by doing eq. (3.10) + eq. (3.13) and eq. (3.11) + eq. (3.14)

$$\frac{\partial \alpha_l}{\partial t} + \mathbf{u} \cdot \nabla \alpha_l = \frac{\rho_g c_g^2 - \rho_l c_l^2}{\frac{\rho_g c_g^2}{\alpha_g} + \frac{\rho_l c_l^2}{\alpha_l}} \nabla \cdot \mathbf{u} \quad (3.18)$$

$$\frac{\partial \rho_g}{\partial t} + \mathbf{u} \cdot \nabla \rho_g + \rho_g \nabla \cdot \mathbf{u} = -\frac{\rho_g}{\alpha_g} \left( \frac{\partial \alpha_g}{\partial t} + \mathbf{u} \cdot \nabla \alpha_g \right) \quad (3.19)$$

$$\frac{\partial \rho_l}{\partial t} + \mathbf{u} \cdot \nabla \rho_l + \rho_l \nabla \cdot \mathbf{u} = -\frac{\rho_l}{\alpha_l} \left( \frac{\partial \alpha_l}{\partial t} + \mathbf{u} \cdot \nabla \alpha_l \right) \quad (3.20)$$

$$\frac{\partial \mathbf{u}}{\partial t} + \mathbf{u} \cdot \nabla \mathbf{u} = -\frac{1}{\rho} \nabla p \quad (3.21)$$

$$\frac{\partial p}{\partial t} + \mathbf{u} \cdot \nabla p = -\frac{1}{\frac{\alpha_l}{\rho_l c_l^2} + \frac{\alpha_g}{\rho_g c_g^2}} \nabla \cdot \mathbf{u} \quad (3.22)$$

where

$$\alpha_g + \alpha_l = 1 \quad (3.23)$$

and the mixture density

$$\rho = \alpha_g \rho_g + \alpha_l \rho_l \quad (3.24)$$

The coefficient

$$\frac{1}{\frac{\alpha_l}{\rho_l c_l^2} + \frac{\alpha_g}{\rho_g c_g^2}}$$

in (3.22) is known in the literature as the Wallis sound speed (see [180, 181]). After some algebraic work, the system (3.18)-(3.22) can be expressed in conservative variables as

$$\frac{\partial \alpha_l}{\partial t} + \mathbf{u} \cdot \nabla \alpha_l = \frac{\rho_g c_g^2 - \rho_l c_l^2}{\frac{\rho_g c_g^2}{\alpha_g} + \frac{\rho_l c_l^2}{\alpha_l}} \nabla \cdot \mathbf{u} \quad (3.25)$$

$$\frac{\partial (\alpha_g \rho_g)}{\partial t} + \nabla (\alpha_g \rho_g \mathbf{u}) = 0 \quad (3.26)$$

$$\frac{\partial (\alpha_l \rho_l)}{\partial t} + \nabla (\alpha_l \rho_l \mathbf{u}) = 0 \quad (3.27)$$

$$\frac{\partial (\rho \mathbf{u})}{\partial t} + \nabla (\rho \mathbf{u} \mathbf{u}) + \nabla p = 0 \quad (3.28)$$

$$\frac{\partial (\rho e)}{\partial t} + \nabla [(\rho e + p) \mathbf{u}] = 0 \quad (3.29)$$

where  $e$  is the specific internal energy of the mixture. As shown in [177], the 5-Equation reduced model (3.25)-(3.29) preserves hyperbolicity and takes into account the compressibility effects in the volume fraction equation.

### 3.3 5-Equation model formulation

The 5-Equation reduced system defined in (3.25)-(3.29) models a liquid-gas mixture in mechanical equilibrium where the phase pressures and velocities are equal. Similarly, there are heat and mass transfer processes during which the phase temperatures and Gibbs Free Energies relax, leading to full thermodynamic equilibrium. The parabolic form of the 5-Equation reduced system (3.25)-(3.29), extended for two gas species, with temperature and mass relaxation, reads (note that the name “5-Equation model” is retained regardless of the number of gas species)

- Volume Fraction

$$\frac{\partial \alpha_l}{\partial t} + \mathbf{u} \cdot \nabla \alpha_l = \frac{\rho_g c_g^2 - \rho_l c_l^2}{\frac{\rho_g c_g^2}{\alpha_g} + \frac{\rho_l c_l^2}{\alpha_l}} \nabla \cdot \mathbf{u} + \frac{Q}{\kappa} + \frac{\dot{\rho}}{\varrho} \quad (3.30)$$

- Continuity

$$\frac{\partial (\alpha_g \rho_g Y_v)}{\partial t} + \nabla \cdot (\alpha_g \rho_g Y_v \mathbf{u}) = \nabla \cdot (\alpha_g \rho_g D_v \nabla Y_v) - \dot{\rho} \quad (3.31)$$

$$\frac{\partial (\alpha_g \rho_g Y_d)}{\partial t} + \nabla \cdot (\alpha_g \rho_g Y_d \mathbf{u}) = \nabla \cdot (\alpha_g \rho_g D_d \nabla Y_d) \quad (3.32)$$

$$\frac{\partial (\alpha_l \rho_l)}{\partial t} + \nabla \cdot (\alpha_l \rho_l \mathbf{u}) = \dot{\rho} \quad (3.33)$$

- Momentum of the mixture

$$\frac{\partial (\rho \mathbf{u})}{\partial t} + \nabla \cdot (\rho \mathbf{u} \mathbf{u} + p) = \nabla \cdot \boldsymbol{\sigma} + \rho \bar{g} \quad (3.34)$$

- Energy of the mixture

$$\frac{\partial (\rho e)}{\partial t} + \nabla \cdot (\rho e \mathbf{u}) = -p \nabla \cdot \mathbf{u} + \boldsymbol{\sigma} : \nabla \mathbf{u} + \nabla \cdot (K \nabla T) + \nabla \cdot \left( \alpha_g \rho_g \sum_{n=v,d} D_n h_n \nabla Y_n \right) \quad (3.35)$$

where  $D_n$  and  $h_n$  are the diffusion coefficient and specific enthalpy of vapor (subscript  $v$ ) or dissolved, inert gas (subscript  $d$ ),  $K$  is the heat diffusion coefficient of the mixture,  $T$  is the temperature of the mixture and the viscous stress tensor  $\boldsymbol{\sigma}$  is defined as

$$\boldsymbol{\sigma} = \mu \left[ \nabla \mathbf{u} + (\nabla \mathbf{u})^T \right] + \left( \mu_{vol} - \frac{2}{3} \mu \right) \mathbf{I} \nabla \cdot \mathbf{u} \quad (3.36)$$

$\mathbf{I}$  is identity matrix,  $\mu$  is molecular viscosity of the mixture and  $\mu_{vol}$  is volumetric viscosity of the mixture. The parameters  $K$ ,  $\mu$  and  $\mu_{vol}$  are given by

$$\mu = \alpha_g \mu_g + \alpha_l \mu_l \quad (3.37)$$

$$\mu_{vol} = \alpha_g \mu_{vol_g} + \alpha_l \mu_{vol_l} \quad (3.38)$$

$$K = \alpha_g K_g + \alpha_l K_l \quad (3.39)$$

The variable  $\dot{\rho}$  is the mass transfer rate per unit volume from vapor to liquid fuel in  $[kg\ s^{-1}\ m^{-3}]$ . The heat transfer rate per unit volume from gas to liquid,  $Q$  in  $[J\ s^{-1}\ m^{-3}]$ , appears only in the volume fraction equation, since its influence on the energy equation is canceled out when summing up the phase energies. The relaxation coefficients  $\kappa$  and  $\varrho$  module the changes in volume fraction due to heat and mass transfer. The calculation of these terms along with  $\dot{\rho}$  and  $Q$  is detailed in Sections 3.3.3 and 3.3.4. The system (3.30)-(3.35) is closed with the mixture variables

$$\alpha_g + \alpha_l = 1 \quad (3.40)$$

$$\rho = \alpha_g \rho_g + \alpha_l \rho_l \quad (3.41)$$

$$\sum_{n=v,d} Y_n = 1 \quad (3.42)$$

$$\rho e = \alpha_g \rho_g e_g + \alpha_l \rho_l e_l \quad (3.43)$$

and appropriate equations of state (EOS), as described in the next Section.

### 3.3.1 Thermodynamic closure

Equations of state are necessary to close the system (3.30)-(3.35), expressing the phase temperatures as a function of the mixture pressure, phase densities and mass fractions. The choice of appropriate EOS is not trivial, since they must provide positive squared speed of sound regardless of the thermodynamic conditions. Failing to do so can certainly lead to numerical instability and solution divergence, as suggested in [182]. Notwithstanding the shortcomings in terms of modeling accuracy, particularly for quasi-incompressible fluids, the Stiffened Gas EOS (SG-EOS) is a suitable choice for the liquid phase, as discussed in [42]. For the gas phase, an ideal gas EOS is used for all species. Phase energies and temperatures are given by

$$e_g(T_g, Y_n) = \sum_{n=v,d} Y_n e_n(T_g) = \sum_{n=v,d} Y_n e_n(T_g^{ref}) + \sum_{n=v,d} \int_{T_g^{ref}}^{T_g} Y_n C_{v_n}(T_g) dT_g \quad (3.44)$$

$$T_g(\rho_g, p, Y_n) = \frac{p}{\rho_g R \sum_{n=v,d} \frac{Y_n}{M_n}} \quad (3.45)$$

$$e_l(\rho_l, p) = \frac{p + \gamma_l \pi}{\rho_l (\gamma_l - 1)} + q \quad (3.46)$$

$$T_l(\rho_l, p) = \frac{p + \pi}{C_{v_l} \rho_l (\gamma_l - 1)} \quad (3.47)$$

where  $T_g^{ref}$  is a reference gas temperature,  $R$  is the ideal gas constant,  $M_n$  the molar mass of gas species  $n$  and  $C_{v_n}$  the specific heat capacity at constant volume of gas species  $n$ . The parameters  $\pi$ ,  $q$ ,  $C_{v_l}$ ,  $\gamma_l$  are characteristic constants of the liquid that approximate the thermodynamic curves. Their calculation is detailed in Appendix A following the method



### 3.3 5-Equation model formulation

---

described in Lemetayer et al. [183] and the Nelder-Mead minimization method described in Lagarias et al. [184].

#### 3.3.2 Mixture temperature

The conservation equation (3.35) of the energy of the mixture requires a mixture temperature  $T$  in order to calculate heat diffusion. The definition of  $T$  is not trivial, since it must satisfy a number of conditions:

- Ensure asymptotic behavior towards pure phases, becoming  $T \rightarrow T_l$  when  $\alpha_l \rightarrow 1$  and  $T \rightarrow T_g$  when  $\alpha_l \rightarrow 0$
- Ensure its validity in both hyperbolic and parabolic systems
- Be compatible with phases modeled using different thermodynamic laws, including variable specific heat capacities with temperature

Invoking eq. (3.43),  $T$  is calculated from

$$\begin{aligned} \rho e(T) &= \alpha_g \rho_g e_g(T_g) + \alpha_l \rho_l e_l(T_l) \\ \alpha_g \rho_g \int C_{v_g}(T) dT + \alpha_l \rho_l C_{v_l} T &= \alpha_g \rho_g \int C_{v_g}(T_g) dT_g + \alpha_l \rho_l C_{v_l} T_l \end{aligned} \quad (3.48)$$

Given the gas and liquid temperatures  $T_g$  and  $T_l$ , there is one single value of  $T$  that satisfies eq. (3.48). The demonstration is as follows

**Proposition.** Assuming that both liquid and gas specific internal energies are strictly monotonically increasing functions with  $x$ , there is only one value  $x = x_3$ , contained in the interval  $x_5 > x_3 > x_1$  that satisfies

$$\varepsilon_1(x_5) + \varepsilon_2(x_1) = \varepsilon_1(x_3) + \varepsilon_2(x_3) \quad (3.49)$$

where  $\varepsilon_k = \alpha_k \rho_k e_k$ , subscript  $k = 1$  denotes gas and  $k = 2$  liquid (or vice-versa).

**Proof.** Let

$$x_5 > x_4 > x_3 > x_2 > x_1 \quad (3.50)$$

$$\varepsilon_1(x_5) + \varepsilon_2(x_1) = \varepsilon_1(x_3) + \varepsilon_2(x_3) \quad (3.51)$$

Because  $\varepsilon_1, \varepsilon_2$  are strictly monotonically increasing, they satisfy the inequality

$$\varepsilon_1(x_4) > \varepsilon_1(x_3) > \varepsilon_1(x_2) \quad (3.52)$$

$$\varepsilon_2(x_4) > \varepsilon_2(x_3) > \varepsilon_2(x_2) \quad (3.53)$$

yielding

$$\varepsilon_1(x_4) + \varepsilon_2(x_4) > \varepsilon_1(x_3) + \varepsilon_2(x_3) > \varepsilon_1(x_2) + \varepsilon_2(x_2) \quad (3.54)$$

Finally, using condition (3.49) into (3.54)

$$\varepsilon_1(x_5) + \varepsilon_2(x_1) > \varepsilon_1(x_2) + \varepsilon_2(x_2) \quad (3.55)$$

$$\varepsilon_1(x_5) + \varepsilon_2(x_1) < \varepsilon_1(x_4) + \varepsilon_2(x_4) \quad (3.56)$$

proving that there is only one value of  $x$  that satisfies (3.49).

Above proposition allows defining a unique temperature of the mixture provided the phase temperatures  $T_g$  and  $T_l$ . Graphically, this can be seen in Figure 3.1, where the internal energy of the mixture per unit volume is plotted as a function of  $T$ . The sum of the phase internal energies per unit volume,  $\alpha_g \rho_g e_g$  and  $\alpha_l \rho_l e_l$ , at  $T_g$  and  $T_l$  must be equal to the sum of  $\alpha_g \rho_g e_g$  and  $\alpha_l \rho_l e_l$  at  $T$ . This satisfies the asymptotic limit  $T \rightarrow T_l$  when  $\alpha_l \rightarrow 1$  and  $T \rightarrow T_g$  when  $\alpha_l \rightarrow 0$ .

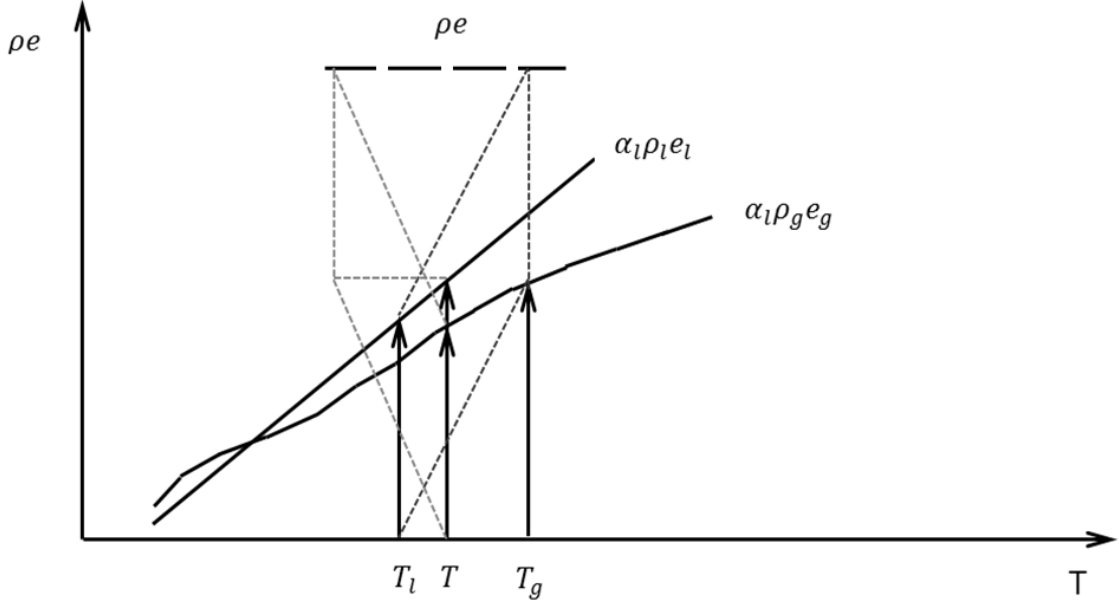


**Figure 3.1:** Internal energy of the mixture per unit volume vs temperature of the mixture. The plot shows the graphical sum of phase internal energies per unit volume

Eq. (3.48) sets a bijective relationship between  $T \leftrightarrow T_g, T_l$  through the mixture pressure  $p$ . For  $T_g$  and  $T_l$  known,  $T$  can be simply obtained from the implicit equation

$$\alpha_g \rho_g \int C_{v_g}(T) dT + \alpha_l \rho_l C_{v_l} T = Const. \quad (3.57)$$

If  $T$  is known and  $T_g, T_l$  are aimed, the inverse process requires support of the EOS in order to express  $T_g(p)$  and  $T_l(p)$ , leading to

$$Const. = \alpha_g \rho_g \int C_{v_g}(T_g(p)) dT_g(p) + \alpha_l \rho_l C_{v_l} T_l(p) \quad (3.58)$$

The heat capacity at constant volume of the mixture per unit volume  $\rho C_v$  is approximated

### 3.3 5-Equation model formulation

---

as

$$\rho C_v = \alpha_g \rho_g C_{v_g} + \alpha_l \rho_l C_{v_l} \quad (3.59)$$

and the specific heat capacity ratio of the mixture  $\gamma$  is given by

$$\frac{1}{\gamma - 1} = \frac{\alpha_g}{\gamma_g - 1} + \frac{\alpha_l}{\gamma_l - 1} \quad (3.60)$$

#### 3.3.3 Heat transfer

Heat is transferred from one phase to the other due to temperature gradients at the interface where  $T_g \neq T_l$ . The impact on volume fraction is governed by  $Q$  and  $\kappa$  in eq. (3.30), which need to be determined. As assumed in [42, 177], heat transfer is infinitely slow compared to mechanical equilibrium, but infinitely fast with respect to mass transfer. Hence, the calculation of heat transfer is decoupled from the parabolic system (3.30)-(3.35) and is formulated as

$$\frac{\partial \alpha_l}{\partial t} = \frac{Q}{\kappa} \quad (3.61)$$

$$\frac{\partial (\alpha_g \rho_g)}{\partial t} = 0 \quad (3.62)$$

$$\frac{\partial (\alpha_l \rho_l)}{\partial t} = 0 \quad (3.63)$$

$$\frac{\partial (\rho \mathbf{u})}{\partial t} = 0 \quad (3.64)$$

$$\frac{\partial (\rho e)}{\partial t} = 0 \quad (3.65)$$

Since heat transfer is infinitely slow compared to mechanical equilibrium, time derivatives of phase pressures satisfy

$$\frac{\partial p_l}{\partial t} = \frac{\partial p_g}{\partial t} = \frac{\partial p}{\partial t} \quad \forall t \quad (3.66)$$

Condition (3.66) is necessary to calculate heat exchange between phases until temperature equilibrium is reached

$$T_l = T_g = T \quad (3.67)$$

The procedure followed in the present work to solve (3.61)-(3.65) is the same as the one described in [42]. In this case, the mixture energy is first decomposed into phase energies. Note that while this assumption works well with smooth solutions, it can result in non-conservation of the mixture energy across interfaces due to numerical error. After decomposing the mixture energy into phase energies  $e_l(\rho_l, p)$  and  $e_g(\rho_g, p)$ , expressing them as a function of partial

densities and pressures, and using condition (3.66), one can arrive to

$$\frac{\partial(\alpha_g \rho_g e_g)}{\partial t} = \alpha_g \rho_g \frac{\partial e_g}{\partial t} = -Q = -\kappa \frac{\partial \alpha_l}{\partial t} \rightarrow \frac{\partial e_g}{\partial t} = -\frac{\kappa}{\alpha_g \rho_g} \frac{\partial \alpha_l}{\partial t} \quad (3.68)$$

$$\frac{\partial(\alpha_l \rho_l e_l)}{\partial t} = \alpha_l \rho_l \frac{\partial e_l}{\partial t} = Q = \kappa \frac{\partial \alpha_l}{\partial t} \rightarrow \frac{\partial e_l}{\partial t} = \frac{\kappa}{\alpha_l \rho_l} \frac{\partial \alpha_l}{\partial t} \quad (3.69)$$

$$\frac{\partial \rho_g}{\partial t} = \frac{\rho_g}{\alpha_g} \frac{\partial \alpha_l}{\partial t} \quad (3.70)$$

$$\frac{\partial \rho_l}{\partial t} = -\frac{\rho_l}{\alpha_l} \frac{\partial \alpha_l}{\partial t} \quad (3.71)$$

$$\frac{\partial p}{\partial t} = \frac{1}{\frac{\partial e_g}{\partial p} \Big|_{\rho_g}} \left( \frac{\partial e_g}{\partial t} - \frac{\partial e_g}{\partial \rho_g} \Big|_p \frac{\partial \rho_g}{\partial t} \right) = \frac{1}{\frac{\partial e_l}{\partial p} \Big|_{\rho_l}} \left( \frac{\partial e_l}{\partial t} - \frac{\partial e_l}{\partial \rho_l} \Big|_p \frac{\partial \rho_l}{\partial t} \right) \quad (3.72)$$

$$\kappa = \frac{-\rho_g \frac{\partial e_g}{\partial \rho_g} \Big|_p - \frac{\rho_l \frac{\partial e_l}{\partial \rho_l} \Big|_p}{\frac{\alpha_g \frac{\partial e_g}{\partial p} \Big|_{\rho_g}}{\frac{\partial e_g}{\partial p} \Big|_{\rho_g}} - \frac{\alpha_l \frac{\partial e_l}{\partial p} \Big|_{\rho_l}}{\frac{\partial e_l}{\partial p} \Big|_{\rho_l}}} \quad (3.73)$$

The partial derivatives in eq. (3.73) can be calculated with the help of the EOS (ideal gas EOS for the gas phase and SG-EOS for the liquid phase)

$$\frac{\partial e_g}{\partial \rho_g} \Big|_p = -\frac{1}{\gamma_g - 1} \frac{p}{\rho_g^2} \quad (3.74)$$

$$\frac{\partial e_g}{\partial p} \Big|_{\rho_g} = \frac{1}{\gamma_g - 1} \frac{1}{\rho_g} \quad (3.75)$$

$$\frac{\partial e_l}{\partial \rho_l} \Big|_p = -\frac{p + \gamma_l \pi}{(\gamma_l - 1) \rho_l^2} \quad (3.76)$$

$$\frac{\partial e_l}{\partial p} \Big|_{\rho_l} = \frac{1}{\gamma_l - 1} \frac{1}{\rho_l} \quad (3.77)$$

Introducing (3.74)-(3.77) into (3.73)

$$\kappa = \frac{\frac{p}{\alpha_g} + \frac{p + \gamma_l \pi}{\alpha_l}}{\frac{\gamma_g - 1}{\alpha_g} + \frac{\gamma_l - 1}{\alpha_l}} \quad (3.78)$$

Once  $\kappa$  is known, the heat transferred  $Q$  can be calculated with (3.61).

### 3.3.4 Mass transfer

Mass transfer from one phase to the other is assumed to be caused by Gibbs free energy disequilibrium at the interface,  $g_g \neq g_l$ . This process is defined once the parameters  $\dot{\rho}$  and  $\varrho$

### 3.3 5-Equation model formulation

---

are provided. The main assumption is that the Gibbs free energy relaxation is infinitely faster than the flow characteristic times but infinitely slower than temperature relaxation. Hence, mass transfer is modeled through

$$\frac{\partial \alpha_l}{\partial t} = \frac{\dot{\rho}}{\varrho} \quad (3.79)$$

$$\frac{\partial (\alpha_g \rho_g)}{\partial t} = -\dot{\rho} \quad (3.80)$$

$$\frac{\partial (\alpha_l \rho_l)}{\partial t} = \dot{\rho} \quad (3.81)$$

$$\frac{\partial (\rho \mathbf{u})}{\partial t} = 0 \quad (3.82)$$

$$\frac{\partial (\rho e)}{\partial t} = 0 \quad (3.83)$$

At any time during the mass transfer process, the system is in mechanical and thermal equilibrium, which introduces constraints in the evolution of pressure and temperature. In addition to (3.66), the condition

$$\frac{\partial T_l}{\partial t} = \frac{\partial T_g}{\partial t} = \frac{\partial T}{\partial t} \quad \forall t \quad (3.84)$$

holds, and mass is transferred between phases until

$$g_g = g_l = g \quad (3.85)$$

The parameters  $\dot{\rho}$  and  $\varrho$  can be calculated by decomposing the mixture energy into phase energies and expressing them as a function of partial densities, species mass fraction, temperature and pressure. This decomposition introduces the interfacial specific internal energy  $e^I$

$$\frac{\partial (\rho e)}{\partial t} = 0 = \frac{\partial (\alpha_g \rho_g e_g)}{\partial t} + \frac{\partial (\alpha_l \rho_l e_l)}{\partial t} = -\dot{\rho} e^I + \dot{\rho} e^I \quad (3.86)$$

$$\frac{\partial (\alpha_g \rho_g e_g)}{\partial t} = -\dot{\rho} e^I \quad (3.87)$$

$$\frac{\partial (\alpha_l \rho_l e_l)}{\partial t} = \dot{\rho} e^I \quad (3.88)$$

where  $e^I$  is the energy associated with the mass exchanged between phases  $\dot{\rho}$ . For two-phase, single-species problems, the mass fraction is always unity independently of mass transfer. This is the case addressed in [42]. For multispecies, however, mass is transferred from liquid to vapor, changing the mass fractions of all species. For this reason, the mass fraction must be retained in the formulation of the specific internal energy. Let denote the vapor species with the subscript  $v$  and the dissolved species with the subscript  $d$  so that

$$Y_v + Y_d = 1 \quad (3.89)$$

Invoking (3.87), one can write for the gas phase

$$\begin{aligned}
 \frac{\partial (\alpha_g \rho_g e_g)}{\partial t} &= -\dot{\rho} e^I \rightarrow \frac{\partial (\alpha_g \rho_g [Y_v e_v + (1 - Y_v) e_d])}{\partial t} = \alpha_g \rho_g Y_v \frac{\partial e_v}{\partial t} + \\
 &\quad e_v \overbrace{\frac{\partial (\alpha_g \rho_g Y_v)}{\partial t}}^{=-\dot{\rho}} + \alpha_g \rho_g (1 - Y_v) \frac{\partial e_d}{\partial t} + e_d \overbrace{\frac{\partial (\alpha_g \rho_g (1 - Y_v))}{\partial t}}^{=0} \rightarrow \\
 Y_v \frac{\partial e_v}{\partial t} + (1 - Y_v) \frac{\partial e_d}{\partial t} &= -\frac{\dot{\rho}}{\alpha_g \rho_g} (e^I - e_v)
 \end{aligned} \tag{3.90}$$

and from (3.88)

$$\frac{\partial (\alpha_l \rho_l e_l)}{\partial t} = \alpha_l \rho_l \frac{\partial e_l}{\partial t} + e_l \overbrace{\frac{\partial (\alpha_l \rho_l)}{\partial t}}^{=\dot{\rho}} = \dot{\rho} e^I \rightarrow \frac{\partial e_l}{\partial t} = \frac{\dot{\rho}}{\alpha_l \rho_l} (e^I - e_l) \tag{3.91}$$

The partial derivatives of the specific internal energies can be expressed in terms of  $Y_n$ ,  $\rho_g$ ,  $p$  and  $T$  for the gas phase, with  $n = v, d$  and  $\rho_l$ ,  $p$ ,  $T$  for the liquid phase

$$\frac{\partial e_n}{\partial t} = \frac{\partial e_n}{\partial \rho_g} \bigg|_{p, Y_n} \frac{\partial \rho_g}{\partial t} + \frac{\partial e_n}{\partial p} \bigg|_{\rho_g, Y_n} \frac{\partial p}{\partial t} + \frac{\partial e_n}{\partial Y_n} \bigg|_{\rho_g, p} \frac{\partial Y_n}{\partial t} \tag{3.92}$$

$$\frac{\partial e_n}{\partial t} = \frac{\partial e_n}{\partial \rho_g} \bigg|_{T, Y_n} \frac{\partial \rho_g}{\partial t} + \frac{\partial e_n}{\partial T} \bigg|_{\rho_g, Y_n} \frac{\partial T}{\partial t} + \frac{\partial e_n}{\partial Y_n} \bigg|_{\rho_g, T} \frac{\partial Y_n}{\partial t} \tag{3.93}$$

$$\frac{\partial e_l}{\partial t} = \frac{\partial e_l}{\partial \rho_l} \bigg|_p \frac{\partial \rho_l}{\partial t} + \frac{\partial e_l}{\partial p} \bigg|_{\rho_l} \frac{\partial p}{\partial t} \tag{3.94}$$

$$\frac{\partial e_l}{\partial t} = \frac{\partial e_l}{\partial \rho_l} \bigg|_T \frac{\partial \rho_l}{\partial t} + \frac{\partial e_l}{\partial T} \bigg|_{\rho_l} \frac{\partial T}{\partial t} \tag{3.95}$$

The partial derivatives

$$\frac{\partial Y_n}{\partial t}, \frac{\partial \rho_g}{\partial t}, \frac{\partial \rho_l}{\partial t}$$

in (3.92)-(3.95) are written as a function of the volume fraction equation using eq. (3.79)-(3.81)

$$\frac{\partial (\alpha_g \rho_g)}{\partial t} = -\dot{\rho} = \rho_g \frac{\partial \alpha_g}{\partial t} + \alpha_g \frac{\partial \rho_g}{\partial t} = \varrho \frac{\partial \alpha_g}{\partial t} \rightarrow \alpha_g \frac{\partial \rho_g}{\partial t} = (\varrho - \rho_g) \frac{\partial \alpha_g}{\partial t} \tag{3.96}$$

$$\frac{\partial (\alpha_g \rho_g Y_v)}{\partial t} = -\dot{\rho} = Y_v \frac{\partial (\alpha_g \rho_g)}{\partial t} + \alpha_g \rho_g \frac{\partial Y_v}{\partial t} = \varrho \frac{\partial \alpha_g}{\partial t} \tag{3.97}$$

$$Y_v \varrho \frac{\partial \alpha_g}{\partial t} + \alpha_g \rho_g \frac{\partial Y_v}{\partial t} = \varrho \frac{\partial \alpha_g}{\partial t} \rightarrow \alpha_g \rho_g \frac{\partial Y_v}{\partial t} = (1 - Y_v) \varrho \frac{\partial \alpha_g}{\partial t} \tag{3.98}$$

$$\frac{\partial (\alpha_l \rho_l)}{\partial t} = \dot{\rho} = \rho_l \frac{\partial \alpha_l}{\partial t} + \alpha_l \frac{\partial \rho_l}{\partial t} = \varrho \frac{\partial \alpha_l}{\partial t} \rightarrow \alpha_l \frac{\partial \rho_l}{\partial t} = (\varrho - \rho_l) \frac{\partial \alpha_l}{\partial t} \tag{3.99}$$

For the gas phase,  $\frac{\partial p}{\partial t}$  can be calculated from eq. (3.92) and (3.90) by substituting (3.96) and (3.98). After some algebra and knowing that because of condition (3.89) it is

$$\frac{\partial Y_v}{\partial t} = -\frac{\partial Y_d}{\partial t} \tag{3.100}$$

### 3.3 5-Equation model formulation

the result is

$$\begin{aligned} \frac{\partial p}{\partial t} = & \left[ \frac{-(e^I - e_v) \varrho + \rho_g \left( (1 - Y_v) \frac{\partial e_d}{\partial \rho_g} \Big|_{p, Y_v} + Y_v \frac{\partial e_v}{\partial \rho_g} \Big|_{p, Y_v} \right) (\varrho - \rho_g)}{\alpha_g \rho_g \left( Y_v \frac{\partial e_v}{\partial p} \Big|_{\rho_g, Y_v} + (1 - Y_v) \frac{\partial e_d}{\partial p} \Big|_{\rho_g, Y_v} \right)} + \right. \\ & \left. + \frac{\left( (1 - Y_v) \frac{\partial e_d}{\partial Y_v} \Big|_{p, \rho_g} + Y_v \frac{\partial e_v}{\partial Y_v} \Big|_{p, \rho_g} \right) (1 - Y_v) \varrho}{\alpha_g \rho_g \left( Y_v \frac{\partial e_v}{\partial p} \Big|_{\rho_g, Y_v} + (1 - Y_v) \frac{\partial e_d}{\partial p} \Big|_{\rho_g, Y_v} \right)} \right] \frac{\partial \alpha_l}{\partial t} \end{aligned} \quad (3.101)$$

The same procedure can be followed to obtain  $\frac{\partial T}{\partial t}$ , this time with eq. (3.96) and (3.98) into (3.93) and (3.90)

$$\begin{aligned} \frac{\partial T}{\partial t} = & \left[ \frac{-(e^I - e_v) \varrho + \rho_g \left( (1 - Y_v) \frac{\partial e_d}{\partial \rho_g} \Big|_{T, Y_v} + Y_v \frac{\partial e_v}{\partial \rho_g} \Big|_{T, Y_v} \right) (\varrho - \rho_g)}{\alpha_g \rho_g \left( Y_v \frac{\partial e_v}{\partial T} \Big|_{\rho_g, Y_v} + (1 - Y_v) \frac{\partial e_d}{\partial T} \Big|_{\rho_g, Y_v} \right)} + \right. \\ & \left. + \frac{\left( (1 - Y_v) \frac{\partial e_d}{\partial Y_v} \Big|_{T, \rho_g} + Y_v \frac{\partial e_v}{\partial Y_v} \Big|_{T, \rho_g} \right) (1 - Y_v) \varrho}{\alpha_g \rho_g \left( Y_v \frac{\partial e_v}{\partial T} \Big|_{\rho_g, Y_v} + (1 - Y_v) \frac{\partial e_d}{\partial T} \Big|_{\rho_g, Y_v} \right)} \right] \frac{\partial \alpha_l}{\partial t} \end{aligned} \quad (3.102)$$

For the liquid phase,  $\frac{\partial p}{\partial t}$  is given by combining eq. (3.94) and (3.91) with the help of eq. (3.99)

$$\frac{\partial p}{\partial t} = \frac{1}{\alpha_l \rho_l \frac{\partial e_l}{\partial p} \Big|_{\rho_l}} \left( (e^I - e_l) \varrho - \rho_l (\varrho - \rho_l) \frac{\partial e_l}{\partial \rho_l} \Big|_p \right) \frac{\partial \alpha_l}{\partial t} \quad (3.103)$$

and for  $\frac{\partial T}{\partial t}$ , with eq. (3.95) and (3.91) with the help of eq. (3.99)

$$\frac{\partial T}{\partial t} = \frac{1}{\alpha_l \rho_l \frac{\partial e_l}{\partial T} \Big|_{\rho_l}} \left( (e^I - e_l) \varrho - \rho_l (\varrho - \rho_l) \frac{\partial e_l}{\partial \rho_l} \Big|_T \right) \frac{\partial \alpha_l}{\partial t} \quad (3.104)$$

The equality in pressure and temperature partial derivatives, eq. (3.66) and (3.84), that holds during the mass transfer process, allows combining on the one hand (3.101) and (3.103) and on the other hand (3.102), (3.104). As the coefficient  $\frac{\partial \alpha_l}{\partial t}$  cancels out, this results in two equations with two unknown variables,  $e^I$  and  $\varrho$ . Before calculating  $e^I$  and  $\varrho$ , the values of

$$\frac{\partial e_n}{\partial \rho_g} \Big|_{p, Y_v}, \quad \frac{\partial e_n}{\partial p} \Big|_{\rho_g, Y_v}, \quad \frac{\partial e_n}{\partial Y_v} \Big|_{p, \rho_g}, \quad \frac{\partial e_n}{\partial \rho_g} \Big|_{T, Y_v}, \quad \frac{\partial e_n}{\partial T} \Big|_{\rho_g, Y_v}, \quad \frac{\partial e_n}{\partial Y_v} \Big|_{T, \rho_g}$$

for  $n = v, d$  are particularized for the case of ideal gas EOS

$$p = \rho_g R_g T = \rho_g R T \left( \frac{Y_v}{M_v} + \frac{1 - Y_v}{M_d} \right) \quad (3.105)$$

with  $M_v, M_d$  the molar weights of the vapor and dissolve, non-condensable species. The specific internal energy of each species can then be written as

$$de_n = C_{v_n}(T) dT = C_{v_n} T \left( \frac{dp}{p} - \frac{d\rho_g}{\rho_g} - \frac{\left( \frac{1}{M_v} - \frac{1}{M_d} \right)}{\left( \frac{Y_v}{M_v} + \frac{1 - Y_v}{M_d} \right)} dY_v \right) \quad (3.106)$$

By comparing (3.106) with (3.92) and (3.93), it is clear that

$$\left. \frac{\partial e_n}{\partial \rho_g} \right|_{p, Y_v} = - \frac{C_{v_n} T}{\rho_g} \quad (3.107)$$

$$\left. \frac{\partial e_n}{\partial p} \right|_{\rho_g, Y_v} = \frac{C_{v_n} T}{p} \quad (3.108)$$

$$\left. \frac{\partial e_n}{\partial Y_v} \right|_{p, \rho_g} = -C_{v_n} T \frac{\left( \frac{1}{M_v} - \frac{1}{M_d} \right)}{\left( \frac{Y_v}{M_v} + \frac{1 - Y_v}{M_d} \right)} \quad (3.109)$$

$$\left. \frac{\partial e_n}{\partial \rho_g} \right|_{T, Y_v} = 0 \quad (3.110)$$

$$\left. \frac{\partial e_n}{\partial T} \right|_{\rho_g, Y_v} = C_{v_n} \quad (3.111)$$

$$\left. \frac{\partial e_n}{\partial Y_v} \right|_{T, \rho_g} = 0 \quad (3.112)$$

As far as the liquid phase is concerned,  $\left. \frac{\partial e_l}{\partial p} \right|_{\rho_l}, \left. \frac{\partial e_l}{\partial \rho_l} \right|_p, \left. \frac{\partial e_l}{\partial T} \right|_{\rho_l}$  and  $\left. \frac{\partial e_l}{\partial \rho_l} \right|_T$  are particularized for the SG-EOS.  $\left. \frac{\partial e_l}{\partial \rho_l} \right|_p$  and  $\left. \frac{\partial e_l}{\partial p} \right|_{\rho_l}$  are given by eq. (3.76) and (3.77) respectively.  $\left. \frac{\partial e_l}{\partial T} \right|_{\rho_l}$  and  $\left. \frac{\partial e_l}{\partial \rho_l} \right|_T$  can be calculated using (3.46) and (3.47)

$$\left. \frac{\partial e_l}{\partial T} \right|_{\rho_l} = C_{v_l} \quad (3.113)$$

$$\left. \frac{\partial e_l}{\partial \rho_l} \right|_T = - \frac{\pi}{\rho_l^2} \quad (3.114)$$

The process of getting  $e^I$  and  $\varrho$  from the combination of (3.101), (3.103) and (3.102), (3.104) is cumbersome, and hence is omitted here for conciseness. Taking into account that

$$C_{v_g} = Y_v C_{v_v} + (1 - Y_v) C_{v_d}$$



### 3.3 5-Equation model formulation

---

one can obtain  $\varrho$  and  $e^I$

$$\varrho = \frac{\phi \left( \frac{p + \gamma_l \pi}{\alpha_l} + \frac{p}{\alpha_g} \right) - \psi \frac{\pi}{\alpha_l \rho_l C_{v_l}}}{-\phi \left[ \frac{(\gamma_l - 1) q}{\alpha_l} + \frac{(\gamma_g - 1)}{\alpha_g} (e_v - (1 + \bar{Y}) C_{v_g} T) \right] + \psi \left[ \frac{e_l - \frac{\pi}{\rho_l}}{\alpha_l \rho_l C_{v_l}} + \frac{e_v}{\alpha_g \rho_g C_{v_g}} \right]} \quad (3.115)$$

$$e^I = \frac{\left( \frac{e_l - \frac{\pi}{\rho_l}}{\alpha_l \rho_l C_{v_l}} + \frac{e_v}{\alpha_g \rho_g C_{v_g}} \right)}{\phi} - \frac{\frac{\pi}{\alpha_l \rho_l C_{v_l}}}{\phi \varrho} \quad (3.116)$$

where the parameters  $\phi$  and  $\psi$  take the value

$$\phi = \left( \frac{1}{\alpha_l \rho_l C_{v_l}} + \frac{1}{\alpha_g \rho_g C_{v_g}} \right) \quad (3.117)$$

$$\psi = \left( \frac{\gamma_l - 1}{\alpha_l} + \frac{\gamma_g - 1}{\alpha_g} \right) \quad (3.118)$$

and the mass fraction parameter

$$\bar{Y} = (1 - Y_v) \frac{\frac{1}{M_v} - \frac{1}{M_d}}{\frac{Y_v}{M_v} + \frac{1 - Y_v}{M_d}} \quad (3.119)$$

Once  $\varrho$  and  $e^I$  are known, the mass exchanged can be calculated from (3.79)

$$\dot{\rho} = \varrho \frac{\partial \alpha_l}{\partial t} \quad (3.120)$$

With (3.120), the mass relaxation process (3.79)-(3.83) is fully determined. The calculation strategy is described in detail in Section 3.4.5.

It is particularly interesting to compare the formulation for two gas species with the one proposed by [42] for single gas species. As shown in Table 3.1, the extension introduces two single differences: the substitution of the specific internal energy of the gas by the specific internal energy of the vapor species, and the influence of mass fraction variation on the energy exchange, accounted by  $\bar{Y}$ . In the limit  $Y_v \rightarrow 1$  the mass fraction parameter becomes

$$y_v \rightarrow 1 \Rightarrow \bar{Y} = (1 - Y_v) \frac{\frac{1}{M_v} - \frac{1}{M_d}}{\frac{Y_v}{M_v} + \frac{1 - Y_v}{M_d}} = 0 \quad ; \quad e_v = e_g$$

and the single species formulation of [42] is recovered.

The application to two species also modifies the equilibrium condition (3.85) which no longer holds. In this case, the equilibrium condition becomes

$$g_l = g_v \quad (3.121)$$

One-species	Two-species
$e_g$	$e_v$
$(e_g - C_{vg}T)$	$(e_v - (1 + \bar{Y}) C_{vg}T)$

**Table 3.1:** Differences between one-species case ([42]) and two-species case in the calculation of  $\varrho$  and  $e^I$

where  $g_v$  is the Gibbs free energy of the vapor which is the only species undergoing phase transition. Condition (3.121) is satisfied when the mixture entropy is maximum, as demonstrated below

- **Entropy condition**

The mixture energy differential  $dE$  can be written as

$$dE = TdS + \frac{p}{\rho^2}d\rho + \mu_g dM_g + \mu_l dM_l \quad (3.122)$$

where  $S$  is mixture entropy and  $M_g, M_l, \mu_g, \mu_l$  are mass and chemical potentials of gas and liquid phase. Eq. (3.80), (3.81), (3.83) yield  $dE = 0$ ,  $d\rho = 0$  and  $dM_g = -dM_l$ . Hence

$$TdS = (\mu_g - \mu_l) dM_g = 0 \rightarrow \mu_g = \mu_l \quad (3.123)$$

and entropy is maximum when the chemical potentials of each phase are equals. For each phase eq. (3.122) can be expressed in terms of specific values as

$$d(M_k e_k) = Td(M_k s_k) - pd\left(\frac{M_k}{\rho_k}\right) + \mu_k dM_k \quad (3.124)$$

$$dM_k \left( e_k - Ts_k + \frac{p}{\rho_k} - \mu_k \right) = M_k \left( -de_k + Tds_k + \frac{p}{\rho_k^2} d\rho_k \right) \quad (3.125)$$

where  $k = l, g$ . For the liquid phase it is

$$de_l = Tds_l + \frac{p}{\rho_l^2} d\rho_l \quad (3.126)$$

and substituting in eq. (3.125)

$$\mu_l = e_l - Ts_l + \frac{p}{\rho_l} = g_l \quad (3.127)$$

In the gas phase there are two components, vapor  $v$  and non-condensable gas  $d$ , hence

$$de_g = Tds_g + \frac{p}{\rho_g^2} d\rho_g + \mu_v dY + \mu_d d(1 - Y_v) \quad (3.128)$$

### 3.4 Numerical Method

---

with

$$\mu_v = \left. \frac{\partial g_g}{\partial Y_v} \right|_{T,p} ; \quad \mu_d = \left. \frac{\partial g_g}{\partial (1 - Y_v)} \right|_{T,p}$$

Using  $g_g = Y_v g_v + (1 - Y_v) g_d$  one arrives to

$$\mu_v = g_v ; \quad \mu_d = g_d \quad (3.129)$$

and eq. (3.128) becomes

$$de_g = T ds_g + \frac{p}{\rho_g^2} d\rho_g + (g_v - g_d) dY_v \quad (3.130)$$

Particularizing (3.125) for the gas phase and introducing eq. (3.130) yields

$$dM_g \left( e_g - T s_g + \frac{p}{\rho_g} - \mu_g \right) = -M_g (g_v - g_d) dY_v \quad (3.131)$$

Since only vapor undergoes phase transition, it can be written

$$\begin{aligned} M_g &= M_v + M_d \rightarrow dM_g = dM_v \rightarrow dM_g = d(Y_v M_g) = M_g dY_v + Y_v dM_g \rightarrow \\ dM_g &= \frac{M_g}{1 - Y_v} dY_v \end{aligned} \quad (3.132)$$

Introducing eq. (3.132) in (3.131)

$$g_g - \mu_g = (1 - Y_v) g_d - (1 - Y_v) g_v \quad (3.133)$$

and decomposing Gibbs free energy of the gas on arrives to

$$Y_v g_v + (1 - Y_v) g_d - \mu_g = (1 - Y_v) g_d - (1 - Y_v) g_v \quad (3.134)$$

$$\mu_g = g_v \quad (3.135)$$

Using eq. (3.135) and (3.127) in the condition for maximum entropy (3.123) yields  $g_l = g_v$ , which is the equilibrium condition (3.121).

## 3.4 Numerical Method

### 3.4.1 Phase-Splitting method

Convective, diffusion and source terms in the 5-Equation model presented in Section 3.2 can be decoupled using the phase-splitting method suggested by [185] in the context of compressible, single-phase flows. This method is particularly effective when combined with the arbitrary Lagrangian-Eulerian (ALE) description used in fuel atomization, evaporation and combustion, since it allows decoupling the mass transfer between discrete liquid particles (Lagrangian phase) and continuous gas vapor (Eulerian phase) from the calculation of diffusion and convective terms. Aiming at using the same numerical framework for both in-nozzle, spray

and combustion computations, the phase-splitting method is extended here to two-phase, two-species Eulerian flows.

As can be seen in Figure 3.2, the phase-splitting method consists of defining a flow-tracking control volume during the calculation of source terms (Stage A) and diffusion terms (Stage B). After these stages, the control volume is forced into the final position, adding the contribution of the convective terms (Stage C). The final position is determined by the final location of the grid points, which is equal to the initial position for fix mesh problems and different for moving mesh.

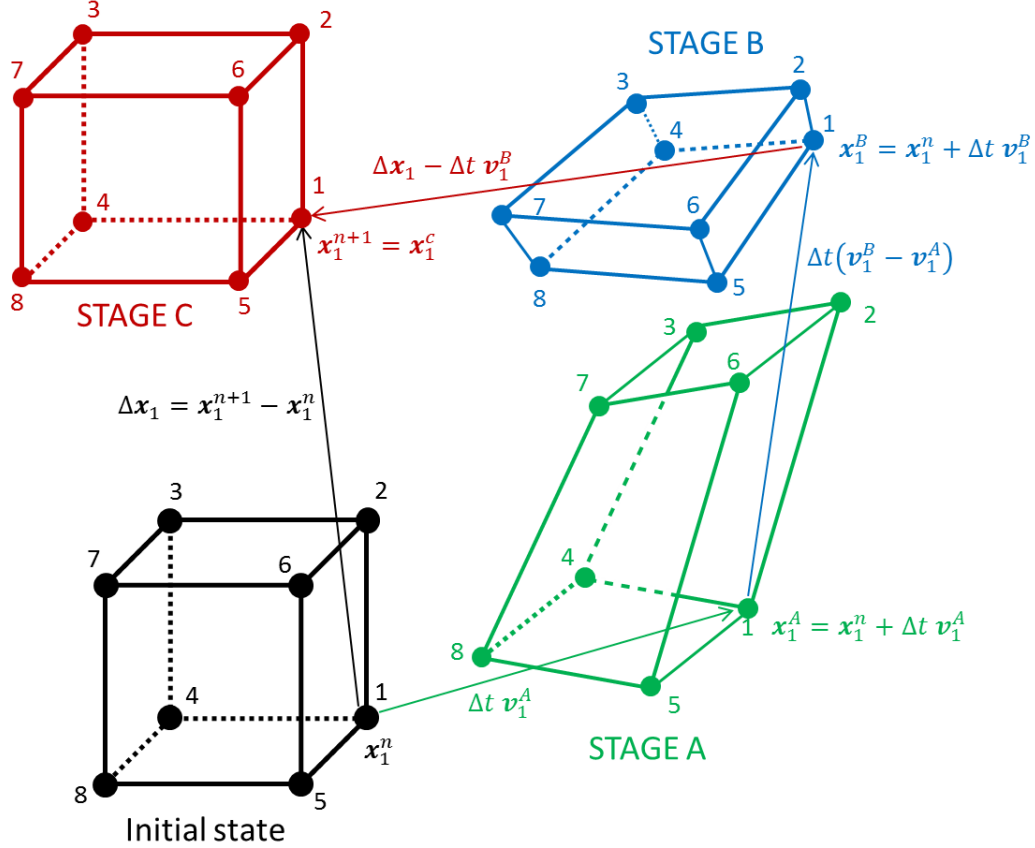


**Figure 3.2:** Flow-tracking control volume in the phase-splitting technique. The control volume moves with the flow in Stage A and B and returns to the final position during Stage C

After Stages A, B and C, heat and mass transfer are calculated in Stages HT and MT respectively. The numerical approach consists of a semi-implicit time integration method where the equations are discretized as follows:

- **STAGE A. Source terms.** Explicit

$$\Psi_k^A = \Psi_k^n + \Delta t \dot{S}_k^n \quad (3.136)$$

- **STAGE B. Diffusion terms.** Implicit

$$\Phi_k^B = \Phi_k^* (\Phi_k^A) + \Delta t C_k^* (\Phi_k^A) Diff (\Phi_k^B) \quad (3.137)$$

### 3.4 Numerical Method

---

- **STAGE C. Convection terms.** Explicit

$$\Psi_k^{n+1} = \Psi_k^B + \Delta t \text{ Flux}(\Phi_k^B) \quad (3.138)$$

- **STAGE HT. Heat transfer term.** Implicit

$$\Psi_k^{HT} = \Psi_k^C + \Delta t Q^{HT} \quad (3.139)$$

- **STAGE MT. Mass transfer term.** Implicit

$$\Psi_k^{MT} = \Psi_k^{HT} + \Delta t \dot{\rho}^{MT} \quad (3.140)$$

with  $k$  denoting liquid, gas or mixture phases,  $\Phi$  the characteristic variables of each conservation equation  $(\alpha_l \rho_l, \alpha_g \rho_g Y_{n_g}, \mathbf{v}, T)$  and  $\Psi$  the conserved variables  $(\alpha_l \rho_l, \alpha_g \rho_g Y_{n_g}, \rho \mathbf{v}, \rho e)$ .  $\dot{S}_k^n$  is the source term of liquid or gas phase at the known starting state  $n$ ,  $Diff$  is the diffusion operator,  $C_k^*$  and  $\Phi_k^*$  are parameters that depend on the thermodynamic conditions at the end of Stage A and  $Flux$  is the convective flux operator. Finally,  $Q$  and  $\dot{\rho}$  are heat and mass transfer between phases, respectively.

The solution strategy is shown in Figure 3.3. First, the source terms are explicitly integrated in time in Stage A. Next, diffusion terms are implicitly integrated in time in Stage B. In this stage, species diffusion is calculated before viscous and heat diffusion, which are computed by solving the coupled velocity-pressure system (VP loop) described in Section 3.4.2. Next, convective terms are explicitly integrated in time in Stage C using a number of sub-cycles with small time-steps limited to ensure numerical stability. Once Stage C is converged, heat transfer is implicitly calculated as described in Section 3.4.4 until thermal equilibrium is attained. Finally, mass transfer is implicitly calculated as described in Section 3.4.5 until reaching chemical equilibrium.

#### 3.4.2 Implicit calculation of diffusion terms

After explicit calculation of the source terms of the mixture model (3.30)-(3.35) in Stage A, diffusion terms are implicitly converged in Stage B through a velocity-pressure (VP) loop. This loop involves the convergence of a coupled system including the momentum, energy and EOS equations. The process is as follows:

##### Species and enthalpy diffusion

Using Eqs. (3.31) and (3.35) and keeping only the terms associated with species diffusion

$$\frac{\partial (\alpha_g \rho_g Y_n)}{\partial t} = \nabla \cdot (\alpha_g \rho_g D_n \nabla Y_n) \quad (3.141)$$

$$\frac{\partial (\rho e)}{\partial t} = \nabla \cdot \left( \alpha_g \rho_g \sum_{n=1}^2 D_n h_n \nabla Y_n \right) \quad (3.142)$$

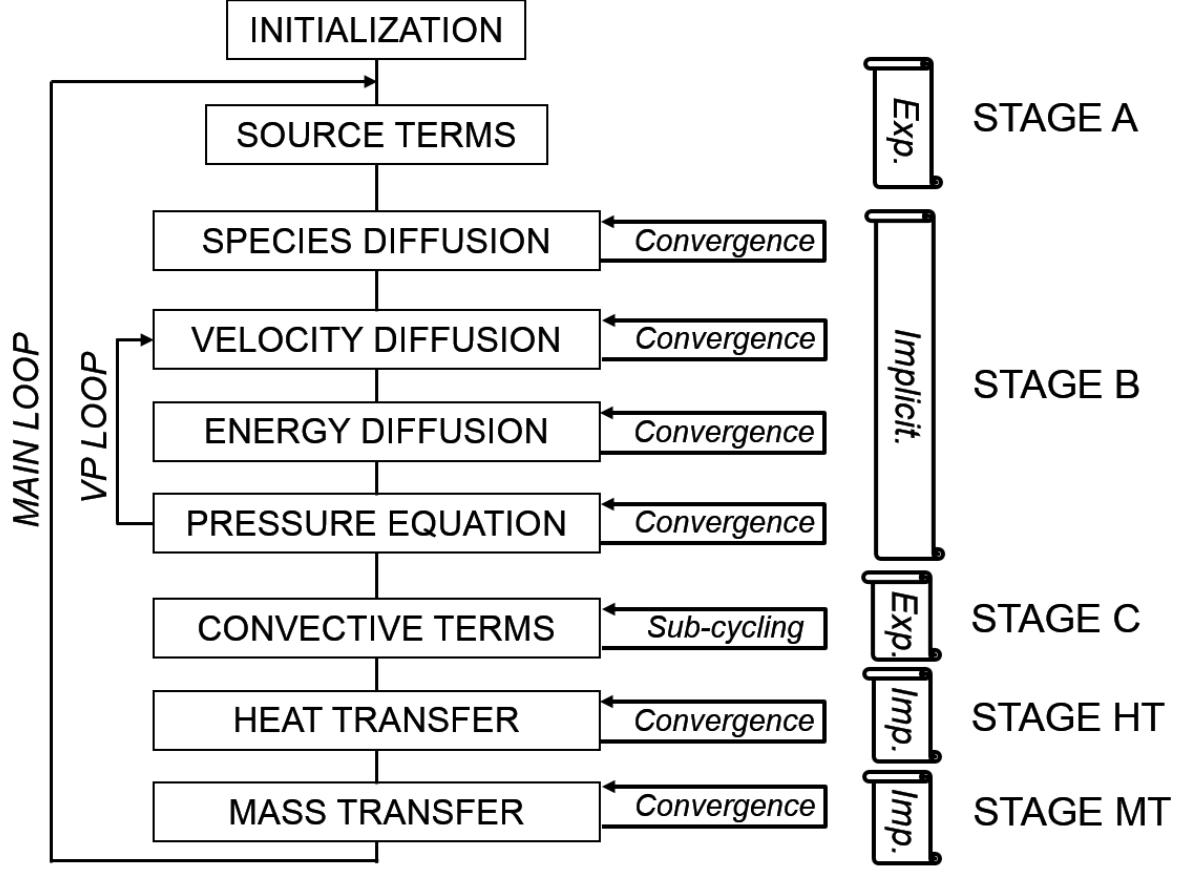


Figure 3.3: Phase-splitting strategy

Expression (3.141) is integrated implicitly as

$$\begin{aligned}
 Y_n^{new} - Y_n^{old} - \frac{\Delta t}{M_g^{new}} \sum_{f=1}^{faces} \left[ (\alpha_g \rho_g D_n)^{old} \left( \nabla \left( Y_n^{new} - Y_n^{old} \right) \right) \right]_f \cdot \mathbf{A}_f^{old} = \\
 = \frac{\Delta t}{M_g^{new}} \sum_{f=1}^{faces} \left[ (\alpha_g \rho_g D_n)^{old} \left( \nabla Y_n^{old} \right) \right]_f \cdot \mathbf{A}_f^{old}
 \end{aligned} \quad (3.143)$$

where “new” denotes the new state and “old” the initial, known state.  $M_g$  is total mass of the gas phase  $M_g = \alpha_g \rho_g Vol$ , “face” refers to the integration cell faces,  $\mathbf{A}$  is the face area and  $\Delta t$  the time-step. With (3.143) converged, the values  $Y_n^{new}$  can be used to add the enthalpy diffusion to the mixture energy equation explicitly

$$e^{new} = e^{old} + \frac{\Delta t}{M^{old}} \sum_{f=1}^{faces} \left[ \alpha_g \rho_g \sum_{n=1}^2 D_n h_n \nabla Y_n^{new} \right]_f \cdot \mathbf{A}_f^{old} \quad (3.144)$$

The new values of  $Y_n$  and  $e$  are used to update the remaining thermodynamic variables with the help of the EOS and the definition of the mixture energy (3.43).

### 3.4 Numerical Method

---

#### Coupled VP loop

In the coupled VP loop, the momentum and energy equations are converged with the support of the EOS. The aim is to write the equations in the form (3.137) so that

$$\mathbf{u}^{new} = \mathbf{u}^* - C_u^* \Delta t \sum_{f=1}^{faces} \boldsymbol{\sigma}(\mathbf{u}^{new}) \cdot \mathbf{A}_f^A \quad (3.145)$$

$$T^{new} = T^* - C_T^* \Delta t \sum_{f=1}^{faces} K_f \nabla T^{new} \cdot \mathbf{A}_f^A \quad (3.146)$$

can be converged iteratively. The momentum equation (3.34) including only diffusion terms reads

$$\frac{\partial(\rho \mathbf{u})}{\partial t} = -\nabla p + \nabla \cdot \boldsymbol{\sigma} \quad (3.147)$$

where the pressure gradient term is included here for convenience rather than in the convective term. Eq. (3.147) can be integrated between Stage A and B as

$$\frac{M^B \mathbf{u}^B - M^A \mathbf{u}^A}{\Delta t} = - \sum_{f=1}^{faces} (\nu_p p^B + (1 - \nu_p) p^A) \mathbf{A}_f^A + \sum_{f=1}^{faces} \boldsymbol{\sigma}(\mathbf{u}^B) \cdot \mathbf{A}_f^A \quad (3.148)$$

The coefficient  $\nu_p$  controls the implicitness of (3.148) and is chosen based on numerical stability. The global mass between A and B is conserved, as demonstrated by summing the continuity equations for all species and phases during Stage B

$$\frac{d}{dt} \int_V \rho dV = 0 \rightarrow M^B = M^A = M \quad (3.149)$$

which allows eq. (3.148) to be recast

$$\mathbf{u}^B = \mathbf{u}^A - \frac{\Delta t}{M} \sum_{f=1}^{faces} (\nu_p p^B + (1 - \nu_p) p^A) \mathbf{A}_f^A + \frac{\Delta t}{M} \sum_{f=1}^{faces} \boldsymbol{\sigma}(\mathbf{u}^B) \cdot \mathbf{A}_f^A \quad (3.150)$$

Comparing (3.150) with (3.145) it can be conclude that for  $\nu_p = 0$

$$\mathbf{u}^* = \mathbf{u}^A - \frac{\Delta t}{M} \sum_{f=1}^{faces} p^A \mathbf{A}_f^A \quad (3.151)$$

$$C_u^* = -\frac{1}{M} \quad (3.152)$$

Eq. (3.150) is looped until convergence of  $\mathbf{u}^B$ . Once  $\mathbf{u}^B$  is known, viscous dissipation is obtained through

$$VD = \Delta t V^A \boldsymbol{\sigma}(\mathbf{u}^B) : \nabla \mathbf{u}^B \quad (3.153)$$

with  $V^A$  the cell volume in Stage A. A similar procedure can be followed to solve the energy equation of the mixture. However, expressing this equation in the form (3.146) is not trivial for two-phase flows. The complexity stems from the need to invert the specific internal energy

of the mixture  $e$  to provide an explicit function of the mixture temperature  $T$ ,

$$e = f(T) \rightarrow T = f^{-1}(e) \quad (3.154)$$

to be used in eq. (3.146). In the present research, we propose consistent definitions of  $T^*$  and  $C_T^*$  needed to solve (3.43). The calculation of  $T^*$  and  $C_T^*$  is mathematically dense, so the reader is referred to Appendix B for a detailed derivation. The energy equation

$$\frac{\partial(\rho e)}{\partial t} = -p \nabla \cdot \mathbf{u} + \boldsymbol{\sigma} : \nabla \mathbf{u} + \nabla \cdot (K \nabla T) \quad (3.155)$$

can be integrated between A and B and expressed in terms of the mixture temperature at B,  $T^B$ . After some algebra, it is possible to write

$$\begin{aligned} T^B = & \frac{T^A + \left( \frac{p^B + p^A}{2} + \alpha_l \pi \right) \frac{V^A}{MC_v} + \frac{VD}{MC_v}}{\frac{p^B + p^A}{2} + \alpha_l \pi} - \\ & \frac{1 + \frac{\alpha_l}{(\gamma_l - 1)} \frac{2}{(p^B + \pi)} + \frac{\alpha_g}{(\gamma_g - 1)} p^B}{\frac{1}{MC_v}} \Delta t \sum_{f=1}^{faces} K_f \nabla T^B \cdot \mathbf{A}_f^A \end{aligned} \quad (3.156)$$

where  $VD$  is viscous dissipation at B given by 3.153,  $C_v$  is specific heat capacity of the mixture at constant volume and  $V^A$  is the mixture volume at A. Comparing (3.156) with (3.146), it can be concluded that

$$T^* = \frac{T^A + \left( \frac{p^B + p^A}{2} + \alpha_l \pi \right) \frac{V^A}{MC_v} + \frac{VD}{MC_v}}{\frac{p^B + p^A}{2} + \alpha_l \pi} \quad (3.157)$$

$$C_T^* = \frac{1}{\frac{p^B + p^A}{2} + \alpha_l \pi} \quad (3.158)$$

It is worth noting that, in the asymptotic limit  $\alpha_g \rightarrow 1$ , the definitions (3.157) and (3.158) recover the values used in [185] for single gas phase

$$T^* = \frac{T^A + \frac{p^B + p^A}{2} \frac{V^A}{MC_v} + \frac{VD}{MC_v}}{\frac{p^B + p^A}{2}} \quad (3.159)$$



### 3.4 Numerical Method

---

$$C_T^* = \frac{\frac{1}{MC_v}}{\frac{p^B + p^A}{1 + \frac{2}{\frac{\alpha_g}{(\gamma_g - 1)} p^B}}} \quad (3.160)$$

hence the definition of  $T^*$  and  $C_T^*$  is consistent. With  $T^*$  and  $C_T^*$  known, eq. (3.146) can be solved for  $T^{new}$ .

The VP loop is closed with a pressure equation derived from the EOS. The aim is to provide a predictor-corrector equation by linearizing the mixture volume around the pressure

$$V^{B+1} \approx V^B + \frac{\partial V^B(p^B)}{\partial p^B} (p^{B+1} - p^B) \quad (3.161)$$

where state  $B + 1$  is close to  $B$ . The mixture volume can be expressed as (see eq. (B.14) in Appendix B)

$$V = V(T, p) = \frac{MC_v T}{\frac{\alpha_l}{(\gamma_l - 1)} (p + \pi) + \frac{\alpha_g}{(\gamma_g - 1)} p} \quad (3.162)$$

and the temperature of the mixture (see eq. (B.17) in Appendix B)

$$MC_v (T^B - T^A) = - \left( \frac{p^B + p^A}{2} + \alpha_l \pi \right) (V^B - V^A) + VD + \Delta t \sum_{f=1}^{faces} K_f \nabla T^B \cdot \mathbf{A}_f^A \quad (3.163)$$

Introducing (3.162) in (3.163) and neglecting viscous dissipation and heat diffusion, the volume of the mixture in Stage B can be expressed as a function of pressure

$$V^B \bar{p}^B - V^A \bar{p}^A = - \left( \frac{p^B + p^A}{2} + \alpha_l \pi \right) (V^B - V^A) \quad (3.164)$$

$$V^B = \frac{V^A \left( \bar{p}^A + \frac{p^B + p^A}{2} + \alpha_l \pi \right)}{\bar{p}^B + \frac{p^B + p^A}{2} + \alpha_l \pi} \quad (3.165)$$

with

$$\bar{p} = \frac{\alpha_l}{\gamma_l - 1} (p + \pi) + \frac{\alpha_g}{\gamma_g - 1} p \quad (3.166)$$

Viscous dissipation and heat diffusion are neglected in eq. (3.164) because their contributions during convergence of the predictor-corrector algorithm tend to zero. Taking the partial derivatives of (3.166) and (3.165)

$$\frac{\partial \bar{p}^B(p^B)}{\partial p^B} = \frac{\alpha_l}{\gamma_l - 1} + \frac{\alpha_g}{\gamma_g - 1} = \frac{1}{\gamma - 1} \quad (3.167)$$

$$\begin{aligned} \frac{\partial V^B(p^B)}{\partial p^B} &= \frac{\frac{1}{2}V^A \left( \bar{p}^B + \frac{p^B + p^A}{2} + \alpha_l \pi \right) - V^A \left( \bar{p}^A + \frac{p^B + p^A}{2} + \alpha_l \pi \right) \left( \frac{1}{\gamma - 1} + \frac{1}{2} \right)}{\left( \bar{p}^B + \frac{p^B + p^A}{2} + \alpha_l \pi \right)^2} = \\ &= - \frac{\frac{V^B}{\gamma - 1} + \frac{1}{2}(V^B - V^A)}{\left( \bar{p}^B + \frac{p^B + p^A}{2} + \alpha_l \pi \right)} \end{aligned} \quad (3.168)$$

Eq. (3.168) describes the variation of mixture volume with pressure during Stage B. Using (3.168) in (3.161)

$$V^{B+1} \approx V^B - \frac{\frac{V^B}{\gamma - 1} + \frac{1}{2}(V^B - V^A)}{\left( \bar{p}^B + \frac{p^B + p^A}{2} + \alpha_l \pi \right)} (p^{B+1} - p^B) \quad (3.169)$$

which is the aforementioned pressure equation. With Eq. (3.150), (3.156) and (3.169) the VP loop is mathematically closed and the changes of  $\mathbf{u}$ ,  $T$  and  $p$  due to diffusion terms can be calculated.

### Solution of the VP loop

The first step to solve the VP loop involves making an initial prediction for the pressure,  $p^p$ , and using this value in the fully implicit ( $\nu_p = 1$ ) momentum equation (3.150) instead of  $p^B$  to obtain  $\mathbf{u}^p$ . Similarly,  $p^p$  is also introduced in the energy equation (3.156) substituting  $p^B$  to get  $T^p$ . With  $T^p$  known,  $p^p$  and  $T^p$  are used in the EOS of the mixture (3.162) to get  $V^p$ .

The second step involves solving for a corrected pressure  $p^c$  and a corrected volume  $V^c$ . Then,  $p^c$ ,  $V^c$  are used in eq. (3.169) to evaluate whether  $p^p$  is the converged pressure or not. First, the volume change is calculated as (see eq. (B.5) in Appendix B)

$$\frac{DV}{Dt} = \int_A \mathbf{u} \cdot \mathbf{n} dA \quad (3.170)$$

which can be integrated between A and the corrected state

$$V^c = V^A + \Delta t \sum_{f=1}^{faces} (\mathbf{u} \cdot \mathbf{A})_f^c \quad (3.171)$$

The corrected cell face velocities multiplied by the corrected cell face areas  $(\mathbf{u} \cdot \mathbf{A})_f^c$  are obtained from the momentum derivative integrated over a control volume and multiplied by the cell face area

$$\frac{\partial(\rho \mathbf{u})}{\partial t} \cdot \frac{\int_V (\cdot) \cdot \mathbf{A}_f dV}{\partial t} \rightarrow \frac{\partial}{\partial t} \int_V \rho \mathbf{u} \cdot \mathbf{A}_f dV = \mathbf{A}_f \cdot \frac{\partial}{\partial t} \int_V \rho \mathbf{u} dV + \frac{\partial \mathbf{A}_f}{\partial t} \cdot \int_V \rho \mathbf{u} dV \quad (3.172)$$

### 3.4 Numerical Method

and from the momentum equation eq. (3.147) integrated over a control volume

$$\frac{\partial(\rho \mathbf{u})}{\partial t} = -\nabla p + \nabla \cdot \boldsymbol{\sigma} \xrightarrow{\int_V()dV} \frac{\partial}{\partial t} \int_V \rho \mathbf{u} dV = - \sum_{ff=1}^{faces} p \mathbf{I} \cdot \mathbf{A}_{ff} + \sum_{ff=1}^{faces} \boldsymbol{\sigma}(\mathbf{u}) \cdot \mathbf{A}_{ff} \quad (3.173)$$

Combining eq. (3.172) and (3.173) one arrives to

$$\frac{\partial}{\partial t} \int_V \rho \mathbf{u} \cdot \mathbf{A}_f dV = \mathbf{A}_f \cdot \left( - \sum_{ff=1}^{faces} p \mathbf{I} \cdot \mathbf{A}_{ff} + \sum_{ff=1}^{faces} \boldsymbol{\sigma}(\mathbf{u}) \cdot \mathbf{A}_{ff} \right) + \frac{\partial \mathbf{A}_f}{\partial t} \cdot \int_V \rho \mathbf{u} dV \quad (3.174)$$

The integration and discretization of (3.174) is staggered, decoupling the process into two stages; an intermediate state  $Ac$  including the viscous terms, and the corrected state  $c$  including the remaining terms. The momentum equation (3.173) can be separated into pressure and viscous terms

$$\frac{\partial}{\partial t} \int_V \rho \mathbf{u} dV = \frac{\partial}{\partial t} \int_V \rho \mathbf{u} dV \Big|_{pressure} + \frac{\partial}{\partial t} \int_V \rho \mathbf{u} dV \Big|_{visc} \quad (3.175)$$

$$\frac{D}{Dt} \int_V \rho \mathbf{u} dV \Big|_{pressure} = - \sum_{ff=1}^{faces} p \mathbf{I} \cdot \mathbf{A}_{ff} \quad (3.176)$$

$$\frac{D}{Dt} \int_V \rho \mathbf{u} dV \Big|_{visc} = \sum_{ff=1}^{faces} \boldsymbol{\sigma}(\mathbf{u}) \cdot \mathbf{A}_{ff} \quad (3.177)$$

Integrating (3.177) between Stage A and state  $Ac$

$$M \frac{\mathbf{u}^{Ac} - \mathbf{u}^A}{\Delta t} = \sum_{ff=1}^{faces} \boldsymbol{\sigma}(\mathbf{u}^{Ac}) \cdot \mathbf{A}_{ff} \quad (3.178)$$

yielding the velocity at the end of state  $Ac$ ,  $\mathbf{u}^{Ac}$ . Eq. (3.174) is integrated and discretized between Stage A and state  $c$  as

$$\begin{aligned} M_f \frac{(\mathbf{u} \cdot \mathbf{A})_f^c - (\mathbf{u} \cdot \mathbf{A})_f^{Ac} + (\mathbf{u} \cdot \mathbf{A})_f^{Ac} - (\mathbf{u} \cdot \mathbf{A})_f^A}{\Delta t} = \\ = -\mathbf{A}_f^A \cdot \sum_{ff=1}^{faces} p^c \mathbf{I} \cdot \mathbf{A}_{ff}^A + \mathbf{A}_f^A \cdot \sum_{ff=1}^{faces} \boldsymbol{\sigma}(\mathbf{u}^{Ac}) \cdot \mathbf{A}_{ff}^A + M_f \frac{\mathbf{A}_f^{Ac} - \mathbf{A}_f^A}{\Delta t} \cdot \mathbf{u}_f^A \end{aligned} \quad (3.179)$$

where the mass swept by the cell face  $f$  in its motion from Stage A to state  $c$ ,  $M_f$ , is interpolated from neighboring cells. Note that the derivative  $\frac{\partial \mathbf{A}_f}{\partial t}$  between Stage A and state  $c$  has been approximated by the derivative between Stage A and state  $Ac$ , leading to an explicit equation in  $(\mathbf{u} \cdot \mathbf{A})_f^c$ . Taking into account (3.178), eq. (3.179) can be simplified as

$$M_f \frac{(\mathbf{u} \cdot \mathbf{A})_f^c - (\mathbf{u} \cdot \mathbf{A})_f^{Ac}}{\Delta t} = -\mathbf{A}_f^A \cdot \sum_{ff=1}^{faces} p^c \mathbf{I} \cdot \mathbf{A}_{ff}^A + M_f \frac{\mathbf{A}_f^{Ac} - \mathbf{A}_f^A}{\Delta t} \cdot \mathbf{u}_f^A \quad (3.180)$$

The cell face velocity  $\mathbf{u}_f^A$  is interpolated from neighboring face vertex velocities, and the

variable  $(\mathbf{u} \cdot \mathbf{A})_f^{Ac}$  is computed as

$$(\mathbf{u} \cdot \mathbf{A})_f^{Ac} = \mathbf{u}_f^{Ac} \cdot \mathbf{A}_f^{Ac} \quad (3.181)$$

with  $\mathbf{u}_f^{Ac}$  given by (3.178) and interpolated from face vertices. The face area in state  $Ac$ ,  $\mathbf{A}_f^{Ac}$ , is built by tracking the position of the neighboring vertices,  $\mathbf{x}_p$ , and linearizing around Stage A

$$\mathbf{A}_f(\mathbf{x}_p^{Ac}) \approx \mathbf{A}_f(\mathbf{x}_p^A + \mathbf{u}_p^A \Delta t) \quad (3.182)$$

Once  $(\mathbf{u} \cdot \mathbf{A})_f^c$  is known from (3.180),  $V^c$  is obtained from (3.171) and the pressure equation (3.169) can be finally particularized for the corrected and predicted states

$$V^c \approx V^p - \frac{\frac{V^p}{\gamma - 1} + \frac{1}{2}(V^p - V^A)}{\left(\bar{p}^p + \frac{p^p + p^A}{2} + \alpha_l \pi\right)} (p^c - p^p) \quad (3.183)$$

When (3.183) is converged, the pressure at the end of Stage B is given by  $p^p$ , along with the remaining characteristic variables  $\mathbf{u}^B$ ,  $T^B$  and  $V^B$ .

### 3.4.3 Explicit calculation of convective terms

Explicit integration of the convective terms is performed in Stage C. The calculation is divided into a number of convective sub-cycles,  $NC$  with an associated time-step  $\Delta t_c$ . The number of convective sub-cycles is determined by a maximum CFL number. The aim is to integrate and discretize the conservation equations between Stage B and C as

$$\Psi_k^C V^C = \Psi_k^B V^B + \sum_{f=1}^{faces} (\Psi_k^B)_f \delta V_f \quad (3.184)$$

with  $\Psi_k^C$  one of  $\alpha_l \rho_l, \alpha_g \rho_g Y_{n_g}, \rho \mathbf{u}, \rho e$ . As shown in Figure 3.4, the magnitude  $\delta V_f$  is the volume swept by face  $f$  when it is forced to move between the position at the end of Stage B to the final position at the end of Stage C

$$\delta V_f = \delta V_f^T \frac{\Delta t_c}{\Delta t} - (\mathbf{u} \cdot \mathbf{A})_f^B \Delta t_c \quad (3.185)$$

where  $(\mathbf{u} \cdot \mathbf{A})_f^B$  is calculated from the converged solution of eq. (3.180) and  $\Delta t_c$  is related to the global time-step  $\Delta t$  through

$$\Delta t = \sum_{n=1}^{NC} \Delta t_{c_n} \quad (3.186)$$

Note that the volume swept by face  $f$  from the initial state to the final state,  $\delta V_f^T$ , is known and equal to 0 for fix mesh problems.

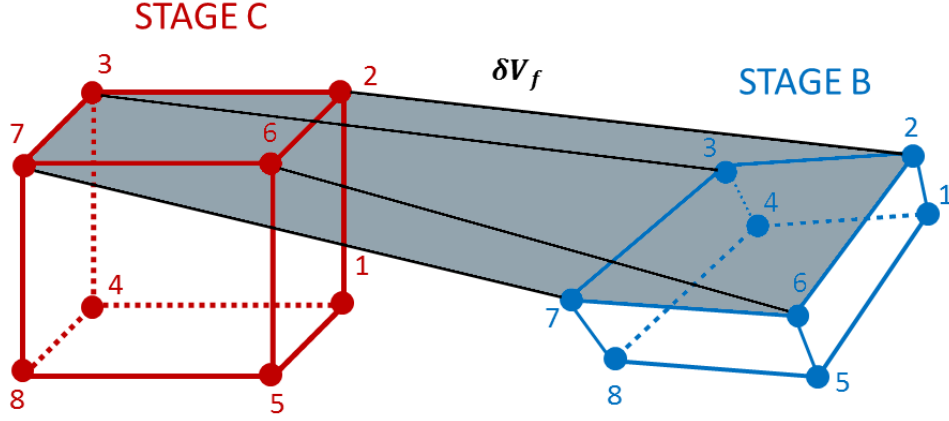


**Figure 3.4:** Definition of the volume swept by face  $f$  between Stages B and C,  $\delta V_f$  (in gray)

#### 3.4.3.1 Interface reconstruction

The conservative variable at the cell face  $(\Psi_k^B)_f$  at the end of Stage B needs to be reconstructed from neighboring cells. The numerical scheme used is a quasi-second-order upwind (QSOU) discretization similar to the one in [185], which is based on the conservative difference scheme proposed by Leer [186]. The QSOU is chosen because it ensures strong monotonicity and smoothness, removing the oscillatory behavior associated with high-order schemes.

Figure 3.5 shows the convention used to describe neighboring cells. Subscript  $f - \frac{1}{2}$  labels the cell to the left of face  $f$ , according to the cell face normal  $\mathbf{n}_f$ . Alternatively, subscript  $f + \frac{1}{2}$  labels the cell to the right of  $f$ . The volume swept by face  $f$  between two consecutive instants  $t^n$  and  $t^{n+1}$  is shown in gray color, denoting the final position of  $f$  as  $f(t^{n+1})$ . The sign convention is also shown, indicating that  $\delta V_f < 0$  when  $f$  moves towards the left cell (direction vector equal to  $-\mathbf{n}_f$ ) and  $\delta V_f > 0$  when  $f$  moves towards the right cell (direction vector equal to  $\mathbf{n}_f$ ).

In unstructured computational domains,  $\Psi_k$  can be reconstructed at the interface using the QSOU scheme as follows

$$(\Psi_k)_f = \begin{cases} (\Psi_k)_{f-\frac{1}{2}} + \frac{1}{2} \left( 1 - \frac{\sum_{ff=1}^{F_{f-\frac{1}{2}}} \delta V_{ff}}{V_{f-\frac{1}{2}}} \right) Sp_f & \text{if } \delta V_f < 0 \\ (\Psi_k)_{f+\frac{1}{2}} + \frac{1}{2} \left( 1 - \frac{\sum_{ff=1}^{F_{f+\frac{1}{2}}} \delta V_{ff}}{V_{f+\frac{1}{2}}} \right) Sp_f & \text{if } \delta V_f > 0 \end{cases} \quad (3.187)$$

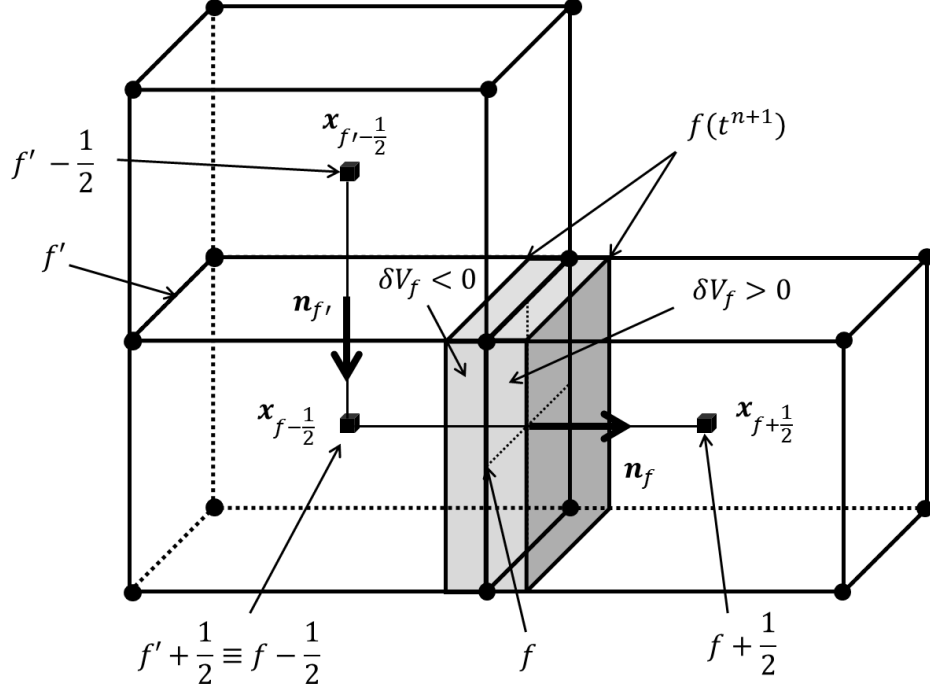


**Figure 3.5:** Schematic representation of face normal and sign criterion for the swept volume  $\delta V_f$

where  $(\Psi_k)_f$  is the reconstructed value at cell face  $f$  and the upper limit of the sum,  $F_{f-\frac{1}{2}}$ , indicates that the sum applies to all the faces of cell  $f - \frac{1}{2}$  (same for  $F_{f+\frac{1}{2}}$  and cell  $f + \frac{1}{2}$ ). The slope at face  $f$  is limited by

$$Sp_f = \min \left[ \max \left( g_{f-\frac{1}{2}}, 0 \right), \max \left( g_{f+\frac{1}{2}}, 0 \right) \right] + \max \left[ \min \left( g_{f-\frac{1}{2}}, 0 \right), \min \left( g_{f+\frac{1}{2}}, 0 \right) \right] \quad (3.188)$$

where

$$g_{f-\frac{1}{2}} = (\Psi_k)_{f-\frac{1}{2}} - (\Psi_k)_{f-\frac{1}{2}}^b \quad (3.189)$$

$$g_{f+\frac{1}{2}} = (\Psi_k)_{f+\frac{1}{2}} - (\Psi_k)_{f+\frac{1}{2}}^b \quad (3.190)$$

$$(\Psi_k)_{f-\frac{1}{2}}^b = \sum_{ff=1}^{F_{f-\frac{1}{2}}} \left\{ \begin{array}{ll} (\Psi_k)_{ff+\frac{1}{2}} \frac{\delta V_{ff}}{F_{ff-\frac{1}{2}}} & \text{if } \delta V_{ff} > 0 \text{ and } \mathbf{n}_{ff} \cdot \frac{(\mathbf{x}_{ff+\frac{1}{2}} - \mathbf{x}_{ff-\frac{1}{2}})}{|\mathbf{x}_{ff+\frac{1}{2}} - \mathbf{x}_{ff-\frac{1}{2}}|} > 0 \\ \sum_{f^*=1} \delta V_{f^*} & \\ (\Psi_k)_{ff-\frac{1}{2}} \frac{(-\delta V_{ff})}{F_{ff+\frac{1}{2}}} & \text{if } \delta V_{ff} < 0 \text{ and } \mathbf{n}_{ff} \cdot \frac{(\mathbf{x}_{ff+\frac{1}{2}} - \mathbf{x}_{ff-\frac{1}{2}})}{|\mathbf{x}_{ff+\frac{1}{2}} - \mathbf{x}_{ff-\frac{1}{2}}|} < 0 \\ \sum_{f^*=1} \delta V_{f^*} & \\ 0 & \text{if } \delta V_{ff} \mathbf{n}_{ff} \cdot \frac{(\mathbf{x}_{ff+\frac{1}{2}} - \mathbf{x}_{ff-\frac{1}{2}})}{|\mathbf{x}_{ff+\frac{1}{2}} - \mathbf{x}_{ff-\frac{1}{2}}|} < 0 \end{array} \right.$$

### 3.4 Numerical Method

$$(3.191)$$

and  $(\Psi_k)_{f+\frac{1}{2}}^b$  is defined by (3.191) but summing for the faces of cell  $f + \frac{1}{2}$ .  $\delta V_f$  controls the amount of “upwinding” of the scheme, maximizing the accuracy whilst maintaining strong monotonicity.

#### 3.4.4 Calculation of heat transfer

After Stage C, all the thermodynamic variables concerning the system without heat and mass transfer are known. Heat transfer is then calculated using eq. (3.62), (3.63), (3.68) and (3.69), which can be integrated between the end of Stage C and the end of the heat transfer process  $HT$  as

$$(\alpha_g \rho_g)^{HT} = (\alpha_g \rho_g)^C \quad (3.192)$$

$$(\alpha_l \rho_l)^{HT} = (\alpha_l \rho_l)^C \quad (3.193)$$

$$(\alpha_g \rho_g e_g)^{HT} = (\alpha_g \rho_g e_g)^C - \int_{\alpha_l^C}^{\alpha_l^{HT}} \kappa(\alpha_l) d\alpha_l \quad (3.194)$$

$$(\alpha_l \rho_l e_l)^{HT} = (\alpha_l \rho_l e_l)^C + \int_{\alpha_l^C}^{\alpha_l^{HT}} \kappa(\alpha_l) d\alpha_l \quad (3.195)$$

The solution process involves making a guess for  $\alpha_l^{HT}$  in order to calculate the integrals in the second term of the right hand side of (3.194) and (3.195). Then, using (3.192) and (3.193) the specific internal energies  $e_g^{HT}$  and  $e_l^{HT}$  are obtained. With  $e_g^{HT}$  and  $e_l^{HT}$  known, the phase temperatures  $T_g^{HT}$  and  $T_l^{HT}$  can be calculated from each EOS,  $T_g^{HT}(e_g^{HT}, \rho_g^{HT})$  and  $T_l^{HT}(e_l^{HT}, \rho_l^{HT})$  since the phase densities are equal to

$$\rho_g^{HT} = \frac{\alpha_g^C \rho_g^C}{(1 - \alpha_l^{HT})} \quad (3.196)$$

$$\rho_l^{HT} = \frac{\alpha_l^C \rho_l^C}{\alpha_l^{HT}} \quad (3.197)$$

The iteration process progresses until temperature equilibrium is reached, this is

$$T_l^{HT} = T_g^{HT} \quad (3.198)$$

and the remaining thermodynamic variables are updated with the converged values.

#### 3.4.5 Calculation of mass transfer

Mass transfer is computed after heat transfer following a similar strategy. Eq. (3.80), (3.81), (3.87) and (3.88) can be integrated between the end of the heat transfer process  $HT$  and the

end of the mass transfer process  $MT$  as

$$(\alpha_g \rho_g)^{MT} = (\alpha_g \rho_g)^{HT} - \int_{\alpha_l^{HT}}^{\alpha_l^{MT}} \varrho(\alpha_l) d\alpha_l \quad (3.199)$$

$$(\alpha_l \rho_l)^{MT} = (\alpha_l \rho_l)^{HT} + \int_{\alpha_l^{HT}}^{\alpha_l^{MT}} \varrho(\alpha_l) d\alpha_l \quad (3.200)$$

$$(\alpha_g \rho_g e_g)^{MT} = (\alpha_g \rho_g e_g)^{HT} - \int_{\alpha_l^{HT}}^{\alpha_l^{MT}} \varrho(\alpha_l) e^I(\alpha_l) d\alpha_l \quad (3.201)$$

$$(\alpha_l \rho_l e_l)^{MT} = (\alpha_l \rho_l e_l)^{HT} + \int_{\alpha_l^{HT}}^{\alpha_l^{MT}} \varrho(\alpha_l) e^I(\alpha_l) d\alpha_l \quad (3.202)$$

The problem is mathematically closed with  $\varrho$  and  $e^I$  given by eq. (3.115) and (3.116), since all the variables can be expressed as a function of  $\alpha_l$ . To calculate the thermodynamic variables at the end of mass transfer, an initial guess  $\alpha_l^{MT}$  is made, using this value to compute the second term of the right hand side of (3.199) -(3.202). First, the phase densities are obtained, then the phase specific internal energies and finally the remaining variables using the EOS. The iterative process is converged when the system is in full thermodynamic equilibrium and the specific Gibbs free energy of the liquid is equal to the specific Gibbs free energy of the vapor

$$g_l^{MT} = g_v^{MT} \quad (3.203)$$

The phase Gibbs free energies for each phase are given by

$$g_v = C_{p_v} T_g - T_g C_{v_v} \ln \frac{T_g^{\gamma_g}}{p^{\gamma_g-1}} \quad (3.204)$$

$$g_l = (\gamma_l C_{v_l} - q') T_l - T_l C_{v_l} \ln \frac{T_l^{\gamma_l}}{(p + \pi)^{\gamma_l-1}} + q \quad (3.205)$$

Calculation of characteristic parameters  $C_{v_l}$ ,  $\gamma_l$ ,  $q$  and the entropy offset  $q'$  is described in Appendix A.

### 3.4.6 Calculation of thermodynamic variables using the EOS

After every calculation stage (Stage A, B, C,  $HT$  and  $MT$ ) all the characteristic variables must be synchronized before proceeding to the next step. This synchronization is done using the EOS (3.44)-(3.47), the mixture energy eq. (3.43) and the mixture temperature (3.48). First the mixture energy equation is rewritten as

$$\rho e = \alpha_l \rho_l \left( \frac{p + \gamma_l \pi}{\rho_l (\gamma_l - 1)} + q \right) + (1 - \alpha_l) \rho_g \left( \sum_{n=1}^2 Y_n e_n^{exp}(T_g) \right) \quad (3.206)$$



### 3.5 Conclusions

---

The specific internal energy of species  $n$ ,  $e_n^{exp}(T_g)$  is measured experimentally and tabulated up to  $T_g = 5000\text{ K}$ . There are two possible situations when updating the variables:  $\alpha_l, \rho_l, \rho_g, \rho_e$  known and  $p, T_g, T_l$  and  $T$  unknown or  $\alpha_l, \rho_l, \rho_g, p$  known and  $T_g, T_l, T, \rho_e$  unknown. Whereas the second case involves a simple explicit calculation, the first scenario requires solving (3.206) implicitly. Since  $e_n^{exp}(T_g)$  is discrete, (3.206) is strictly non-differentiable, which prevents the use of implicit solvers with high-order of convergence (i.e. Newton-Raphson). For this reason, the conventional secant method is chosen (order of convergence  $\approx 1.62$  [187]), enhanced by a suitable choice of the initial guess vector. The secant method shows to be a robust solver that, provided the smooth variation of  $e_n^{exp}(T_g)$ , yields a relatively fast convergence. With  $p$  converged,  $\rho_e$  is given by (3.206),  $T_g$  and  $T_l$  by (3.45) and (3.47) respectively, and the mixture temperature by (3.48).

To conclude the numerical method description, Appendix C shows the solution method used in the code IFP-C3D.

### 3.5 Conclusions

A 5-Equation model for compressible two-phase, two-species flows was developed. It was intended for liquid-gas flows operating under high pressure conditions where the liquid phase presents some level of compressibility (i. e. high pressure Diesel injection) and the gas phase is composed of liquid vapor and dissolved, non-condensable gas. The model was proposed in order to increase the numerical robustness and efficiency of available 7-Equation multifluid models. Additionally, it aimed at improving the predictive capability of the 7-Equation model in flows with high density gradients.

The 5-Equation model was reduced from a 7-Equation, multifluid model assuming instantaneous velocity and pressure equilibrium. Heat and mass transfer are taken into account by assuming temperature and Gibbs free energy equilibrium. Phase pressures and velocities relax infinitely faster than the phase temperatures, which in turn relax infinitely faster than the Gibbs free energies. The mixture temperature was defined so that is consistent with the resolution of both hyperbolic and parabolic systems. The thermodynamic closure involved ideal gas EOS for the gas phase and SG-EOS for the liquid phase, calculating the constitutive parameters based on experimental curves of phase enthalpy and saturation volume.

A phase-splitting method was used to decouple the calculation of source terms, diffusion terms and convection terms. First, the source terms were calculated explicitly, using first order discretization in time. Next, the diffusion terms were calculated implicitly solving a coupled velocity-pressure loop. The solution process involved solving the momentum and energy equations expressed as a function of mixture velocity and mixture temperature. The coefficients required to express the equations in such a way were derived in the context of two-phase flows. The loop was closed with a predictor-corrector equation for the pressure used to determine whether the solution was converged or not. Convective terms were finally calculated, sub-cycling with small time-steps that satisfy the stability condition. Reconstruction at interfaces was performed with a Quasi-Second Order Upwind scheme that ensured strong monotonicity and smoothness of the solution.

Once the homogeneous system was converged, heat and mass transfer were calculated separately. During the heat transfer process, all the thermodynamic variables were updated depending on the amount of energy transferred from one phase to the other until the phase temperatures were equal. Similarly, during the mass transfer process the thermodynamic variables changed depending on the mass transferred between phases and the energy associated with it until the specific Gibbs free energies of the liquid and vapor were equal. While the heat transfer process was similar to that of the single-species case, the mass transfer process was different owing to mass fraction variation. In this context, the mass transfer model was extended to two-species, one of them non-condensable, modifying the interfacial energy and the interfacial density.

## Chapter 4

---

# 5-Equation model validation

---

---

### 4.1 Introduction

Reference data regarding two-phase, two-species compressible flows available in the literature are very scarce. Although these type of flows have been deeply investigated under low pressure conditions [188, 14, 9, 189, 6, 190], there is a lack of experimental data under high pressure conditions. This stems from difficult experimental accessibility caused by dense materials and very small geometries. Furthermore, the complexity of measuring different gas species with light absorption based methods has also contributed to this lack of information. To the best of our knowledge, there are no experimental studies discerning between gas species in two-phase flows under high pressure conditions. For this reason, experimental measurements of void fraction in a single hole injector at low injection pressure [9] are used together with available numerical results [76] to validate the model.

The Chapter is organized as follows. In the next three Sections the 5-Equation model is validated against three test cases, namely shock tube, water cavitation tube and two-phase expansion tube, which test the hyperbolic system when the gas phase contains only vapor. The shock tube problem compares the proposed 5-Equation model with a 7-Equation model already available in the IFP-C3D code, focusing on accuracy and computational performance. The water cavitation tube problem tests the ability of the 5-Equation model to deal with heat transfer and phase transition induced by strong expansion waves. In this case, the results are compared with those generated by Zein et al. [42] using their 7-Equation model. The two-phase expansion tube also tests the ability to deal with heat and mass transfer induced by strong expansion waves. In this case, however, experimental data are available regarding the velocity of the vaporization front. The next Section of the Chapter is dedicated to the single hole injector problem, testing the complete functionality of the 5-Equation model (two-phase, two-species flow with viscous and heat diffusion). The results are compared with experimental measurements of void fraction [9] and with numerical data [76]. Finally, conclusions are drawn in the last Section.

## 4.2 Shock tube

Figure 4.1 shows the computational domain of the shock tube problem, which consists of a 1 m long, square cross-section tube separated into two different regions and filled with liquid and vapor n-dodecane. Initially ( $t = 0$  s), the left side of the tube ( $x < 0.5$  m) is filled with 0.001% of vapor ( $\alpha_g = 10^{-5}$ ) and the rest of liquid ( $\alpha_l = 1 - 10^{-5}$ ) at temperature 300 K and pressure 200 MPa. The right side of the tube ( $x > 0.5$  m) is filled with 0.001% of liquid ( $\alpha_l = 10^{-5}$ ) and the rest of vapor ( $\alpha_g = 1 - 10^{-5}$ ) at 300 K and 50 MPa. At  $t = 0$  s, both phases are quiescent. The characteristic parameters of the n-dodecane liquid are

$$\gamma_l = 2.35 \quad ; \quad C_{v_l} = 1077 \frac{J}{kgK} \quad ; \quad q = -755000 \frac{J}{kg} \quad ; \quad \pi = 4 \cdot 10^8 Pa \quad (4.1)$$

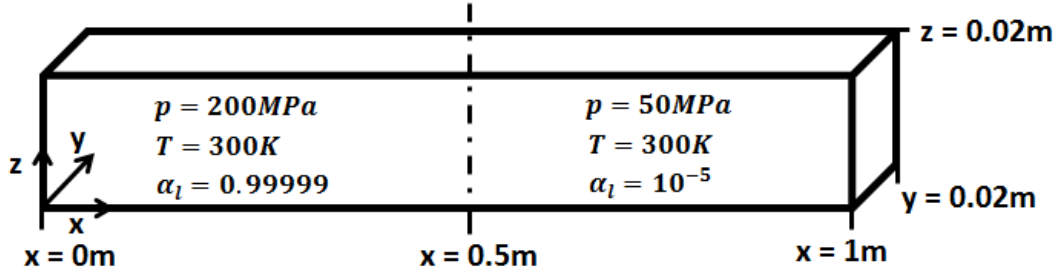


Figure 4.1: Initial conditions and dimensions of the shock tube test case

The computational domain consists of 1000 longitudinally equispaced cells in the x-direction, 2 in the y-direction and 2 in the z-direction, for a total of 4000 cells. The 2 cells used in y and z are the minimum number of cells allowed by the code to impose the wall boundary conditions with slip velocities, which are the ones used at the boundaries. For a boundary face  $f$  located between cells  $f - \frac{1}{2}$  (ghost cell outside the domain) and  $f + \frac{1}{2}$  (first cell inside the domain), this boundary condition is defined as

$$\mathbf{v}_{f-\frac{1}{2}} \cdot \mathbf{n} = -\mathbf{v}_{f+\frac{1}{2}} \cdot \mathbf{n} \quad ; \quad \mathbf{v}_{f-\frac{1}{2}} - \left( \mathbf{v}_{f-\frac{1}{2}} \cdot \mathbf{n} \right) \mathbf{n} = \mathbf{v}_{f+\frac{1}{2}} - \left( \mathbf{v}_{f+\frac{1}{2}} \cdot \mathbf{n} \right) \mathbf{n} \quad (4.2)$$

where  $\mathbf{n}$  is normal to the wall and the thermodynamic variables are copied from cell  $f + \frac{1}{2}$  to  $f - \frac{1}{2}$ . The time-step used during the simulation is  $\Delta t = 2 \cdot 10^{-8}$  s.

Figure 4.2 plots pressure, velocity, mixture density and liquid volume fraction at time  $t = 5 \cdot 10^{-4}$  s, comparing the 5-Equation model with the analytical solution for pure phases and the results yielded by a 7-Equation model available in IFP-C3D. Both 5-Equation and 7-Equation models capture the right-going shock wave, the left-going rarefaction wave and the contact discontinuity between the shock and the rarefaction. The QSOU reconstruction provides good resolution near jumps, particularly in the volume fraction and mixture density plots. Regarding the pressure plot, there is a higher discrepancy between the 7-Equation model and the analytical solution near the initial discontinuity (located at  $x = 0.32$  m at  $t = 5 \cdot 10^{-4}$  s). At the contact discontinuity,  $x = 0.54$  m, there is an overshoot in the 5-Equation model that does not appear in the 7-Equation model. This is linked to the non-conservative terms in the volume fraction equation and the numerical errors absorbed by the volume fraction,

## 4.2 Shock tube

affecting the EOS of the mixture and thus the pressure. In the 7-Equation model, pressure relaxes at the end of the solution process and is less sensitive to errors in volume fraction. The velocity distribution indicates that the 5-Equation model is more accurate than the 7-Equation model in the region between the shock wave and the contact wave ( $0.54\text{ m} < x < 0.6\text{ m}$ ). In particular, the 7-Equation model exhibits an overshoot right after the shock wave that does not appear in the 5-Equation model.

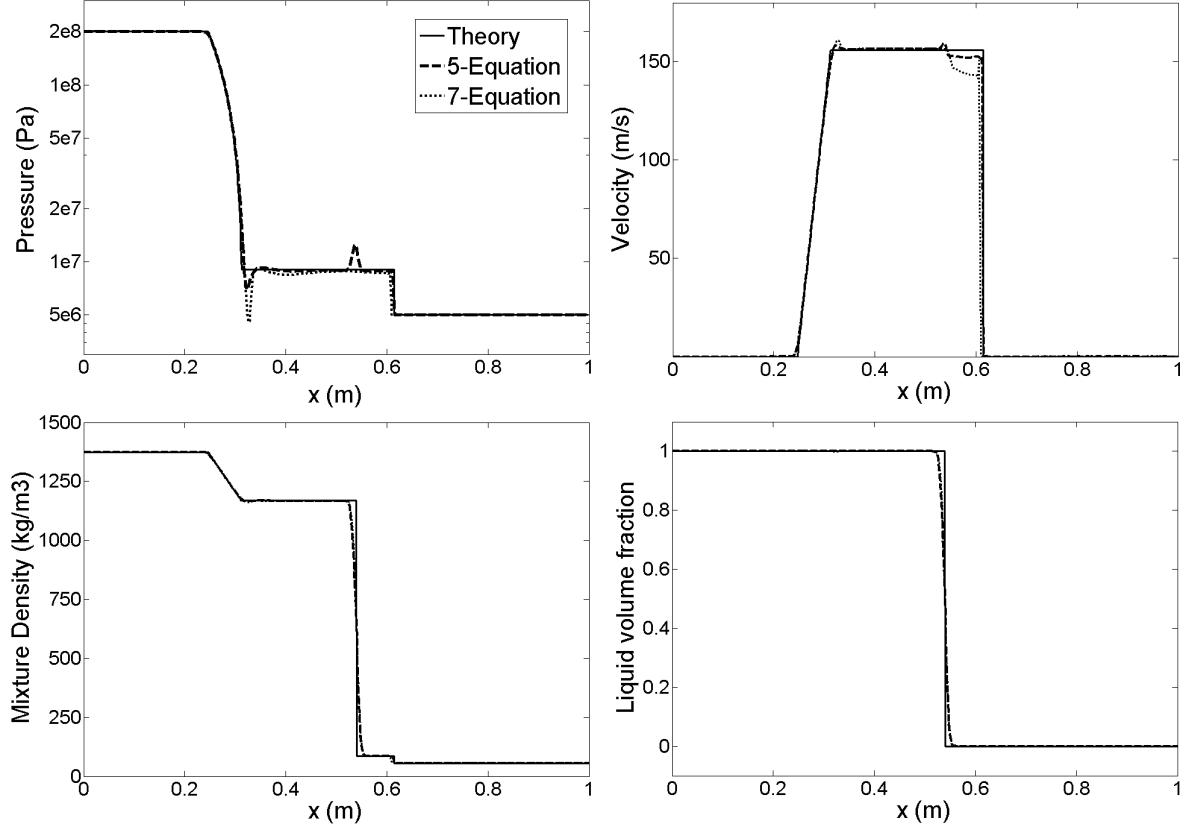


**Figure 4.2:** Shock tube test case results at  $t = 5.10^{-4}\text{ s}$ . 5-Equation and 7-Equation results are compared with the analytical solution (labeled “Theory”)

Another important feature of the 5-Equation model is the volume fraction compressibility taken into account by the first term of the right-hand side of eq. (3.30). In order to evaluate the impact of this term on the solution, the same test case is run increasing the amount of dissolved phase, initializing  $\alpha_g = 10^{-3}$ ,  $\alpha_l = 1 - 10^{-3}$  on the left side  $x < 0.5\text{ m}$  and  $\alpha_g = 1 - 10^{-3}$ ,  $\alpha_l = 10^{-3}$  on the right side  $x > 0.5\text{ m}$ . Under these conditions, the aforementioned term has a greater impact on the volume fraction advection and subsequently on the remaining thermodynamic variables.

Figure 4.3 compares the results at  $t = 5 \cdot 10^{-4}\text{ s}$  with those yielded by 7-Equation model. The analytical solution for pure phases is also included as “Reference”. Volume fraction compressibility modifies the velocity variation across the rarefaction wave from a linear to a non-linear profile. Similarly, the quasi-linear pressure variation across the rarefaction changes into non-linear (note that the pressure plot in Figure 4.3 is expressed in logarithmic scale). As a consequence of the higher gas volume fraction after the rarefaction, which increases by one order of magnitude, the tail of the rarefaction is slowed down due to lower sound speed. This is more severe in the 7-Equation model, since the gas expansion predicted ( $\alpha_g = 0.02$ ) is

higher than the one predicted by the 5-Equation model ( $\alpha_g = 0.01$ ). Regarding the right-going shock wave, the difference between both models is small, with the 5-Equation model yielding pressure and velocity slightly closer to the Reference curve.

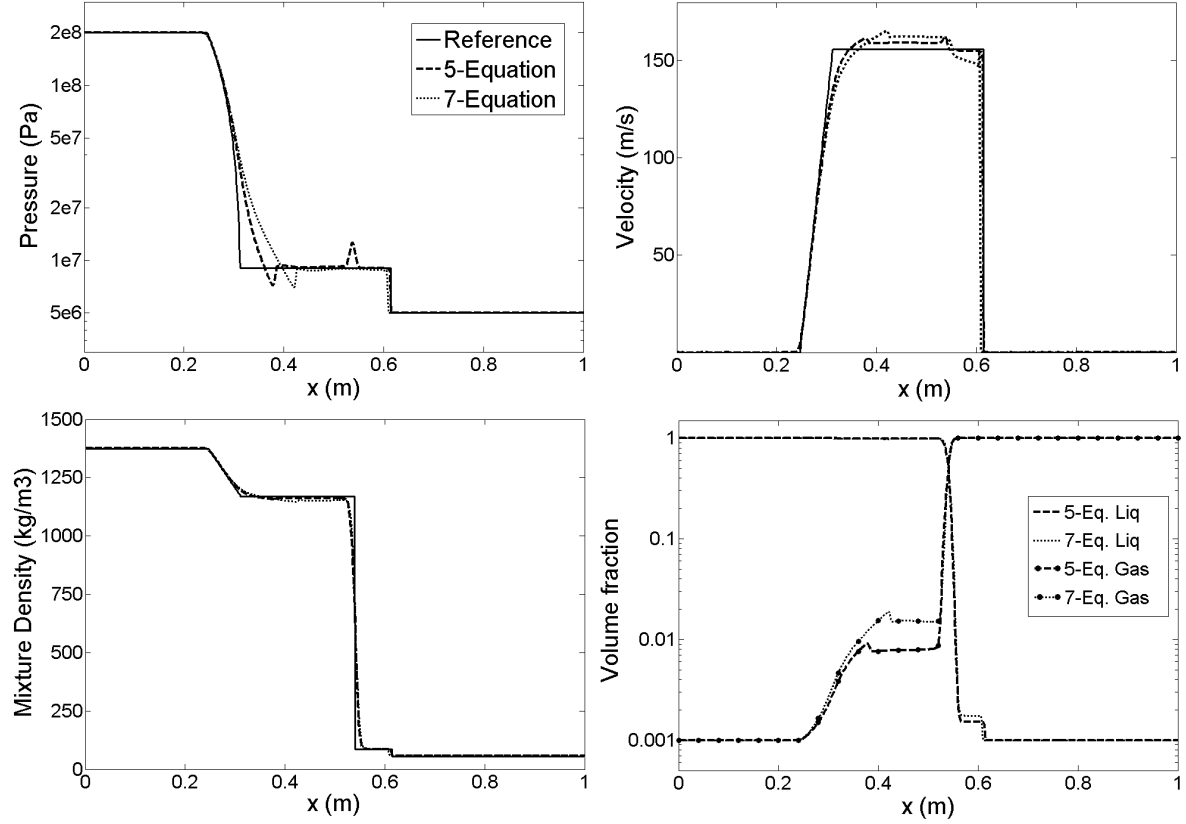


**Figure 4.3:** Shock tube test case results at  $t = 5.10^{-4}s$  with increased dissolved phase ( $\alpha_g = 10^{-3}$ ,  $\alpha_l = 1 - 10^{-3}$  at  $x < 0.5m$  and  $\alpha_g = 1 - 10^{-3}$ ,  $\alpha_l = 10^{-3}$  at  $x > 0.5m$ ). 5-Equation and 7-Equation results are compared with the analytical solution for pure phases (labeled “Reference”)

#### 4.2.1 Computational performance

The proposed 5-Equation model has some advantages over the 7-Equation model in terms of robustness and computational efficiency. Pressure and velocity relaxation enforced in the 7-Equation model at the end of every computational time-step can lead to numerical instabilities, especially when dealing with high interfacial pressure gradients  $(p_l - p_g) / \Delta x \gg 0$ . This stems from the stiff relaxation process, where the converged phase pressures are forced to satisfy  $p_l = p_g$ . Alternatively, the 5-Equation model integrates the condition  $p_l = p_g$  in the model definition, enforcing it not only after convergence of all the thermodynamic variables but during the convergence process itself.

As far as the computational efficiency is concerned, Table 4.1 compares the computational cost of the simulations discussed above. The 5-Equation model reduces significantly the cost in all the cases mainly due to less equations to be solved. In the first case reported (dissolved gas phase  $\alpha = 10^{-5}$ ), the 5-Equation model yields an improvement of 21% respect to the 7-Equation model in CPU time needed to compute one time-step. As the dissolved quantity increases to  $\alpha = 10^{-3}$ , the computational time difference is reduced to 10%. This is partly

### 4.3 Water cavitation tube

due to iterative process used to solve the EOS of the mixture, which requires more iterations until convergence.

	7-Equation $\alpha = 10^{-5}$	5-Equation $\alpha = 10^{-5}$	7-Equation $\alpha = 10^{-3}$	5-Equation $\alpha = 10^{-3}$
CPU time to compute one time-step	$2.52 \cdot 10^{-2} s$	$1.97 \cdot 10^{-2} s$	$2.56 \cdot 10^{-2} s$	$2.52 \cdot 10^{-2} s$
Relative time	100%	78.4%	101.82%	91.1%

**Table 4.1:** Computational efficiency of the 5-Equation model compared with the 7-Equation model implemented in IFP-C3D. The computational times are recorded in the shock tube problem calculations

### 4.3 Water cavitation tube

The water cavitation tube allows evaluating the mass transfer process defined in Section 3.4.5. As shown in Figure 4.4, the test consists of a 1m long tube filled with a mixture of  $\alpha_l = 0.99$  liquid water and  $\alpha_g = 0.01$  water vapor. The liquid water density is taken as  $\rho_l = 1150 \text{ kg/m}^3$  at 1 bar. The left side of the tube ( $x < 0.5 \text{ m}$ ) is initialized with negative velocity  $u = -2 \text{ m/s}$  and the right side of the tube ( $x \geq 0.5 \text{ m}$ ) with positive velocity  $u = 2 \text{ m/s}$ . At  $t = 0 \text{ s}$ , the system is released, generating two symmetric expansion waves moving towards the ends of the tube. The constitutive parameters of the liquid water are

$$\gamma_l = 2.35 \quad ; \quad C_{v_l} = 1816 \frac{J}{kgK} \quad ; \quad q = -1167000 \frac{J}{kg} \quad ; \quad \pi = 10^9 \text{ Pa}$$

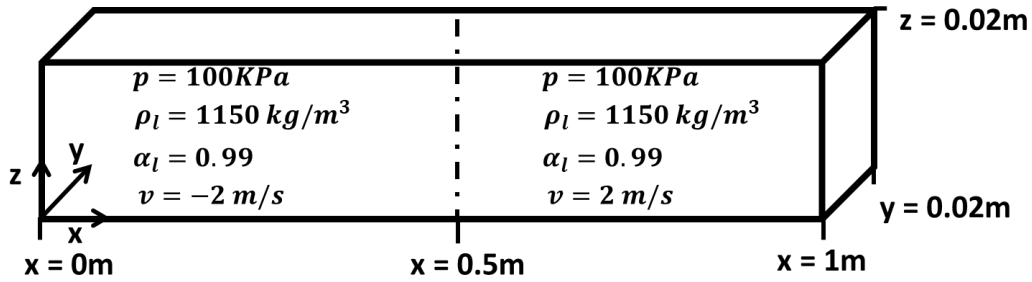


**Figure 4.4:** Initial conditions and dimensions of the water cavitation tube test case

The computational domain consists of 1000 longitudinally equispaced cells in the x-direction, 2 in the y-direction and 2 in the z-direction, for a total of 4000 cells. The boundaries at  $y = 0 \text{ m}$ ,  $y = 0.02 \text{ m}$ ,  $z = 0 \text{ m}$  and  $z = 0.02 \text{ m}$  are set to walls with slip velocities as described in equation (4.2) and the boundaries at  $x = 0 \text{ m}$ ,  $x = 1 \text{ m}$  are set to non-reflecting boundaries. The time-step used is  $\Delta t = 10^{-7} \text{ s}$ .

The results obtained with the 5-Equation model with and without mass transfer are compared with the numerical data reported by [42] using their 7-Equation model. Figure 4.5 shows this

comparison for the case without mass relaxation at  $t = 3.2ms$ . An excellent agreement is found between the two models in all quantities. As far as the undershoot in the mixture density and the overshoot in the vapor volume fraction are concerned, they are due to the initial discontinuity, and are not propagated further away. Pressure across the expansion waves drops close to 0 until the thermodynamic equilibrium is achieved. The non-linear variation of velocity is generated due to vapor volume fraction expansion, which increases to 0.1.

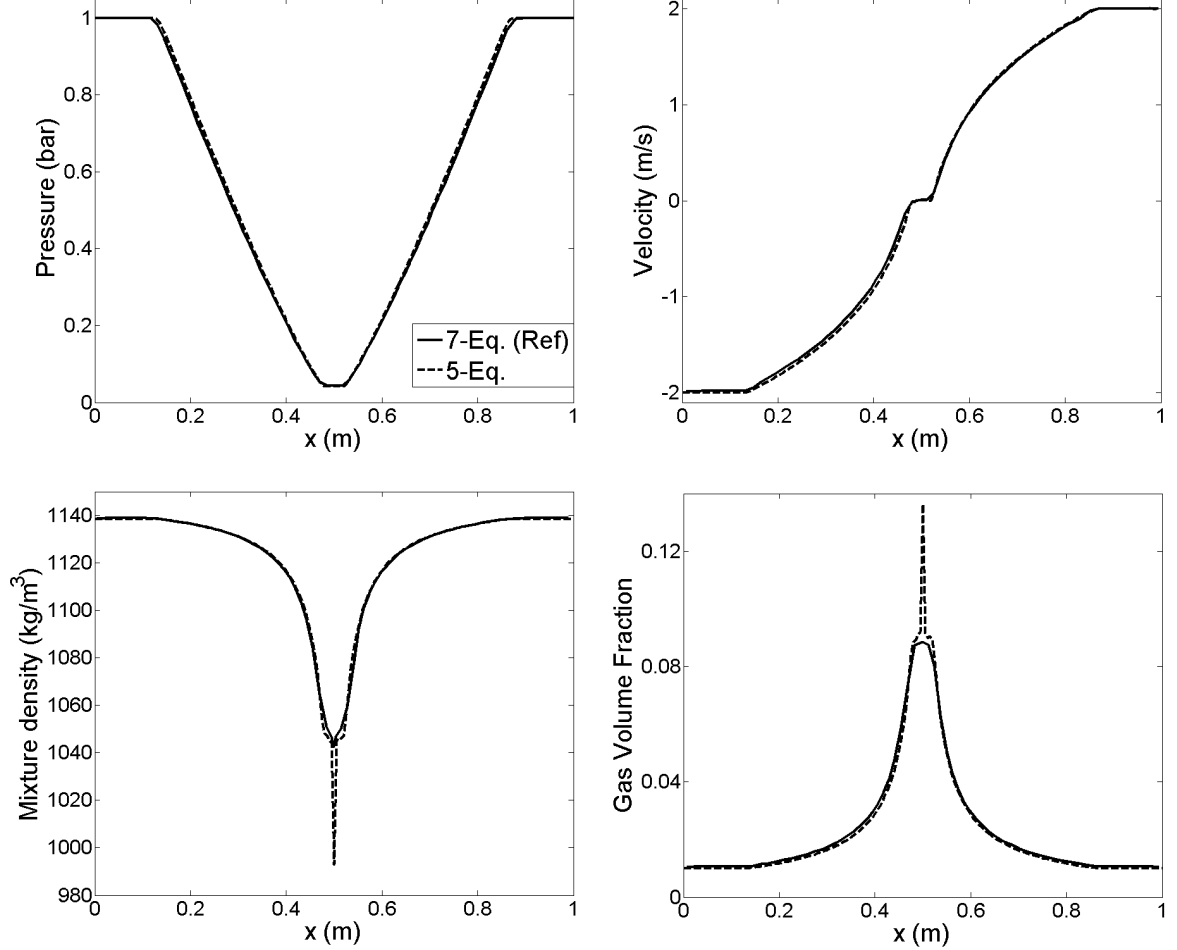


**Figure 4.5:** Water cavitation tube without mass transfer at  $t = 3.2ms$ . Comparison between 5-Equation model and 7-Equation model (Ref. [42])

Figure 4.6 compares both 5-Equation and 7-Equation models at  $t = 3.2ms$  enabling mass transfer. When the pressure drop in the middle of the tube reaches the vaporization pressure, a certain amount of liquid vaporizes to keep constant pressure equal to the vapor pressure. The outgoing expansion waves leave a vaporization front containing  $\alpha_g \approx 0.02$  moving at  $u = 1.5m/s$ . A good agreement is observed in terms of pressure. Regarding the velocity distribution, the 5-Equation model predicts lower velocity after the expansion wave ( $x > 0.3m$  and  $x < 0.7m$ ), which is linked to higher volume fraction predicted in the same region (higher content of vapor decreases wave propagation speed and vaporization front velocity). Similarly, the flow velocity near  $x = 0.5m$  is linked to the broader volume fraction peak. Slow outgoing waves are triggered immediately after  $t = 0s$ , yielding a central region with very low velocity and a relatively constant gas volume fraction  $\alpha_g \approx 0.2$ .



#### 4.4 Two-phase expansion tube

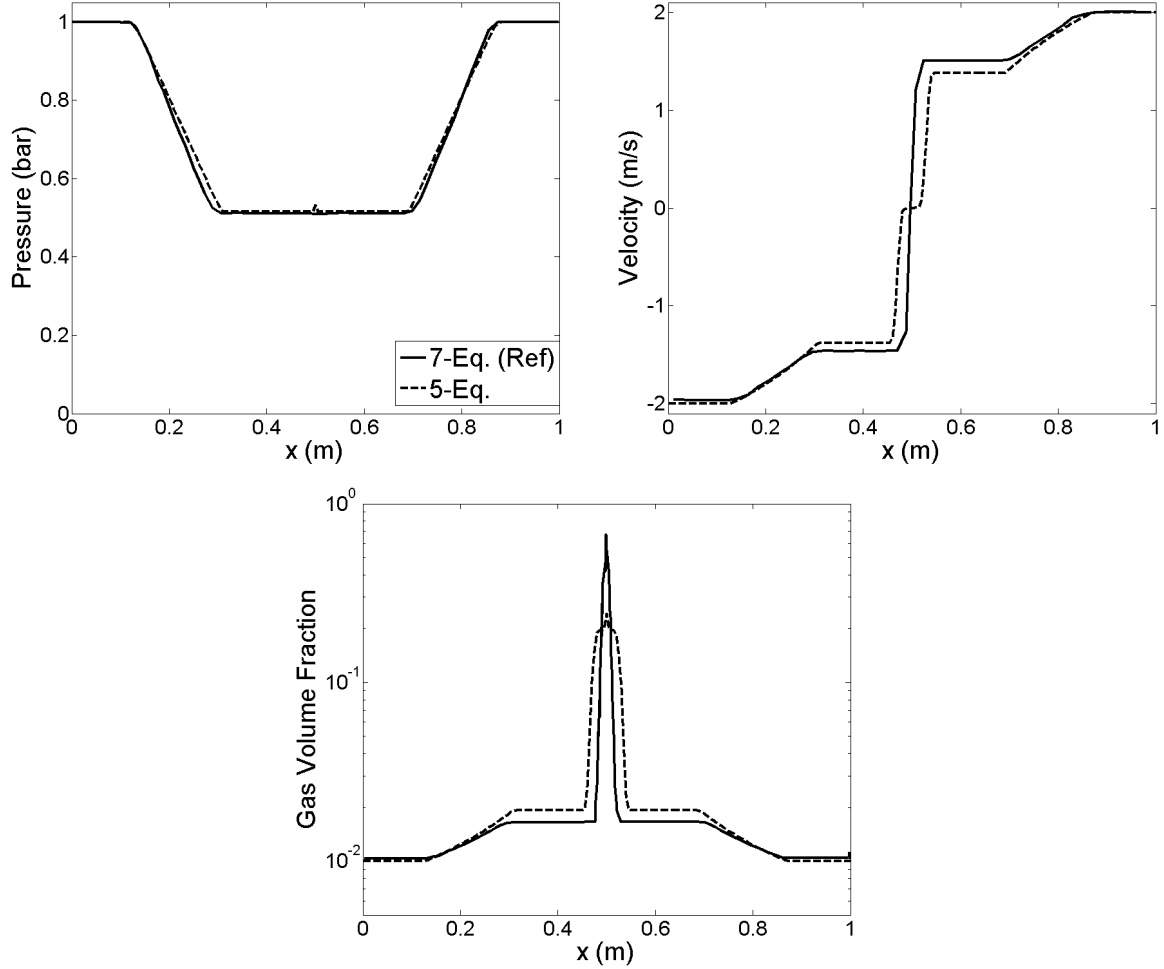


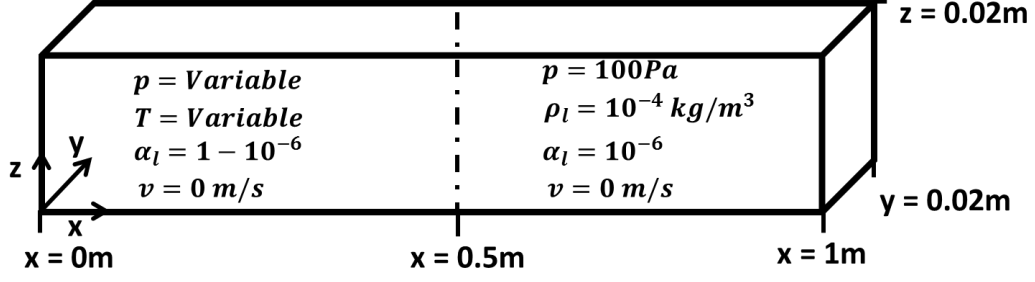
**Figure 4.6:** Water cavitation tube with mass transfer enabled at  $t = 3.2ms$ . Comparison between 5-Equation model and 7-Equation model (Ref. [42])

#### 4.4 Two-phase expansion tube

This test case is furnished with a well documented series of experiments conducted by Simões-Moreira et al. [191] and with numerical results obtained with a 7-Equation model [42]. Figure 4.7 shows the initial set-up, consisting of a liquid column of dodecane (same constitutive parameters as in the shock tube case) suddenly expanded into a low pressure chamber initially filled with dodecane vapor with density  $\rho_g = 10^{-4} kg/m^3$  and pressure  $p = 1 mbar$ . The computational domain consists of 1000 equispaced cells placed in x-direction and 2 cells in y and z-direction. The boundaries  $y = 0$  m,  $y = 0.02$  m,  $z = 0$  m and  $z = 0.02$  m are set to walls with slip velocities (Eq. 4.2), and the boundaries at  $x = 0$  m and  $x = 1$  m to non-reflecting boundaries. The time-step used is  $\Delta t = 10^{-8}$  s.

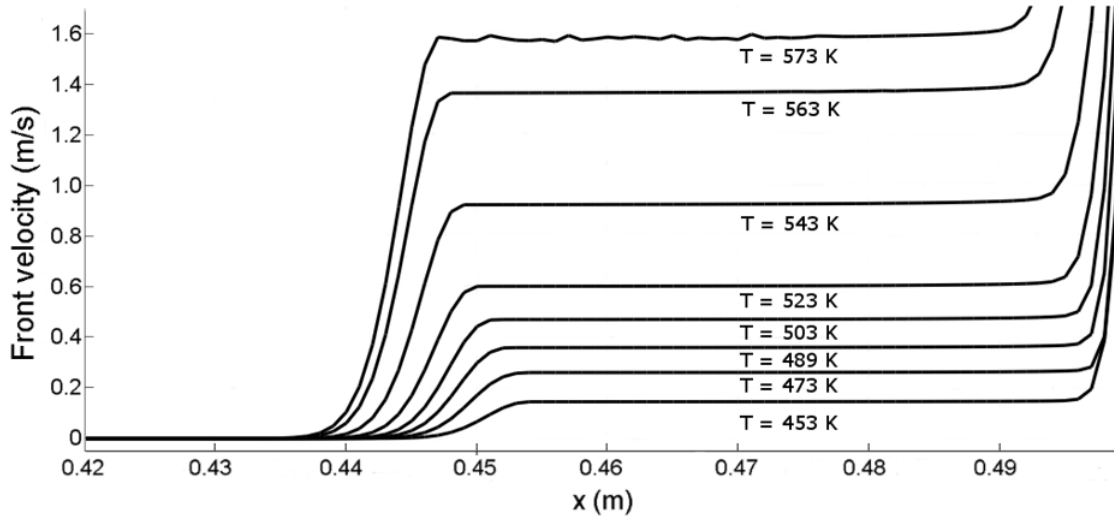
The problem features an expansion wave moving along the liquid column starting from the liquid-vapor interface. As the expansion wave progresses, the static pressure drops to the vapor pressure, triggering a vaporization front where mass transfer occurs. In the experiments, the vaporization front velocity was measured for the initial liquid temperatures shown in Table 4.2. In the numerical tests, initial liquid temperature has to be provided together with the initial pressure. For consistency, the values of initial pressure used in [42] are also used for

the 5-Equation model simulations.



**Figure 4.7:** Initial conditions and dimensions of the two-phase expansion tube

Figure 4.8 plots the vaporization front velocity at  $t = 4.26 \cdot 10^{-5} s$  for all the initial liquid temperatures considered. Higher liquid temperatures generate higher vaporization front velocities and faster left-going expansion waves. Noteworthy, the velocity is remarkably constant in all the cases and only at  $T = 573 K$  there is a small oscillation across the front. Near  $x = 0.5 m$  the front velocity increases sharply due to the initial discontinuity, which is found to be restricted to  $x > 0.49 m$  in all the cases.



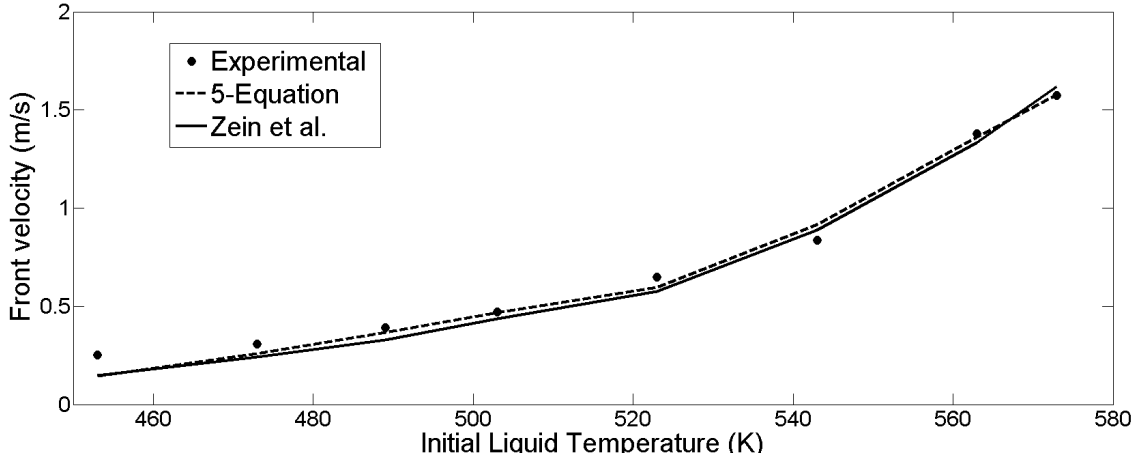
**Figure 4.8:** Two-phase expansion tube tests using the 5-Equation model. The vapor front velocity is plotted for various initial liquid temperatures at  $t = 4.26 \cdot 10^{-5} s$

Table 4.2 compares the 5-Equation model results with the experimental data, indicating the initial temperature of the liquid, the initial pressure of the liquid used in the 5-Equation simulations and the vaporization front velocity. It should be noted that higher initial temperatures of the liquid lead to higher pressures to keep constant liquid density. Figure 4.9 plots the vapor front velocities shown in Table 4.2 together with the values provided by [42]. A good agreement is found between the 5-Equation model and the experimental data. The largest differences appear at low temperatures, suggesting that the constitutive equations may be less suitable to model the real liquid behavior under such thermodynamic conditions.

## 4.5 Single hole injector

$T$ (K)	$p$ (Pa)	$U_{exp}$ (experimental)	$U_{vap}$ (5-Equation)
453	1.5	0.2537	0.1436
473	2.2	0.3091	0.2597
489	3.0	0.3908	0.3672
503	3.9	0.4710	0.4683
523	5.0	0.6482	0.5968
543	7.5	0.8362	0.9161
563	11.0	1.3802	1.3609
573	13.0	1.5744	1.5773

**Table 4.2:** Initial liquid temperature and pressure and vaporization front velocities



**Figure 4.9:** Vaporization front velocity for different initial liquid temperatures. The 5-Equation model is compared with experimental data and with the 7-Equation model of Zein et al. [42]

## 4.5 Single hole injector

### 4.5.1 Problem set-up

The proposed 5-Equation model is used to simulate a single hole injector under low pressure conditions and high cavitation number. The results are compared with void fraction measurements reported in [9]. Although these measurements do not distinguish between different species, the authors note that a certain amount of dissolved gas is initially embedded in the liquid fuel as a result of pressurized storage using  $N_2$ . To further support the validation, the numerical results provided by [76] using a multi-fluid model and a homogeneous mixture model are also utilized. In this case, the numerical results do provide the distribution of void discerning between vapor and non-condensable gas.

The single hole injector geometry is sketched in Figure 4.10 together with the experimental test conditions used in [9] and the fuel properties. The injector consists of a cylindrical nozzle of length 2.5 mm, diameter 0.5 mm and sharp inlet edges wedged between two symmetric

ducts of diameter 2.5 mm. The working fluid is Viscor 16 BR, a non-degasified, high-viscosity gasoline surrogate typically used in experiments involving cavitating nozzles. High cavitation number  $CN = 11.2$  and low Reynolds number  $Re = 1.58 \cdot 10^4$  are attained with a relatively low injection pressure  $p_{Inj} = 10.6 \text{ bar}$  and low back pressure  $p_{out} = 0.87 \text{ bar}$ .

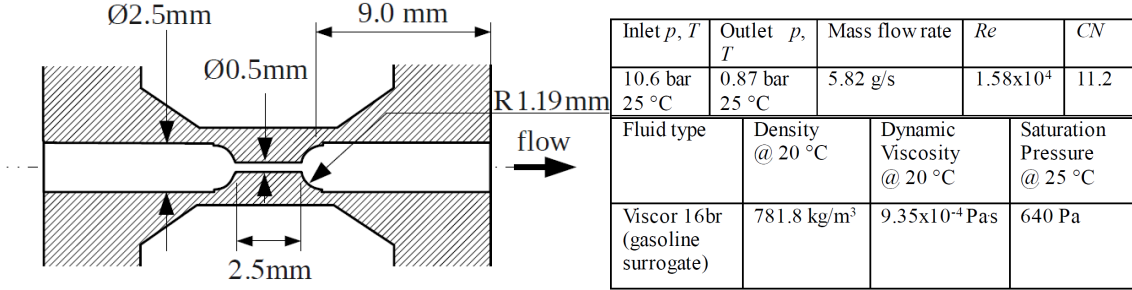


**Figure 4.10:** Single hole injector geometry and experimental test conditions. Figures reproduced from [9]

Figure 4.11 illustrates the 3D computational mesh by showing the mid-cut plane along the nozzle axis. It consists of a 90° sector of  $\sim 375,000$  hexahedral cells where 154,000 cells are distributed along the nozzle hole and 221,000 cells are used in the rest of the domain. For consistency, this resolution is chosen similar to the one used in [76]. 50 cells are located along the radial direction in the nozzle hole and clustered near the wall, leading to a characteristic cell size of approximately  $9 \mu\text{m}$ . 100 cells are equally distributed along the nozzle hole (except for the clustering near the inlet and outlet), leading to a characteristic cell size of  $\sim 25 \mu\text{m}$ . Although the computational domain extends 3.75 mm upstream of the nozzle hole inlet and 3.75 mm downstream of the nozzle hole outlet, both sides are not symmetrically meshed. More cells are used in the inlet part of the injector, particularly in the first 2.5 mm starting from the domain inflow.

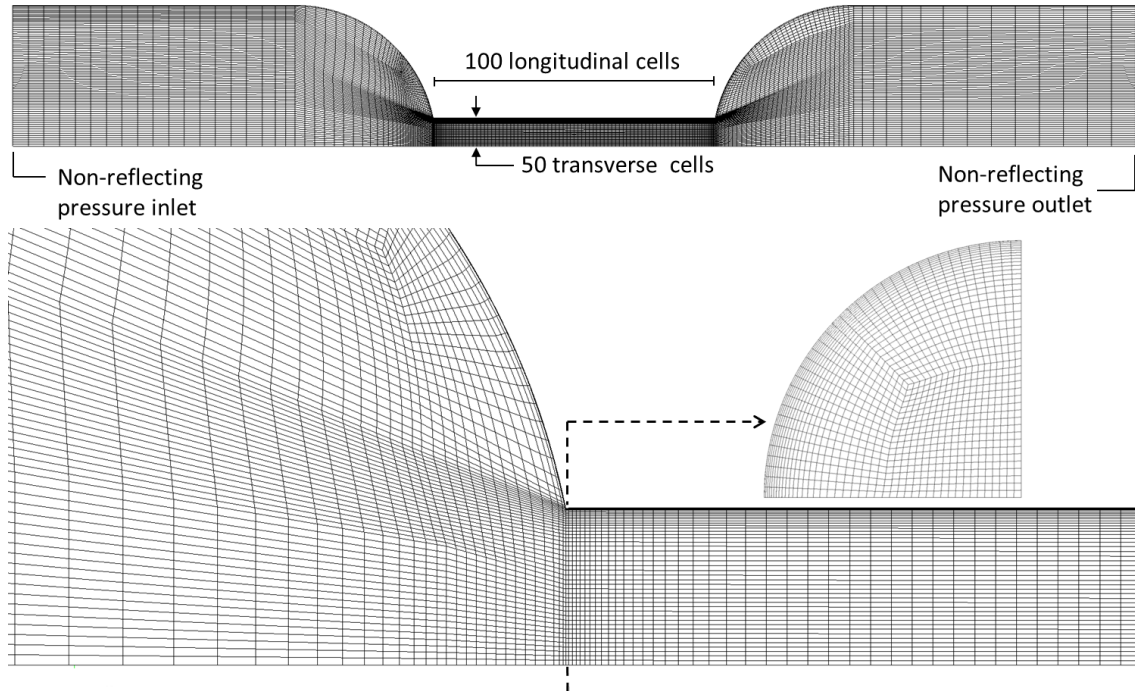


**Figure 4.11:** Single hole injector mesh and boundary conditions

## 4.5 Single hole injector

Table 4.3 shows the numerical set up together with the settings used in [76] for their numerical tests. These tests compared two different approaches: a homogeneous, multiphase mixture model coupled with Homogeneous Relaxation Model (HRM) to account for cavitation (referred to as “Mixture\_HRM”) and a non-homogeneous, multi-fluid approach coupled with a cavitation model based on the Rayleigh-Plesset equation (referred to as “Multifluid\_RP”). The main difference between HRM and Gibbs Free Energy based models is that the former assumes thermal non-equilibrium, retaining two different phase temperatures, and the latter assumes thermal equilibrium, relaxing the phase temperatures. Regarding flow compressibility, only the 5-Equation model treats the liquid phase as compressible using the SG-EOS. In this test case, the compressibility effects are negligible due to low injection pressure and the velocity induced is far from the speed of sound of the liquid. The last point to highlight is the absence of turbulence model in the 5-Equation case. The integration of such a model into the 5-Equation approach using the semi-implicit numerical framework described in Section 3.4 is feasible but non-trivial. Unfortunately, time limitation during the development of this research work prevented the implementation and testing of a conventional  $k - \varepsilon$  model. The effects associated with the absence of turbulence model are acknowledged, and the integration of a functional  $k - \varepsilon$  is proposed for future developments.

	<b>5-Equation</b>	<b>Mixture_HRM</b>	<b>Multifluid_RP</b>
Numerical code	IFP-C3D	CONVERGE	FIRE
Fluid model	Homogeneous model	Mixture model	Multi-fluid model
Cavitation model	Gibbs Energy based	HRM	Rayleigh-Plesset
Phases / Species	liq. , gas / vapor, air	liq. , gas / vapor, air	liq. , gas / vapor, air
Initial dissolved gas at the inlet	$2 \cdot 10^{-5}$ by mass	$2 \cdot 10^{-5}$ by mass	$2 \cdot 10^{-5}$ by mass
Compressibility liquid / gas	Comp./Comp.	Incomp. / Comp.	Incomp. / Comp.
Turbulence model	No turbulence	$k - \varepsilon$	$k - \varepsilon$
Characteristic cell size inside nozzle	$9\mu\text{m}$	$9\mu\text{m}$	$9\mu\text{m}$
Geometry	90 degree sector with periodic BC	90 degree sector with periodic BC	90 degree sector with periodic BC
Pressure-velocity coupling scheme	VP-loop	PISO	SIMPLEC
Time integration	1 <sup>st</sup> order semi-implicit	Euler 1 <sup>st</sup> order	Euler 1 <sup>st</sup> order
Spatial discretization	2 <sup>nd</sup> order	2 <sup>nd</sup> order	2 <sup>nd</sup> order
Time step	$5 \cdot 10^{-9}\text{s}$	lower than $5 \cdot 10^{-9}\text{s}$	lower than $5 \cdot 10^{-8}\text{s}$

**Table 4.3:** Summary of simulation settings. The Mixture\_HRM and the Multifluid\_RP models settings are reproduced from [76]

The semi-implicit discretization used in IFP-C3D enables using a relatively high time-step

even when the liquid phase is quasi-incompressible. In particular, the time-step  $5 \cdot 10^{-9} s$  is of the order of the one used in the Mixture\_HRM case. As discussed in [76], the initial non-condensable, dissolved gas mass fraction  $2 \cdot 10^{-5}$  is the standard value for gasoline (or water) exposed to ambient pressure [192]. This mass fraction is converted into the initial dissolved gas volume fraction by means of

$$\alpha_g = \frac{\frac{Y_g}{\rho_g}}{\frac{Y_g}{\rho_g} + \frac{Y_l}{\rho_l}} ; \quad Y_g = \frac{\text{Mass gas}}{\text{Mass gas} + \text{Mass liq.}} ; \quad Y_l = \frac{\text{Mass liq}}{\text{Mass gas} + \text{Mass liq.}} \quad (4.3)$$

yielding  $\alpha_g = 1.31 \cdot 10^{-3}$ , which was also the value used by the authors in the Multifluid\_RP case. As far as the boundary conditions are concerned, non-reflecting pressure inlet and outlet are chosen to avoid wave reflections inside the domain. A detailed explanation of non-reflecting pressure boundaries can be found in Blazek [193]. The azimuthal boundary conditions are set to periodic boundaries and the remaining external surfaces to walls with no slip velocities. Finally, the characteristic parameters of the Viscor 16BR are calculated as described in Appendix A, yielding

$$\gamma_l = 2.42 ; \quad C_{v_l} = 1020 \frac{J}{kgK} ; \quad q = -1173000 \frac{J}{kg} ; \quad \pi = 4 \cdot 10^8 Pa \quad (4.4)$$

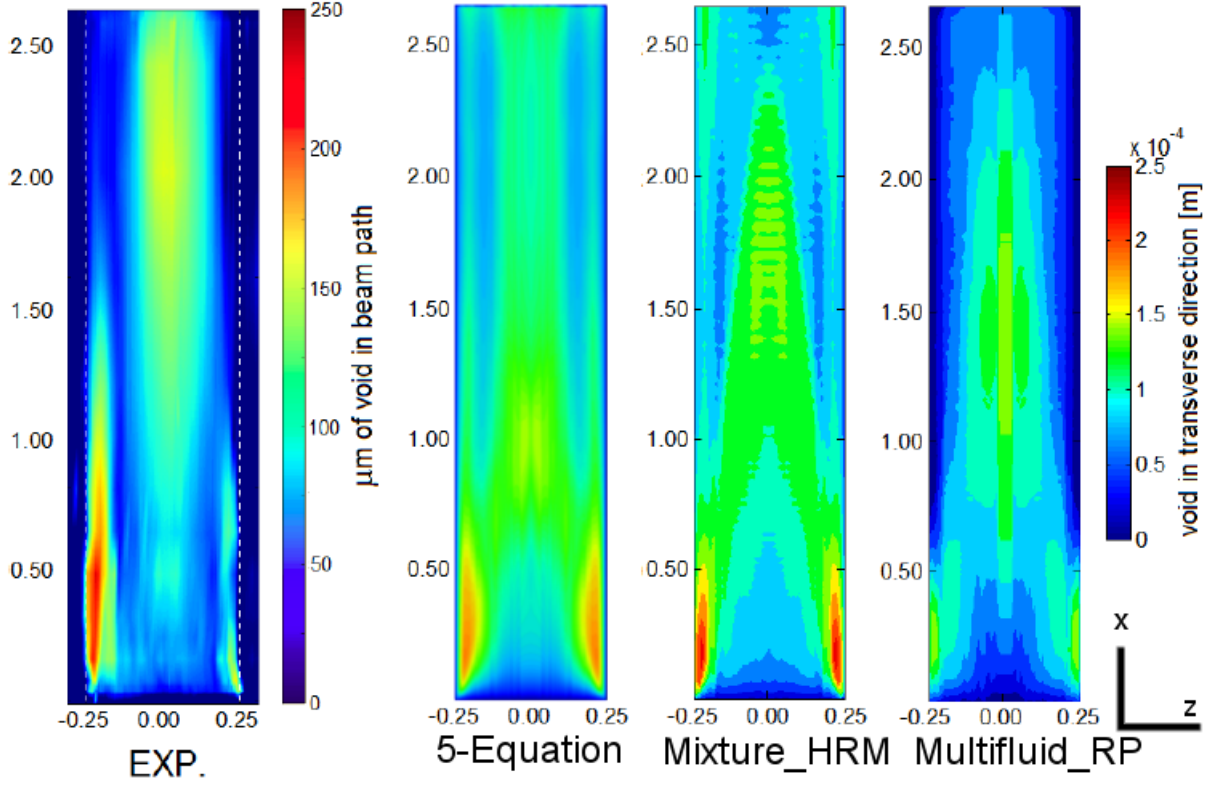
### 4.5.2 Analysis of results

Figure 4.12 shows the integrated void fraction along line-of-sight beams perpendicular to the nozzle hole. As pointed out in [9], the asymmetry found in the experimental results at the inlet corners is likely due to small machining imperfections. The left inlet corner ( $z = -0.25$  mm) is slightly sharper than the right inlet corner ( $z = 0.25$  mm), inducing higher flow turning and acceleration and generating more gas.

The experimental results show two important phenomena: gas formation near the inlet corners and gas formation further downstream along the nozzle hole centerline. The authors in [9] suggest that the gas found near the inlet corners is mainly composed of vapor, and that the gas along the hole centerline is mainly composed of non-condensable gas that expands subject to low pressure. Their hypothesis is supported by the fact that both regions are relatively disconnected, only a small amount of vapor being diffused into the central region. The authors also suggest that the amount of vapor that would form in a perfectly symmetric nozzle would be lower than that measured on the left inlet corner but higher than that measured on the right inlet corner. According to this, the Mixture\_HRM model overpredicts cavitation, since the amount of gas captured is similar to that measured on the left inlet corner. Alternatively, the Multifluid\_RP model underpredicts cavitation, since the amount of gas captured is similar to that measured on the right inlet corner. As for the 5-Equation model, the amount of gas captured lies in between, in agreement with the predictions made by the authors. Regarding gas formation along the hole centerline, all the models predict inaccurately the axial location of the void fraction peak. Among them, the 5-Equation model is the one that shifts the peak

#### 4.5 Single hole injector

closer to the inlet. On the other hand, only the 5-Equation model captures gas expansion up to the hole exit as in the experiment. This is noteworthy considering the fact that the void fraction peak occurs earlier.



**Figure 4.12:** Void fraction integrated along the transverse direction. Experimental data compared with the 5-Equation, Mixture\_HRM and Multifluid\_RP results. Dimensions are in mm

The ability to predict the disconnection between vapor at the inlet corners and gas expansion along the centerline is regarded as very important in [9]. Looking at Figure 4.12, it is clear that the Multifluid\_RP model predicts the disconnection more accurately than the others. Notwithstanding, the close-up view of the 5-Equation case shown in Figure 4.13 evidences that both regions are partially disconnected (note that the color-map has been re-scaled). Although it is quantitatively not accurate, it does predict the phenomenon to some extent.

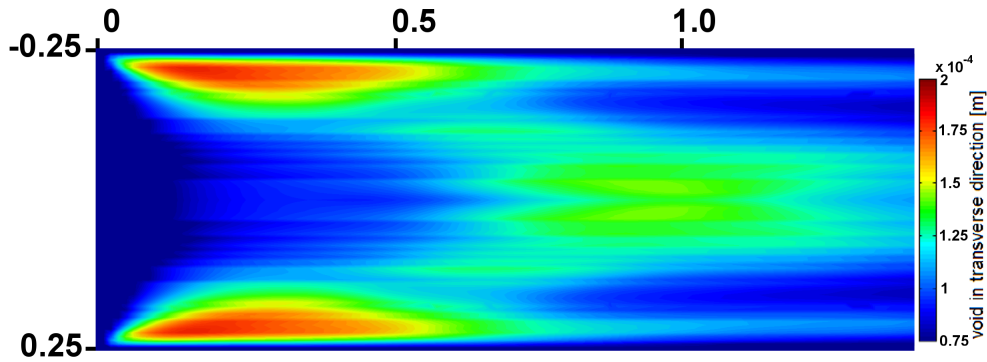


**Figure 4.13:** Close-up view of the 5-Equation model void fraction integrated along the transverse direction. Dimensions are in mm

Figure 4.14 compares axial velocity on the mid-cut plane. As the flow detaches from the walls near the nozzle inlet, the effective area is reduced, increasing velocity along the vena contracta. Flow separation is more intense in the 5-Equation case and reattachment is only attained in the last part of the hole. The resulting pressure distribution along the centerline is plotted in Figure 4.15, showing that the pressure drop does not reach saturation conditions. However, as inferred from Figure 4.12 the pressure is sufficiently low to generate intense gas expansion along the hole centerline. Pressure recovery starts around 1mm downstream of the hole inlet, which can explain why the void fraction peak along the hole centerline is shifted upstream.

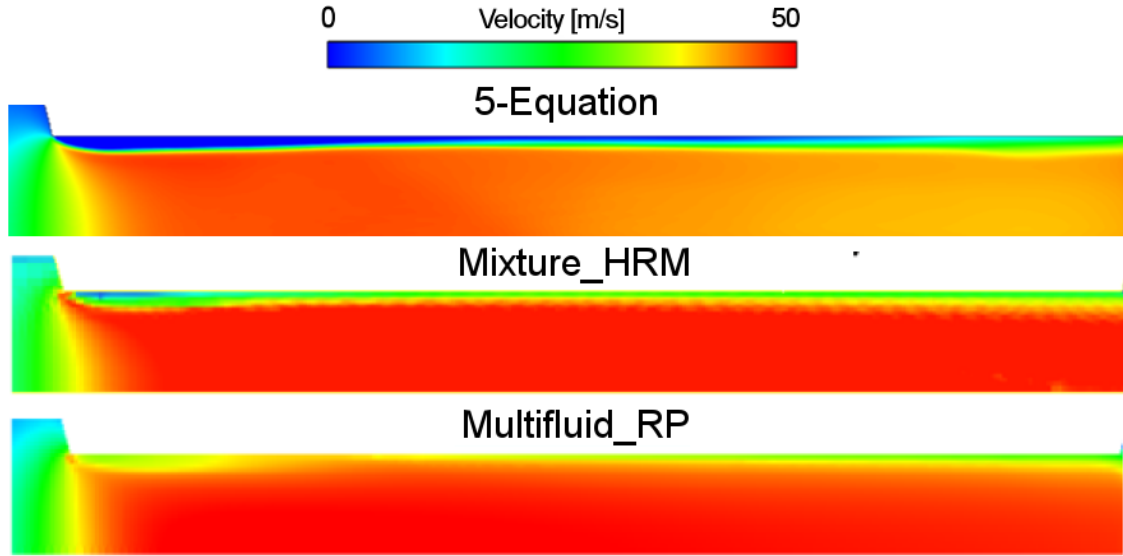


**Figure 4.14:** Pressure and axial velocity color iso-levels along the mid-cut plane through the nozzle axis. Obtained with 5-Equation model

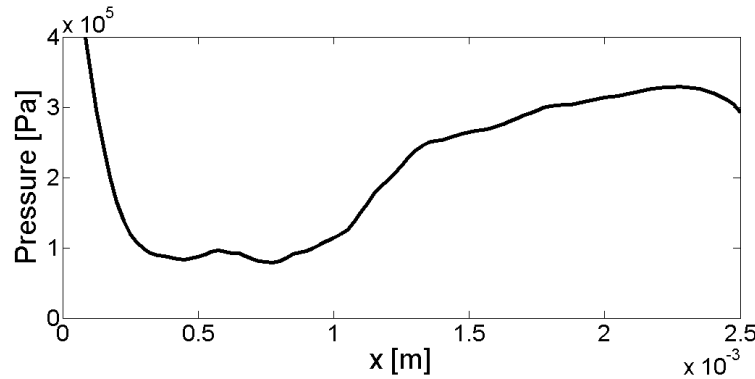


**Figure 4.15:** Pressure distribution along nozzle centerline

The ability of the 5-Equation model to predict cavitation and non-condensable gas expansion can be assessed with help of Figure 4.16. In order to compare the 5-Equation model with the Mixture\_HRM and Multifluid\_RP models, vapor and air mass fractions yielded by the 5-Equation model are converted into volume fractions as

$$\alpha_{vap} = Y_{vap}\alpha_g \quad ; \quad \alpha_{air} = Y_{air}\alpha_g \quad (4.5)$$



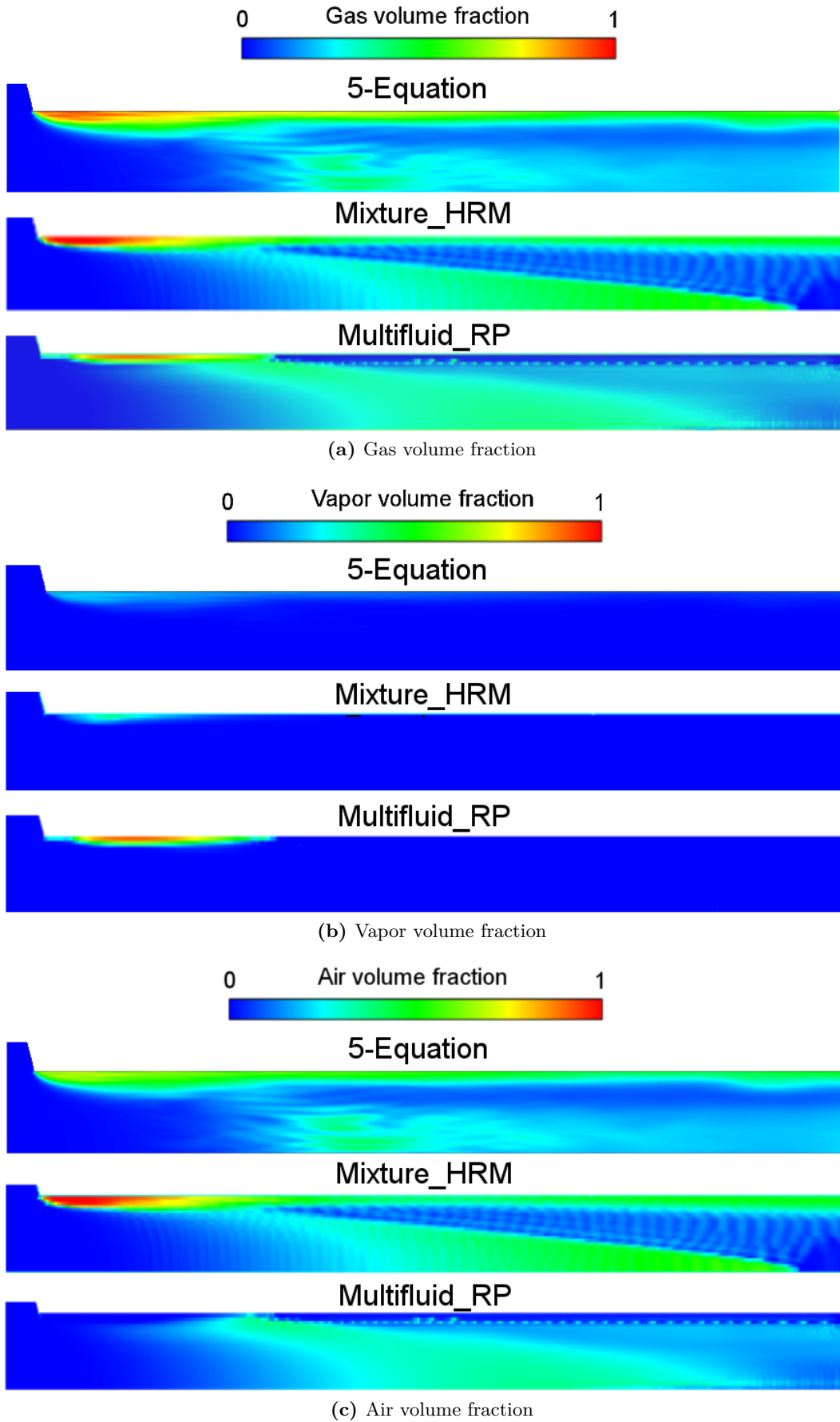


**Figure 4.16:** Comparison of gas, vapor and air color iso-levels on the mid-cut plane. Mixture\_HRM and Multifluid\_RP results are reproduced from [76]

The disconnection between the gas near the upper wall and the gas along the centerline is better predicted by the 5-Equation model. The gas generated at the inlet corner is mostly filled with vapor in the Multifluid\_RP and with air in the Mixture\_HRM. In the 5-Equation model both species coexist in this area, air expansion being more intense than cavitation. The oblique wave developing from the upper separation region towards the centerline induces a sudden decrease of air volume fraction towards the exit in the Mixture\_HRM and Multifluid\_RP models. In the Multifluid\_RP the jump is smoother but still causes intense air compaction. In the 5-Equation model, the oblique wave is much weaker and a relatively constant amount of air reaches the hole exit.

Some of the discrepancies between the 5-Equation model and the other two numerical approaches can be caused by the absence of a turbulence model. As reported in [76], turbulent fluctuations trigger local pressure values below the vapor pressure that enhance cavitation. These fluctuations have a significant impact on air expansion, since they reduce the amount of air contained in the gas as vapor increases. Turbulence also affects the position of the volume fraction peak along the centerline, shifting it closer to the hole exit and reducing air compaction. Finally, flow reattachment would be enhanced with a turbulence model, thus yielding results closer to the Mixture\_HRM model.

## 4.6 Conclusions

The 5-Equation model performance was evaluated in four different cases: shock tube, water cavitation tube, two-phase expansion tube and single hole injector. The shock tube test case was used to validate the hyperbolic system without heat and mass transfer. The 5-Equation model results were compared with the analytical solution for pure phases and with the results yielded by a 7-Equation model already available in IFP-C3D. The 5-Equation model showed to be slightly more accurate than the 7-Equation model and led to significant improvements in computational efficiency, reducing the computational cost by as much as 20%. On the other hand, the 5-Equation model was very sensitive to numerical errors associated with non-conservative terms in the volume fraction equation, leading to pressure overshoot across the liquid-gas interface. The effects of dissolved gas were also assessed by increasing the amount of gas embedded in the liquid phase. The results showed that the expansion wave is particularly sensitive to this increment, causing non-linear variation of pressure, velocity, mixture density and volume fraction.

The water cavitation tube problem was used to validate the hyperbolic system with and without heat and mass transfer. The problem studied the flow field subject to two symmetric, outgoing expansion waves. The 5-Equation model was compared with a 7-Equation model available in the literature. Excellent agreement was found between the two approaches in the case without mass transfer. In the case with mass transfer enabled, both models predicted very similar pressure distribution but showed some discrepancies in velocity and gas volume fraction. The 5-Equation model predicted slightly higher amount of vapor within the vaporization front, leading to lower velocities. Moreover, the model also captured a broader volume fraction peak in the center of the tube, associated with low-speed waves propagating away from the initial discontinuity.

## 4.6 Conclusions

---

The ability of the 5-Equation model to predict mass transfer after flow expansion was further assessed by comparing the 5-Equation model results with experimental and numerical data available in the literature. In the experiments, the vaporization front velocity behind a strong expansion wave was measured for different initial temperatures of the liquid. The numerical data available used as reference were obtained using a 7-Equation model with imposed values of liquid pressure to keep constant liquid density. These values of pressure together with the liquid temperatures of the experiments were also used in the 5-Equation model simulations. The results were in very good agreement with the experiments and with the reference numerical data, especially within the range  $T = 480 - 570$  K. At lower initial liquid temperatures, the solution deteriorates probably because of the constitutive EOS parameters becoming less suitable under such conditions.

The last problem considered was a single hole injector operating under low injection pressure conditions. This case was used to validate the full model, including diffusion terms, heat and mass transfer and the ability to deal with two species in the gas phase. The working fluid was a liquid-gas mixture with both vapor and dissolved air species. The results were in good qualitative agreement with the experiments, comparable to other numerical approaches found in the literature, including a mixture model based on HRM cavitation model and a multifluid model coupled with a Rayleigh-Plesset based cavitation model. The 5-Equation model predicted cavitation near the hole inlet corners reasonably well and the disconnection between this feature and gas expansion along the centerline. It also captured gas expansion up to the hole exit, which was not predicted by the other two models. On the other hand, it shifted the gas expansion peak upstream with respect to the experimental position, which could be partly due to the absence of a turbulence model.

Overall, the 5-Equation model performance is very encouraging. Future work should involve its application to high injection pressure problems where the liquid compressibility effects become important. It would also require the implementation of a turbulence model, provided that higher injection pressures would lead to higher Reynolds numbers.



## Part III

# Exploring nozzle geometry impact on internal nozzle flow and primary breakup



## Chapter 5

---

# Investigation strategy and simulation methodology

---

### 5.1 Investigation strategy

Experimental measurements of near-nozzle spray suggest that the primary breakup process is highly dependent on the in-nozzle flow dynamics. The simulation and analysis methodology described in this Chapter aims at providing the necessary tools for identifying this link, determining how the in-nozzle flow dynamics are correlated with the main atomization mechanisms. This approach will be used to analyze the simulation results presented in Chapters 6 and 7.

Owing to relatively good resolution very close to the injector, X-ray PCI images are used as reference to characterize the near-nozzle flow. The elevated cost of X-ray PCI technology prevents its application to a large number of nozzles, thus forcing to select specific configurations. For this work, X-ray PCI images characterizing the full injection event (needle opening, full needle lift and needle closing) are available for three designs of primary industrial interest, namely “Reference nozzle”, “Sharp edge nozzle” and “HP hole nozzle”, sketched in Figure 5.1. The Reference nozzle is the baseline design, the other designs representing variations of specific design parameters. The interest of these configurations lies in their remarkably different performances. Whereas the Reference nozzle provides a good balance between efficiency and atomization, Sharp edge nozzles enhance atomization at the expense of efficiency. On the other hand, HP (High Performance) hole nozzles, which are currently under production, provide high flow efficiency and spray momentum due to increased hole taper (conicity) but relatively poor atomization under low back pressure conditions. Only X-ray images at constant full needle lift are considered in this study except for the Reference nozzle case, for which visualizations during needle opening at  $t = 0.1$  ms (51.3  $\mu\text{m}$  needle lift) and  $t = 0.12$  ms (66  $\mu\text{m}$  needle lift) after start of injection are used.

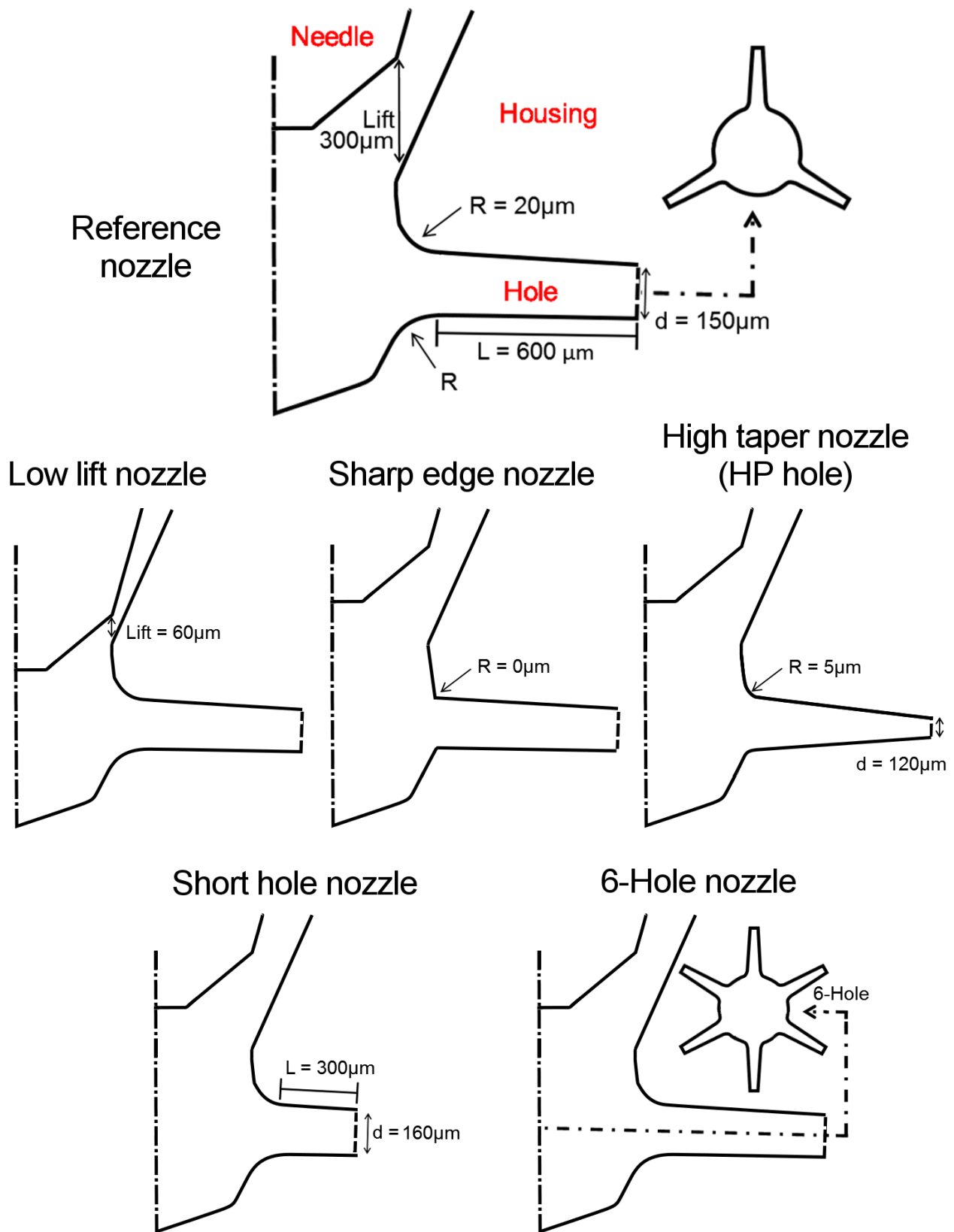


**Figure 5.1:** Nozzle designs considered. The Reference nozzle is the baseline design and only modified parameters are indicated on the other nozzles



## 5.1 Investigation strategy

All the aforementioned designs have three axisymmetric nozzle holes. This is the maximum number of holes to avoid polluting line-of-sight measurements perpendicular to the spray without using additional equipment to reflect the illuminating beam. X-ray measurements taken for each designs at five injection pressures are available: 400 bar, 800 bar, 1200 bar, 1600 bar and 2000 bar. Back pressure is always equal to 1 bar to minimize light scattering and absorption, which would lead to very limited resolution under typical Diesel injection back pressures of  $\sim 70$  bar. Using 1 bar back pressure hardly allows direct extrapolation of the results to real Diesel injection operating at full load, especially in terms of near-nozzle flow atomization. However, it is reasonable to assume that, even at 1 bar back pressure, some of the in-nozzle flow perturbations contributing to atomization are likely to develop.

As can be seen in Figure 5.2, X-ray images evidence the strong dynamic behavior of near-nozzle spray, including multiple flow scales and structures. Even for the same design, the morphology changes over time at constant (full) needle lift, particularly in the Reference nozzle case. These results suggest that only numerical methods able to deal with this highly dynamic, multi-scale problem can reproduce the correct spray behavior. LES is thus selected to simulate in-nozzle and near-nozzle flow, aiming at identifying the link between vortex dynamics and atomization.

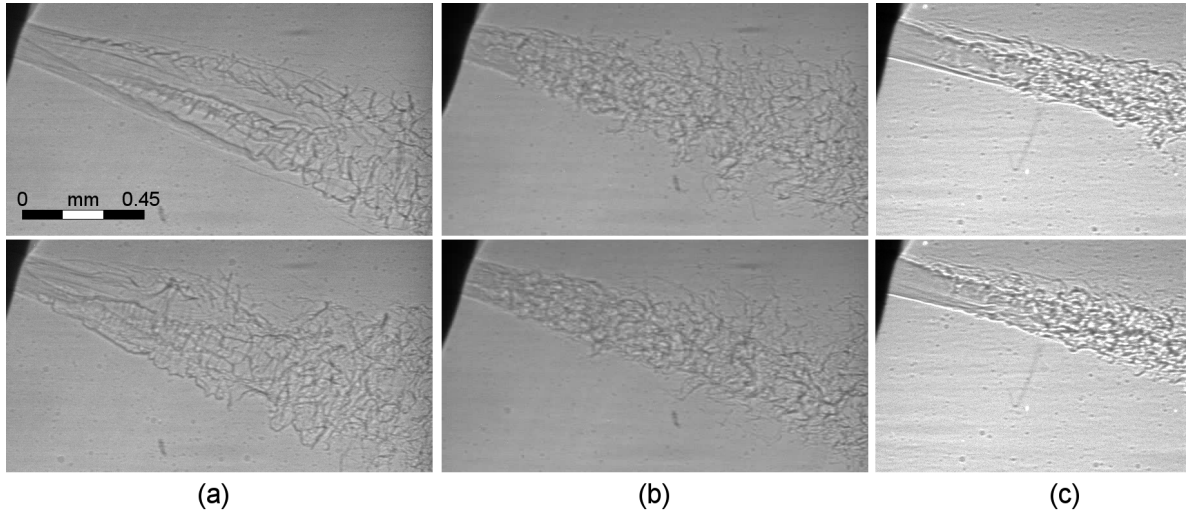


**Figure 5.2:** X-ray PCI images of near-nozzle flow at 800 bar injection pressure. (a) Reference nozzle; (b) Sharp edge nozzle; (c) HP hole nozzle. For each nozzle the images are shown at two different times (top and bottom) during full needle lift

LES of in-nozzle and near-nozzle flow including liquid and vapor compressibility as well as heat transfer is beyond the scope of this work due to its numerical complexity and high computational cost. For this reason, all the simulations conducted assume incompressible, isothermal liquid and vapor with constant fuel properties. Although this simplifying hypothesis seems justified for relatively low injection pressures, liquid compressibility and fuel property variation become very important at higher pressures. It is considered that these effects should not be neglected for injection pressures higher than 800 bar (Mach number  $\sim 0.3$ ). Thus, only X-ray PCI images and LES at 800 bar are considered.

Apart from the nozzle designs previously mentioned, Figure 5.1 shows two additional configuration: Short hole and 6-Hole. The simulation results obtained in these geometries cannot be correlated with X-ray images as no experimental data are available. The interest of

Short hole nozzles lies in their ability to enhance sac vortex dynamics, which play a dominant role in turbulence generation and mixing. As for the 6-Hole nozzle, the reduced sac flow activity resembles more that found in real Diesel injectors, which typically have 8 or more holes. Owing to the relatively large diameter ( $150\mu\text{m}$ ) of the Reference nozzle, the maximum number of holes is limited to 6 in order to avoid hole overlapping.

The LES computations conducted are summarized in Table 5.1 along with available X-ray data and corresponding operating conditions for the six nozzle designs depicted in Figure 5.1. All the geometries have been simulated considering only in-nozzle flow and static needle lift, even for the Low lift nozzle. In this case, it is assumed that the needle motion effect is relatively small as long as the needle speed is low compared with the flow velocity ( $\sim 1\text{ m/s}$  vs  $\sim 100\text{ m/s}$ ). Only one simulation including both in-nozzle and near-nozzle flows has been performed using the HP hole geometry, which is the only nozzle yielding negligible cavitation. The reason is that modeling cavitation outside the nozzle while using high resolution interface tracking methods was not possible, as it would require accounting for expansion and collapse of small bubbles and nuclei.

		Reference	Low lift	Sharp edge	HP hole	Short hole	6-Hole
Data availability	X-ray	Yes	Yes	Yes	Yes	No	No
	LES in-nozzle	Yes	Yes	Yes	Yes	Yes	Yes
	LES in-nozzle and near-nozzle	No	No	No	Yes	No	No
Injection pressure	X-ray	400, 800, 1200, 1600 and 2000 bar				-	-
	LES in-nozzle	800 bar					
	LES in-nozzle and near-nozzle	-	-	-	800 bar	-	-
Back pressure		1 bar					
Number of holes		3	3	3	3	3	6

**Table 5.1:** Summary of experimental data available (X-ray) and numerical simulations (LES in-nozzle, LES in-nozzle + near-nozzle) conducted

This Chapter is divided into three Sections. First, Section 5.2 describes the methodology used to extract characteristic length scales from the X-ray images, which are very useful to correlate with the LES results. Second, Section 5.3 details the methodology for in-nozzle flow simulation, including computational domain and numerical setup, mesh generation, boundary conditions and flow initialization. The cavitation model evaluation is also included at the end of this Section. Finally, Section 5.4 is devoted to the methodology for simultaneous in-nozzle and near-nozzle flow simulation, detailing the mesh generation and numerical setup.

## 5.2 X-ray image processing

The amount of information that can be extracted from the X-ray images is limited. The three-dimensional structure of the spray is transformed into a two-dimensional image where

## 5.2 X-ray image processing

droplets and ligaments aligned with the X-ray beam overlap with the liquid core. It is therefore impossible to obtain reliable information about droplet size and droplet distribution. Notwithstanding, it is possible to identify coherent patterns that repeat in space and time and use them to correlate with breakup structures observed in the LES results. To this end, two-dimensional FFT (2D FFT) and one-dimensional FFT (1D FFT) are applied to the X-ray images. Owing to the relatively small X-ray image size ( $\sim 1.5$  mm) and the need for an even smaller region of interest (ROI), the methods focus on characteristic length scales smaller than the nozzle diameter. This is deemed sufficient to capture structures possibly linked to high frequency perturbations originated inside the nozzle.

2D FFT transforms a two-dimensional ROI from the X-ray image into the two-dimensional frequency domain based on gray-scale light intensity. While it works very well when the ROI is composed of homogeneous patterns, it is less useful for heterogeneous patterns (like the one shown in Figure 5.2a) due to the presence of large scales of the order of the ROI itself. An example of 2D FFT applied to X-ray images of the Sharp edge nozzle is shown in Figure 5.3. As indicated in Figure 5.3a, the ROI is a 440x210 pixel rectangular window of 2.4D wide and 7D long (D is the nozzle diameter  $D = 150 \mu\text{m}$ ) symmetric with respect to the nozzle hole axis. Figure 5.3b reproduces the power spectrum in a 512x512 pixel window based on light intensity inside the ROI. X and Y axes denote the frequencies in both directions, so that  $F_x$  are frequencies along X direction and  $F_y$  along Y direction. The smallest length scale that can be captured in X or Y is 2 pixels, thus yielding maximum values of  $F_x$  or  $F_y$  equal to 0.5. Three-dimensional digitalization of the power spectrum is shown in Figure 5.3c using normalized light intensity in the Z axis. These results are processed in order to find the dominant frequency, namely the one with maximum normalized light intensity. Since the spectrum is symmetric with respect to the axes, only positive values of  $F_x$  are retained for further analysis. Moreover, frequencies associated with length scales larger than the nozzle diameter are neglected, thus restricting the search domain to

$$(F_x, F_y) \in S \mid S = \left\{ \begin{array}{l} F_x > 0 \\ \left| \sqrt{F_x^2 + F_y^2} \right| > F_D \end{array} \right. \quad (5.1)$$

where the frequency associated with the nozzle diameter  $F_D = 0.0167 \text{ pixel}^{-1}$  is converted from length scale using

$$F_D = F_{\text{Max}} \frac{L_{\text{min}}}{D} = 0.5 [\text{pixels}^{-1}] \cdot \frac{L_{\text{min}} [\text{pixels}]}{D [\text{pixels}]} = 0.5 \cdot \frac{2}{60} = 0.0167 [\text{pixels}^{-1}] \quad (5.2)$$

Once the frequency with maximum power is found, it is converted into length scale using

$$L_{\text{MP}} = L_{\text{min}} [\text{pixels}] \frac{F_{\text{Max}} [\text{pixels}^{-1}]}{F_{\text{MP}} [\text{pixels}^{-1}]} = 2 [\text{pixels}] \frac{0.5 [\text{pixels}^{-1}]}{\sqrt{F_{x_{\text{MP}}}^2 + F_{y_{\text{MP}}}^2} [\text{pixels}^{-1}]} \quad (5.3)$$

where  $F_{x_{\text{MP}}}$ ,  $F_{y_{\text{MP}}}$  are X and Y components of frequency with maximum power and  $L_{\text{MP}}$  is the characteristic length scale.  $L_{\text{MP}}$  is stored for each X-ray image and used to build the probability density function (pdf) plotted in Figure 5.3d. The pdf is calculated as

$$\text{pdf}(L_{\text{MP}}) = \frac{1}{\sqrt{2\pi}\sigma^2} e^{-\frac{(L_{\text{MP}} - \mu)^2}{2\sigma^2}} \quad (5.4)$$

where  $\mu$  is mean and  $\sigma^2$  is variance. Although the population is small (22 images in total during full needle lift), these results provide a reasonable overview of characteristic length scales smaller than the nozzle diameter.

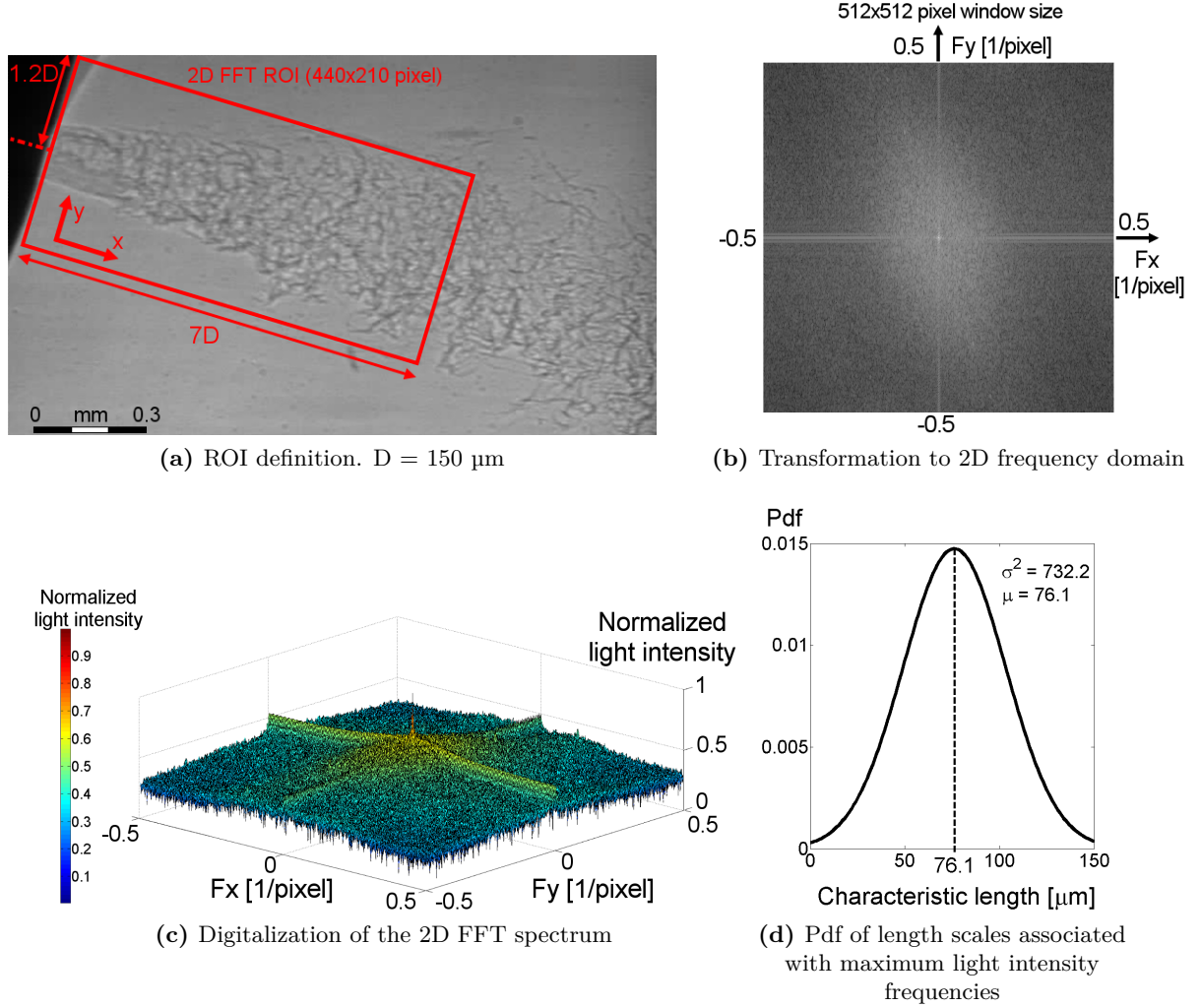


**Figure 5.3:** 2D FFT image processing of the Sharp edge nozzle

1D FFT transforms light intensity into the frequency domain along specific lines. It performs well when the ROI is composed of either homogeneous or heterogeneous patterns as long as the largest scales are avoided. However, it retains less information than the 2D FFT. The application concept of 1D FFT is similar to that of 2D FFT. Figure 5.4a illustrates this method as applied to the Sharp edge nozzle, involving five different lines of length  $7D$  starting from the nozzle exit. Line 3 is coincident with the nozzle axis and the starting point of Lines 1 and 5 is  $Y = D/2$  and  $Y = -D/2$  respectively. Line 2 is equidistant from Line 1 and 3 and Line 4 is equidistant from Line 3 and 5. In the Sharp edge nozzle, dispersion angles  $\alpha = 6^\circ$  and  $\beta = 6^\circ$  are selected due to the relatively symmetric and stable spray pattern observed over time. Regarding the number of lines, it was found that using more than five lines does not change the results owing to limited resolution of the X-ray images.

Using the same sampling lines for all the nozzles is not the best choice due to dispersion angle variation in the Reference nozzle and to the lack of liquid-gas interface structures near the HP

## 5.2 X-ray image processing

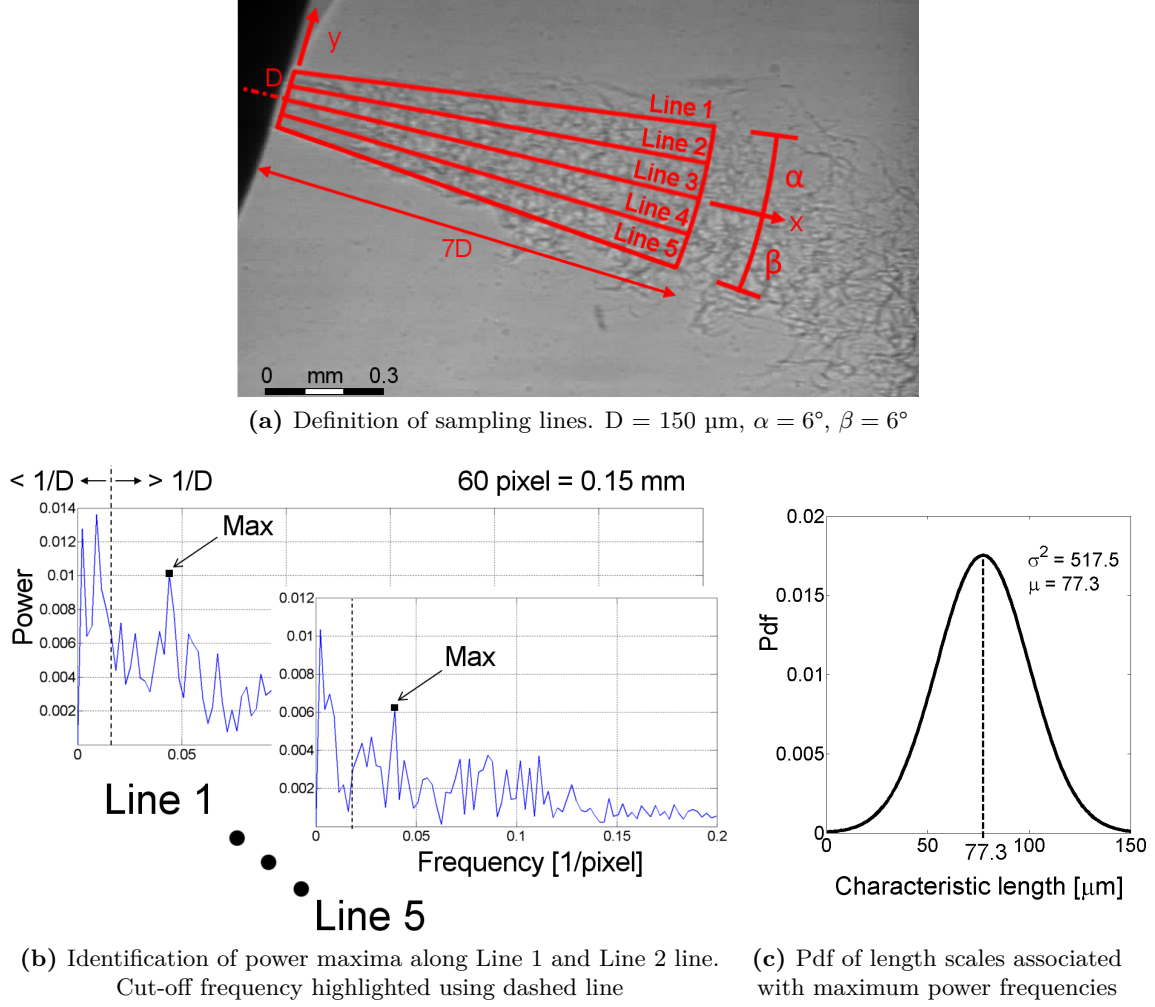


**Figure 5.4:** 1D-directional FFT of the Sharp edge nozzle

hole nozzle exit. Table 5.2 summarizes the number of sampling lines together with the X-offset (distance between the starting points of the sampling lines and the hole exit) and the values of  $\alpha$  and  $\beta$  used for each nozzle. In order to ensure that five lines are always inside the spray, the angles  $\alpha$  and  $\beta$  are reduced to  $\alpha = 5^\circ$ ,  $\beta = 4^\circ$  in the Reference nozzle. Unfortunately, the results are slightly biased towards low frequencies due to strong anisotropy and large scales. Regarding the HP hole nozzle, Figure 5.2c shows that the interface structures start developing approximately one diameter downstream of the nozzle exit. Furthermore, the dispersion angle is very small and asymmetric with respect to the nozzle axis. Hence, four lines are defined starting  $120 \mu\text{m}$  (HP hole diameter) away from the hole exit with  $\alpha = 5^\circ$ ,  $\beta = 2^\circ$ .

Light intensity distribution over the sampling lines is transformed into the frequency domain. Figure 5.4b plots the power spectrum of Line 1 and Line 5, indicating the range of frequencies above the cut-off frequency associated with length scales smaller than the nozzle diameter  $D$ . The frequency above the cut-off with maximum power is stored for each line to build the statistical population. Using a set of 22 X-ray images, the population is composed of 110 elements in the Reference and Sharp edge nozzles and 88 in the HP hole nozzle. Figure 5.4c plots the resulting probability function in the Sharp edge nozzle case obtained after normalization of the results.

	Reference	Sharp edge	HP hole
Number of lines	5	5	4
X-offset	0	0	120 $\mu\text{m}$
$\alpha$	5°	6°	5°
$\beta$	4°	6°	2°

**Table 5.2:** 1D FFT setup parameters

## 5.3 LES of in-nozzle flow

### 5.3.1 Model setup

All the simulations have been computed using the commercial software ANSYS Fluent. The so-called Embedded LES approach is followed, solving part of the flow with URANS and the rest with LES. This allows increasing mesh resolution in the region of interest, which is solved using LES, while coarsening the mesh in the URANS domain where quality criteria relax. The mixture model available in ANSYS Fluent [194] is employed (described in Appendix D for completeness), assuming incompressible, isothermal, liquid-vapor mixture with interfacial equilibrium. The LES approach, also detailed in Appendix D, is mathematically closed using the WALE sub-grid scale viscosity model [150] owing to its ability to predict turbulence generation in regions with rotation and strain and to reproduce the correct flow behavior near walls.

Regarding mass transfer model, the Zwart-Gerber-Belamri cavitation model (Zwart et al. [195]) described in Appendix D is used with vaporization and condensation coefficients taken as  $F_{vap} = 500$  and  $F_{cond} = 0.05$ . These values have been extensively used in similar simulations at Delphi, yielding good agreement between numerical and experimental data. Nonetheless, the impact of  $F_{vap}$  and  $F_{cond}$  on the flow structures is analyzed in detail in Section 5.3.5.

Finally, Diesel is modeled using constant density  $\rho_l = 730 \text{ kg m}^{-3}$  and dynamic viscosity  $\mu_l = 2.4 \cdot 10^{-3} \text{ kg m}^{-1} \text{ s}^{-1}$  for the liquid phase and constant density  $\rho_v = 1 \text{ kg m}^{-3}$  and dynamic viscosity  $\mu_v = 7 \cdot 10^{-6} \text{ kg m}^{-1} \text{ s}^{-1}$  for the vapor phase.

### 5.3.2 Mesh generation and boundary conditions

In order to detail the computational domain used as well as the retained meshes and boundary conditions, the procedure applied to the Reference nozzle is discussed, an equivalent approach having been used for the other hole designs. Figure 5.5 shows the computational domain consisting of a 120° sector divided into different regions, namely seat, sac, hole and discharge volume. It extends approximately 2 mm above the seat, which is the point where the distance between needle and housing is minimum, and 1 mm downstream of the hole exit. Since the region of interest is the volume between the seat and hole exit, the inlet and outlet planes are moved away from this region in order to reduce the impact of inlet and outlet boundary conditions.

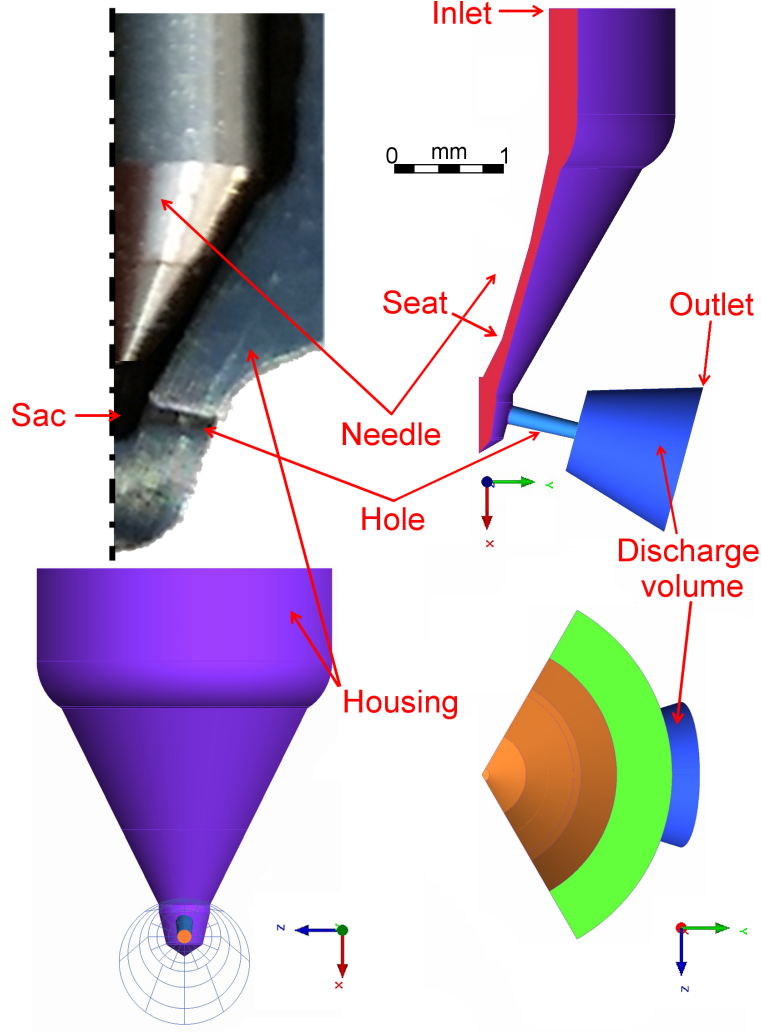


**Figure 5.5:** Computational domain of Reference nozzle case. Nozzle side view (top-left), geometry side view (top-right), geometry front view (bottom-left) and top view (bottom-right)

The computational mesh of the Reference nozzle is shown in Figure 5.6. The domain is decomposed into three subdomains, each with specific mesh characteristics, leading to the appearance of two interfaces that must be adequately treated:

- **Subdomain 1.** Extends from the inlet to  $\sim 450 \mu\text{m}$  above the needle seat. Composed of 200,000 tetrahedral cells of  $\sim 50 \mu\text{m}$  maximum size and prism cells near the walls to capture the boundary layer. Tetrahedral cells are employed as they offer good flexibility when transitioning from coarse to fine meshes. URANS  $k-\omega$  SST is used in this domain, providing reasonable estimates of velocity and pressure fields at Interface 1 even with coarse mesh resolution.
- **Subdomain 2.** Fully hexahedral domain consisting of 10 million cells distributed over the needle seat, sac, hole and the region immediately after the hole exit. The characteristic cell size  $\sim 1 \mu\text{m}$  is a compromise between computational cost and amount of resolved turbulent kinetic energy. The smallest cell size near the walls is  $\sim 0.1 \mu\text{m}$  to attain  $y^+ < 1$ , gradually increasing with a predefined growth ratio 1.03. The quality criteria includes a minimum cell angle of  $28^\circ$ , a maximum volume change between



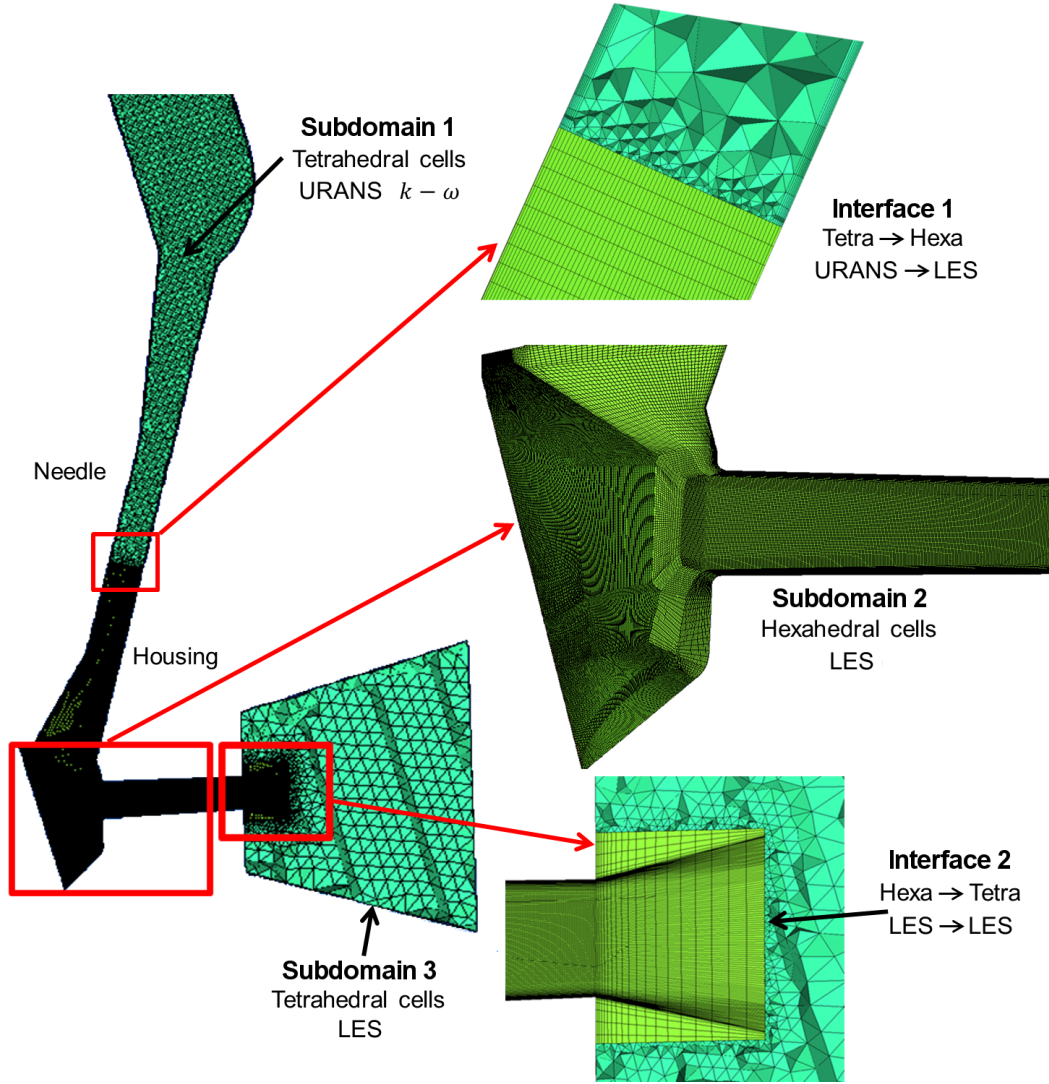


**Figure 5.6:** Computational mesh of the Reference nozzle. Side view of mid-cut plane

neighboring cells of 10, a maximum aspect ratio of 70 in the boundary layer and a minimum 3D determinant (normalized, triple product of the vectors departing from one cell node) of 0.3. Since mesh resolution in this domain is maintained relatively constant, its extension upstream of the needle seat is limited by the computational cost. LES is used to resolve the multi-scale problem originated in the sac and nozzle hole.

- **Interface 1.** Interface between Subdomain 1 and Subdomain 2. The tetrahedral elements of Subdomain 1 are smoothly refined to match the hexahedral cell size of Subdomain 2. At the interface, the velocity and pressure fields are simply interpolated from Subdomain 1 to Subdomain 2 without converting TKE from URANS to resolved turbulence in LES. As discussed below, there are different methods to transfer TKE from URANS to LES, all of them having significant impact on vortex structures if the interface is located close to the nozzle hole. Since it is not possible to assess which model is more accurate, the interface is moved away from the sac to the position indicated, where velocity is low ( $\sim 25$  m/s, Reynolds number  $< 1500$ ) and the flow can be assumed to be relatively laminar.
- **Subdomain 3.** Fully tetrahedral domain composed of approximately 80,000 elements



### 5.3 LES of in-nozzle flow

---

with characteristic size  $\sim 60 \mu\text{m}$  distributed over the discharge volume. The outlet plane is moved away from the hole outlet to reduce the impact of eventual back flow. Since there is no interest in resolving the flow dynamics downstream of the hole exit, the discharge volume is meshed prioritizing computational cost over resolution. LES is used here to avoid possible numerical issues arising when transferring data from LES back to URANS.

- **Interface 2.** Interface between hexahedral elements of Subdomain 2 and tetrahedral elements of Subdomain 3. Velocity and pressure fields are simply interpolated from LES of Subdomain 2 to LES of Subdomain 3 to reduce computational time.

There are different methods available for data transfer between URANS and LES at Interface 1. For instance, the spectral synthesizer (Kraichnan [196], Smirnov et al. [197]) introduces random velocity fluctuations into the LES domain based on URANS turbulence intensity. The vortex method (Sergent [198], Mathey et al. [199]) consists of a finite number of artificial 2D vortices generated at the URANS-LES interface normal to the streamwise direction. These vortices are based on the Lagrangian form of the 2D evolution equation of the vorticity and the Biot-Savart law. With this technique, information about the vorticity field is introduced by artificial vortices from the  $k-\omega$  SST domain to the LES domain. As reported in Appendix E, the impact of both methods on local turbulence generation and vortex structures is significant. However, the absence of quantitative experimental data to validate the predictions by either method does not allow drawing conclusions on which one yields the most accurate results. Thus, it was decided to use simple interpolation and to move the interface upstream of the sac where turbulence is low, reducing the impact on the flow near the hole entrance.

Figure 5.7 shows the different internal interfaces of the computational mesh, as well as the external surfaces to which the following boundary conditions were applied:

- **Pressure inlet.** Applied to the INLET plane above the first needle truncation setting constant pressure equal to 800 bar. Only liquid phase is allowed to enter the domain. Constant turbulence intensity 5% and turbulent viscosity ratio 10 are imposed (recommended values for  $k-\omega$  SST model, see [194]). Flow velocity in this area is low ( $\sim 3 \text{ m/s}$ , Reynolds number  $< 1000$ ) and turbulence intensity is not a critical parameter.
- **No-slip wall.** Applied to NEEDLE, HOUSING, HOLE and DISCHARGE VOLUME surfaces.
- **Periodic boundary condition.** Applied to PERIODIC BOUNDARIES surfaces. Rotational periodic boundaries at  $120^\circ$ .
- **Interior interface.** Applied to URANS-LES INT. (non-conformal), HOLE OUTLET (conformal) and HEXA-TETRA INT. (non-conformal). Flow variables are simply interpolated at non-conformal interfaces. HOLE OUTLET surface is defined to monitor integral quantities such as mass flow rate, axial and non-axial kinetic energy, pressure and velocity.
- **Pressure outlet.** Applied to the OUTLET plane setting constant pressure equal to 1 bar and liquid for eventual backflow.

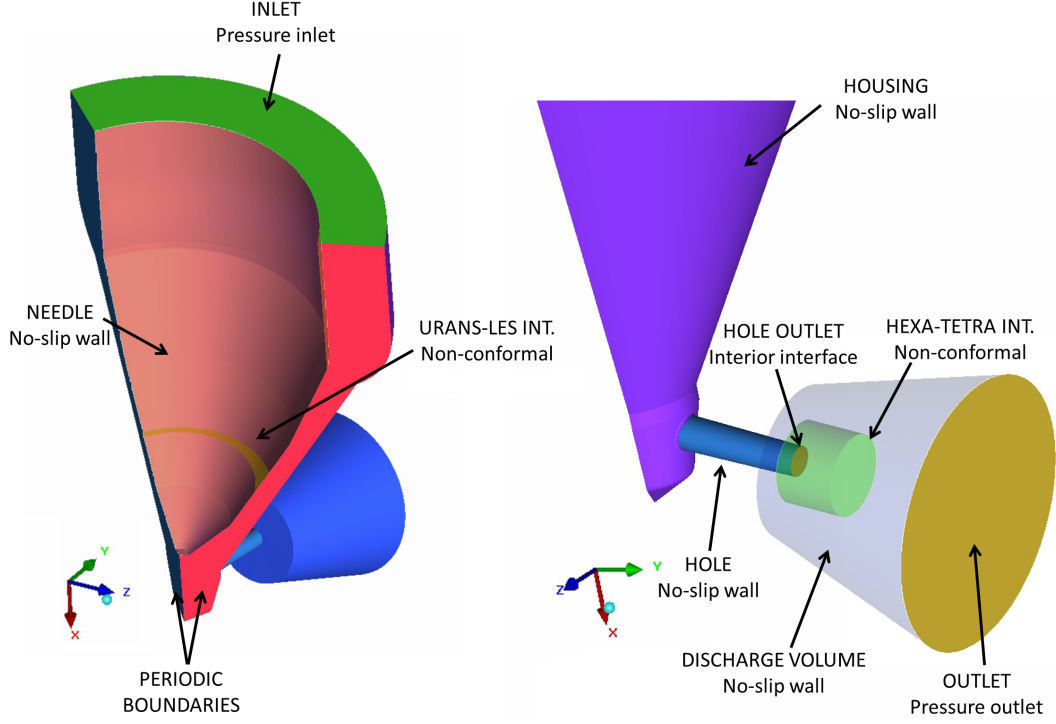


**Figure 5.7:** Boundary conditions and internal interfaces

### 5.3.3 Numerical setup, flow initialization and workflow

Both URANS and LES domains are solved using the SIMPLEC algorithm (Vandoormaal et al. [200]), advancing the solution with a fully implicit, second order time-accurate scheme. The time step is chosen equal to  $\Delta t = 5 \cdot 10^{-9}$ s to ensure a CFL number close to unity in the most critical regions of the LES domain. As for the spatial discretization, the momentum equation is discretized with a second order upwind scheme in the URANS domain and with a bounded central differencing scheme in the LES domain. The bounded central differencing scheme is a good choice for LES, since it offers small numerical dissipation and sufficient numerical stability. Pressure interpolation at the interface is done in both cases with the PRESTO algorithm [194] and calculation of gradients and derivatives is performed using the Least Squares Cell-Based method, preserving second-order spatial accuracy. Finally, the volume fraction equation is discretized with a first order upwind scheme, sacrificing accuracy at the expense of numerical stability, and the  $k - \omega$  equations with a second order upwind scheme.

Correct flow initialization is paramount in LES, as it can have a significant impact on the solution statistics. In order to reduce this impact, the simulation is stabilized, starting from initial conditions, during a specific amount of time before collecting data for statistical analysis. The characteristic time  $t_c$  for a fluid particle to cross the entire domain under steady conditions can be estimated as

$$t_c \approx \frac{\rho_l \text{Vol}}{\dot{m}} \quad (5.5)$$

where  $\rho_l$  is the liquid density, Vol is the volume of the computational domain and  $\dot{m}$  is the

### 5.3 LES of in-nozzle flow

mass flow rate, yielding

$$\dot{m} \approx 0.0054 \text{ kg/s} ; \quad \rho_l = 730 \text{ kg/m}^3 ; \quad \text{Vol} = 3.85 \cdot 10^{-9} \text{ m}^3 \rightarrow t_c \approx 5.20 \cdot 10^{-4} \text{ s}$$

which is approximately 0.5 ms. However, this overall flow-through time is much longer than the flow-through time associated with the high velocities found in the sac and hole, which can be estimated as

$$t_c^{hole} \approx \frac{\rho_l \text{Vol}^{hole}}{\dot{m}} ; \quad \dot{m} \approx 0.0054 \text{ kg/s} ; \quad \rho_l = 730 \text{ kg/m}^3 \quad (5.6)$$

$$\text{Vol}^{hole} = 4.2 \cdot 10^{-11} \text{ m}^3 \rightarrow t_c^{hole} \approx 5.70 \cdot 10^{-6} \text{ s} \approx 6 \mu\text{s}$$

where  $\text{Vol}^{hole}$  is the volume comprised between hole inlet and outlet.

The computational cost of initializing the flow field during 0.5 ms using LES resolution exceeds by far the available resources. As shown in the initialization strategy sketched in Figure 5.8, a precursor URANS  $k - \omega$  is used instead to simulate the first 0.5 ms in a coarser mesh, aiming at establishing a mean flow in the domain starting from the initial conditions. Initially, the whole domain is filled with quiescent liquid at outlet pressure 1bar. At the end of the precursor URANS the flow field is interpolated into the final mesh depicted in Figure 5.6. During the decoupling stage, the Embedded LES calculation goes on 50  $\mu\text{s}$  more (approximately 9 hole flow-through times), which suffices to obtain statistical convergence and to remove the effect of both precursor URANS and mesh interpolation. This is illustrated in Figure 5.9 by showing temporal evolution of mass flow rate (MFR) at the inlet plane and at the hole outlet during the precursor URANS, decoupling stage and sampling stage in the Sharp edge nozzle case. Note that the time interval in the precursor URANS is 0-0.5 ms and in the decoupling and sampling stages 0-0.15 ms as time is reset after mesh interpolation. After 0.1 ms of precursor URANS simulation, MFR stabilizes around 4.9E-3 kg/s in both inlet and outlet planes. This time can be slightly larger for other nozzles (i.e. Short hole nozzle stabilizes after 0.2 ms) but all converge before  $t = 0.5 \text{ ms}$ . During the decoupling stage, mesh interpolation and transition to LES causes both inlet and outlet MFR to drop during 0-30  $\mu\text{s}$ , recovering towards  $t = 40 \mu\text{s}$ . Finally, the average MFR is stable and equal to 4.92E-3 kg/s during the sampling stage where data is collected for further post-processing.

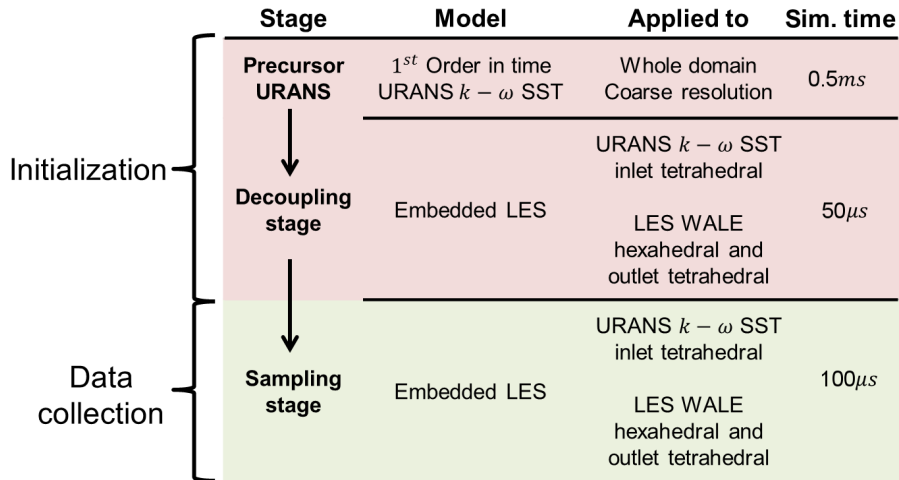
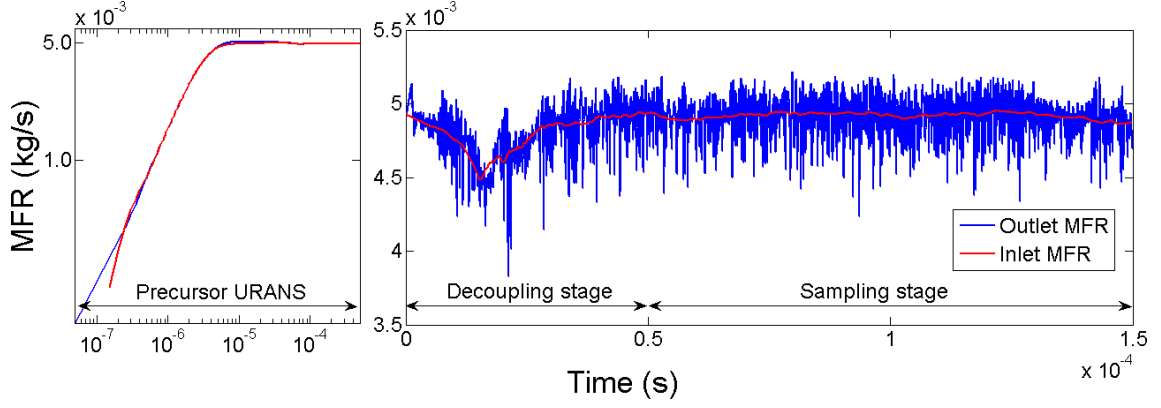


Figure 5.8: Simulation strategy



**Figure 5.9:** Mass flow rate at the INLET and HOLE OUTLET planes during Precursor URANS, decoupling stage and Sampling stage. Sharp edge nozzle

### 5.3.4 Verification of mesh resolution for LES

Figure 5.10 shows instantaneous  $y^+$  color iso-levels on the housing and hole. The small characteristic cell size used near walls ensures  $y^+ < 2$  in the whole LES domain and  $y^+ < 1$  near walls of interest, namely the hole inlet and the walls along the hole. The hole inlet rounding has approximately  $y^+ = 0.9$ , ensuring enough resolution for the small eddies generated in the upper shear layer. Even though resolving the boundary layer at the bottom of the sac and to the sides of the hole is not as important as near the hole inlet,  $y^+ < 1$  is achieved in most of the sac walls. It must be noted that despite being an instantaneous field, Figure 5.10 is representative of  $y^+$  observed during the simulation.

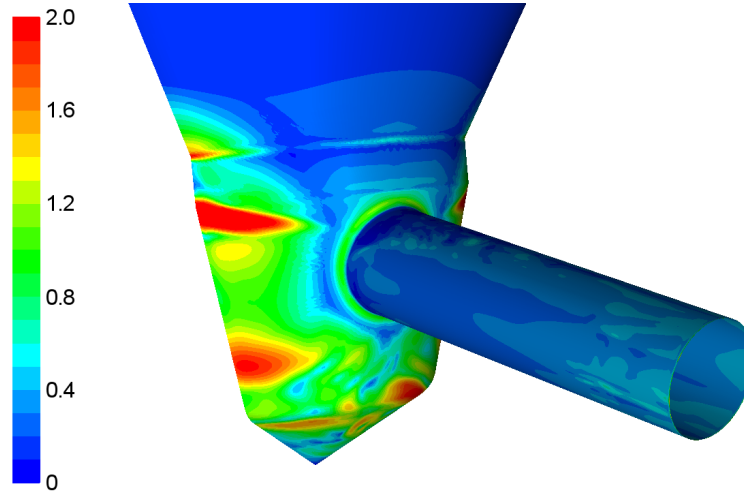


**Figure 5.10:**  $y^+$  color iso-levels on the housing and hole. Reference nozzle

Spatial and temporal resolution can be assessed through SGS viscosity ratio and cell-based CFL number. The SGS viscosity ratio is defined as the SGS viscosity divided by the molecular viscosity. The cell-based CFL number is given by

$$CFL_{cell} = \frac{|V| \Delta t}{\Delta} \quad (5.7)$$

### 5.3 LES of in-nozzle flow

where  $|V|$  is the local velocity,  $\Delta t$  the time step and  $\Delta$  the characteristic cell size computed as

$$\Delta = \text{Cell volume}^{1/3}$$

Instantaneous and averaged fields of both quantities are shown in Figure 5.11. Instantaneous SGS viscosity ratio remains below 1 in most of the domain, except for the upper and lower shear layers and the string vortices shed from the sac, where they reach a maximum of 5. This maximum value is never exceeded during the simulation at any point of the domain, leading to well-resolved turbulent structures. As suggested by averaged SGS viscosity ratio color iso-levels, locally high values of modeled turbulence within these structures is not persistent over time, yielding maximum time-averaged values below 0.5. Regarding the cell-based CFL number, it is below 1 everywhere inside the nozzle hole except for the upper inlet rounding, where it peaks at 5 due to strong flow acceleration before separation from the wall. Both instantaneous and averaged fields are quantitatively very similar, denoting relatively stable temporal resolution of vortex structures. In view of this, the retained time step  $\Delta t = 5 \cdot 10^{-9}$ s is deemed sufficient to provide a reasonably good resolution of turbulence scales and vortex structures.

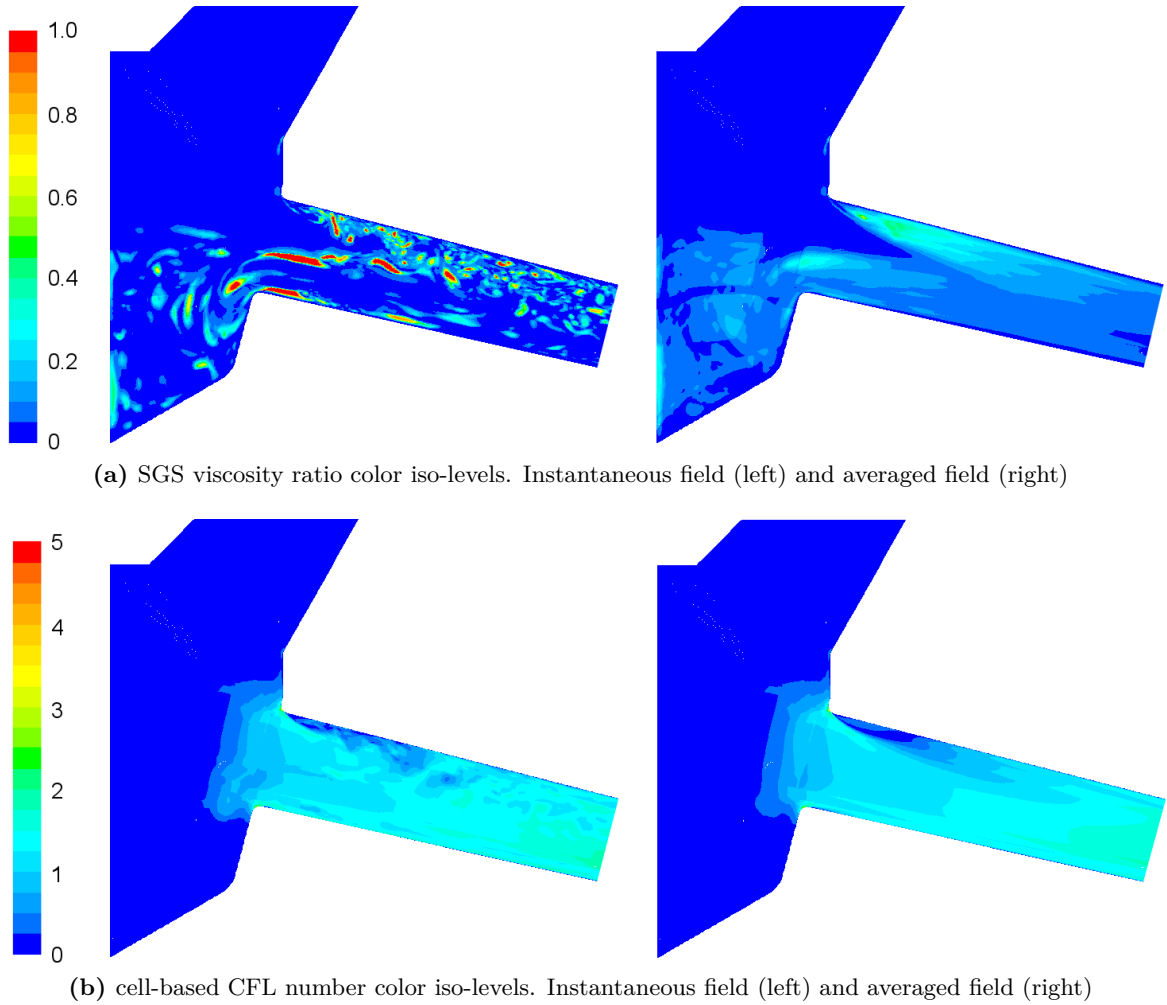


**Figure 5.11:** SGS viscosity ratio and cell-based CFL number. Reference nozzle mid-cut plane

### 5.3.5 Cavitation model evaluation

The Zwart-Gerber-Belamri cavitation model is adjustable through the coefficients  $F_{vap}$  and  $F_{cond}$ , determining the vaporization or condensation rate for a given pressure drop at the liquid-vapor interface. Although the values  $F_{vap} = 50$  and  $F_{cond} = 0.01$  suggested in [194] are suitable for a wide range of problems, experience shows that  $F_{vap} = 500$  and  $F_{cond} = 0.05$  yield better results in nozzle flows. The objective of this Section is to evaluate qualitatively the impact of  $F_{vap}$  and  $F_{cond}$  on the numerical predictions, especially on vortex formation and turbulence generation. To this end, two different simulations performed in the Reference nozzle are compared, one set with  $F_{vap} = 50$ ,  $F_{cond} = 0.01$ , referred to as “Reference Cavitation” settings and the other with  $F_{vap} = 500$ ,  $F_{cond} = 0.05$ , referred to as “Enhanced Cavitation” settings. In this test the sampling stage was limited to 50  $\mu$ s due to limited computational resources.

Figure 5.12 compares average velocity, resolved turbulent kinetic energy and average vapor fraction color iso-levels on the mid-cut plane. Velocity distribution and resolved TKE are very similar both qualitatively and quantitatively. In particular, resolved TKE in the upper separation region and near the lower inlet edge has almost the same position, distribution and intensity regardless of the cavitation model coefficients, suggesting a relative insensitivity of turbulence to these parameters. Average vapor volume fraction color iso-levels confirm that the amount of vapor volume fraction predicted with Enhanced Cavitation settings is consistently higher over time than with Reference Cavitation settings.

The effect of cavitation model parameters on vortex dynamics and vapor formation can be assessed using normalized Q-criterion and vapor volume fraction iso-surfaces colored by velocity and pressure respectively. Figure 5.13 compares these magnitudes at two different times  $t_1$  and  $t_2$ , showing very similar structures at the same simulation time. At time  $t_1$ , the large, counter-rotating vortices coming from the sac, known as string vortices, break down into smaller scales in the first half of the hole. Small, isotropic scales detaching from the upper inlet rounding and scattering further downstream are predicted similarly in both cases. The interaction between these eddies and the string vortices causes the latter to break, collapsing the cavitation string as suggested by vapor iso-surfaces. Even though condensation is promoted with  $F_{cond} = 0.05$ , there is no significant difference in the cavitation structures generated. This suggests that cavitation formation is mainly determined by the string vortices and their interaction with the upper vortices, which is similar regardless of the values used for  $F_{vap}$ ,  $F_{cond}$ .

At  $t_2$  the interaction between the string vortices and the upper shear layer is weak, letting the former reach the hole outlet without breaking down. Centrifugal forces keep pressure equal to vapor pressure (1000 Pa) in the vortex core, limiting vapor collapse even with  $F_{cond} = 0.05$ . The main difference between the two model configurations is the amount of vapor produced on the upper inlet edge at  $t_1$  and  $t_2$ . With Enhanced Cavitation settings more vapor appears in this area and survives further downstream along the upper wall. Notwithstanding, this does not seem to affect the formation of vortical structures in the upper inlet edge, at least from a qualitative standpoint.

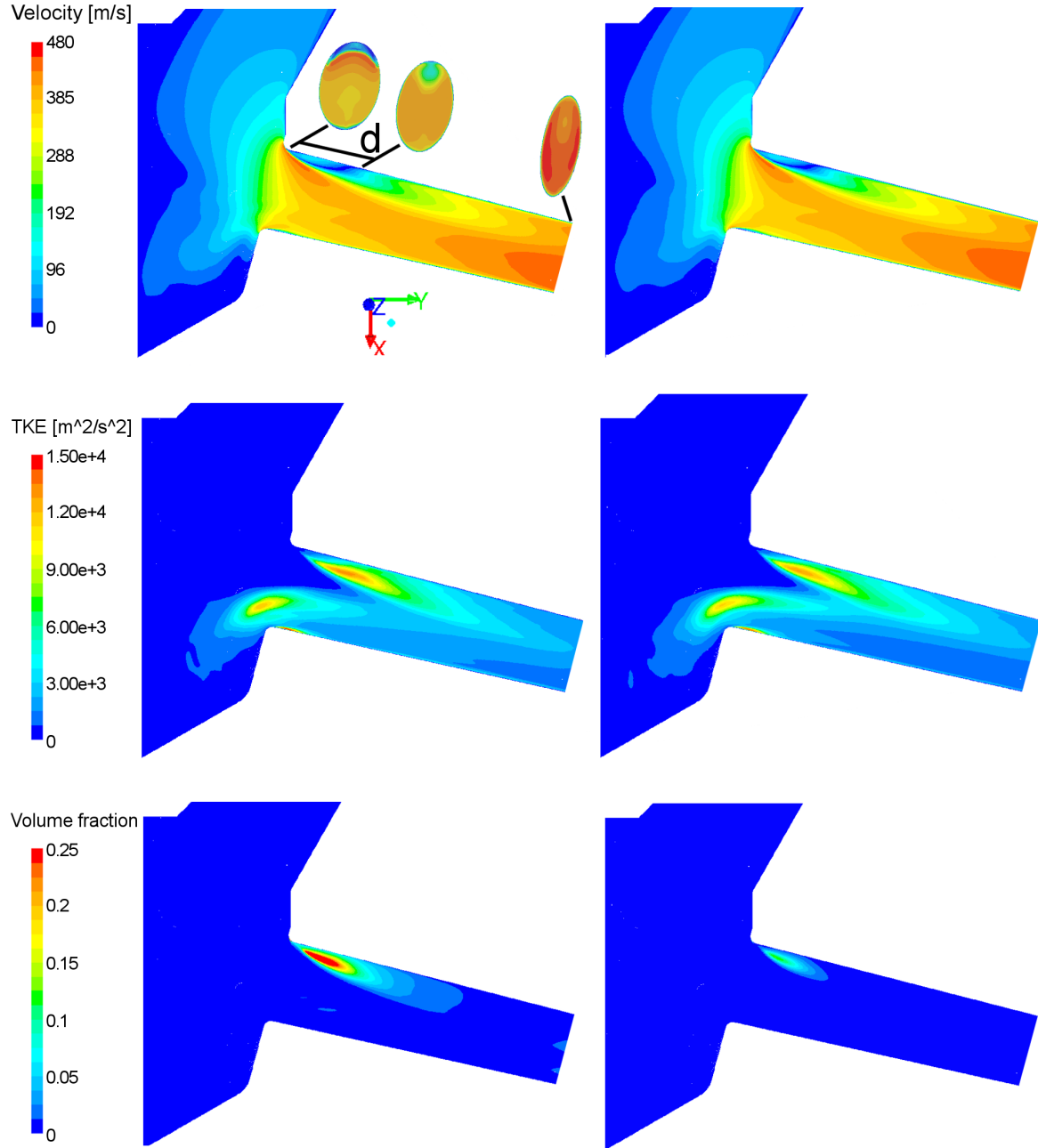


**Figure 5.12:** Average velocity (top), resolved turbulent kinetic energy (middle) and average vapor volume fraction (bottom) color iso-levels on the mid-plane ( $z = 0$ ) for the Enhanced Cavitation (left) and Reference Cavitation (right)

The cavitation model parameters affect all the integral magnitudes depending on the mixture density, which decreases linearly as volume fraction increases. For instance, mass flow rate is 10% lower and discharge coefficient 1% with Enhanced Cavitation settings. Even though experience at Delphi suggests that this setup is suitable for a wide range of injection conditions, it is interesting to see that vortex structures, turbulence and velocity are relatively insensitive to  $F_{vap}$ ,  $F_{cond}$ . These results are very important, since they support the idea that the formation of dominant structures inside the nozzle is independent of the cavitation model calibration.

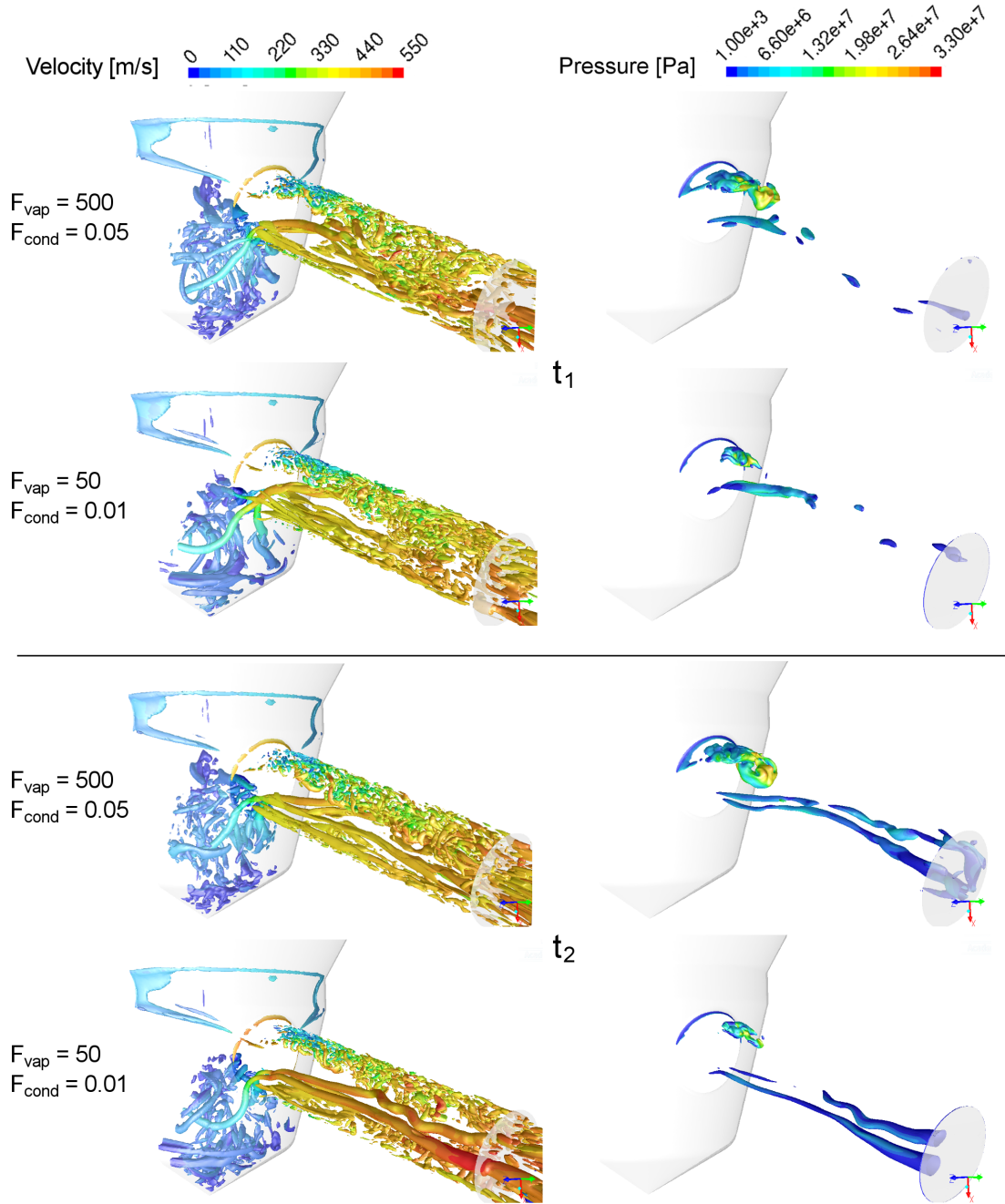


**Figure 5.13:** Comparison of Q-criterion iso-surfaces of value 0.2 (left) and volume fraction iso-surfaces of value 0.1 (right) at times  $t_1$  and  $t_2$ .  $t_1$  is the same in both simulations (same for  $t_2$ )

## 5.4 LES of in-nozzle and near-nozzle flow

The objective of simultaneous simulation of in-nozzle and near-nozzle flow is to provide direct comparison with X-ray images. This can be very useful to assess the validity of qualitative correlations formulated between simulations of in-nozzle flow and X-ray images of near-nozzle spray. In order to capture the main atomization mechanisms without droplet evaporation, a coupled Volume of Fluid - Level Set method is used [194]. The main advantage of this approach is that, while benefiting from accurate interface reconstruction provided by the Level Set method, it uses the Volume of Fluid formulation to overcome the deficiencies associated



## 5.4 LES of in-nozzle and near-nozzle flow

with volume conservation of the Level Set function [106].

A big disadvantage of Level Set methods inherited by the coupled Volume of Fluid - Level Set is that they are not mature enough to be used in cavitating flows. Tracking the interface of very small nuclei embedded in the fluid, including their growth and collapse, is extremely difficult from a numerical standpoint. The characteristic size of nuclei (i.e.  $1\text{ }\mu\text{m}$  or below, Giannadakis et al. [72]) is several orders of magnitude smaller than the characteristic dimension of the problem, so the resolution required by interface tracking methods cannot be reached. In view of this shortcoming, coupled Volume of Fluid - Level Set is applied to the HP hole nozzle, which is the only non-cavitating nozzle studied.

### 5.4.1 Computational domain and mesh generation

The computational domain used for simultaneous simulation of in-nozzle and near-nozzle flow is shown in Figure 5.14. For simplicity, only the LES domain is depicted, since the URANS domain is unchanged with respect to Figure 5.6. The LES domain is meshed using only hexahedral elements with the quality criteria described in Section 5.3.2 for Subdomain 2. The discharge volume is extended 2 mm downstream of the hole exit and is discretized using 350 equally spaced cells along the direction of the hole axis (characteristic cell size  $\sim 5.7\text{ }\mu\text{m}$ ), 125 radially distributed cells ( $\sim 6\text{ }\mu\text{m}$ ) and 260 cells in the azimuthal direction ( $\sim 8\text{ }\mu\text{m}$ ). The total number of cells is approximately 15 million distributed over the discharge volume (8.5 million) and inside the nozzle (6.5 million). Regarding the boundary and operating conditions, they are the same as those detailed in Section 5.3.2. The only difference is the possible backflow at the outlet, which is composed of air.

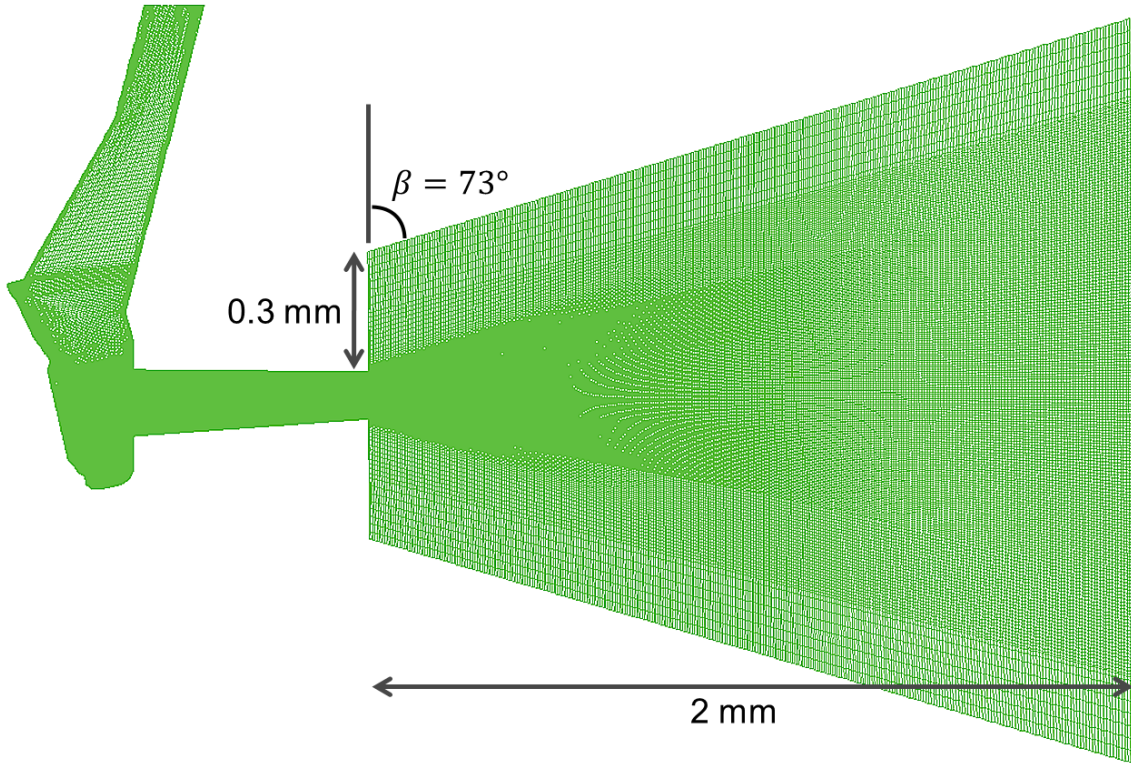


**Figure 5.14:** Mesh definition of the coupled internal nozzle - spray simulation

High mesh resolution is necessary in the discharge volume to resolve small droplets detaching from the liquid core. Ideally, the smallest droplets that can be accurately captured with cells of size  $\sim 5 \mu\text{m}$  have a characteristic diameter of  $\sim 10 \mu\text{m}$ . However, the liquid-gas interface smears due to numerical diffusion and other discretization errors, causing small droplets to disappear from the computational domain. Taking this into account, one should not expect to capture droplets smaller than  $\sim 10 \mu\text{m}$  near the outlet and  $\sim 3 \mu\text{m}$  near the hole exit in the mesh of Figure 5.14.

### 5.4.2 Model setup and verification of mesh resolution for LES

The numerical setup is similar to the one used for LES of in-nozzle flow. The mixture model described in Appendix D is solved together with a conservation equation for the Level Set function [194], which is defined as

$$\varphi(\mathbf{x}, t) = \begin{cases} |d| & \mathbf{x} \in \text{Liquid phase} \\ 0 & \mathbf{x} \in \text{Interface} \\ -|d| & \mathbf{x} \in \text{Gas phase} \end{cases}$$

$d$  being the shortest distance from point  $\mathbf{x}$  to the interface. The liquid phase is Diesel fuel with constant density  $\rho_l = 730 \text{ kg m}^{-3}$  and dynamic viscosity  $\mu_l = 2.4 \cdot 10^{-3} \text{ kg m}^{-1} \text{ s}^{-1}$ , and the gas phase is air with constant density  $\rho_a = 1.225 \text{ kg m}^{-3}$  and dynamic viscosity  $\mu_a = 1.7894 \cdot 10^{-5} \text{ kg m}^{-1} \text{ s}^{-1}$ . Regarding spatial and temporal discretization, the same schemes as those detailed in Section 5.3.3 are used with identical time step  $\Delta t = 5 \cdot 10^{-9} \text{ s}$ , adding a second order upwind scheme for the Level Set function equation. As for the interface reconstruction method, the piece-wise linear scheme proposed by [98] is selected, assuming that the liquid-air interface has a linear slope within each cell.

The problem initialization and work flow are also very similar to those used for LES of in-nozzle simulations. The differences lie in the initial conditions of the precursor URANS, which consist of liquid phase inside the nozzle and air in the discharge volume, and in the amount of time allocated to the decoupling stage, which is increased from  $50 \mu\text{s}$  to  $75 \mu\text{s}$  due to longer flow-through time. Although keeping  $100 \mu\text{s}$  for the sampling stage reduces the number of flow-through times sampled, it is deemed acceptable to provide statistically significant results.

Temporal and spatial resolution are assessed in Figure 5.15 using instantaneous SGS viscosity ratio and cell-based CFL number color iso-levels. The largest values of SGS viscosity ratio are found in the upper shear layer inside the nozzle and further downstream at the end of the spray. The maximum value is located right after the hole inlet rounding and is always below 2, but rarely exceeds 1.5. Finally, its increase near the outlet stems to some extent from cell coarsening in the azimuthal and radial directions. Regarding the cell-based CFL number, the maximum values near the hole entrance and at the hole exit plane are always below 5. High values in these two regions are due to strong flow acceleration at the hole inlet and smooth cell refinement at the hole outlet. Towards the end of the domain, radial and azimuthal mesh coarsening cause the CFL number to decrease, reaching values below 1 in the second half of the discharge volume.

The Level Set function and liquid volume fraction can be used to estimate liquid-gas interface

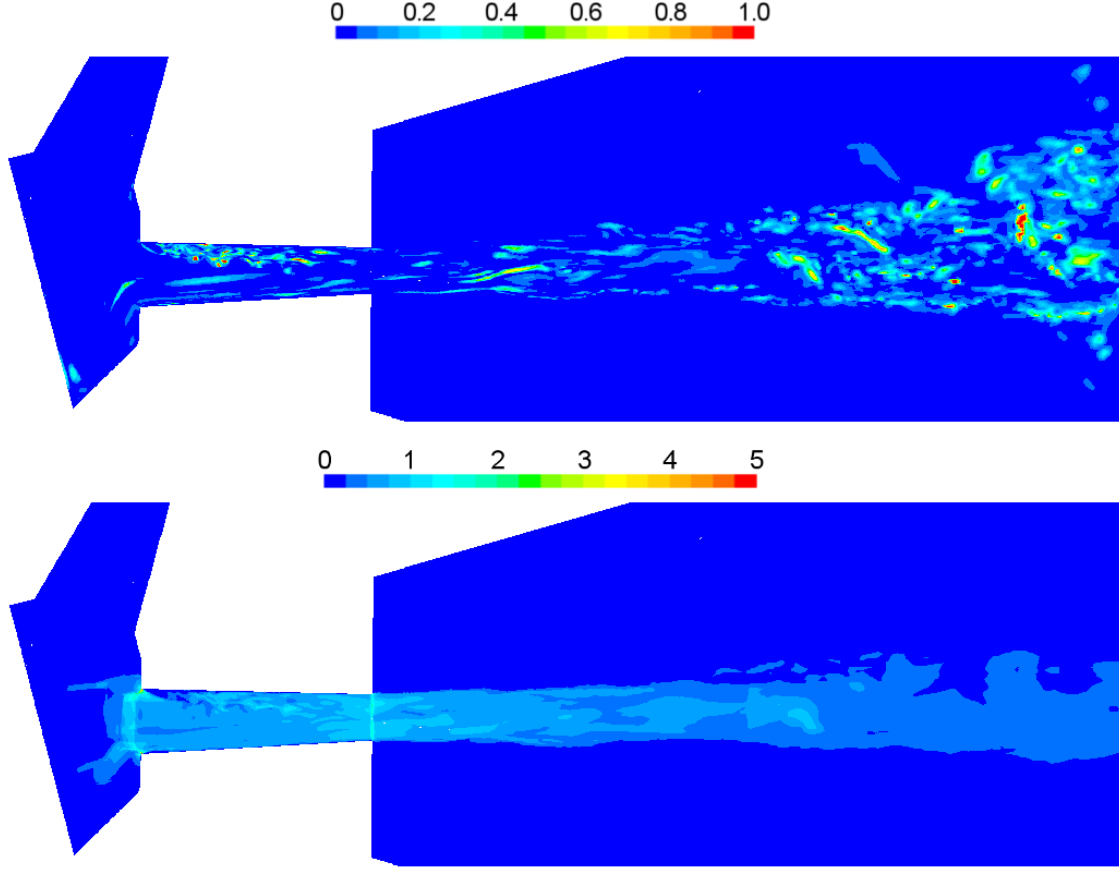


**Figure 5.15:** Instantaneous SGS viscosity ratio (top) and cell-based CFL number (bottom)

smearing, which is a consequence of numerical diffusion of the level-set function  $\varphi$  as the liquid-gas interface is convected downstream of the hole exit. This process is sketched in Figure 5.16 for a single droplet. Initially, the droplet is bounded by a sharp interface  $\varphi = 0$  where the liquid volume fraction jumps from  $\alpha_l = 0$  outside to  $\alpha_l = 1$  inside the droplet. After a number of time steps the interface smears, leading to smooth volume fraction variation across the interface. In this new state, the region where  $\alpha_l = 1$  is restricted to some cells in the center of the droplet, bounded by a surface where  $\varphi = 0$ . As highlighted, the thickness of the diffused interface can be estimated using the distance  $d_{1\%}$  between low volume fraction iso-surfaces, i.e.  $\alpha_l = 0.01$ , and the surface  $\varphi = 0$ .

A reasonable approximation is to assume symmetric interface diffusion, so that the ideally non-diffused interface is located at  $r + \frac{1}{2}d_{1\%}$  from the droplet core. For large droplets and ligaments, the distance between the core and the interface where  $\varphi = 0$  is  $r > 0$ . However, for smaller, spherical droplets away from the intact liquid core,  $\alpha_l = 1$  is reached only in one or very few cells, leading to  $r \sim 0$ . In such cases,  $d_{1\%}$  is a reasonable estimate of the actual characteristic droplet size. Figure 5.17 depicts liquid volume fraction iso-surfaces 0.01 colored by  $d_{1\%}$  (note that these iso-surfaces do not show the actual droplet size but the outer boundary of the diffused interface), separating droplets smaller than  $5 \mu\text{m}$  from larger droplets. The results suggest that droplets with  $d_{1\%} < 5 \mu\text{m}$  are resolved only very close to the liquid core during breakup initiation. Further downstream, only larger droplets and ligaments with  $d_{1\%} > 5 \mu\text{m}$  are predicted, denoting dissipation of droplets smaller than  $5 \mu\text{m}$ . Overall, the mesh is fine enough to capture breakup of a wide range of structures down to  $\sim 5\text{-}10 \mu\text{m}$ ,

especially during breakup initiation, but dissipates the smallest droplets towards the outlet.

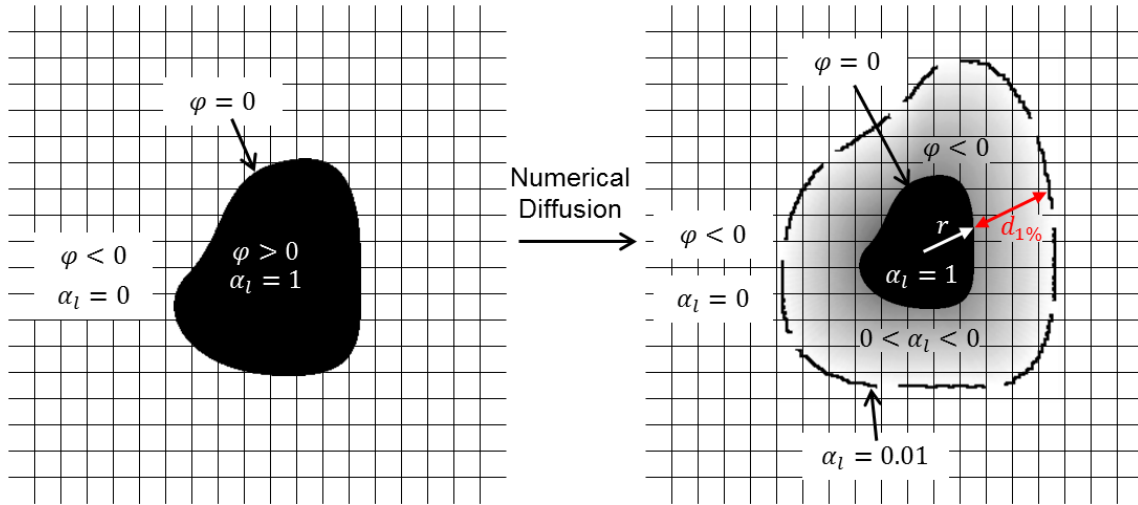


**Figure 5.16:** Sketch of interface smearing due to numerical diffusion. Sharp interface (left) and diffused interface (right)

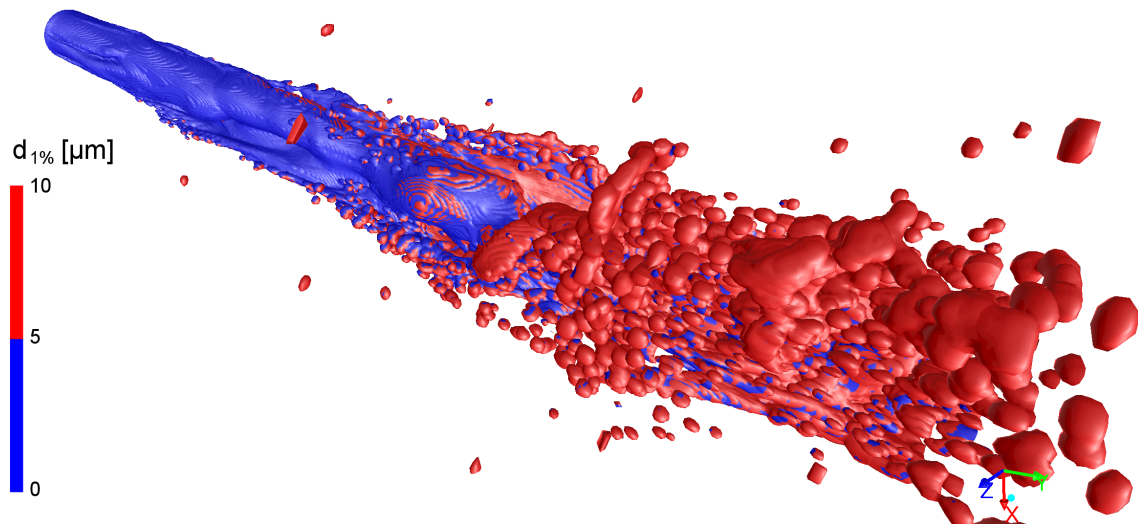


**Figure 5.17:** Estimation of droplet size based on  $d_{1\%}$ . Liquid volume fraction iso-surfaces 0.01 colored by  $d_{1\%}$

## Chapter 6

---

# Analysis of LES of in-nozzle flow

---

---

### 6.1 Introduction

The objective of the work presented in this Chapter is to analyze the LES results in order to identify dominant processes developing inside the nozzle, which contribute to flow mixing and can have an impact on primary breakup. The results yielded by LES of in-nozzle flow are discussed for each of the designs. The lack of numerical data outside the nozzle prevents direct comparison between LES and X-ray. Hence, only qualitative correlation between in-nozzle vortices and near-nozzle flow structures is provided.

The next five Sections in the Chapter address different geometry effects, comparing the Reference nozzle with either the Low lift nozzle (needle lift effect, Section 6.2), Sharp edge nozzle (hole inlet rounding effect, Section 6.3), Short hole nozzle (hole length effect, Section 6.4), 6-Hole nozzle (hole number effect, Section 6.5) or HP hole nozzle (hole taper effect, Section 6.6). For clarity in the discussion, the Reference nozzle is renamed in each Section depending on the geometrical feature addressed: High lift nozzle (needle lift effect), Rounded nozzle (hole inlet rounding effect), Long hole nozzle (hole length effect), 3-Hole nozzle (hole number effect) and Low taper nozzle (hole taper effect). Possible correlations between LES of in-nozzle flow and X-ray images of near-nozzle spray are formulated in the needle lift effect and hole inlet rounding effect Sections, since X-ray data are available for the Reference, Low lift and Sharp edge nozzles. Finally, all the findings are summarized in Section 6.7.

Some of the results presented in this Chapter have been presented at THIESEL 2016 conference and LES4ICE 2016 conference.

## 6.2 Needle lift effect

### 6.2.1 LES of in-nozzle flow

The influence of needle lift on vortex dynamics and cavitation generation is shown in Figure 6.1 by comparing instantaneous Q-criterion and vapor iso-surfaces in the Low lift nozzle (60  $\mu\text{m}$  needle lift) and High lift nozzle (300  $\mu\text{m}$  needle lift) cases. Small, homogeneously distributed scales appear at low lift. Intense sac activity causes flow structures to break down into smaller scales, resulting in a homogeneous amalgamation of small vortices entering the hole at relatively low velocities. These vortices promote flow mixing and generate cavitation pockets along the hole, leading to scattered vapor structures at the hole outlet. Enhanced sac activity stems from the sharper flow turning, which results in greater amount of flow forced to recirculate in the sac. Figure 6.2 illustrates this behavior through mean velocity color iso-levels and streamlines on the mid-cut plane, showing that while at high needle lift most of the fluid accelerates from the seat directly into the hole, only a thin layer does so at low needle lift.

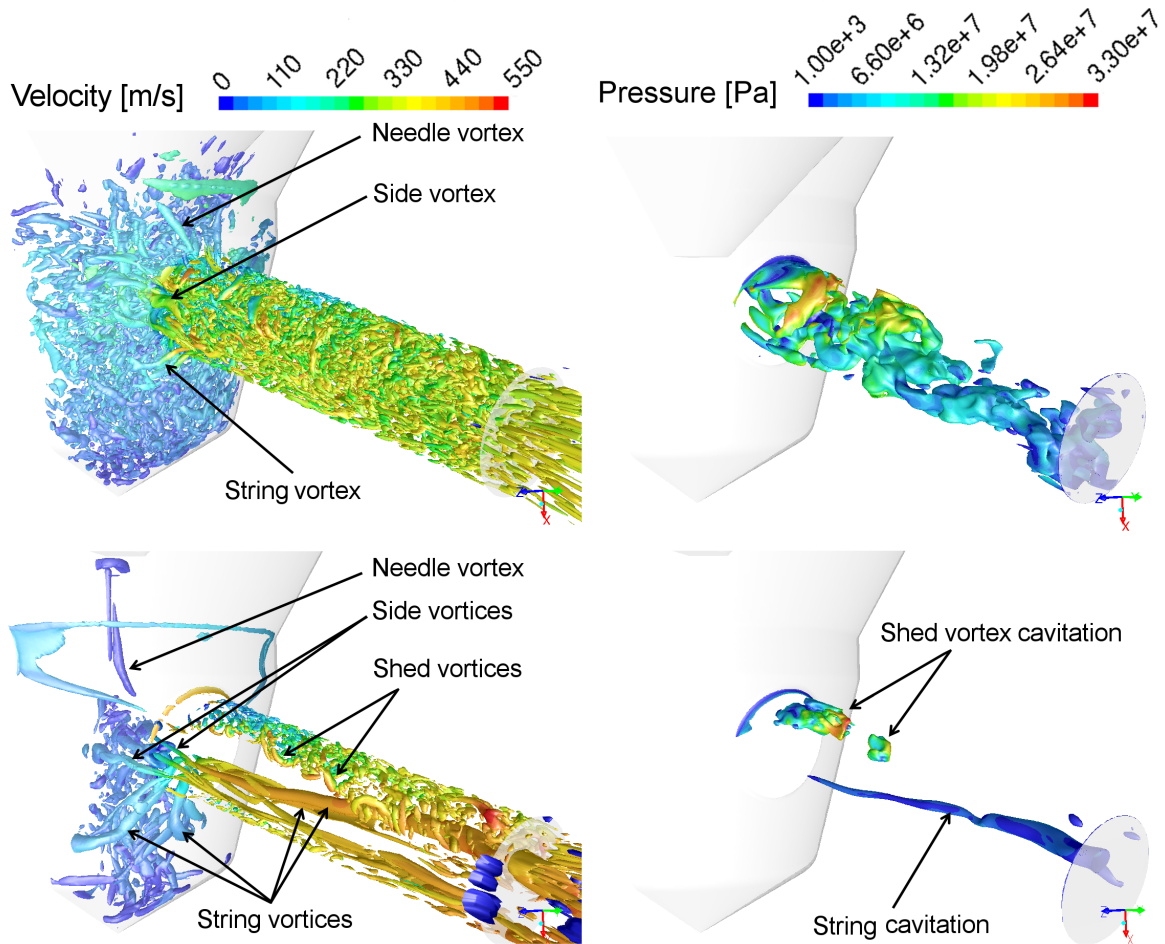


**Figure 6.1:** Comparison between Low lift nozzle (top) and High lift (bottom). Instantaneous normalized Q-criterion iso-surfaces of value 0.2 (left); vapor volume fraction iso-surfaces of value 0.1 (right)



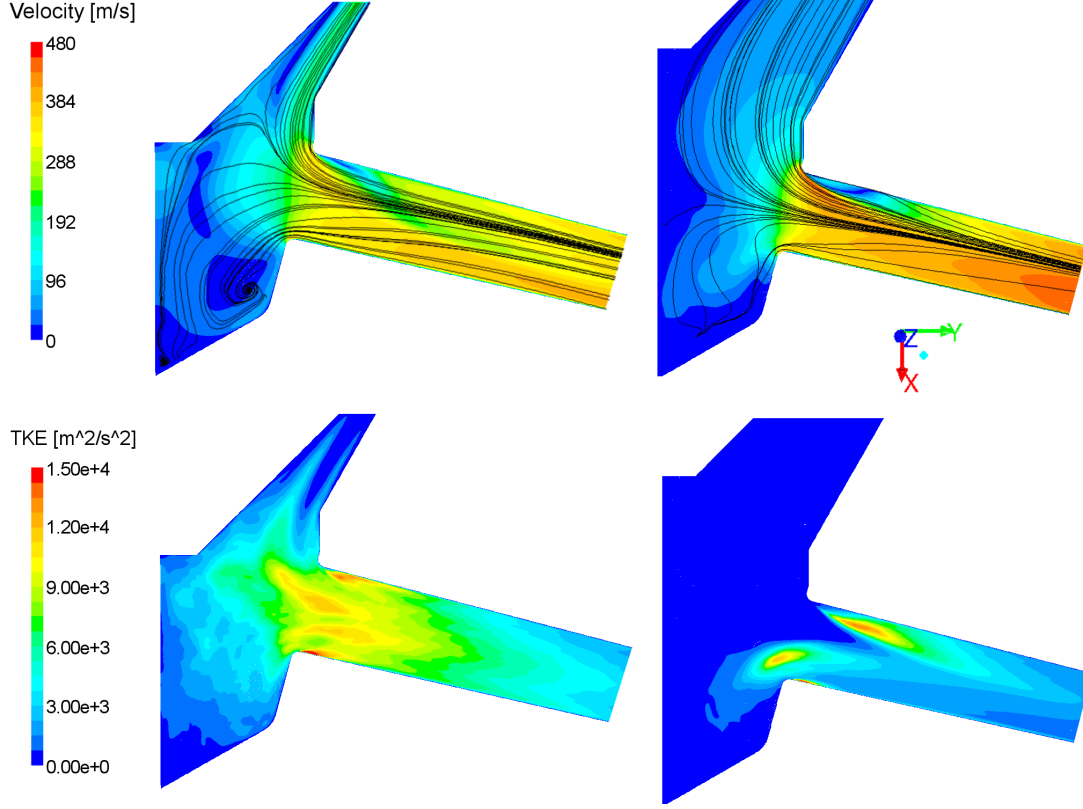


**Figure 6.2:** Average velocity and streamlines (top) and resolved turbulent kinetic energy (bottom) on the mid-cut plane ( $z=0$ ). Low lift nozzle (left); High lift nozzle (right)

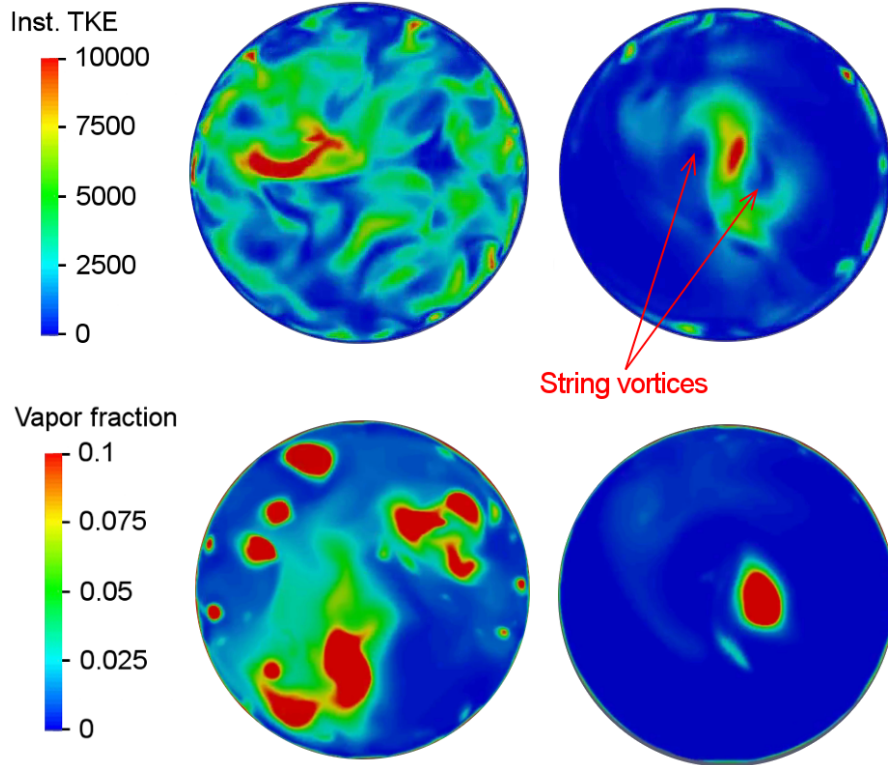
At high lift, the vortex structures consist of a combination of long, regular vortices and small, isotropic scales. Four main features can be observed: the string vortices coming from the sac, the side vortices developing above the string vortices, the needle vortex detaching from the needle tip and the shed vortices periodically generating at the upper hole inlet rounding. Both string and side vortices are pairs of counter-rotating vortices caused by sac flow recirculation, with the string vortices generally being more intense due to strong flow turning at the bottom of the sac. The needle vortex propagates from the needle tip to the hole driven by the bulk flow coming from the seat. This vortex is weak at high lift due to the relatively long distance between needle and hole. The shed vortices developing on the upper side are horseshoe-like structures surrounded by a cloud of small, isotropic scales. They are separated from the other vortices by a region of negligible vorticity occupied by the bulk flow accelerated from the seat into the hole (region with no Q-criterion iso-surfaces). When approaching the hole outlet, the upper eddies interact with the string, side and needle vortices, enhancing mixing and flow unsteadiness at the outlet. In the instant shown this interaction is not strong enough to break down the string vortices, which survive until they reach the hole exit along with the cavitation string formed in the vortex core. On the other hand, the shed vortices dissipate as they move downstream, leading to pressure recovery and bubble collapse in the second half of the hole.

Figure 6.2 also depicts resolved turbulent kinetic energy color iso-levels calculated as the average of  $N$  instantaneous resolved TKE fields

$$\text{TKE} = \sum_{n=1}^N \frac{\text{Inst. TKE}_n}{N} = \frac{1}{2} \sum_{n=1}^N \frac{[(V_x - \bar{V}_x)_n^2 + (V_y - \bar{V}_y)_n^2 + (V_z - \bar{V}_z)_n^2]}{N} \quad (6.1)$$

where  $N = 20000$ ,  $V_x$ ,  $V_y$ ,  $V_z$  are instantaneous velocity components and  $\bar{V}_x$ ,  $\bar{V}_y$ ,  $\bar{V}_z$  are averaged velocity components. The results suggest that turbulence is promoted at low lift, especially at the hole inlet and in the center of the sac. Apart from turbulence generation on the upper and lower shear layers, TKE increases due to the string and side vortices, which become more intense as a consequence of their proximity to the needle tip. At high lift, however, TKE is mainly produced in the upper shear layer and in the string vortices.

Figure 6.3 shows instantaneous resolved TKE and vapor volume fraction color iso-levels on the hole outlet. At low lift, small scales are responsible for a more homogeneous distribution of TKE and vapor. Although cavitation is mainly generated inside these scales, it can also form locally between them due to flow shear. At high lift, turbulence and cavitation are mainly caused by the string vortices developing in the center of the hole. The low vapor outside the string vortex core is partly due to the centrifugal force exerted on the surrounding fluid; the flow is squashed against the walls, reordering the streamlines and decreasing turbulence. The interaction between the string vortices themselves results in a highly unstable motion where one of the vortices eventually strengthens at the expense of the other, leading to one single cavitation string at the hole outlet.



**Figure 6.3:** Instantaneous resolved turbulent kinetic energy in  $m^2/s^2$  (top) and vapor volume fraction (bottom) at the hole outlet. Low lift nozzle (left); High lift nozzle (right)

In order to identify the energy-carrying structures at the hole outlet, Proper Orthogonal Decomposition (POD) is applied to in-plane velocities (a detailed description of the applied POD method is provided in Appendix F). Although this provides information only about non-axial patterns, it is very useful to link them to the features highlighted by Q-criterion iso-surfaces. For each nozzle, Figure 6.4 shows Mode 0, Mode 1, Mode 2 and Mode 20 at the hole exit using streamlines of normalized in-plane velocities, and Figure 6.5 compares modal



## 6.2 Needle lift effect

and accumulated energies. Mode 20 is shown as it is the only mode that has the same energy at low and high needle lift. At low lift, Mode 0 shows a large counter-clockwise vortex occupying most of the outlet. It draws attention to the fact that, even though the computational domain is symmetric with respect to the mid-cut plane ( $y = 0$  in the hole-centered coordinate system of Figure 6.4), there is a dominant rotation direction. In Mode 1 and Mode 2, however, a very similar vortex appears with opposite rotation direction. In fact, Figure 6.5 shows that the energy of Mode 0 (19.1%) is approximately equal to the sum of Mode 1 and Mode 2 energies (20%), indicating that there is not such dominant rotation direction. Mode 0, Mode 1 and Mode 2 contain up to 40% of accumulated energy, suggesting that this large, single vortex is transporting the smaller, homogeneously distributed scales captured by Q-criterion iso-surfaces in Figure 6.1.

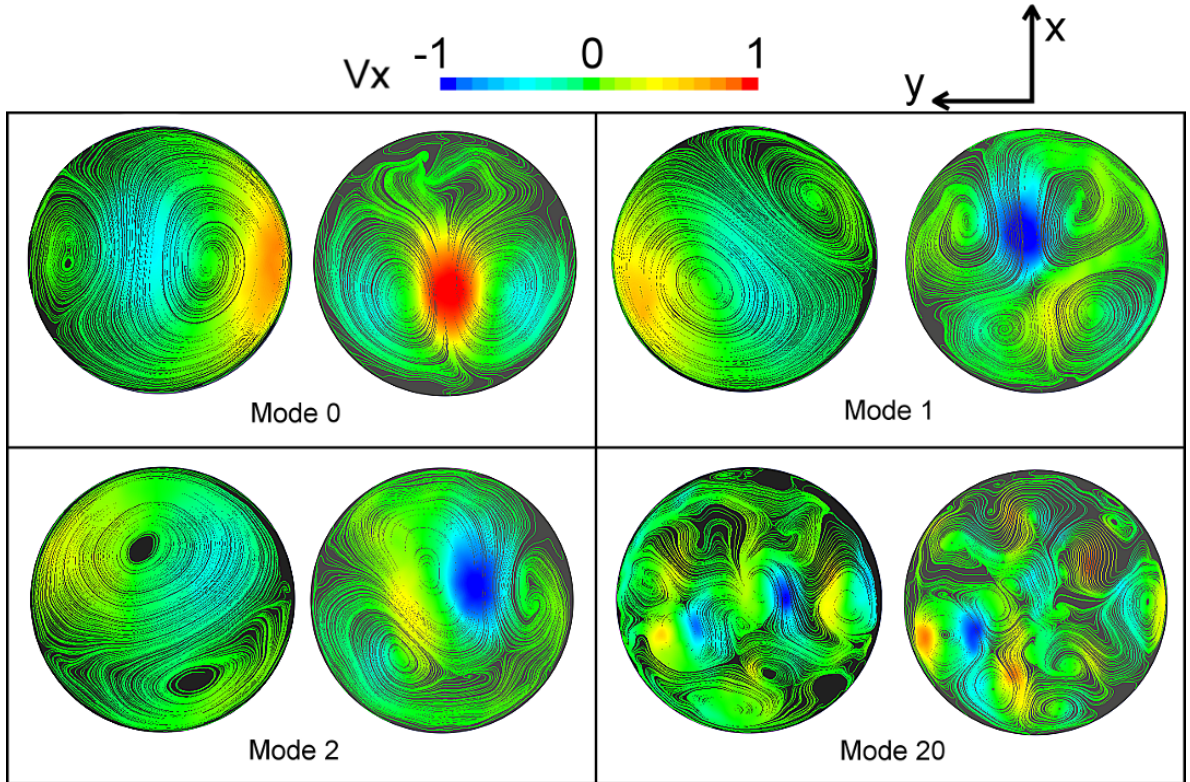


**Figure 6.4:** POD modes based on in-plane velocities at the hole outlet. Streamlines colored by vertical velocity  $V_x$  normalized by the maximum value. For each pair: Low lift (left); High lift (right)

The first three modes at low lift are completely different from their counterparts at high lift. Mode 0 shows two counter-rotating vortices on the lower half of the High lift nozzle hole, confirming the strong influence of the string vortices. The pattern predicted in Mode 1 preserves these structures on the lower half and includes the side vortices on the upper half, which have less energy associated. The large centered vortex in Mode 2 is due to the helical motion of the upper shear layer (“horseshoe” vortex detached from the upper inlet rounding). There is not a preferred rotation direction for this vortex, pictured in Mode 2 as clockwise-rotating, and so the energy is balanced by analogous counter-clockwise structures in subsequent modes.

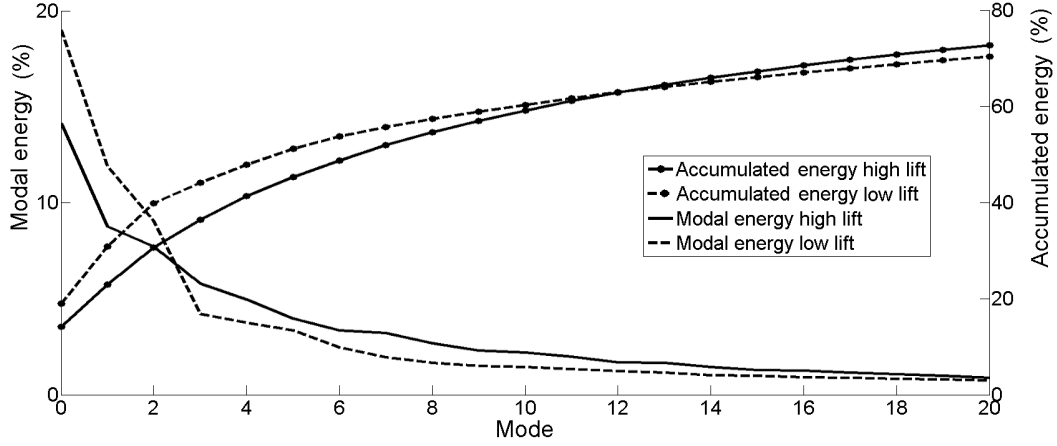


**Figure 6.5:** Modal energy and accumulated energy of POD modes 0-20

The accumulated energy shows that Modes 0-2 amount to 40% of the energy at low lift and to 30% at high lift, indicating that large scales transport comparatively more energy at low lift. This is interesting since Q-criterion iso-surfaces seem to suggest that small scales are dominant in the Low lift nozzle case. However, the accumulated energy up to Mode 20, which predicts vortices with a characteristic length scale of  $\sim 25 \mu\text{m}$  (approximately 1/6 of the outlet diameter), is 70% at low lift and 73% at high lift. This means that modes above Mode 20 associated with scales smaller than  $\sim 25 \mu\text{m}$  account for 30% and 27% of the energy respectively. Hence, not only the large scales but also the small scales contain more energy at low lift.

### 6.2.2 Correlation between LES of in-nozzle flow and X-ray images of near-nozzle flow

Similarly to the LES results, X-ray images show very different near-nozzle flow patterns at high and low needle lifts. Figure 6.6 depicts vortex and cavitation structures together with X-ray images at different instants. Some of the structures predicted numerically are compatible with the features observed in X-ray. At low lift, both LES and X-ray seem to capture small, homogeneously distributed structures at the hole exit. In LES, small eddies and cavitation pockets are scattered all over the nozzle. In X-ray, small structures exit the nozzle and spread downstream, inducing a wide range of scales and dispersion angle variation. Although X-ray images do not allow distinguishing whether the features observed are liquid-vapor interfaces, liquid-air interfaces or a combination of both, qualitative correlation between LES and X-ray is plausible in terms of length scales at the hole exit.

At high needle lift, both LES and X-ray images show strong pattern variation over time, transitioning between large, regular structures and small, regular or irregular structures. At time  $t'_1$  LES predicts large vortices on the lower half of the hole, one single vortex with string cavitation in the center and small scales on the upper side. At  $t'_2$ , large vortices are broken down into smaller, well-distributed scales causing negligible cavitation at the hole exit. Finally, the two counter-rotating string vortices with string cavitation reach the exit at  $t'_3$ . Regarding the X-ray images, the interface at the hole outlet seems to split into two large unperturbed structures at  $t = 0.66 \text{ ms}$  with no evidence of small scales within the first 0.6 mm. At  $t =$

## 6.2 Needle lift effect

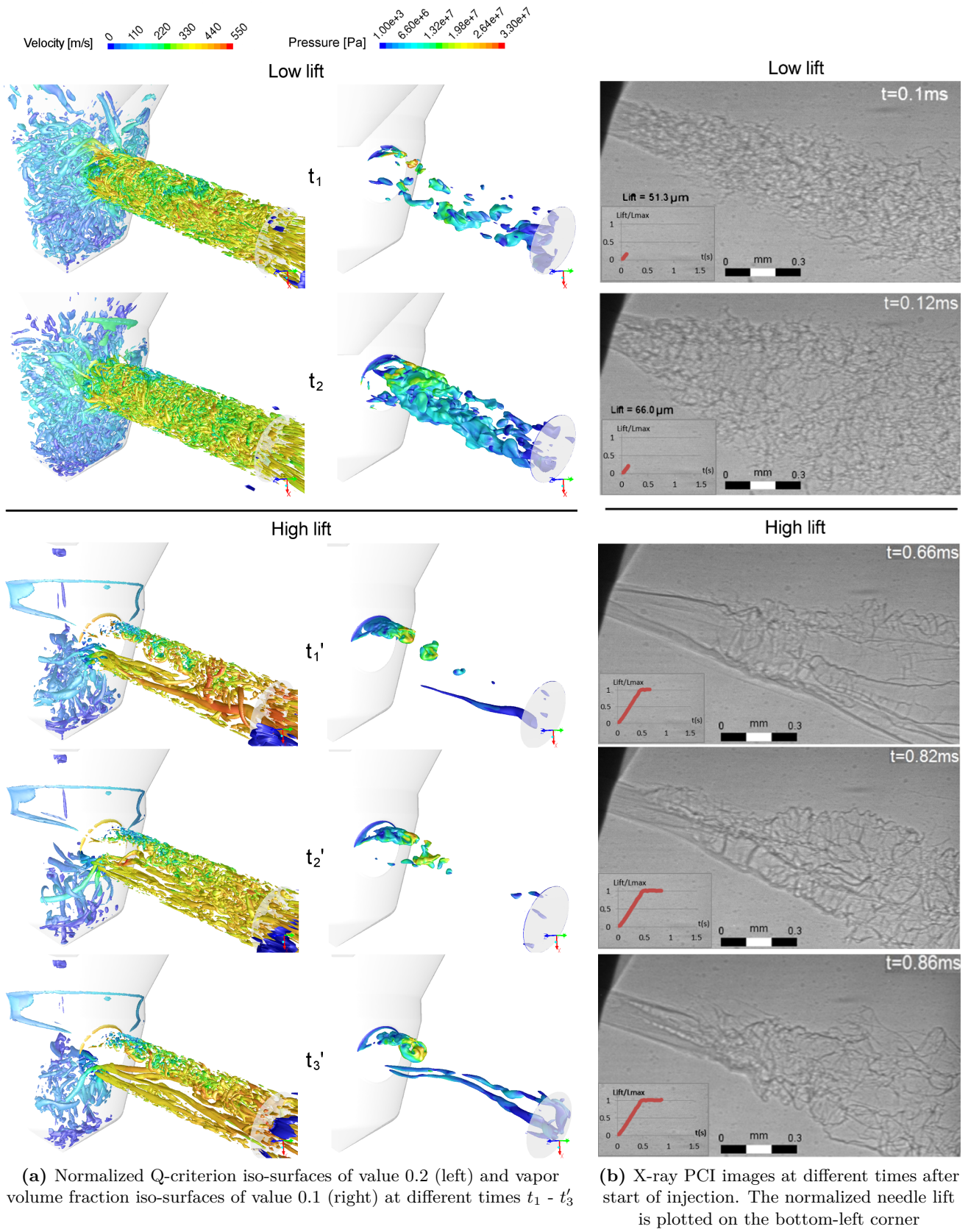


**Figure 6.6:** LES results and X-ray images at low lift (static needle 60  $\mu\text{m}$  in LES; moving needle 51.3  $\mu\text{m}$  and 66.0  $\mu\text{m}$  in X-ray) and high lift (300  $\mu\text{m}$ )

0.82 ms, however, breakup initiation does not occur at the hole exit but approximately 0.2 mm downstream, where small structures appear on the upper side. At  $t = 0.86$  ms, breakup initiation also occurs after the hole exit but in this case both on the upper side and in the middle of the near-nozzle flow.

Among the possible reasons that could explain the X-ray spray pattern variation at high lift, a reasonable hypothesis is that low pressure in the string vortex core enhances cavitation and ambient air entrainment into the near-nozzle flow, leading to the interface splitting observed at  $t = 0.66$  ms and  $t = 0.86$  ms. To illustrate this idea, Figure 6.7 shows pressure color iso-levels at the hole exit and vapor volume fraction iso-surfaces together with close-up views of X-ray images at  $t = 0.66$  ms and  $t = 0.82$  ms. When the string cavitation reaches the outlet, time  $t'_1$ , sub-atmospheric pressure generates an adverse pressure gradient that can trigger similar breakup initiation to that observed at  $t = 0.66$  ms in X-ray. On the other hand, if the string vortex is broken down along the hole, time  $t'_2$ , pressure recovers and cavitation collapses, leading to static pressure over 1 bar at the outlet. In that case, relatively unperturbed structures similar to those observed in X-ray at  $t = 0.82$  ms could be expected during a hypothetical spray breakup.

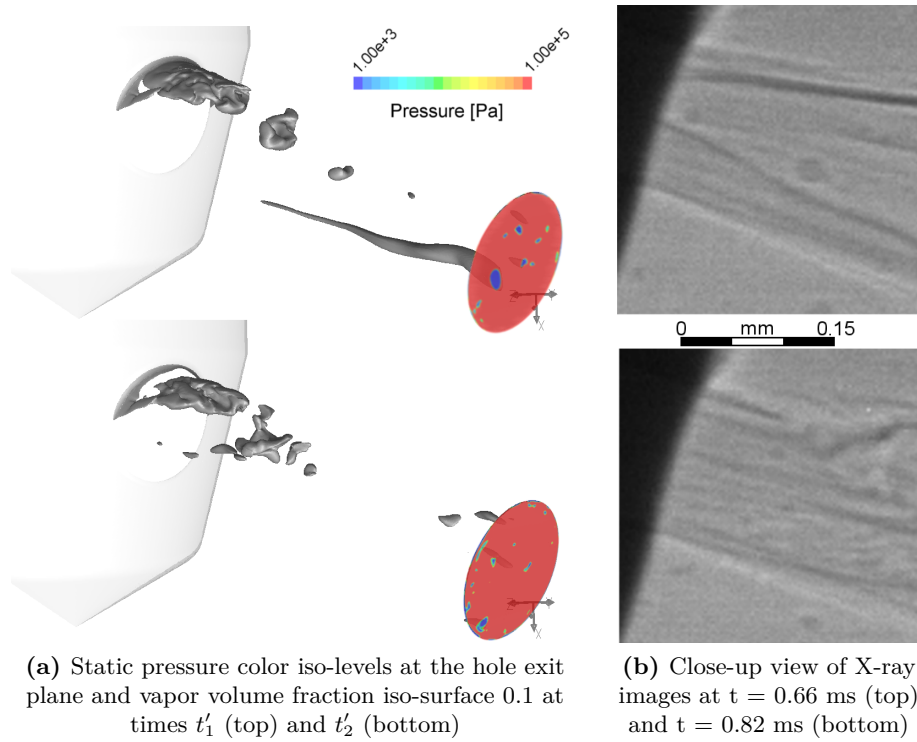


**Figure 6.7:** Link between string vortex and low pressure at the hole exit and possible correlation with X-ray breakup initiation at high lift

The interpretation provided suggests that large scale vortices developing inside the nozzle at high lift have an important impact on the near-nozzle spray pattern observed in X-ray. Further downstream, smaller interface structures appear at  $t = 0.66$  ms,  $t = 0.82$  ms and  $t = 0.86$  ms, first on the upper side and then in the rest of the jet. The fact that the upper side is consistently more perturbed than the lower side can be correlated with the vortex distribution inside the nozzle, where small scales appear mainly on the upper side of the hole.



### 6.3 Hole inlet rounding effect

Although these small vortices might also be correlated with small interface structures further downstream, the aerodynamic effects are likely to play a more important role in this region.

## 6.3 Hole inlet rounding effect

### 6.3.1 LES of in-nozzle flow

Reducing the hole inlet rounding from  $20\text{ }\mu\text{m}$  as in the Rounded nozzle (Reference nozzle) to  $0\text{ }\mu\text{m}$  as in the Sharp edge nozzle increases flow acceleration and turbulence at the hole entrance, leading to different vortex and cavitation structures. As shown in Figure 6.8, flow velocity increases due to stronger flow turning, enhancing turbulence generation on the upper side and at the lower hole inlet edge. Flow separation also increases, shifting the upper mixing layer towards the hole outlet. Noteworthy, the resolved TKE associated with the string vortices in the Rounded nozzle is slightly higher than in the Sharp edge nozzle. This is caused by weaker sac recirculation; a sharper inlet edge increases velocity at the hole entrance but decreases rotational velocity of the flow recirculating in the sac responsible for string vortex formation.

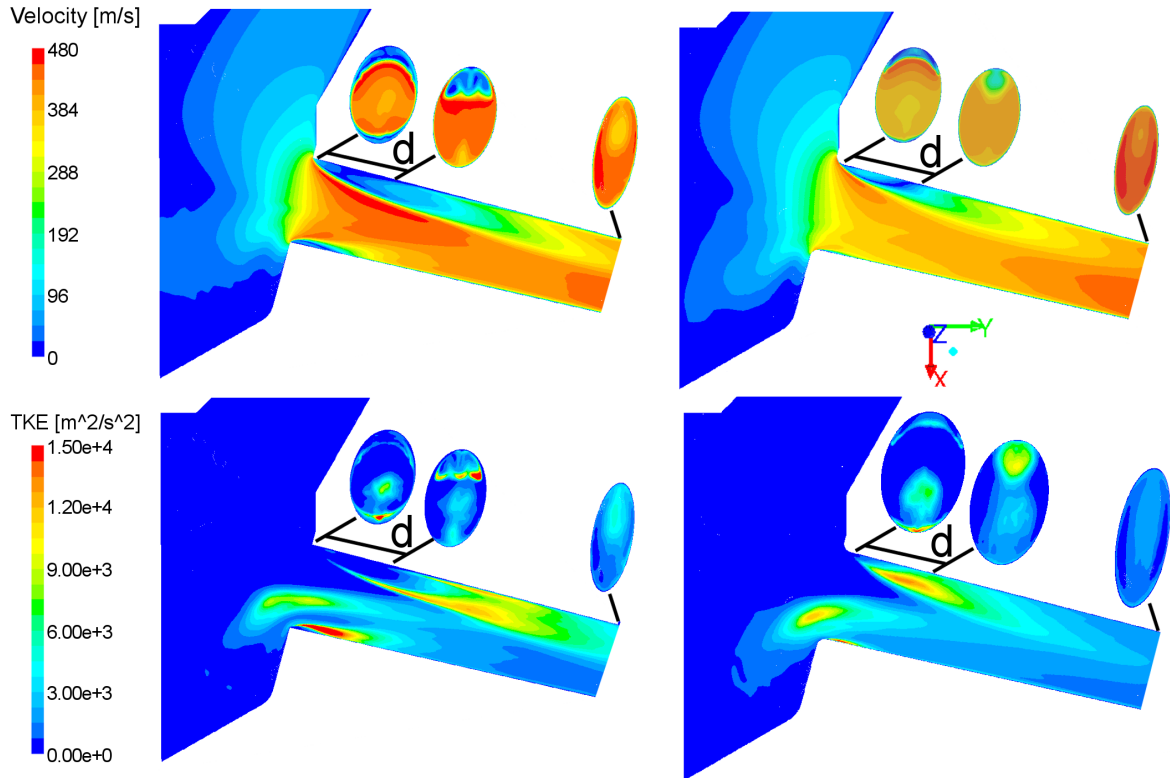


**Figure 6.8:** Average velocity (top) and resolved TKE (bottom) on the mid-cut plane ( $z=0$ ). Sharp edge nozzle (left); Rounded nozzle (right).  $d = 150\text{ }\mu\text{m}$

The effect of hole inlet rounding on vortex dynamics and cavitation is shown in Figure 6.9 at different times  $t_1$ ,  $t_2$  and  $t'_1$ ,  $t'_2$ . LES predicts a distribution of vortex and vapor structures relatively constant over time in the Sharp edge nozzle, contrasting with the strong temporal variation observed in the Rounded nozzle. On the one hand, flow separation on the upper

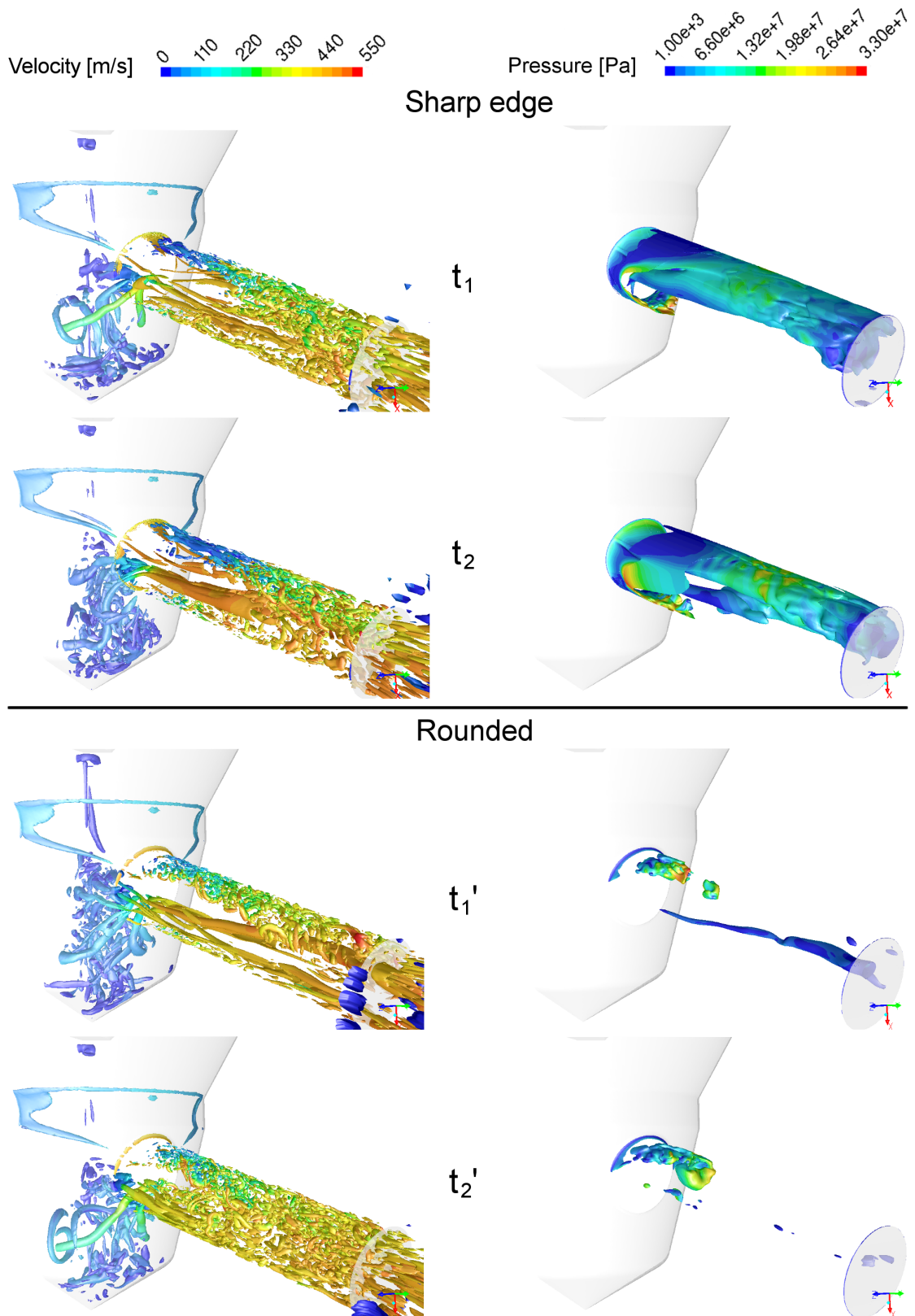


**Figure 6.9:** Comparison between Sharp edge nozzle and Rounded (Reference) nozzle results at different instants  $t_1$ ,  $t_2$  and  $t'_1$ ,  $t'_2$ . Instantaneous normalized Q-criterion iso-surfaces of value 0.2 colored by velocity (left); vapor volume fraction iso-surfaces of value 0.1 colored by static pressure (right)

### 6.3 Hole inlet rounding effect

side of the hole triggers intense cavitation mixed by small turbulent structures generated in the shear layer. Pressure increase after flow reattachment is not high enough to collapse the vapor, so a large amount of cavitation reaches the outlet. On the other hand, the string vortex breaks down along the hole as a result of the interaction with the shear layer, feeding the upper side with more vapor. The shear layer developed in the Sharp edge nozzle is always sufficiently strong to break down the string vortex along the hole, preventing string cavitation from reaching the outlet.

Instantaneous TKE and vapor volume fraction color iso-levels at the hole exit shown in Figure 6.10 evidence the impact of flow separation and the resulting shear layer on turbulence generation in the Sharp edge nozzle. In this case, small scales are responsible for a relatively homogeneous distribution of TKE and vapor on the upper side of the hole. Although small scales also affect TKE in the Rounded nozzle, their effect is largely exceeded by that of the string vortices. High TKE and vapor on the upper half of the Sharp edge nozzle contrasts with low TKE and cavitation outside the string vortices in the Rounded nozzle, meaning that flow mixing near walls is more efficient in the former. Finally, the lack of vapor and turbulence at the bottom in both cases is linked to larger and weaker vortical structures developing in this region.

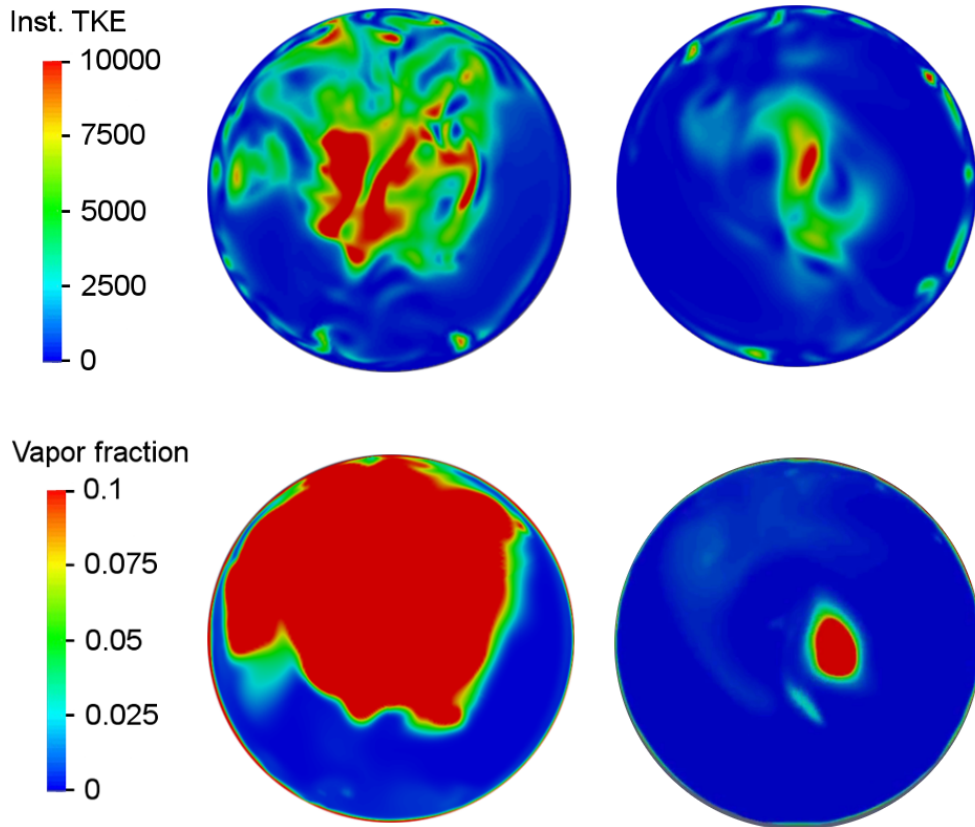


**Figure 6.10:** Instantaneous resolved turbulent kinetic energy in  $m^2/s^2$  (top) and vapor volume fraction (bottom) at the hole exit. Sharp edge nozzle (left); Rounded nozzle (right)

Temporal evolution of mass flow rate (MFR) at the hole exit can be utilized to identify coherent phenomena associated with vortex dynamics. This variable is useful for two reasons: it is sensitive to cavitation and it is affected by changes in axial velocity induced by the vortices. Figure 6.11 plots MFR together with their corresponding power spectra. The inverse FFT of

the low-pass filtered spectrum below 100 kHz is overlapped with the original signal to highlight low frequency oscillations. The results for both nozzles show two local maxima: one at 40 kHz and the other at around 2 MHz. In the Sharp edge nozzle, the 40 kHz frequency (referred to as “low frequency”) has slightly less power than the 2.3 MHz frequency (referred to as “high frequency”). Conversely, the 40 kHz frequency has significantly more power than the 2.1 MHz frequency in the Rounded nozzle. Comparatively, the high frequency event becomes more important in the Sharp edge nozzle, suggesting that it is directly related to hole inlet rounding.

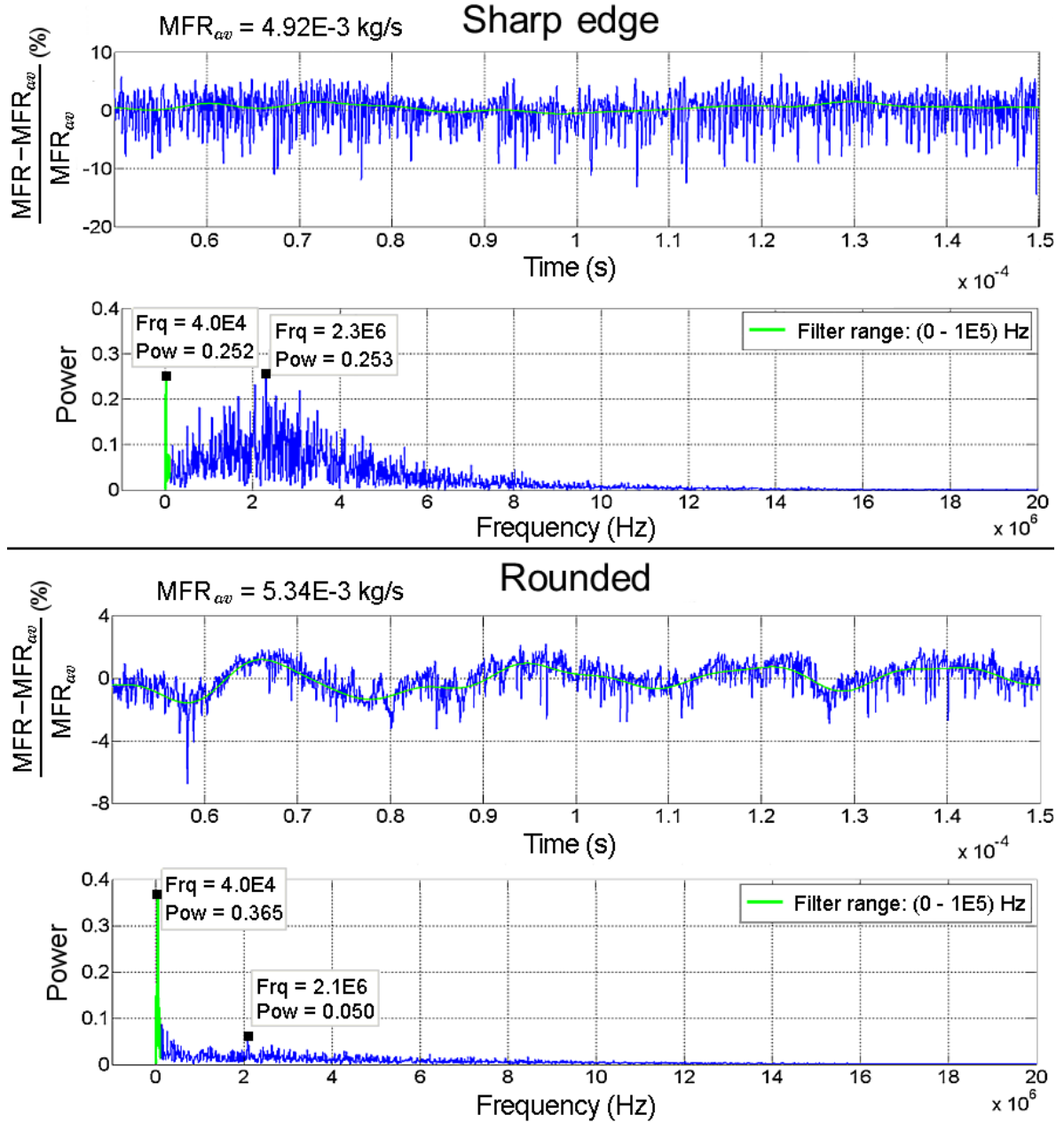


**Figure 6.11:** Temporal evolution of mass flow rate at the hole outlet and corresponding power spectrum. The inverse FFT of the the low-pass filtered spectrum below 100 kHz is plotted in green



### 6.3 Hole inlet rounding effect

#### 6.3.1.1 High frequency event

Inspection of instantaneous vapor volume fraction and velocity fields can help identify the cause of the high frequency event. Figure 6.12 shows time evolution of mass flow rate at the Sharp edge nozzle outlet along with instantaneous vapor and velocity color iso-levels at four different times  $t_1 - t_4$  separated by  $T/2$  seconds, where  $T$  is the period corresponding to the frequency with maximum power in Figure 6.11

$$T = \frac{1}{2.3 \cdot 10^6 \text{ Hz}} = 0.00435 \cdot 10^{-4} \text{ s}$$

At  $t_1$ , the results show a trough in MFR caused by intense cavitation and relatively low velocity at the hole outlet triggered by the shed vortex. At  $t_2$ , the shed vortex has exited the domain and the next one still has not reached the outlet, yielding low vapor, high velocity and a peak in MFR. The next vortex passes through the outlet at  $t_3$ , again leading to a drop in MFR. In this case, it is a bit weaker than at  $t_1$ , leading to less cavitation and slightly higher MFR. Finally, at  $t_4$  no shed vortex is passing through the outlet and MFR increases again. In view of these results, it can be concluded that the high frequency event is driven by the shed vortices. The amplitude of MFR oscillations depends also on the cavitation generated by the string vortices, which fed the upper side with large amounts of vapor.

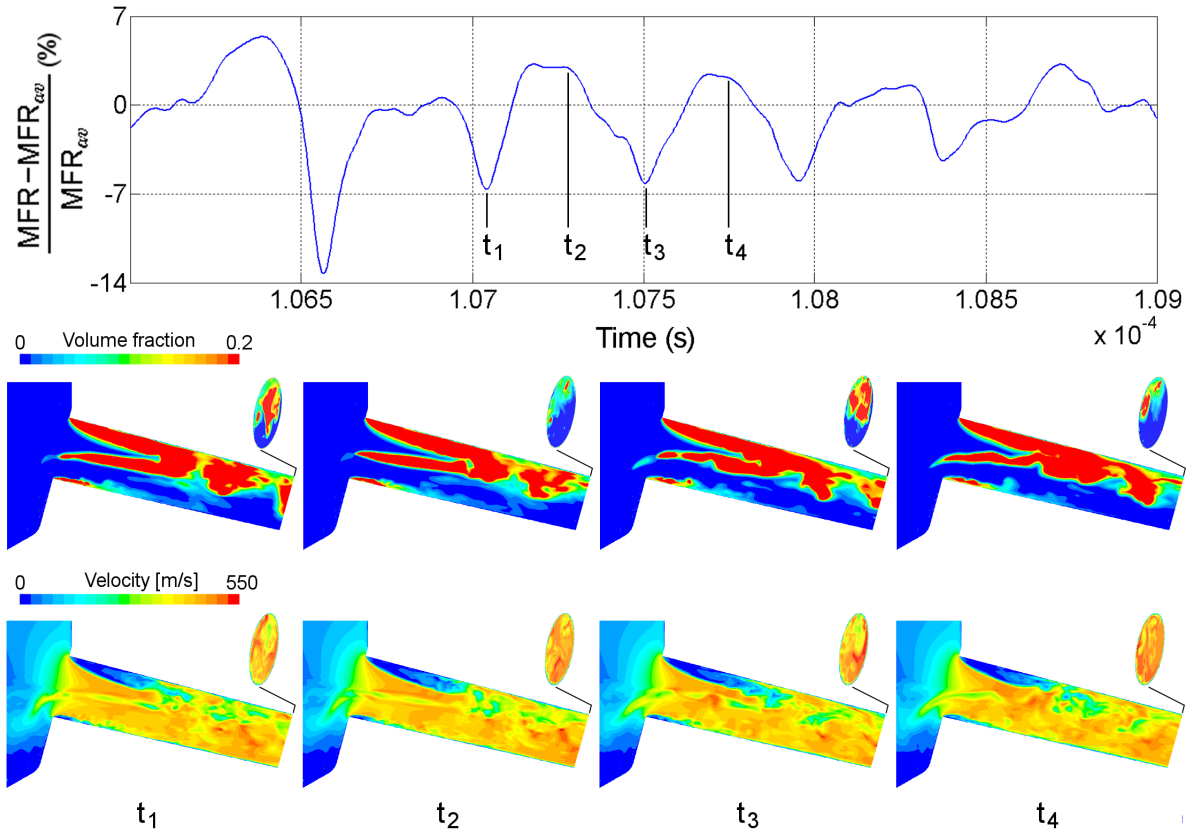


**Figure 6.12:** Mass flow rate (MFR) at the Sharp edge nozzle outlet (top), instantaneous vapor volume fraction and velocity color iso-levels in the mid-cut plane and at the hole outlet (bottom)

The reason why the high frequency event is more important in the Sharp edge nozzle is explained using Figure 6.13. Increased flow turning causes strong shed vortices and cavitation

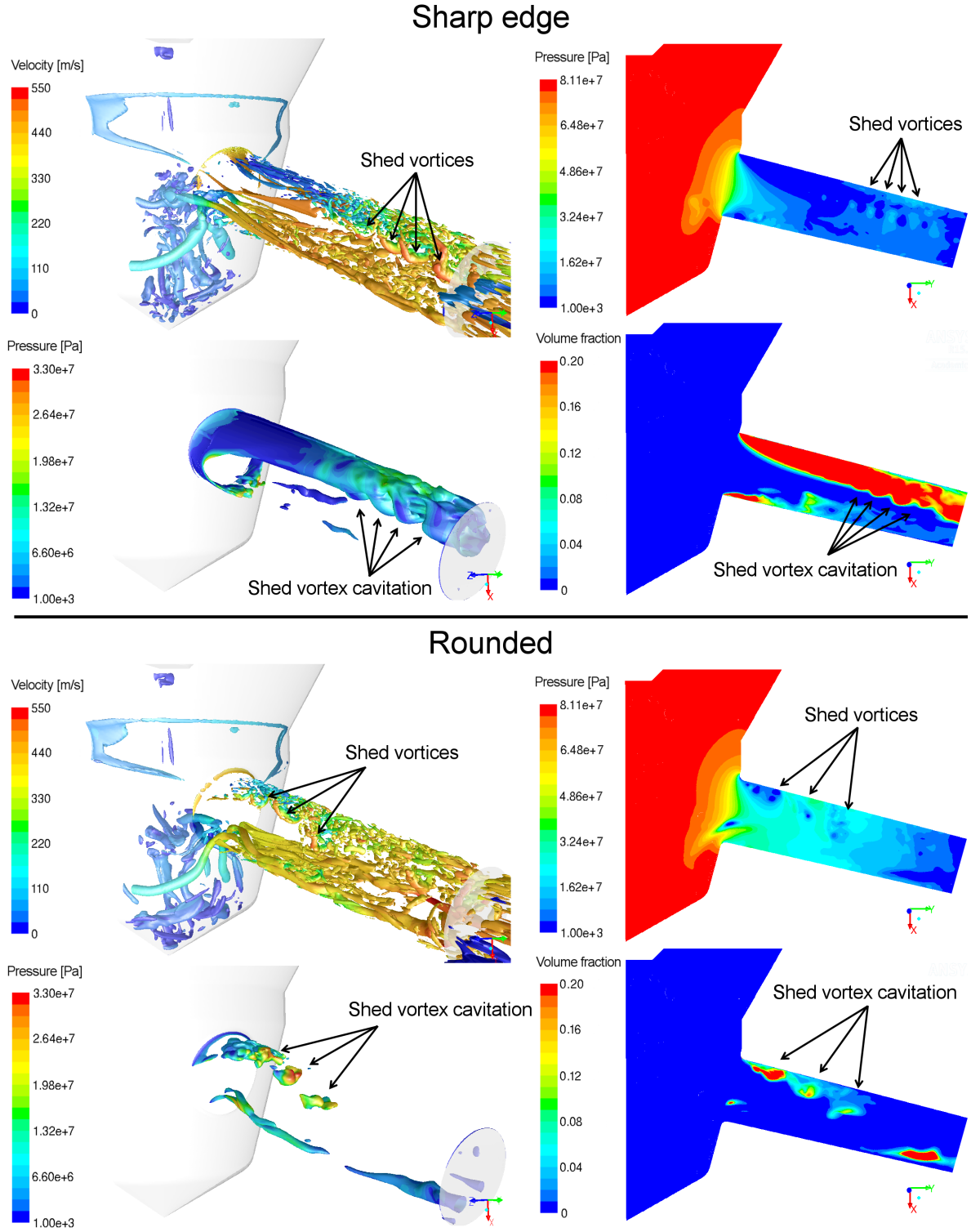


**Figure 6.13:** For each nozzle, from top to bottom and from left to right: Normalized Q-criterion iso-surfaces of value 0.2; vapor volume fraction iso-surfaces of value 0.1; static pressure on the mid-cut plane; vapor volume fraction on the mid-cut plane

in the second half of the hole. Q-criterion iso-surfaces capture these vortices as horseshoe-like structures lying in the shear layer between the high-velocity stream at the bottom and the low-velocity flow near the upper wall. As suggested by volume fraction iso-surfaces, the resulting vortex street generates large cavitation pockets leaving the nozzle intermittently. The

### 6.3 Hole inlet rounding effect

---

fluctuation between high pressure pockets with small amount of cavitation and low pressure pockets with more cavitation is also captured by pressure and volume fraction color iso-levels. Relatively small distance between the onset of shed vortices and the nozzle outlet impedes their dissipation to a large extent. Consequently, they preserve most of their energy until the nozzle outlet, leading to an intense high frequency event.

Cavitation onset and intensity are very different in the Rounded nozzle. As opposed to the Sharp edge nozzle, shed vortices form at the upper hole inlet edge and dissipate towards the middle of the hole owing to the interaction with the stream of negligible vorticity entering directly from the seat. Pressure and vapor color iso-levels evidence this behavior, showing pressure increase and cavitation collapse in the vortex core as it travels downstream. This is confirmed by vapor volume fraction and Q-criterion iso-surfaces, which capture the three-dimensional structure of cavitation pockets associated with shed vortices. As can be observed, the third vortex indicated (farthest from the hole inlet) is already breaking down into smaller scales unable to induce cavitation further downstream. As a consequence, the amount of vapor at the hole outlet is small and the high frequency event is weak.

#### 6.3.1.2 Low frequency event

Vortex dynamics governing the low frequency event are identified in Figure 6.14 using six different instantaneous fields of Q-criterion and volume fraction iso-surfaces. A simplified description of this phenomenon observed in the Rounded nozzle is presented, each instant  $t_1$  to  $t_6$  illustrating different changes in vortex structures and cavitation. Although the low frequency event also happens in the Sharp edge nozzle, it is much less evident than in the Rounded nozzle, as inferred from Figure 6.11.

The main parameters affecting the low frequency event are the distance from the string vortices to the lower hole inlet edge and their orientation at the hole entrance. At  $t_1$  they enter the hole close to the lower edge aligned with the bottom wall. In this stage the interaction with the lower edge is strong and they break down within the first half of the hole, yielding negligible cavitation and a homogeneous distribution of smaller scales at the outlet. The absence of cavitation leads to a maximum in relative MFR. At  $t_2$  the string vortices move up, away from the lower edge, and exit the sac approximately from the center of the hole inlet oriented towards the upper wall. In this case, they penetrate the upper shear layer and travel along the wall till the outlet. As a result, relative MFR decreases not only because of cavitation but also because of effective energy transfer between axial and non-axial kinetic energy caused by the string vortices. At  $t_3$  they move back near the lower edge but in this case keeping the orientation towards the upper wall. The distortion caused first by the lower shear layer and later by the upper shear layer is sufficient to break them down, yielding a disconnected distribution of weak cavitation along the string. MFR increases but not as much as in  $t_1$ , where the strings are broken closer to the inlet. At  $t_4$  they move up again but in this case steeper than at  $t_2$ , impinging onto the upper shear layer closer to the upper hole inlet edge. In this region the shear layer is more intense and weakens them significantly. Although they still reach the nozzle exit, they transport less cavitation than at  $t_2$  and thus yield higher relative MFR. Finally, after  $t_4$  the process repeats:  $t_5$  is analogous to  $t_1$ , showing string vortices close to the lower edge along the wall, and  $t_6$  is analogous to  $t_2$ , where they exit the sac from the center of the hole inlet and reach the outlet relatively unaffected by the upper shear layer.

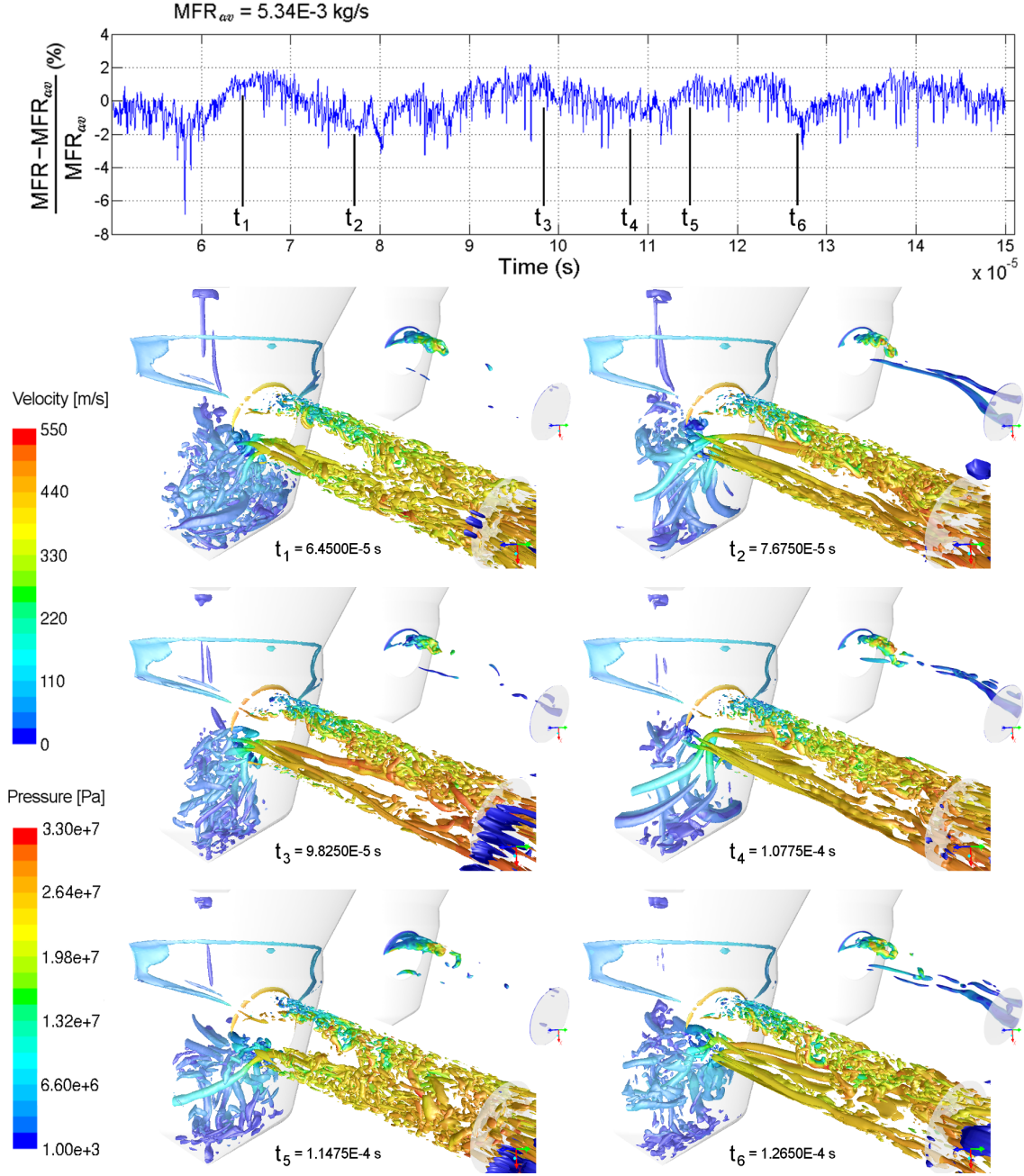


**Figure 6.14:** Low frequency event in the Rounded nozzle. Relative MFR at the hole exit (top). For each time  $t_1 - t_6$  represented: Normalized Q-criterion iso-surfaces colored by velocity (front) and vapor volume fraction iso-surfaces 0.1 colored by pressure (back)

The process described above is a simplified version of the complex dynamics captured by LES. For instance, the string vortices are sometimes distorted by needle or side vortices, causing early breakup even before entering the hole. Other times, string and side vortices combine, enhancing cavitation and non-axial kinetic energy. Notwithstanding these effects, the low frequency event is mainly driven by the string vortices.

### 6.3 Hole inlet rounding effect

---

#### 6.3.2 Correlation between LES of in-nozzle flow and X-ray images of near-nozzle flow

Hole inlet rounding has an important impact on near-nozzle flow. Figure 6.15 shows X-ray visualizations of both Rounded and Sharp edge nozzles at different times after start of injection as well as Q-criterion and vapor iso-surfaces inside the nozzle. Regarding the Sharp edge design, X-ray images show similar interface structures at  $t = 0.56$  ms,  $t = 0.8$  ms and  $t = 0.9$  ms, consisting of pockets of high projected density (dark-gray) interspersed with pockets of lower projected density (light-gray). Near the nozzle these interface structures are relatively isotropic and well distributed across the spray, forming small scales that scatter further downstream driven by aerodynamic effects. The presence of light-gray areas close to the nozzle suggests that either cavitation, ambient air or a mixture of both is being issued to the chamber. A closer look to the first 150  $\mu\text{m}$  reveals that these areas appear mainly on the upper half of the near-nozzle flow, distorting this side to a larger extent. This is a bit more evident at  $t = 0.8$  ms, where light-gray transverse structures develop in that region. Finally, the dispersion angle is relatively constant over time and only at  $t = 0.8$  ms it becomes slightly larger.

Some of the differences in terms of vortex dynamics inside the nozzle can be correlated with the differences observed in X-ray. The most evident of them is the amount of cavitation predicted at the outlet. Whereas many vapor structures exit from the Sharp edge nozzle (times  $t_1$ ,  $t_2$  and  $t_3$ ), less cavitation reaches the outlet in the Rounded nozzle, mostly driven by the string vortex (time  $t'_1$ ). Similarly, X-ray images show homogeneous distribution of small liquid-gas interface structures in the Sharp edge nozzle but localized splitting of large interface structures in the Rounded nozzle. Moreover, small scales predominate on the upper side of the near-nozzle flow in the Sharp edge, which can be correlated with more cavitation transported on the upper side of the hole.

Another similarity is that LES predicts smaller scales on the upper side of the hole in both cases and X-ray shows interface distortion promoted on that side of the jet. In the Rounded nozzle case, however, near-nozzle interface structures are relatively unperturbed at  $t = 0.56$  ms. A possible explanation for this behavior is that the flow is being squashed between the string vortex and the wall subject to centrifugal force, damping non-axial fluctuations away from the string and aligning the streamlines with the hole axis. This agrees with the results shown back in Figure 6.10, where TKE around the walls is very low. Such a flow configuration at the outlet would reduce shear between the ambient air and the liquid surface and therefore interface distortion.

X-ray visualizations included in Figure 6.6 (High lift case) and Figure 6.15 show remarkably unstable dispersion angle in the Rounded nozzle. Unfortunately, the 50kHz sampling frequency used in X-ray measurements provided images every 20 $\mu\text{s}$ , insufficient to confirm if the dispersion angle variation matches the 40kHz frequency of the low frequency event. Hence, it can only be concluded that the structures observed in LES and X-ray behave in the same manner: relatively stable vortices and cavitation inside the Sharp edge nozzle with a stable pattern outside, and unstable vortices and cavitation inside the Rounded nozzle with unstable pattern outside.



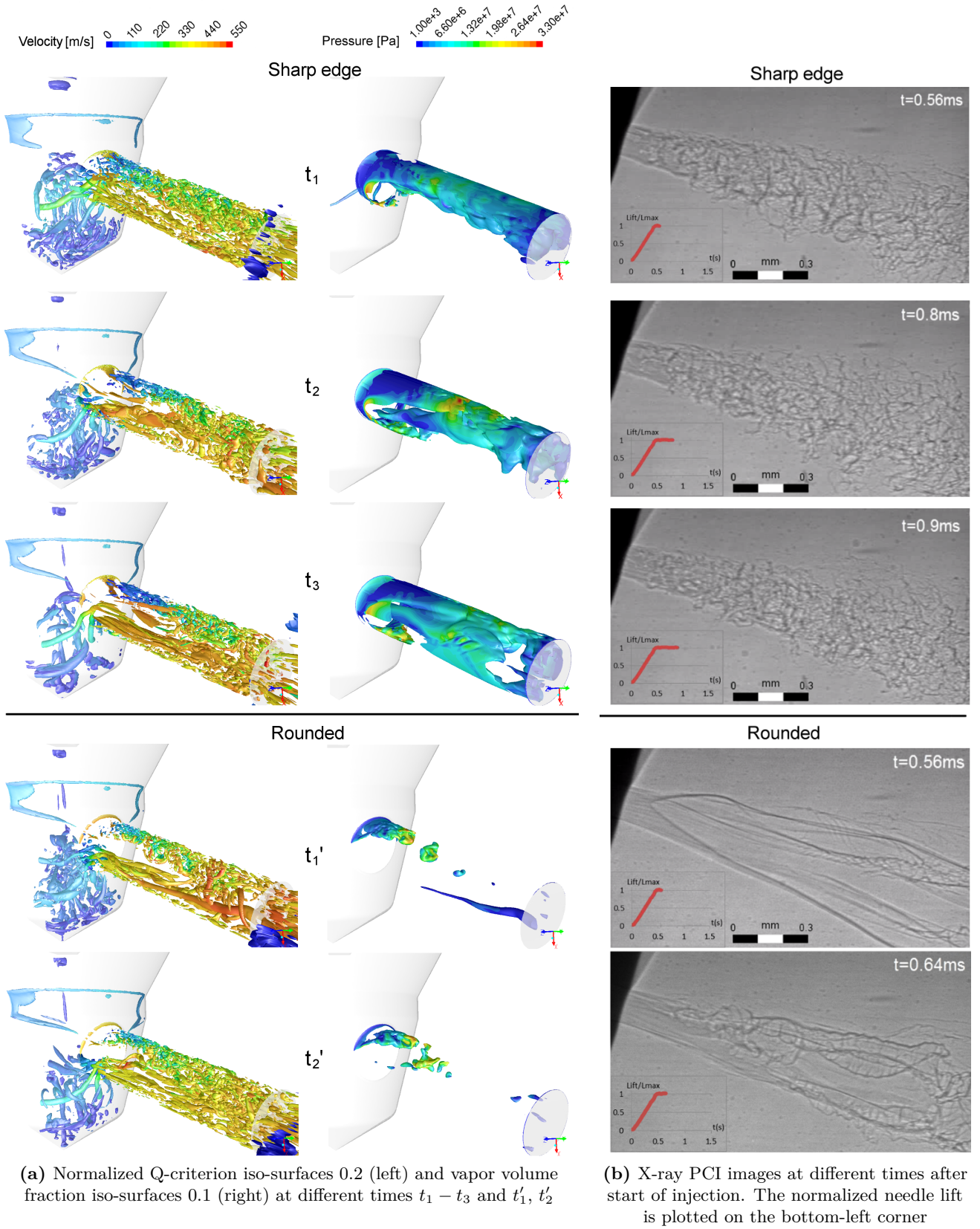


**Figure 6.15:** LES results and X-ray images of Sharp edge and Rounded (Reference) nozzle

### 6.3 Hole inlet rounding effect

Identification of characteristic length scales in the near-nozzle region can be useful to further correlate the high frequency event with X-ray interface structures. To this end, X-ray image processing was conducted as detailed in Section 5.2. The analysis includes 2D FFT and 1D FFT of the Sharp edge nozzle and 1D FFT of the Rounded nozzle. Figure 6.16 shows the gaussian distribution of length scales  $L_{MP}$  given in equation 5.3 obtained with the frequencies of maximum power of each X-ray image. As can be seen, 2D FFT and 1D FFT yield very similar mean values 76-77  $\mu\text{m}$  in the Sharp edge nozzle, meaning that both methods predict a dominant length scale of the order of one half of the nozzle diameter. The smaller variance featured by the 1D FFT is linked to the selectivity associated with this method. As far as the Rounded nozzle is concerned, the maximum shifts towards larger length scales and the variance increases, partly because of spray anisotropy and strong spray angle variation. For this reason, these results are less accurate than the Sharp edge nozzle results and therefore less significant.

The characteristic length scale of shed vortices predicted in LES can be estimated by tracking low pressure pockets at the hole exit. The resulting average length scales are 65  $\mu\text{m}$  in the Sharp edge nozzle and 84  $\mu\text{m}$  in the Rounded nozzle. Table 6.1 compares these magnitudes with the characteristic length scales obtained from X-ray image processing. Although LES predicts smaller scales, around 15% in the Sharp edge nozzle and 7% in the Rounded nozzle, both follow the same trend: characteristic length scales increase with hole inlet rounding.

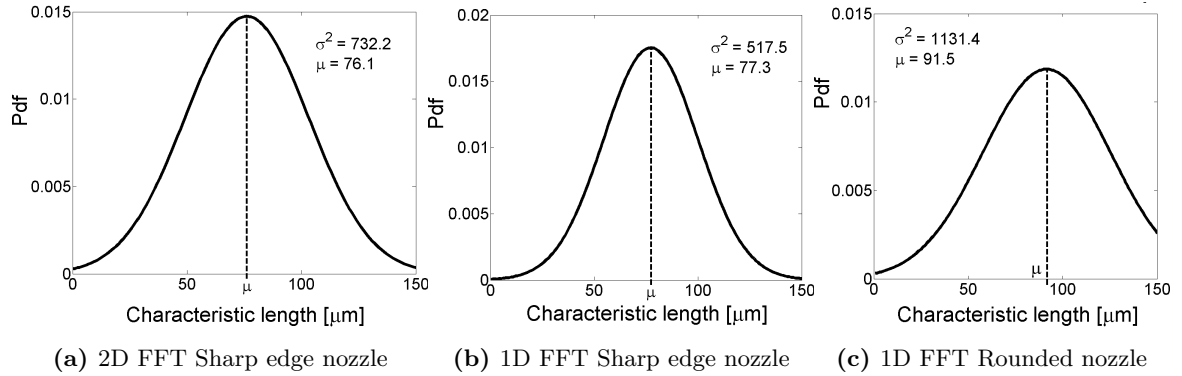


**Figure 6.16:** Gaussian distribution of characteristic length scales

	X-ray image processing		LES
	2D FFT	1D FFT	
Sharp edge	76.1 $\mu\text{m}$	77.3 $\mu\text{m}$	65 $\mu\text{m}$
Rounded	-	91.5 $\mu\text{m}$	84 $\mu\text{m}$

**Table 6.1:** Comparison between shed vortex length scale (LES) and interface structure length scale (X-ray)

Figure 6.17 illustrates qualitatively the characteristic length scales using pressure and vapor color iso-levels and close-up views of near-nozzle flow. Whereas the scales can be easily identified based upon the distance between low pressure pockets, X-ray images are much more difficult to interpret. Notwithstanding, there are two particular images in the Sharp edge nozzle, namely at  $t = 0.64$  ms and  $t = 0.86$  ms, where it is possible to see relatively

equispaced structures (in dark gray) transverse to the spray exiting the nozzle from the upper side. At  $t = 0.84$  ms and  $t = 1.02$  ms they are not clear, particularly at  $t = 1.02$  ms where a rather isotropic distribution is already developing very close to the outlet. As far as the Rounded nozzle is concerned, the characteristic length scale can be identified on the lower side at  $t = 0.84$  ms and at  $t = 0.9$  ms but not at  $t = 1$  ms. At  $t = 0.86$  ms there is also a regular distribution of small, transverse scales connecting split interfaces of dark gray color. These structures appear closer to the nozzle than in the other cases, particularly on the upper side of the jet.

Overall, although aerodynamic forces are likely to affect the characteristic length scales, it is reasonable to assume that the onset of coherent perturbations occurs inside the nozzle, especially in view of Figure 6.17 where the periodic structures appear within 2-3 nozzle diameters from the outlet in all the cases.

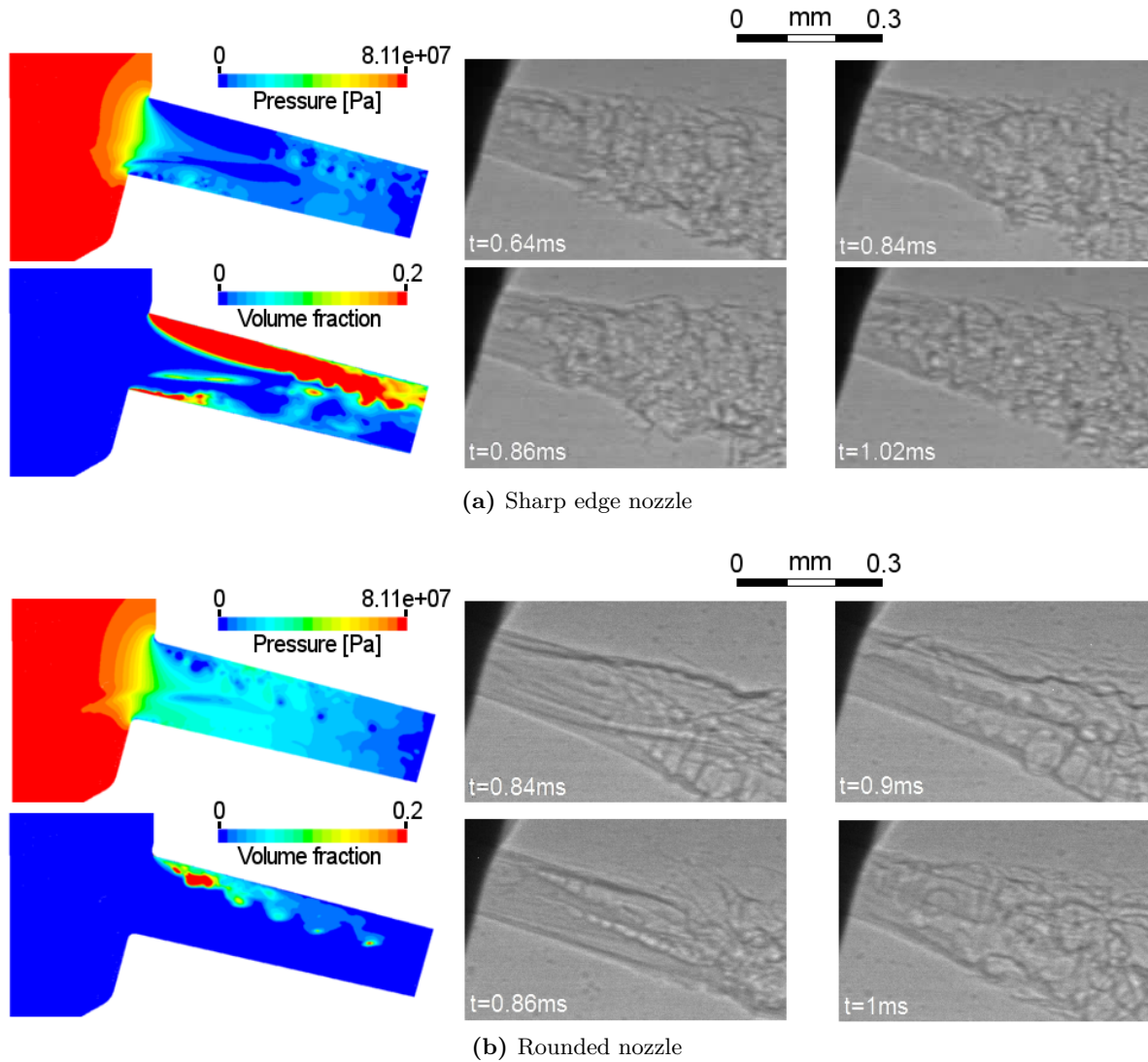


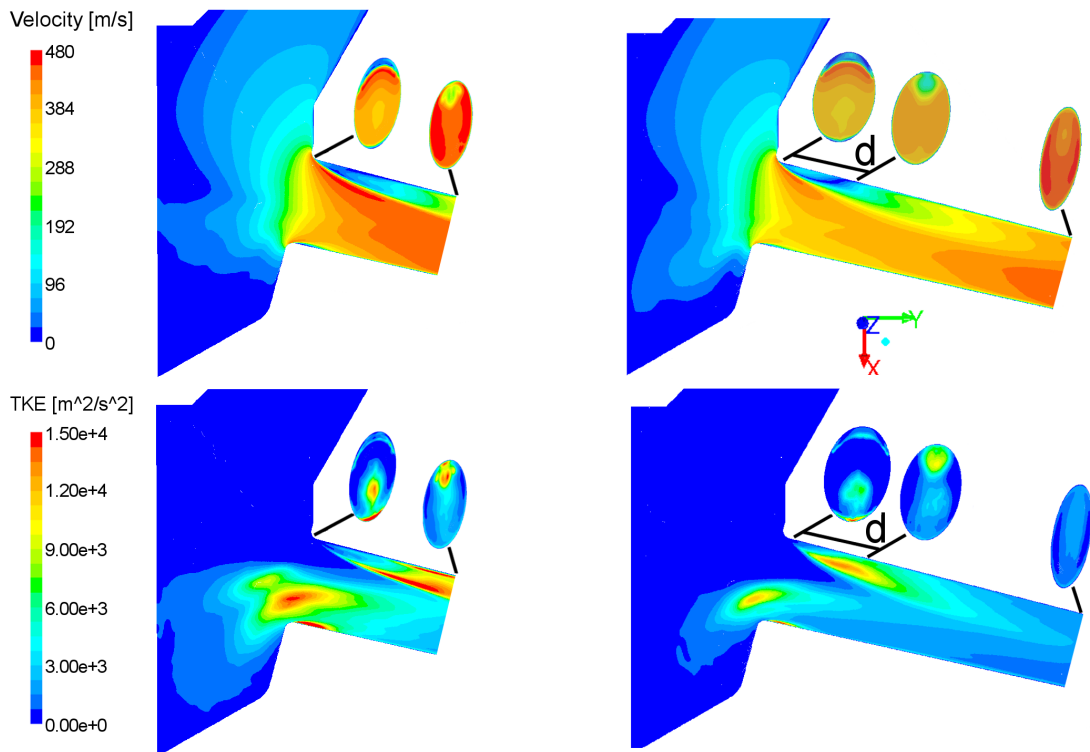
**Figure 6.17:** Proposed correlation between shed vortices and X-ray interface structures. Pressure and volume fraction color iso-levels (left); close-up view of near-nozzle X-ray at different times after start of injection (middle and right)



## 6.4 Hole length effect

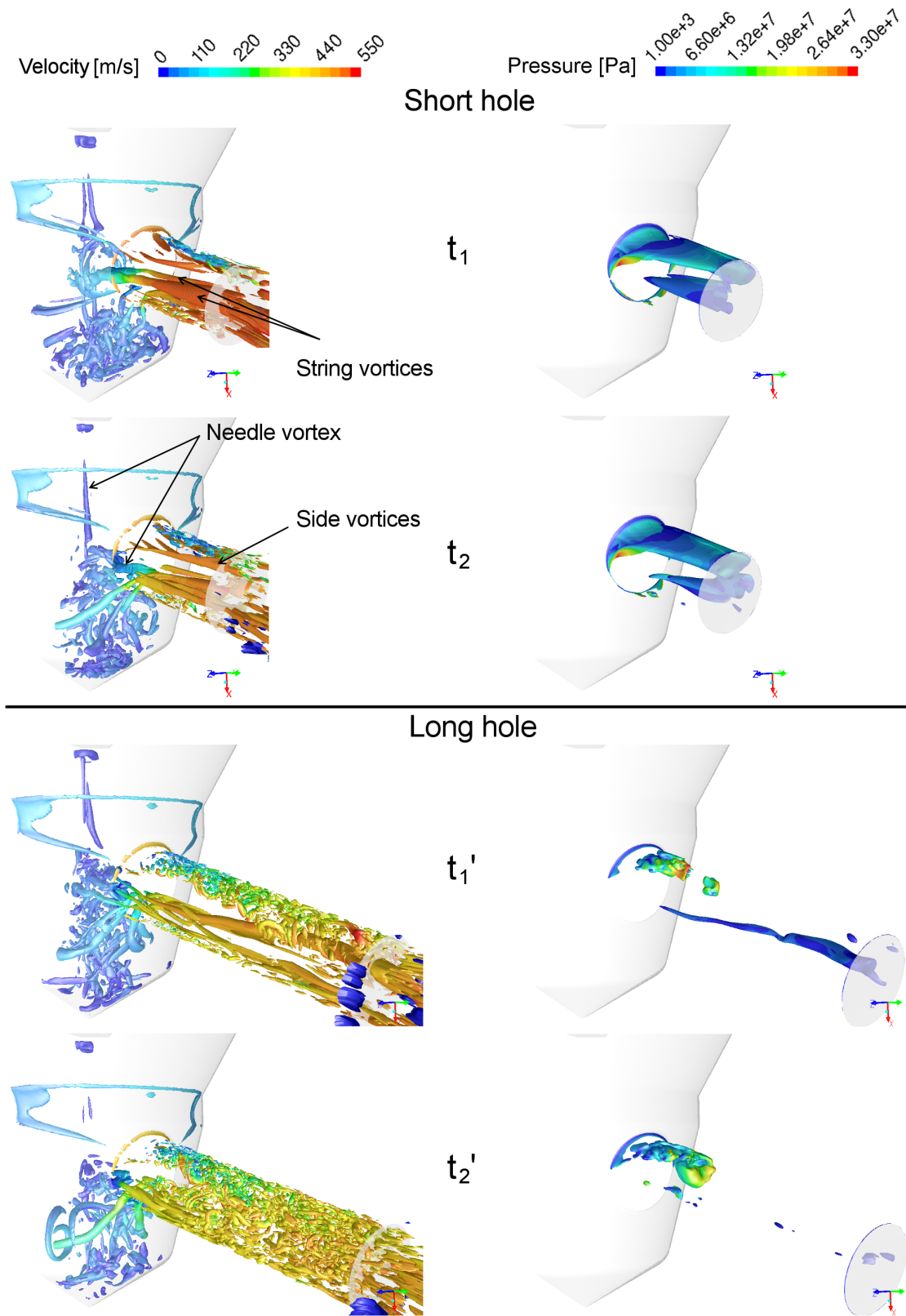
Hole length effect is assessed by comparing the Long hole nozzle (Reference nozzle) with the Short hole nozzle, which has the same geometry but one half of the hole length (600  $\mu\text{m}$  vs 300  $\mu\text{m}$ ). Since the hole taper (conicity) is fixed, the outlet diameter increases from 150  $\mu\text{m}$  to 160  $\mu\text{m}$ , hindering the comparison of integral quantities such as mass flow rate, discharge coefficient or total amount of vapor. Nevertheless, other features such as vortex and cavitation dynamics, velocity distribution and turbulence generation are comparable.

Figure 6.18 shows how smaller hole length increases the average velocity inside the nozzle due to stronger flow acceleration at the hole inlet. Flow separation reaches the outlet, reducing the effective area and increasing the velocity gradient along the vena contracta. Although resolved TKE generation is very intense in the upper mixing layer close to the outlet, it is insufficient to induce reattachment of the high-speed flow. This is partly due to the fact that the mixing layer is shifted towards the outlet with shorter hole, delaying the production of turbulence that contributes to the reattachment. Another consequence of stronger acceleration at the hole inlet is that the centrifugal force exerted on the turning flow increases, and so does the amount of fluid diverted into the sac. The resulting string vortices are more intense and produce more TKE. Finally, the side vortices trigger a third region of high TKE above the string vortices in the Short hole nozzle.



**Figure 6.18:** Average velocity (top) and resolved TKE (bottom) on the mid-cut plane ( $z=0$ ). Short hole nozzle (left); Long hole nozzle (right). Cross-sectional distributions are shown at the hole inlet and at the outlet

As shown in Figure 6.19, decreasing the hole length also has an important impact on the temporal evolution of vortex and cavitation structures. Transition between large and small



**Figure 6.19:** Comparison between Short hole and Long hole (Reference) nozzle results at different instants  $t_1$ ,  $t_2$  and  $t'_1$ ,  $t'_2$ . Instantaneous normalized Q-criterion iso-surfaces of value 0.2 colored by velocity (left); vapor volume fraction iso-surfaces of value 0.1 colored by static pressure (right)

## 6.4 Hole length effect

scales observed in the Long hole nozzle is replaced by the constant presence of large scales generating inside the sac and surviving to the hole exit in the Short hole nozzle. In particular, the string vortices, the needle vortex and the side vortices do not break down. Additionally, the amount of small scales emerging on the upper side of the hole is significantly reduced owing to weaker shear layer and TKE generation near the upper hole inlet rounding. As it has been shown in Figure 6.18, TKE is higher further downstream but not near the inlet where small scales form.

Vapor iso-surfaces highlight two cavitation strings developing below the separation region. This configuration is very stable and is subject to small changes over time, leading to well-defined cavitation structures on the upper side and inside the string vortices at the end of the hole. Figure 6.20 illustrates this by showing instantaneous vapor volume fraction and instantaneous TKE color iso-levels at the hole outlet. While only one cavitation string reaches the outlet in the Long hole nozzle, two relatively symmetric cavitation strings reach it in the Short hole nozzle in addition to cavitation induced by flow separation. Similarly, TKE is more intense in the Short hole nozzle, especially in the area between the string vortices and the upper shear layer. It is also noteworthy that cavitation and TKE are very low away from the string vortices and from the upper shear layer. As in the Long hole nozzle, this is linked to turbulence decay caused by centrifugal forces squashing the flow against the walls.

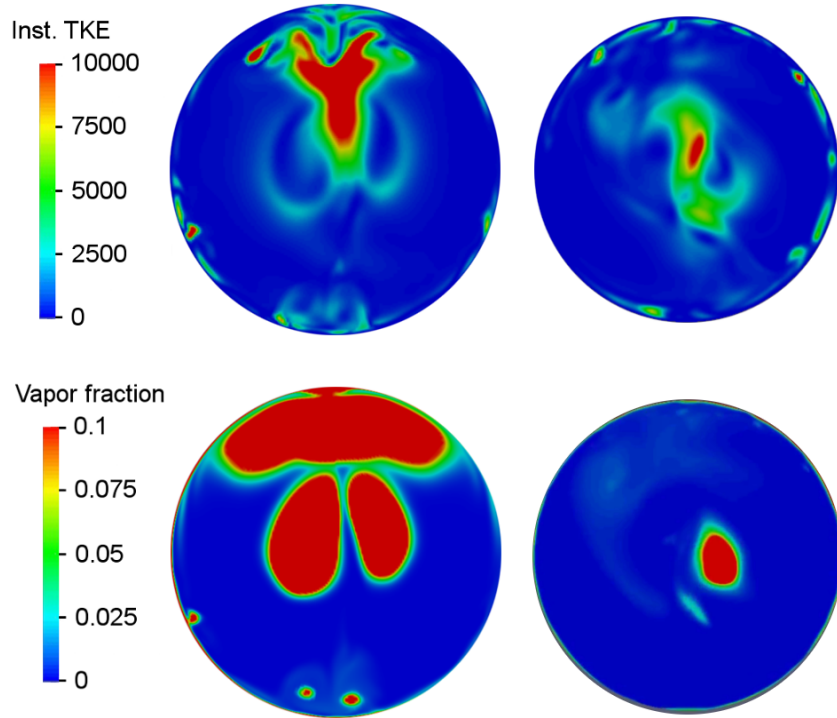


**Figure 6.20:** Instantaneous resolved turbulent kinetic energy in  $m^2/s^2$  (top) and vapor volume fraction (bottom) at the hole exit. Short hole nozzle (left); Long hole nozzle (right)

The link between vortex dynamics and dominant frequencies arising when shortening the nozzle hole can be assessed using the temporal evolution of mass flow rate at the Short hole nozzle outlet. Figure 6.21 plots this variable along with its corresponding FFT. Four different instants  $t_1 - t_4$  are selected to explain the link between MFR and vortex structures using Q-criterion and vapor iso-surfaces for each case. The power spectrum highlights a dominant

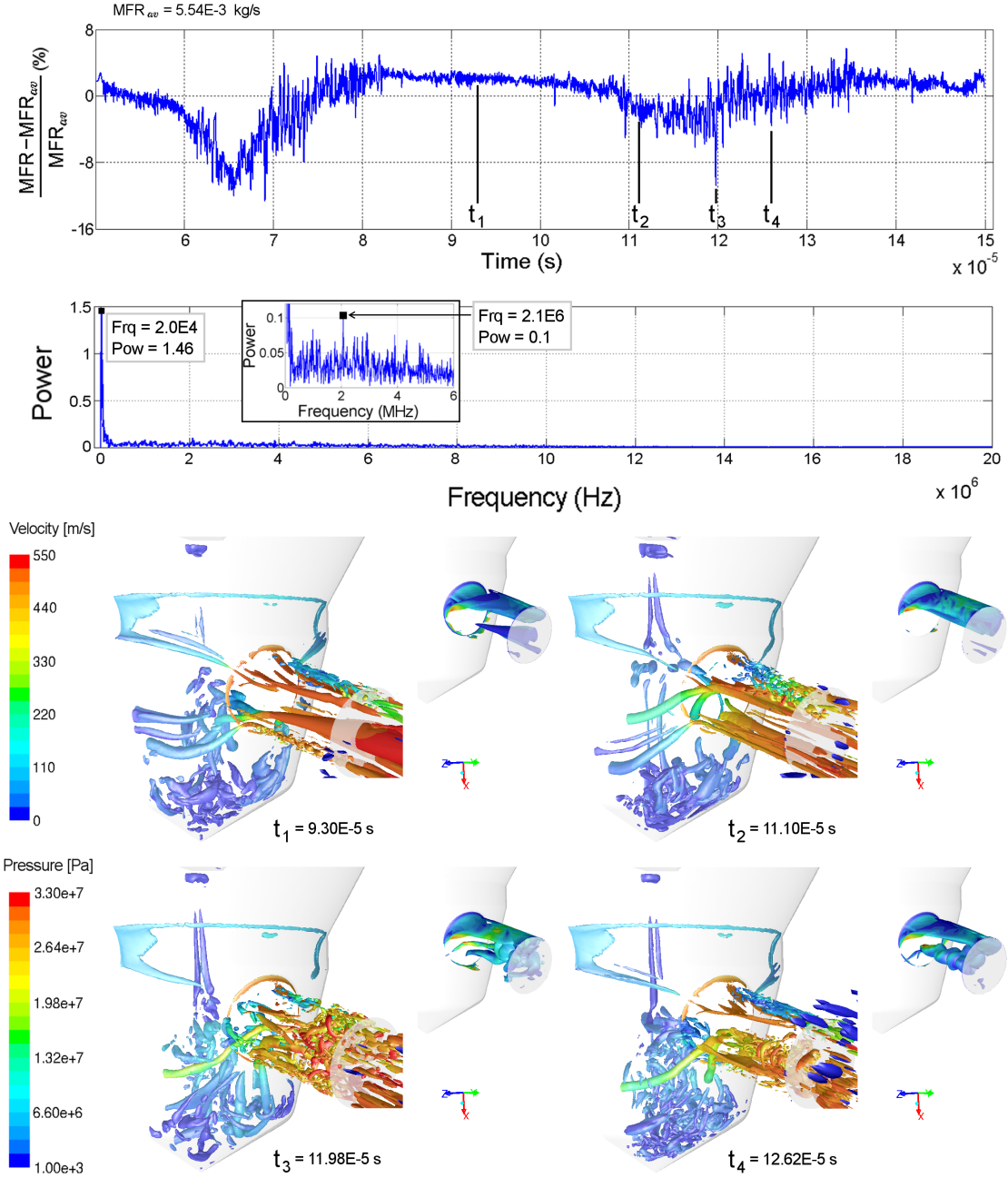


**Figure 6.21:** From top to bottom: Mass flow rate (MFR); power spectrum showing a close-up view of the frequency interval 0-6 MHz; normalized Q-criterion iso-surfaces of value 0.2 colored by velocity (front) and vapor volume fraction iso-surfaces of value 0.1 colored by pressure (back)

frequency 20 kHz peaking at 1.46. This frequency is associated with the long period oscillation observed in MFR with minima at 65  $\mu$ s and 120  $\mu$ s. At  $t_1$ , MFR is high and fairly constant, corresponding to a stable configuration where the string vortices exit the nozzle from the center of the hole and do not interact with the upper shear layer. Cavitation is comparably low and is localized on the upper side and in the string vortex core. At  $t_2$  the string vortices have moved upwards close to the upper hole inlet edge, allowing other vortices to enter the hole from the lower side. Although the string vortices are located right under the shear layer they do not break down, feeding the upper side with more cavitation. They grow over time, increasing flow instability and the amount of vapor at the outlet until they eventually

## 6.4 Hole length effect

---

collide with the shear layer (time  $t_3$ ). At this point, the strings break down and trigger a very short event consisting of small scales scattering large amounts of vapor over the outlet. Subsequently, at  $t_4$  the string vortices move downwards and start a reconstruction process where small scales are slowly transformed into large scales. Finally, the strings stabilize in the center of the hole as in  $t_1$  and the process repeats.

The power spectrum draws attention to the fact that the frequency associated with the low frequency event (20 kHz) in the Short hole nozzle is half of the frequency observed in the Long hole nozzle (40 kHz, Rounded nozzle case in Figure 6.11). Despite not knowing whether this direct relation between hole length and frequency holds for other lengths, as the results cannot be compared with other nozzles studied, the analysis clearly suggests that the low frequency decreases with hole length. Regarding the high frequency event driven by shed vortices, hole length affects its power but not its frequency. As shown in the close-up view included in Figure 6.21, there is a locally dominant frequency at 2.1 MHz, which is the same as in the Long hole nozzle (see Rounded nozzle case in Figure 6.11). This means that while the contribution of shed vortices to MFR oscillations decreases with hole length, this parameter does not alter the shedding frequency. These oscillations are particularly small in the range 85  $\mu$ s - 100  $\mu$ s due to the stable configuration depicted at  $t_1$ . In this state, shed vortices do not induce pockets of vapor disconnected from the flow separation region but a wave-like deformation of volume fraction iso-surfaces close to the outlet. When the interaction shed vortex - string vortex intensifies between 110  $\mu$ s and 140  $\mu$ s, the shear layer becomes more unstable and the amplitude of high frequency oscillations grows.

The leading role of string vortices and their impact on flow structures at the outlet are further supported by POD results. For each nozzle, Figure 6.22 compares Mode 0, Mode 1, Mode 2 and Mode 20 at the hole exit using streamlines of normalized in-plane velocities, and Figure 6.23 plots modal energy and accumulated energy for modes 0 - 20. Mode 0 shows the string vortices on the lower half of the hole in both nozzles. However, these structures contain as much as 33% of the energy in the Short hole nozzle and only 23% in the Long hole nozzle (summing the contributions of string vortices in Mode 0 and Mode 1), confirming their increasing importance with shorter hole. Mode 0 also shows the side vortices near the upper wall in the Short hole but not in the Long hole nozzle, where they generally break down into smaller structures as shown before in Figure 6.19.

Modal energy decreases significantly from Mode 0 to Mode 1, which accounts for 11% of the energy in the Short hole nozzle. Mode 1 features an intense clockwise rotating vortex at the top, which is analogous to the central vortex predicted in Mode 2 of the Long hole nozzle. As in the latter, it is due to the helical motion of the upper shear layer (“horseshoe” vortex detached from the upper hole inlet rounding). The reason why it is much smaller is that it is driven by the upper shear layer, which in the Short hole nozzle is restricted to the upper side but in the Long hole nozzle grows and moves downwards along the hole. Regarding Mode 2, the Short hole nozzle exhibits two big counter-rotating vortices analogous to the upper vortices predicted in Mode 1 of the Long hole nozzle. They are partly caused by side vortices and partly by weak structures eventually generated above the string vortices when these are close to the lower wall.

Finally, Mode 20 shows that scales down to  $\sim 25$   $\mu$ m contain 83% of the energy in the Short hole nozzle, a 12% more than for the Long hole nozzle. Hence, scales below  $\sim 25$   $\mu$ m account



for less energy, suggesting that large scales become more important with shorter hole.

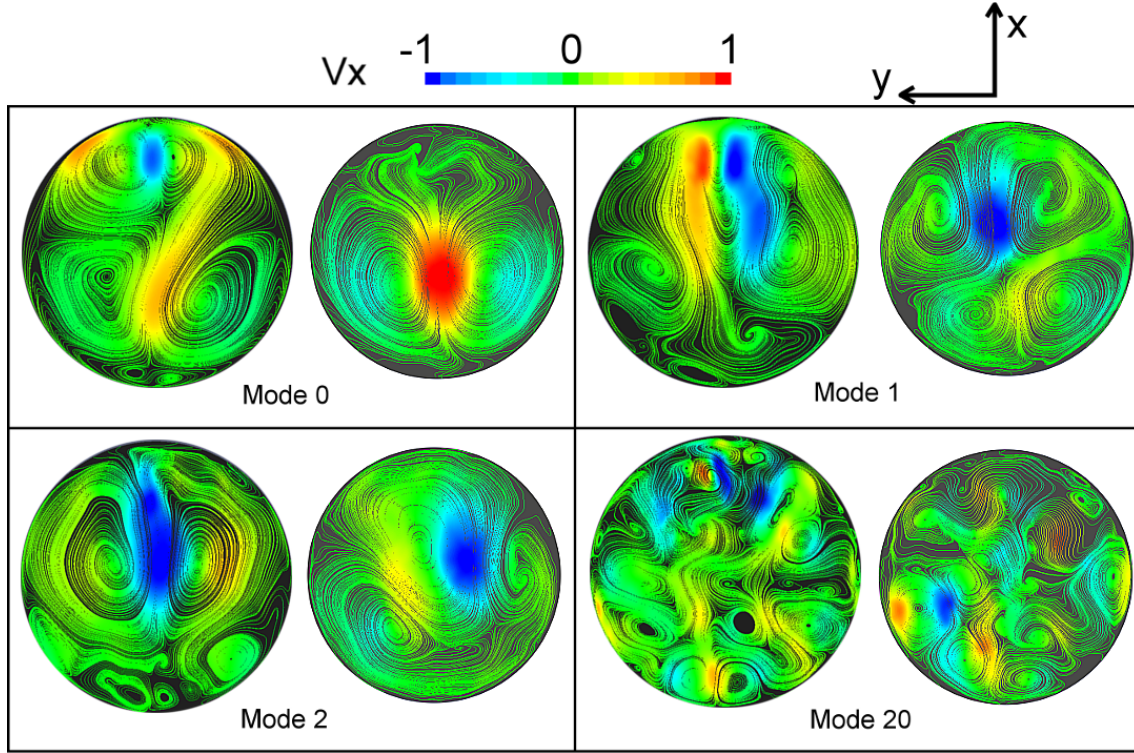


**Figure 6.22:** POD modes based on in-plane velocities at the hole outlet. Streamlines colored by vertical velocity  $V_x$  normalized by the maximum value. For each pair: Short hole (left); Long hole (right)

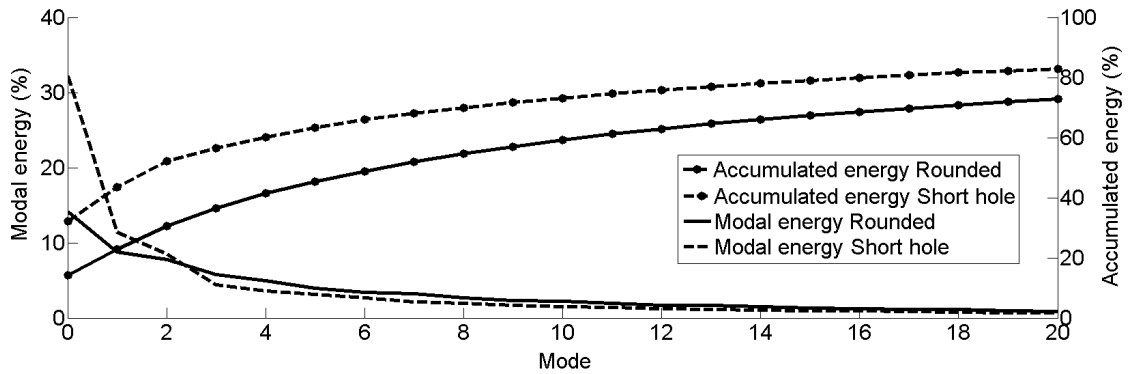


**Figure 6.23:** POD modal energy and accumulated energy comparing the hole length effect

## 6.5 Hole number effect

Hole number effect is assessed by comparing the 3-Hole nozzle (Reference nozzle) with the 6-Hole nozzle. Increasing the number of holes while keeping constant hole inlet diameter reduces the size of the sac compared to the hole. As shown in Figure 6.24, the main consequence of this configuration is that most of the flow moves from the seat directly into the hole instead of recirculating in the sac. In the 3-Hole nozzle, approximately half of the hole inlet is occupied by streamlines coming from the seat and the other half by streamlines coming

## 6.5 Hole number effect

from the sac. In the 6-Hole nozzle, only 1/4 of the hole inlet is occupied by streamlines coming from the sac. In this case, more flow starts accelerating further upstream before turning into the hole, causing more separation. Notwithstanding, reattachment is still possible before the outlet due to intense turbulence generation, as suggested by TKE color iso-levels. The effect of string vortices on TKE is opposite: TKE decreases with 6 holes and the string moves close to the lower hole inlet edge squashed by the large amount of flow coming from the seat. The resulting distribution of turbulence involves an area of very low TKE developing in the center of the hole up to 1/2 of the hole length followed by an area where the upper shear layer and the flow coming from the sac mix.

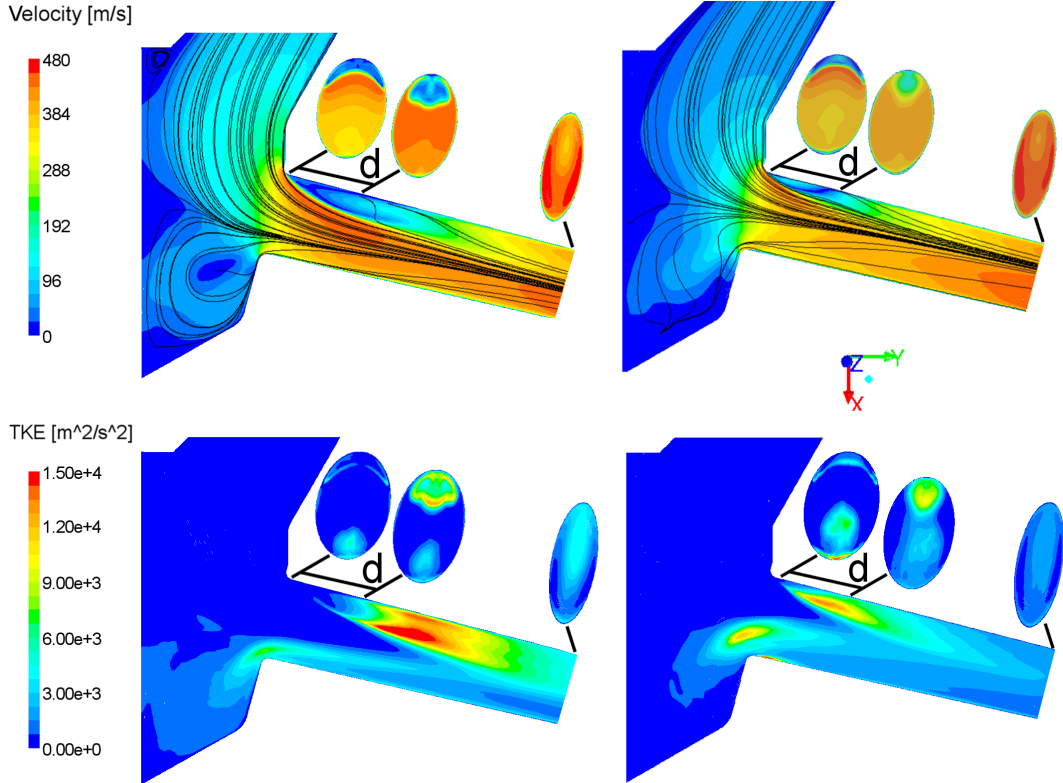


**Figure 6.24:** Average velocity and streamlines (top) and resolved TKE (bottom) on the mid-cut plane ( $z=0$ ). 6-Hole nozzle (left); 3-Hole nozzle (right). Cross-sectional distributions are shown at the hole inlet,  $d = 150 \mu\text{m}$  and outlet.

Figure 6.25 suggests that vortex and cavitation structures are largely affected by the number of holes, showing enhanced shed vortices and weakened string vortices in the 6-Hole nozzle. There are three different regions along the hole; the upper region, including the shear layer, shed vortices and small, isotropic vortices; the middle region, occupied by a stream of negligible vorticity; and the lower region, where large, anisotropic structures propagate along the bottom wall. Shed vortices developing on the upper side are dominant, growing and moving toward the center of the hole as they travel downstream. These vortices comprise not only the horseshoe-like structures observed at  $t_1$  but also the small eddies transported by them. Regardless of whether the horseshoe-like structures preserve their integrity along the hole ( $t_1$ ) or break down into smaller scales ( $t_2$ ), they yield intense cavitation intermittently expelled from the outlet. In fact, vapor volume fraction iso-surfaces indicate that the shed vortices are responsible for most of the vapor at the hole exit. Although large vortices at the

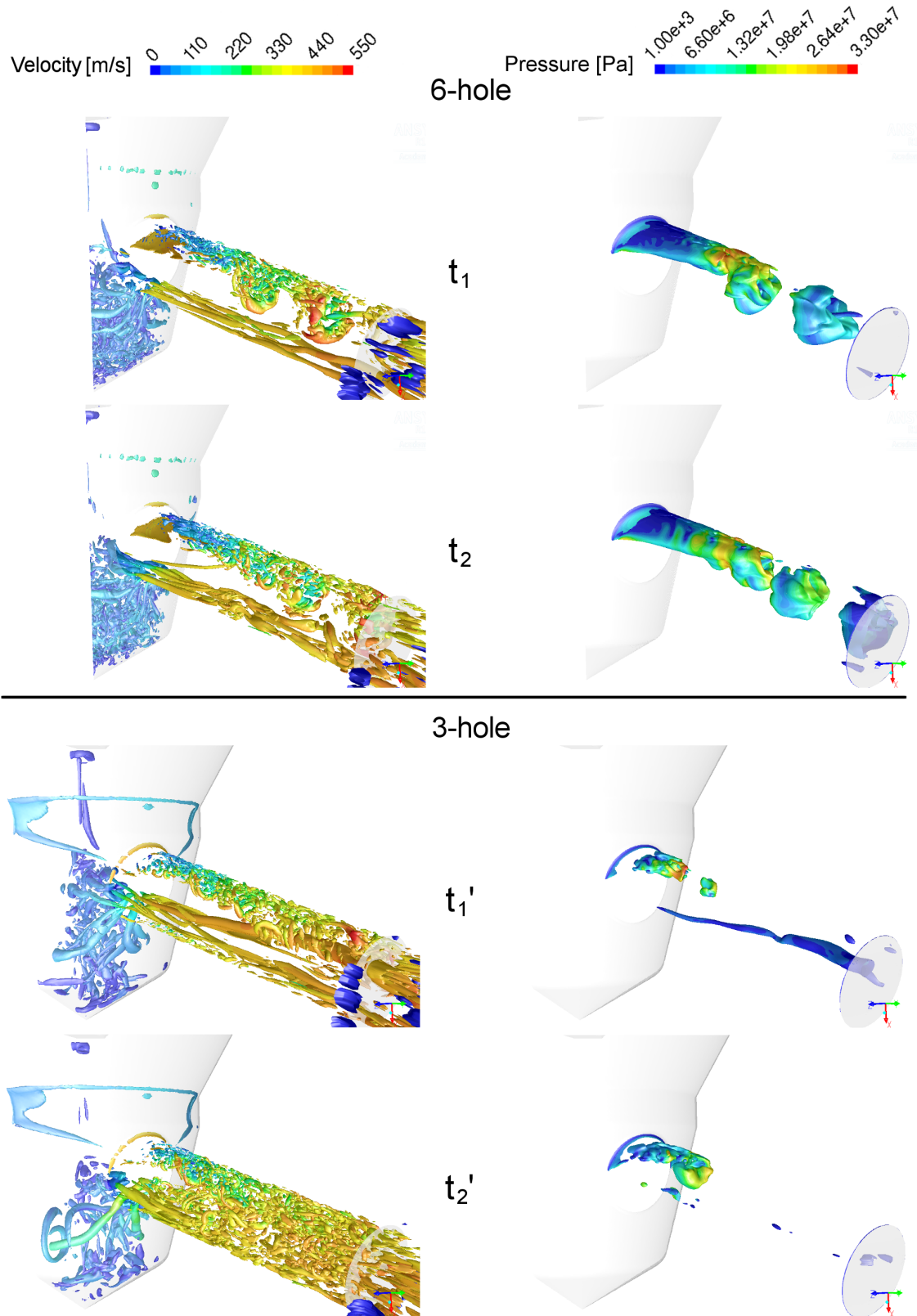


**Figure 6.25:** Comparison between 6-Hole and 3-Hole (Reference) nozzle results at different instants  $t_1$ ,  $t_2$  and  $t'_1$ ,  $t'_2$ . Instantaneous normalized Q-criterion iso-surfaces of value 0.2 colored by velocity (left); vapor volume fraction iso-surfaces of value 0.1 colored by static pressure (right)



## 6.5 Hole number effect

bottom can also trigger cavitation, the amount is small compared to that of the shed vortices.

As sac flow recirculation diminishes in the 6-Hole nozzle, the string vortices weaken and lose capacity to penetrate the high-velocity stream coming from the seat. Moreover, they are pushed down against the bottom wall and remain confined to this region as they travel downstream. Occasionally, the string vortices detach from the bottom wall ( $t_2$ ) but never reach the upper shear layer, at least within the first 3/4 of the hole length. This results in a very stable flow configuration, suppressing low frequency excitation. This is a major difference with respect to the 3-Hole nozzle, where string vortices are responsible for the low frequency event.

As shown in Figure 6.26, temporal evolution of mass flow rate at the outlet of the 6-Hole nozzle evidences on the one hand the importance of the high frequency event associated with shed vortices and on the other hand the suppression of low frequency oscillations caused by the string vortices. Unlike the 3-Hole nozzle, where one high frequency at 2.1 MHz stands above the rest (Figure 6.11), there are three dominant frequencies of very similar power at 1.9 MHz, 2.1 MHz and 2.3 MHz associated with the shedding phenomenon. The reason is that the high frequency event in the 6-Hole nozzle is dominant and the spectrum becomes more sensitive to small deviations of the shedding frequency.

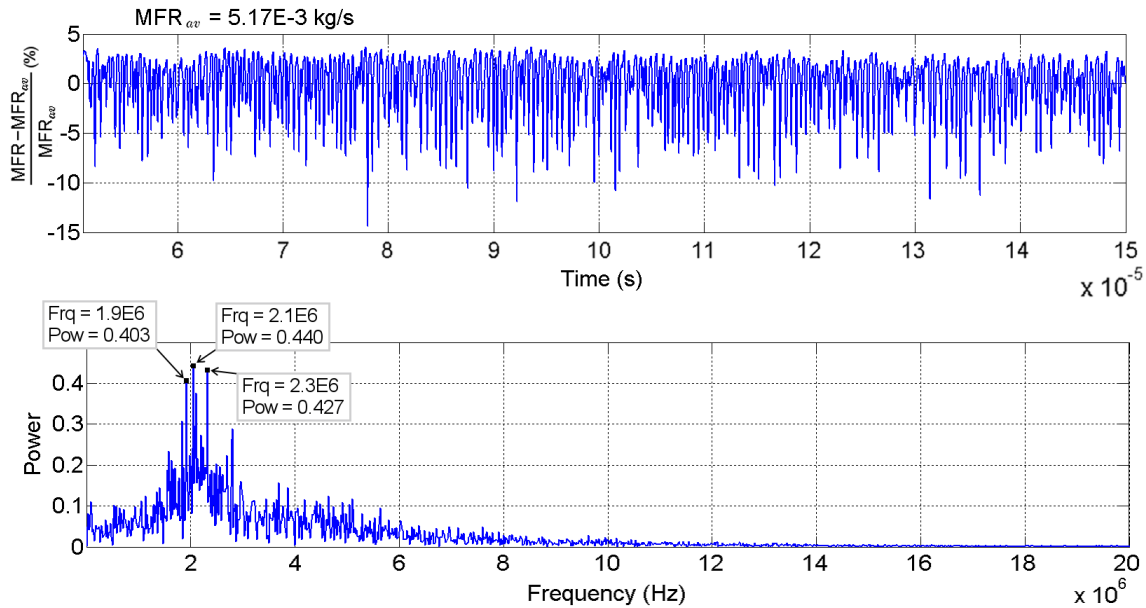


**Figure 6.26:** Mass flow rate at the 6-Hole nozzle outlet (top) and its power spectrum (bottom)

In view of the results, it can be concluded that increasing the number of holes reduces the impact of string vortices, intensifies vortex shedding and, if anything, increases slightly the shedding frequency. Hence, it might seem that production nozzles with 8-12 holes are subject to the effects of high frequency vortices but not to low frequency fluctuations. However, such nozzles typically have smaller holes (i.e inlet diameter  $\sim 100 \mu\text{m}$ ), keeping the sac relatively larger than the hole and enabling sac flow recirculation. Although the present technological trend is towards increasing the number of holes, the effect of string vortices can be significant whenever sac flow recirculation is important.

## 6.6 Hole taper effect

This Section compares the Low taper nozzle (Reference nozzle) with the High taper nozzle (HP hole) described in Figure 5.1 in order to identify the effect of hole taper on the main flow structures. Apart from higher taper attained by decreasing the outlet diameter from  $150\ \mu\text{m}$  to  $120\ \mu\text{m}$ , the hole inlet radius is reduced from  $20\ \mu\text{m}$  to  $5\ \mu\text{m}$  and the hole is moved  $50\ \mu\text{m}$  down to reproduce the production nozzle geometry. The results discussed in this Section were obtained using the two-phase (fuel vapor and fuel liquid) mixture model described in Section 5.3.

Figure 6.27 shows that, whereas the flow is mainly accelerated near the hole inlet of the Low taper nozzle, velocity increases gradually along the hole of the High taper nozzle due to significant reduction of the cross-section area. Even though the High taper nozzle has sharper hole inlet edge, which increases acceleration near the entrance, the velocity gradient in this area is smaller, suggesting that the taper effect is dominant over the hole inlet rounding effect. Lower acceleration at the hole inlet leads to weaker shear layer and turbulence generation on the upper side of the hole. This can be better seen in the cross-sectional distribution of resolved TKE at  $l/d = 1$ , where it hardly exceeds  $3000\ \text{m}^2/\text{s}^2$ . Sac flow recirculation decreases in the High taper nozzle due to weaker centrifugal force exerted on the turning flow. As a consequence, the string vortices are less intense and TKE generation decreases on the lower side of the hole.

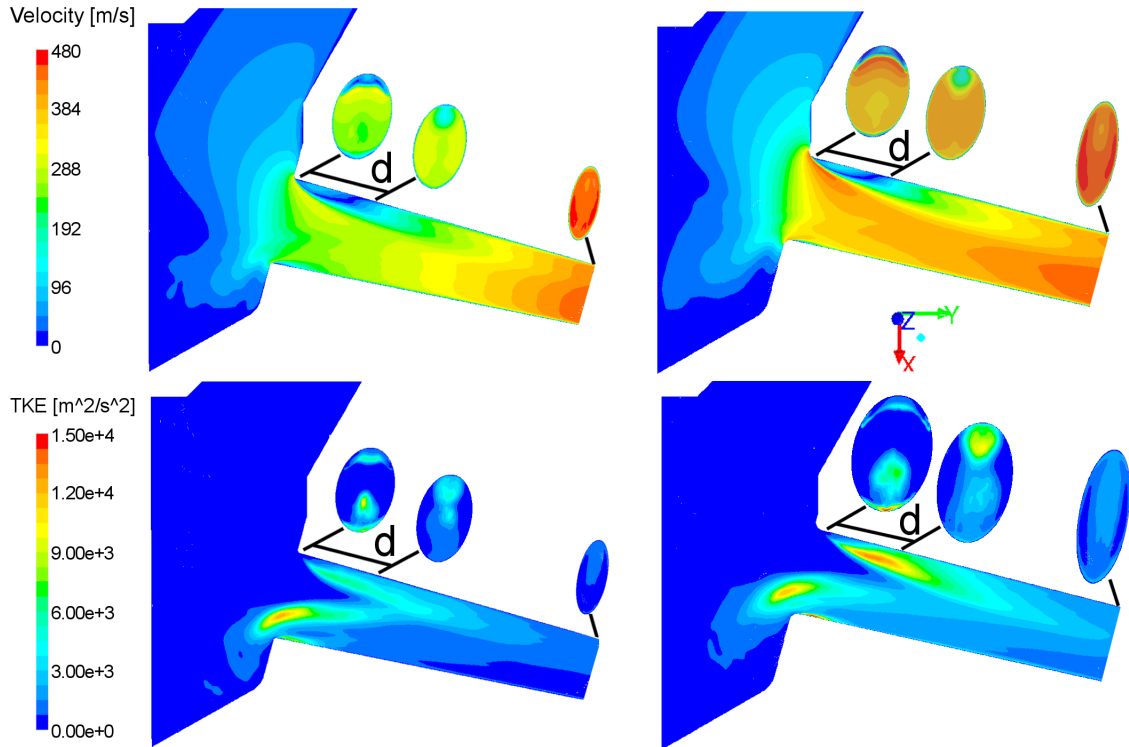


**Figure 6.27:** Average velocity (top) and resolved TKE (bottom) on the mid-cut plane ( $z=0$ ). High taper nozzle (left); Low taper nozzle (right). Cross-sectional distributions are shown at the hole inlet, at  $l/d = 1$  ( $d = 150\ \mu\text{m}$ ) and at the outlet

Vortex and cavitation structures are shown in Figure 6.28 at different instants  $t_1, t_2, t'_1, t'_2$ . It draws attention to the fact that, despite the absence of cavitation in the High taper nozzle,

## 6.6 Hole taper effect

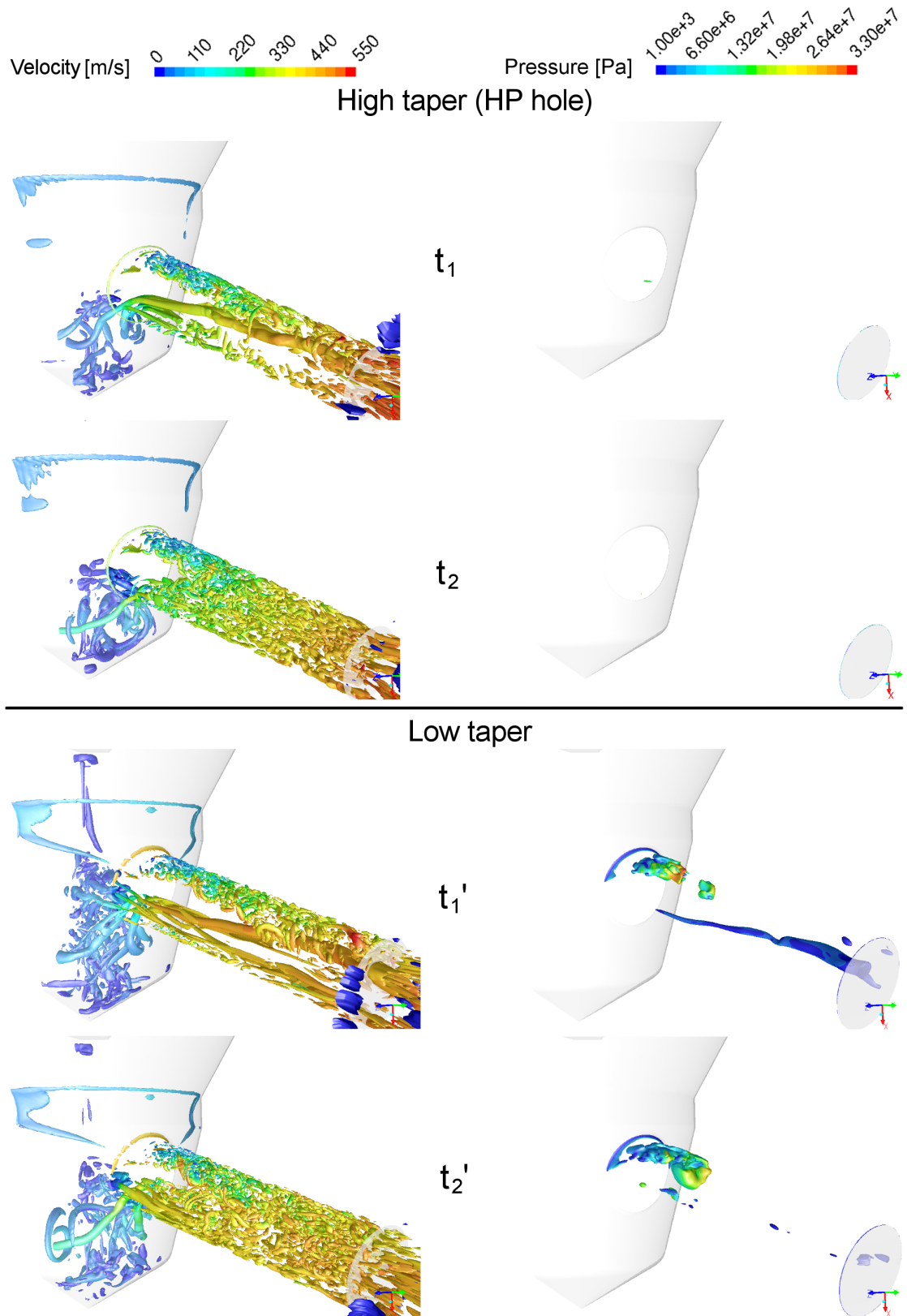


**Figure 6.28:** Comparison between High taper (HP hole) and Low taper (Reference) nozzles results at different instants  $t_1$ ,  $t_2$  and  $t'_1$ ,  $t'_2$ . Instantaneous normalized Q-criterion iso-surfaces of value 0.2 colored by velocity (left); vapor volume fraction iso-surfaces of value 0.1 colored by static pressure (right)

vortex structures are remarkably similar in both cases. At  $t_1$  and  $t'_1$ , Q-criterion iso-surfaces show a heterogeneous distribution of small scales on the upper side of the hole, large string vortices in the center and stretched vortices near the lower wall. The large vortices formed in the High taper nozzle are weaker, inducing local pressures that do not reach cavitation conditions. In fact, the long vortices developing near the bottom wall cannot preserve their integrity and break down along the hole. At  $t_2$  and  $t'_2$  the string vortices break up at the lower hole inlet edge, yielding a homogeneous distribution of small scales scattered all over the nozzle hole. Regardless of the flow configuration, weaker sac flow recirculation leads to less vortical structures in the sac of the High taper nozzle, particularly in the shear layer between the string vortices.

Figure 6.29 suggests that, despite yielding similar vortex scales, both nozzles induce different resolved TKE distribution at the hole exit. Instants (a), (b) and (a'), (b') occur when one or both string vortices reach the hole exit and instants (c), (c') when they break down along the hole. Regarding the High taper nozzle, resolved TKE is relatively homogeneous over the exit plane in the three cases (a), (b) and (c), suggesting that turbulence generation induced by the string vortices is of the order of that induced by smaller, isotropic scales. For this reason, even when the string vortices do not reach the outlet, case (c), TKE distribution is akin to (a) and (b). Although the outer flow is still squashed against the walls due to string vortex rotation, the resulting centrifugal force is significantly smaller than in the Low taper nozzle and is insufficient to damp TKE triggered by the small scales.

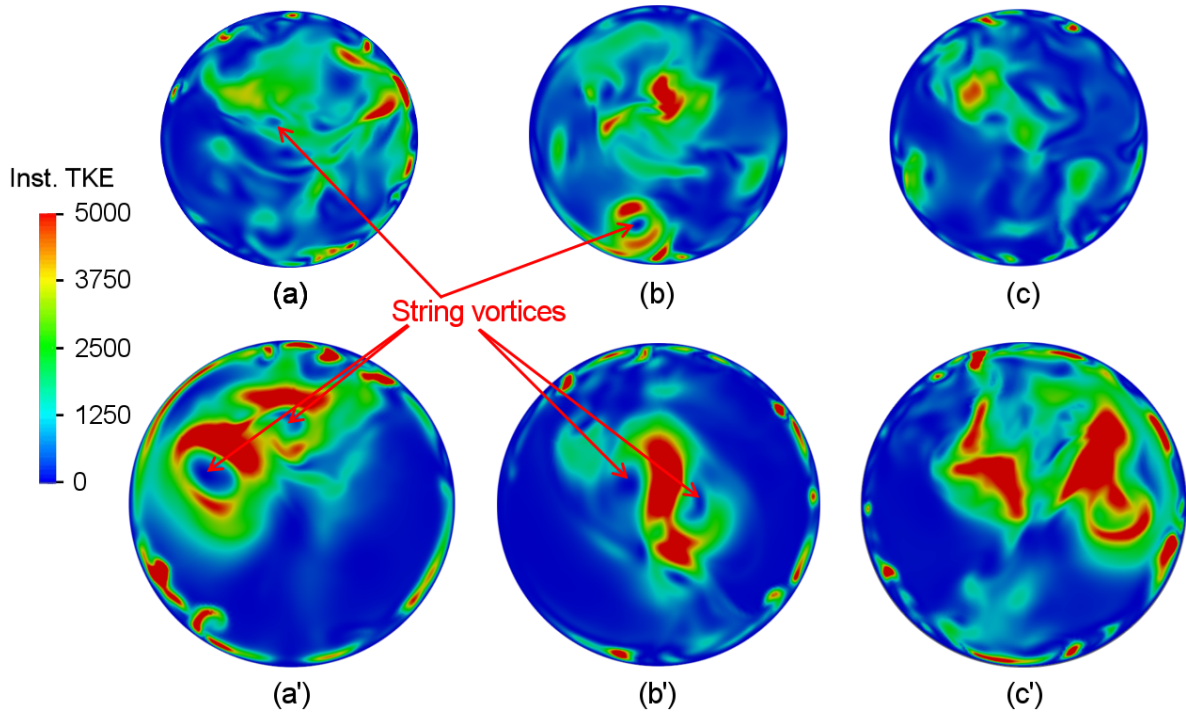


**Figure 6.29:** Instantaneous resolved TKE [ $m^2/s^2$ ] on the outlet plane at different instants (a)-(c), (a')-(c'). High taper nozzle (top) and Low taper nozzle (bottom)

In the Low taper nozzle, string vortices are responsible for most of the turbulence generation, especially when they survive until the hole exit. These vortices impose a strong rotation that damps turbulence far from them, reducing the impact of smaller scales. The resulting

## 6.6 Hole taper effect

---

distribution is depicted in (a') and (b'), showing a region of high instantaneous TKE around the string vortices and very low TKE away from them. When the strings break down along the hole before reaching the outlet, (c'), TKE is better distributed over the exit plane. However, there are still areas where turbulence decreases significantly. The reason is that, although the string vortices do not reach the end of the hole, they provoke intense flow rotation that propagates to the outlet, enhancing TKE in the part of the hole where they are located. Hence, they indirectly affect turbulence generation, even though their effect is not as intense as when they reach the outlet.

Unlike in previous Sections, vortex dynamics cannot be assessed using the temporal evolution of mass flow rate due to absence of cavitation in the High taper nozzle. A good alternative is to use temporal evolution of axial kinetic energy (AKE) integrated over the outlet plane. This variable is sensitive to changes in axial velocity induced by the main vortical structures. Figure 6.30 plots AKE over time, highlighting six instants  $t_1 - t_6$  associated with events triggered by different vortex structures. The power spectrum shows that the low frequency event is dominant over the high frequency event. Furthermore, the frequencies with maximum power are 40 kHz and 2.1 MHz respectively, which are equal to those of the Low taper nozzle (see Figure 6.11, Rounded nozzle case), suggesting that they are unaffected by hole taper.

While the high frequency event associated with the shed vortices is very similar in both nozzles, there are some differences in how the string vortex dynamics drive the low frequency event. First, it is worth noting that large vortices aligned with the hole axis effectively transfer AKE to non-axial kinetic energy (NAKE), which only takes into account velocity components perpendicular to the axis. Conversely, small, isotropic scales affect axial and non-axial velocity components similarly and therefore yield relatively homogeneous distribution of kinetic energy. At  $t_1$  there is a global minimum (excluding the one at 60  $\mu$ s) of AKE caused by the string vortices, which induce flow rotation on the upper side, and by large scales on the lower side. At  $t_2$ , the string vortices move down near the lower hole inlet edge and break up as a consequence of the interaction with the lower shear layer. AKE increases driven by the resulting small vortices, which effectively transfer NAKE to AKE as they travel toward the exit. At  $t_3$  the string vortices impinge directly on the lower hole inlet edge, breaking up even before entering the hole and yielding small scales with high AKE. This flow state lasts until  $t_4$ , when the string vortices suddenly move up and release large scales along the bottom wall. As the string vortices move upward, their interaction with the lower shear layer becomes weaker and they survive further downstream. At  $t_5$  they enter the hole through the center, oriented toward the upper side, and survive until the exit, leading to a local minimum of AKE because of the energy transfer from AKE to NAKE. As can be seen, AKE at  $t_5$  does not decrease as much as at  $t_1$  even though the string vortex reaches the outlet. This is due to the large scales near the bottom wall at  $t_1$  that do not appear at  $t_5$ . After  $t_5$ , the string vortices keep moving up, strengthening the interaction with the upper shear layer and decomposing into small, isotropic scales within the first half of the hole. Finally, at  $t_6$  the large scales break down along the hole and AKE reaches a local maximum owing to energy transfer from NAKE to AKE. In this case AKE is lower than at  $t_3$  due to the presence of string vortex feeding the upper side with rotating flow.

As mentioned before, the power spectrum draws attention to the fact that the high frequency event occurs at the same frequency 2.1 MHz in both nozzles. A hypothesis is that the effect of two of the variables governing vortex generation in the vicinity of the hole inlet edge, namely

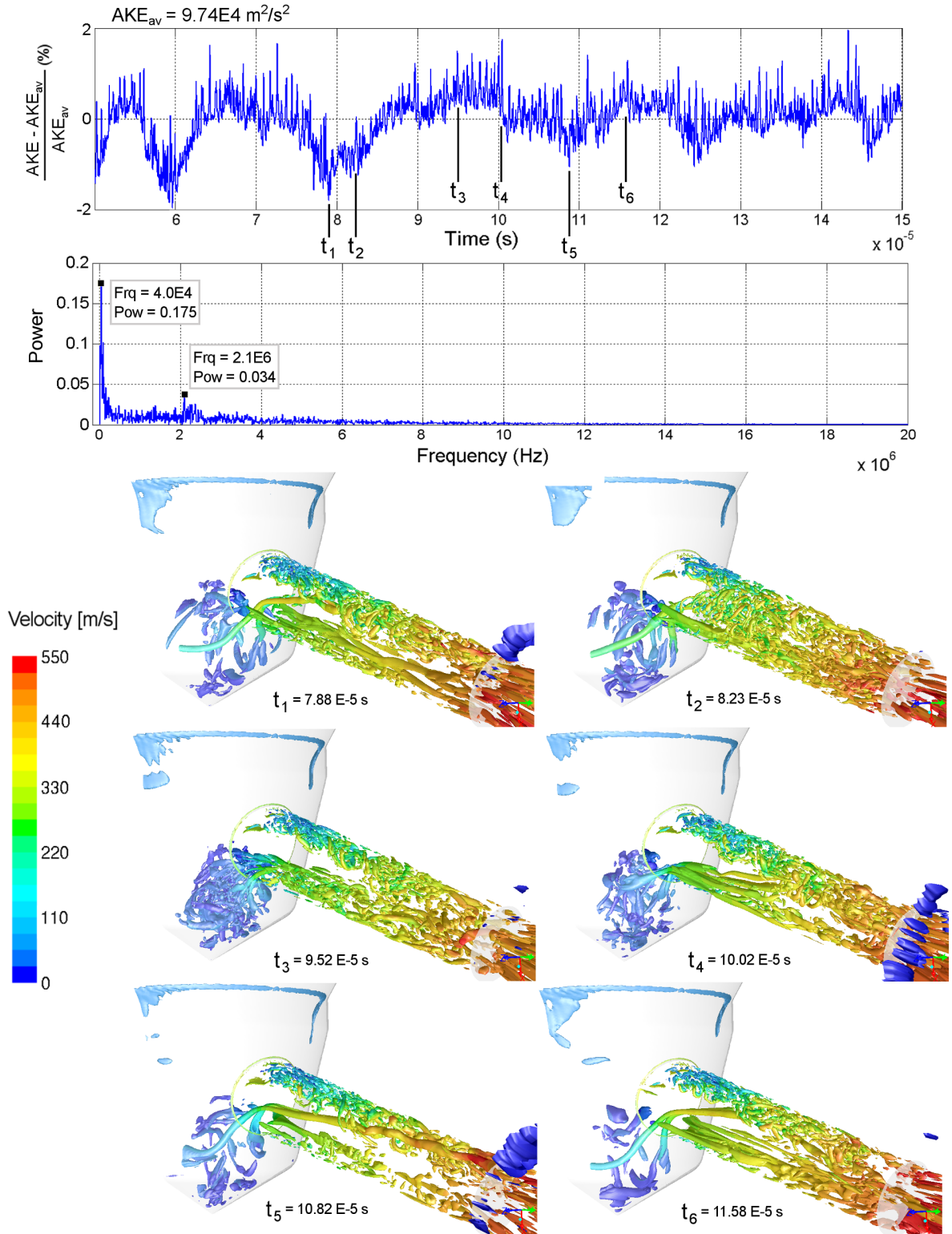


**Figure 6.30:** Axial kinetic energy (AKE) integrated over the High taper (HP hole) nozzle exit and its corresponding power spectrum. Normalized Q-criterion iso-surfaces of value 0.2 are shown for each instant  $t_1 - t_6$  indicated

flow velocity and inlet rounding diameter, counter each other to some extent. If one assumes that, by analogy with the von Kármán vortex street phenomenon, the Strouhal number (St) is relatively constant for a sufficiently high Reynolds number, then the vortex shedding frequency



## 6.7 Conclusions

$f$  can be estimated as

$$St = f \frac{d}{V} \approx Const. \rightarrow f = F\left(\frac{V}{d}\right) \quad (6.2)$$

where  $V$  is the flow velocity at the hole inlet edge and  $d$  the rounding diameter. Provided two different nozzles, the shedding frequencies of nozzle 1 and nozzle 2 are

$$\frac{V_1}{d_1} \sim \frac{V_2}{d_2} \rightarrow F\left(\frac{V_1}{d_1}\right) \sim F\left(\frac{V_2}{d_2}\right) \rightarrow f_1 \sim f_2 \quad (6.3)$$

In order to have similar shedding frequencies an increase of hole inlet rounding diameter has to be compensated with an increase of flow velocity. This behavior is illustrated in Figure 6.31, showing that flow velocity at the upper hole inlet edge is lower in the High taper nozzle, which also has smaller hole inlet rounding diameter. The shed vortices generate at the same rate and stretch further downstream depending on the velocity gradient along the hole, which is significantly higher in the High taper nozzle. Hence, the distance between shed vortices near the hole outlet increases with hole taper.

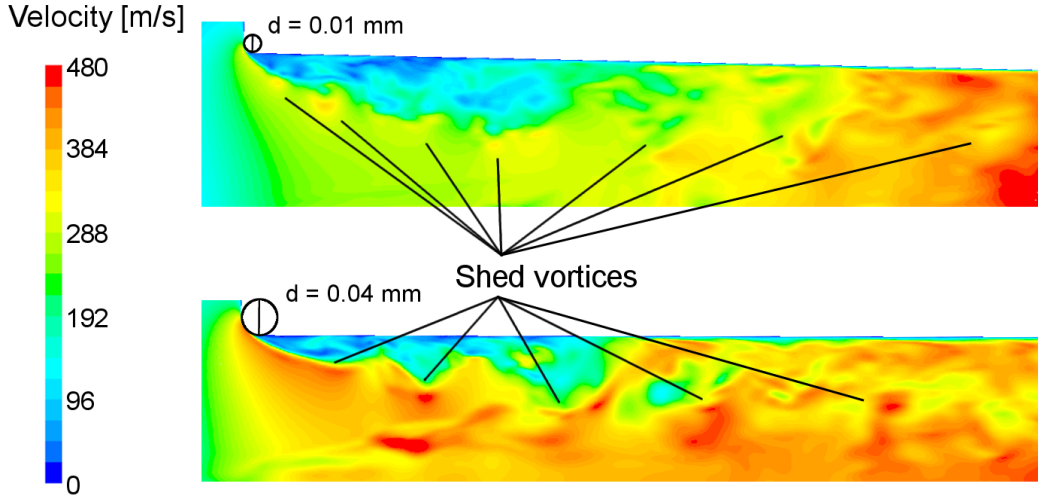


**Figure 6.31:** Instantaneous velocity color iso-levels on the mid-cut plane near the upper hole inlet edge. High taper nozzle (top), Low taper nozzle (bottom)

## 6.7 Conclusions

The impact of nozzle geometry on nozzle flow and primary breakup was investigated by applying LES to a number of nozzle designs with contrasting features. Based upon a Reference nozzle, five variants were utilized in order to assess the effect of needle lift (Low lift nozzle), hole inlet rounding (Sharp edge nozzle), hole length (Short hole nozzle), hole number (6-Hole nozzle) and hole taper (HP hole nozzle). In-nozzle flow simulations of all the cases were carried out, focusing on vortex dynamics and cavitation formation. Regarding the needle lift effect and the hole inlet rounding effect, where X-ray images were available, a number of similarities between in-nozzle vortex dynamics and near-nozzle flow structures were identified.

At low needle lift, both LES and X-ray exhibited relatively stable flow pattern with small

variations over time. LES predicts intense sac flow activity and small, homogeneously distributed structures in the hole, promoting turbulence generation, mixing and cavitation. These structures seem to correlate with X-ray images, which showed small interface structures scattering downstream of the nozzle and large dispersion angle. At high lift, both LES and X-ray methods showed strong flow pattern variation over time, transitioning between large, regular structures and small, regular or irregular structures. Several features were observed inside the nozzle: string vortices coming from the sac, side vortices developing above the string vortices, needle vortex detaching from the needle tip and shed vortices periodically generated at the upper hole inlet rounding. Among them, the string vortices were responsible for low turbulence near the walls and intense cavitation strings, which could be correlated with localized interface breakup observed in X-ray images.

String vortices and shed vortices were key to understanding the impact of hole inlet rounding on in-nozzle flow. A sharper hole inlet edge promoted vortex shedding, turbulence generation and mixing on the upper side of the hole. The intense shear layer broke up the string vortices, leading to a relatively homogeneous distribution of small scales and cavitation at the hole outlet. Similarly, X-ray images of the Sharp edge nozzle showed breakup initiation predominantly on the upper side and small, isotropic structures scattering downstream. The resulting interaction between string vortices and shed vortices induced two important phenomena: a low frequency event (40 kHz) and a high frequency event ( $\sim 2$  MHz). The low frequency event was caused by the string vortices moving all over the nozzle, sometimes breaking down near the hole inlet, other times surviving to the outlet. This event was much weaker in the Sharp edge nozzle, where the strings were permanently broken up by the upper shear layer. The high frequency event was triggered by shed vortices reaching the outlet periodically. These low-velocity vortices transported large amounts of vapor, reducing axial kinetic energy and mass flow rate. The resulting flow pattern was compatible with liquid-gas interface observed in X-ray images, where regularly distributed structures appeared very close to the nozzle hole. 2D FFT and 1D FFT analysis suggested that these structures could be correlated with shed vortices.

Decreasing hole length resulted in flow separation and cavitation at the outlet, reducing the effective area and increasing velocity at the hole inlet and along the vena contracta. Stronger flow turning led to intense sac flow recirculation, enhancing string vortices and other large scales developing in the sac. As a consequence, the string vortices became dominant, as confirmed by POD analysis of in-plane velocities at the hole outlet. Noteworthy, the resulting low frequency event occurred at 20 kHz, which is half of the 40 kHz predicted in the Long hole nozzle. Although this correlation between frequency and hole length has not been further confirmed, it seems that reducing hole length slowed down the motion of string vortices and thus decreased the frequency.

Increasing the number of holes reduced the space for sac flow recirculation and diverted more flow from the seat directly into the sac, causing intense vortex shedding and turbulence generation on the upper side at the expense of sac flow recirculation. Shed vortices were dominant and the string vortices weaken significantly, squashed by the bulk flow with negligible vorticity coming from the seat. As a consequence, the low frequency event disappeared and the high frequency event intensified, highlighting a range of dominant frequencies 1.9 - 2.3 MHz. The resulting flow structures did not vary significantly over time, consisting of small scales around the shed vortices and large cavitation pockets on the upper



## 6.7 Conclusions

---

side, high velocity flow in the middle and large scales at the bottom. Assuming that shed vortices trigger ligament separation in the primary breakup region, a 6-Hole nozzle like the one considered would hypothetically produce a very stable spray pattern with good atomization.

Finally, high taper reduced turbulence generation and cavitation formation. Although the High taper nozzle (production nozzle) has also smaller inlet rounding radius than the Low taper nozzle, the results suggested that hole taper effect was dominant. The flow was gradually accelerated along the nozzle rather than at the hole inlet, reducing vortex shedding and sac flow recirculation. Notwithstanding, the resulting vortex dynamics were very similar in both nozzles, yielding shed vortices and string vortices that, although weaker, were still dominant features. At the outlet, turbulence generation induced by small scales was of the order of that induced by string and shed vortices. As a consequence, turbulence was homogeneously distributed over the outlet rather than localized near the strings, as occurred with lower taper. Analysis of axial kinetic energy showed that the characteristic frequencies of the low frequency event (40 kHz) and the high frequency event (2.1 MHz) were the same in both nozzles. The reason why the high frequency in particular was the same could be that increasing hole taper and decreasing hole inlet rounding had opposite effects: while higher taper reduced flow velocity at the inlet and the shedding frequency, smaller rounding increased the frequency. Confirmation of this hypothesis would require further investigation of the vortex shedding phenomenon using more nozzles with different taper.



## Chapter 7

---

# Analysis of LES of in-nozzle and near-nozzle flow

---

---

### 7.1 Introduction

The objective of the work presented in this Chapter is to provide direct comparison between LES results and X-ray images for the only non-cavitating case: the HP hole nozzle. The numerical results presented in the following Sections were yielded by simultaneous simulation of in-nozzle and near-nozzle flow using VOF + Level Set approach described in Section 5.4 of Chapter 5. It should be recalled that the aim is to provide qualitative comparison between LES and X-ray in order to understand the impact of vortex flow on primary breakup. Quantitative comparison is generally not possible provided the limited quantitative information that can be extracted from X-ray images.

The Chapter is divided into three Sections. First, the link between vortex dynamics and liquid-gas interface structures developing outside the nozzle is discussed in detail in Section 7.2. Next, LES results and X-ray images are compared at different instants in Section 7.3. This comparison involves different views of liquid volume fraction iso-surfaces that, although do not reproduce the line-of-sight density projection provided by X-ray, are sufficient to correlate prominent structures. Finally, conclusions are drawn in Section 7.4.

The results presented in this Chapter have been published in MTZ worldwide [201].

### 7.2 Link between vortex dynamics and liquid-gas interface

Understanding how the vortices that originate inside the nozzle affect the near-nozzle spray is paramount to link the atomization process to the nozzle geometry. Figure 7.1 shows liquid volume fraction iso-surfaces developing outside the nozzle together with two different views

of Q-criterion iso-surfaces both inside and outside the nozzle. Looking at the front view of Q-criterion iso-surfaces, when the shed vortices reach the outlet they trigger pulsating instabilities that result in vortices developing on the surface of the jet. These vortices are referred to in the Figure as “Surface vortices”.

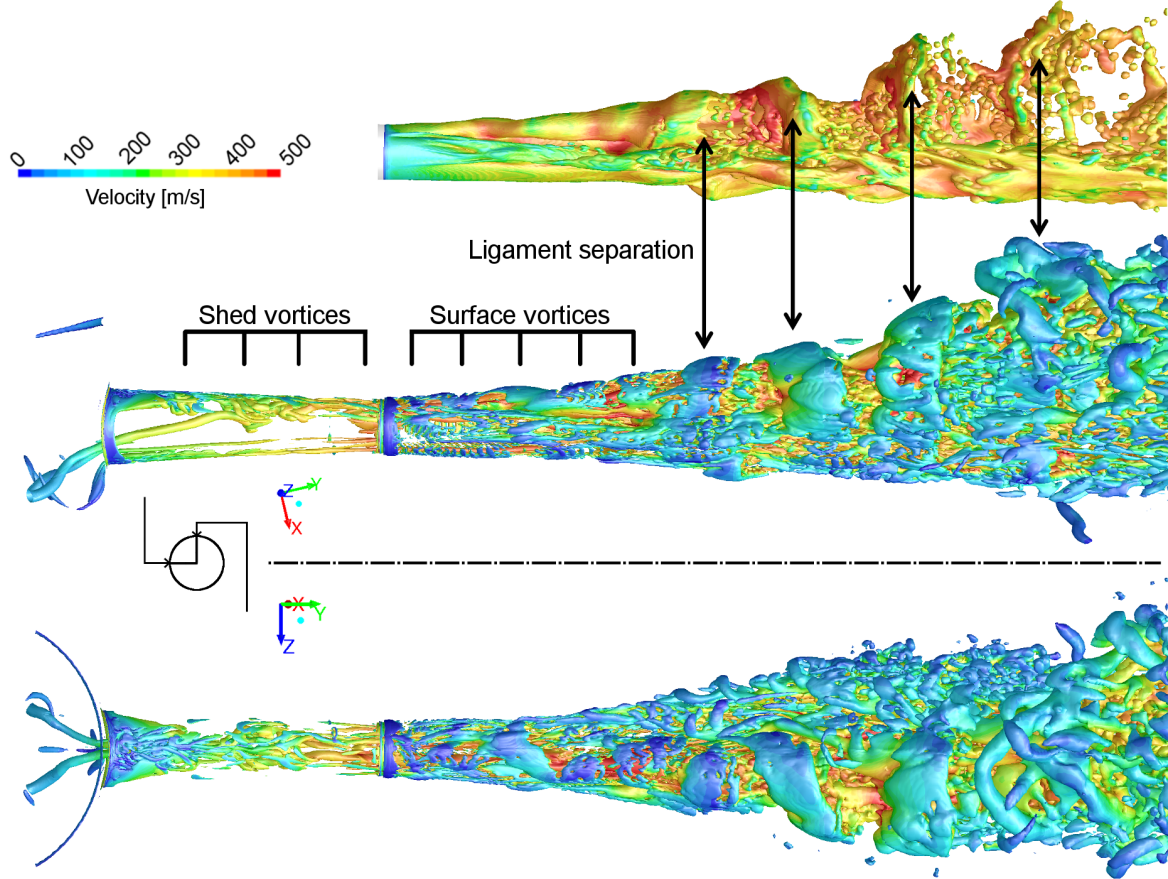


**Figure 7.1:** Instantaneous liquid volume fraction iso-surface of value 0.1 (top), Q-criterion iso-surfaces of value  $10^{13} s^{-2}$ , front view (middle), Q-criterion iso-surfaces of value  $10^{13} s^{-2}$ , top view (bottom)

Surface vortices are low velocity wave-like structures rolling up around the spray and departing regularly from the hole outlet. As they move downstream, they grow subject to the interaction with the surrounding air, promoting air entrainment and ligament separation especially on the upper side of the spray (see liquid volume fraction iso-surfaces). This vortex-driven ligament breakup process is illustrated in Figure 7.2 using a time sequence of instantaneous flow fields. At  $t_0$ , the string vortices interact with the shed vortices close to the hole exit, creating a local flow instability that is transferred to the near-nozzle flow. At  $t_0 + 0.45 \mu s$  this instability triggers the inception of a surface vortex, causing deformation of the liquid jet. At  $t_0 + 2 \mu s$  the surface vortex has grown significantly, boosted by aerodynamic interaction, and rolls up the liquid-gas interface. Finally, at  $t_0 + 5 \mu s$  it breaks up into smaller vortices, which drive the atomization of the parent ligament into smaller ligaments and droplets. Comparing Q-criterion and liquid volume fraction iso-surfaces, it draws attention to the fact that there are many more small vortices than droplets near the outlet of the domain. On the one hand this is because only the strongest vortices developing inside the cloud are able to break up the liquid structures, and on the other hand because droplets smaller than  $5\text{-}10 \mu m$  are not

## 7.2 Link between vortex dynamics and liquid-gas interface

captured due to limited mesh resolution.

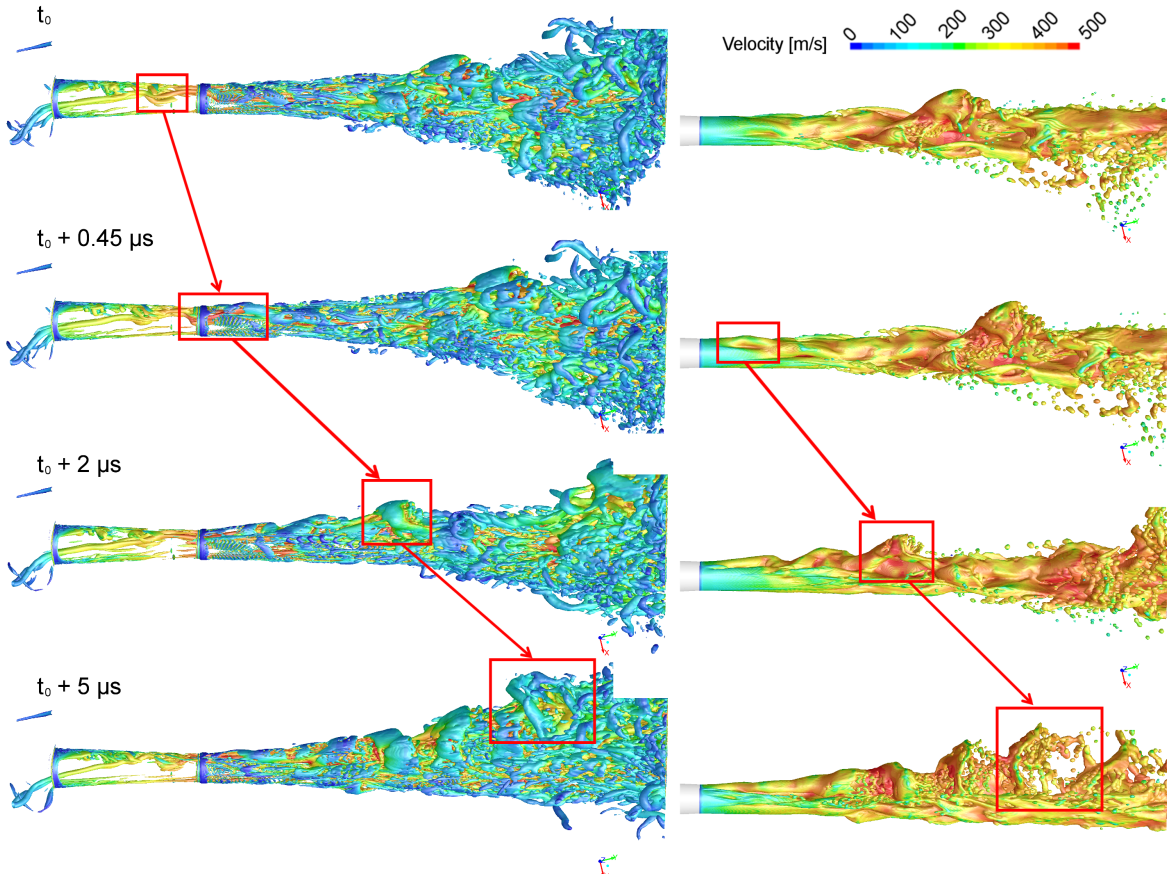


**Figure 7.2:** Front view of Q-criterion iso-surfaces of value  $10^{13} s^{-2}$  (left) and liquid volume fraction iso-surfaces of value 0.1 (right) at successive times after  $t_0$

The temporal evolution of axial kinetic energy (AKE) integrated over transverse planes at different streamwise locations can be useful to further investigate the link between shed vortices and surface vortices. Figure 7.3 shows this variable at the hole exit and at the plane located 2 mm downstream (outlet of computational domain). As can be seen, the amplitude of AKE oscillations is higher 2 mm downstream, which stems from the distorting effect of liquid-air interaction. The normalized power spectra are relatively well correlated, indicating that flow features inducing AKE variations at the hole exit reach the outlet of the computational domain. In particular, the dominant frequencies associated with shed vortices (1.2 MHz) and surface vortices (1.3 MHz) are very similar, suggesting that there is a strong correlation between these two phenomena. Noteworthy, the shed vortex frequency at the hole exit is smaller than that obtained with the mixture model regarding LES of in-nozzle flow in Section 6.6 of Chapter 6. In particular, whereas the VOF + Level Set method used for simultaneous simulation of in-nozzle and near-nozzle yields 1.2 MHz, the mixture model used for in-nozzle flow simulations yielded 2.1 MHz. Although the impact of the model is evident from a quantitative standpoint, the shed vortices are still dominant features.

A breakup pattern like the one shown in Figures 7.1 and 7.2 occurs when the string vortices move up quickly, whipping the shed vortices and transferring them upward momentum. Referring back to Figure 7.1 in particular, the top view of the spray exhibits a remarkable

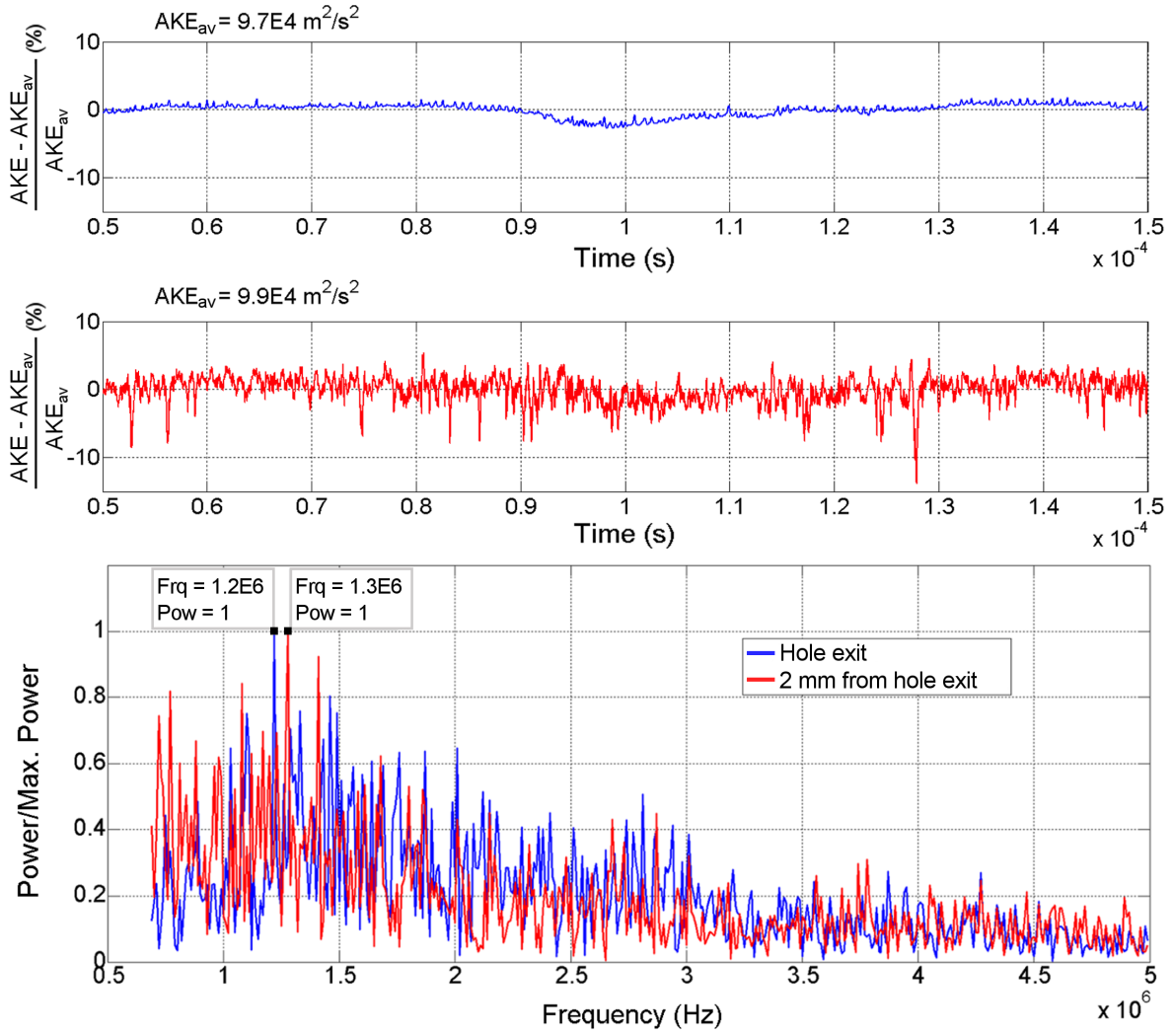


**Figure 7.3:** Temporal evolution of AKE integrated over the hole exit plane (top) and over the plane 2 mm downstream of the hole exit (middle). Normalized spectra of AKE in the range 0.5-5 MHz (bottom)

asymmetry in terms of vortex structures, showing large surface vortices on one side and smaller, isotropic scales on the other side. This behavior is governed by the string vortices. These structures move inside the hole, oscillating vertically and horizontally, and can exit the nozzle from any point at the hole exit. Depending on where they are located, their interaction with the shed vortices is different and thus the resulting breakup. Figures 7.4 and 7.5 depict the resulting spray morphology when the string vortices move vertically and horizontally using front and bottom views of vortex structure and liquid-gas interface at different instants. Each case (a)-(d) and (a')-(d') shows in-nozzle vortices at a given instant on the left side of the image and near-nozzle vortices and liquid-gas interface structures slightly after (when the flow has traveled approximately 4-5 nozzle hole diameters) on the right side of the image.

As far as the vertical motion of the string vortices is concerned (plane X-Y), Figure 7.4 shows that at the hole exit they can be either paired in the center (a); paired on the upper side (b); paired on the lower side (c); or separated, one on the upper side and the other closer to the bottom wall (d). If paired in the center, they barely affect the external interface of the jet



## 7.2 Link between vortex dynamics and liquid-gas interface

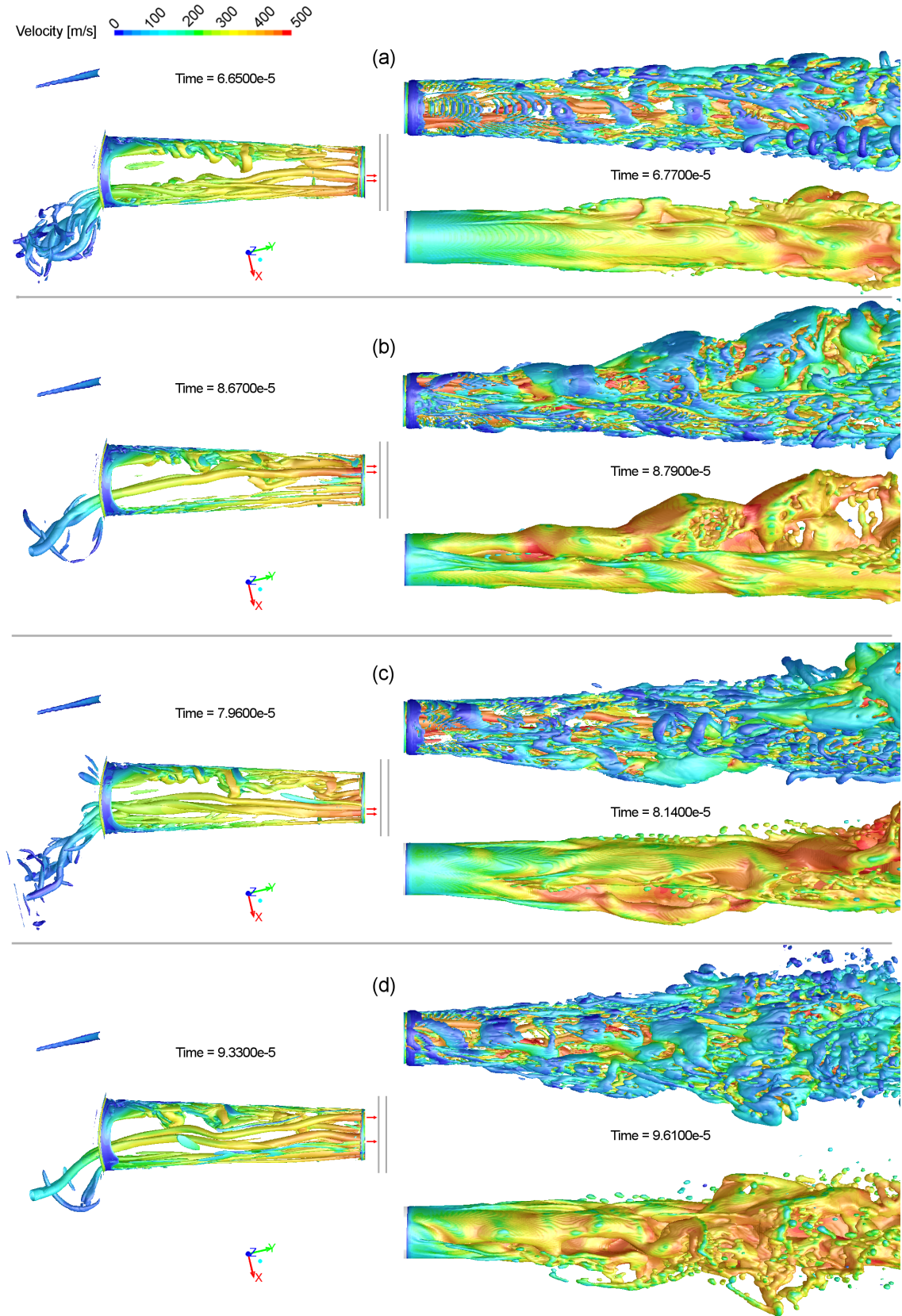


**Figure 7.4:** Front view of instantaneous vortex structures and liquid-gas interface at different instants. For each case (a)-(d): Q-criterion iso-surfaces of value  $10^{13} s^{-2}$  at the time specified (left); Q-criterion iso-surfaces of value  $10^{13} s^{-2}$  (top-right) and liquid volume fraction iso-surface of value 0.1 (bottom-right) at the time specified. Red arrows at the outlet denote the location of string vortices

and the surface vortices are weak, yielding a narrow jet composed of large surface vortices and a relatively small amount of small scales. In this case, atomization is reduced and spray flapping decreases. If the string vortices are paired on the upper side, the interaction with the shed vortices is strong and the resulting surface vortices are able to induce ligament separation and breakup. This is the case presented before in Figures 7.1 and 7.2. Since the instability is generated very close to the upper side, the lower side of the spray is relatively unaffected and interface distortion is very weak. Conversely, when the string vortices are paired at the bottom of the hole, surface instabilities are stronger on the lower side and thus interface distortion. Comparing cases (b) and (c), liquid breakup on the upper side of the jet in case (b) is clearly more intense than on the lower side in case (c) owing to the location of shed vortices. In fact, liquid breakup on the lower side is generally not driven by shed vortices but by a sudden movement of the string vortices toward the bottom wall, whipping the bulk flow and transferring downward momentum. The resulting spray morphology is therefore very different: while transverse ligaments separate from the upper side in (b), large ligaments relatively aligned with the spray axis protrude from the jet on the lower side in (c).

Besides cases (a), (b) and (c), which appear frequently, there is a much less frequent case where the string vortices separate from each other vertically at the hole exit (d), one at the top and the other closer to the bottom wall. In this configuration, shed vortex instabilities propagate on the upper and lower sides, causing transverse structures and ligament separation in both regions. Although interface distortion on the lower side can be stronger than in (c), jet breakup on the upper side is significantly weaker than in (b). Hence, breakup is most intense when the strings are paired on the upper side and combine with the shed vortices.

Vortex-driven ligament breakup perpendicular to the X-Y plane is different as long as the horizontal motion of string vortices is more or less symmetric with respect to that plane. Figure 7.5 presents four cases (a')-(d') where the string vortices can be either paired in the center (a'); paired at the back of the hole,  $Z < 0$  (b'); paired at the front,  $Z > 0$  (c'); or separated, one at the front and the other at the back (d'). When the vortices are paired in the center, surface instabilities are weak and so it is liquid-gas interface distortion. Cases (b') and (c') are analogous, showing intense surface vortices either at the front or at the back depending on the position of the strings. In these two cases, the shed vortices interact with the strings and cause instabilities that lead to ligament separation on the sides of the spray. The resulting vortex cloud can be very asymmetric, composed of large transverse surface vortices on the same side of the strings and small, isotropic scales on the other side, as in the bottom view of Figure 7.1. Noteworthy, there is a higher amount of small droplets on the side with small vortices, suggesting that surface vortices are not the only mechanism inducing liquid breakup. Finally, case (d') is less frequent than the other three and occurs only during very short periods of time. In this case the interaction between strings and shed vortices is strong, enhancing surface distortion on both sides and triggering a more or less symmetric spray.

The eight cases described (a)-(d), (a')-(d') are simplifications of possible vortex configurations. There are other features apart from the string and shed vortices that can contribute to interface deformation and breakup. For instance, side vortices on the upper side and large scales developing near the lower wall can have non-negligible impact on atomization. Figure 7.6 shows the link between some of these structures inside the nozzle and liquid-gas interface outside the nozzle. Side vortices propagating along the top wall transfer non-axial momentum to the spray and initiate liquid breakup on the upper side by twisting the interface. The



## 7.2 Link between vortex dynamics and liquid-gas interface

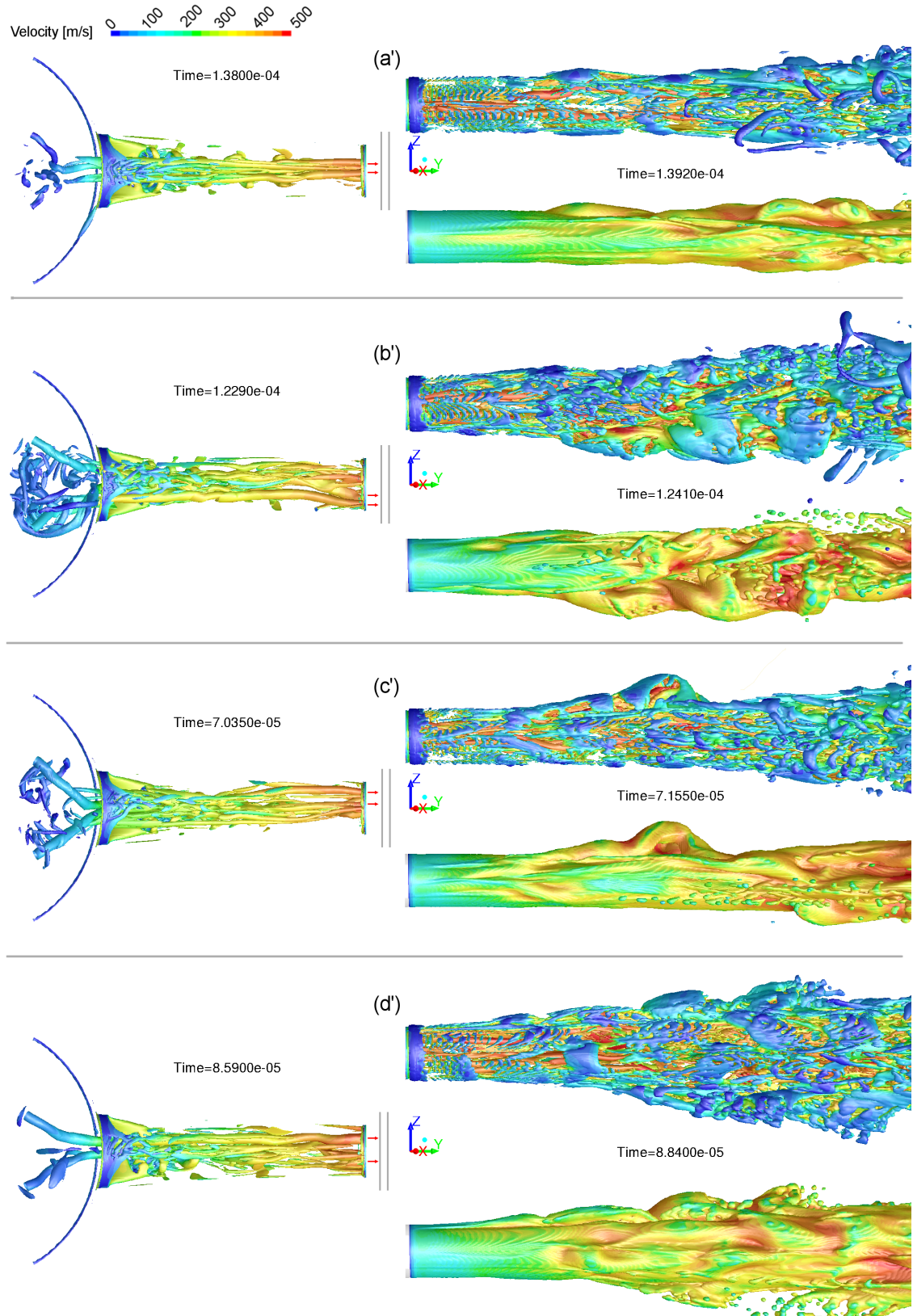


**Figure 7.5:** Bottom view of instantaneous vortex structures and liquid-gas interface at different instants. For each case (a')-(d'): Q-criterion iso-surfaces of value  $10^{13} s^{-2}$  at the time specified (left); Q-criterion iso-surfaces of value  $10^{13} s^{-2}$  (top-right); and liquid volume fraction iso-surface of value 0.1 (bottom-right) at the time specified. Red arrows at the outlet indicate the location of string vortices

resulting deformation is added to that caused by the string vortices, which trigger thick ligaments protruding from the liquid core in the middle of the jet. Large vortices coming from the sac and surviving to the hole exit are responsible for oblique liquid streaks departing from the lower half of the hole. These structures often merge with the string vortices and generate large liquid streaks across the spray. Finally, weak slender vortices form near the hole exit at the bottom wall and trigger long filaments that easily break up into small droplets. Notwithstanding the fact that all the aforementioned structures have a certain impact on the atomization process, the string vortices are mainly responsible for the whip-like motion of the spray and the asymmetries arising, and the shed vortices are mainly responsible for ligament breakup.

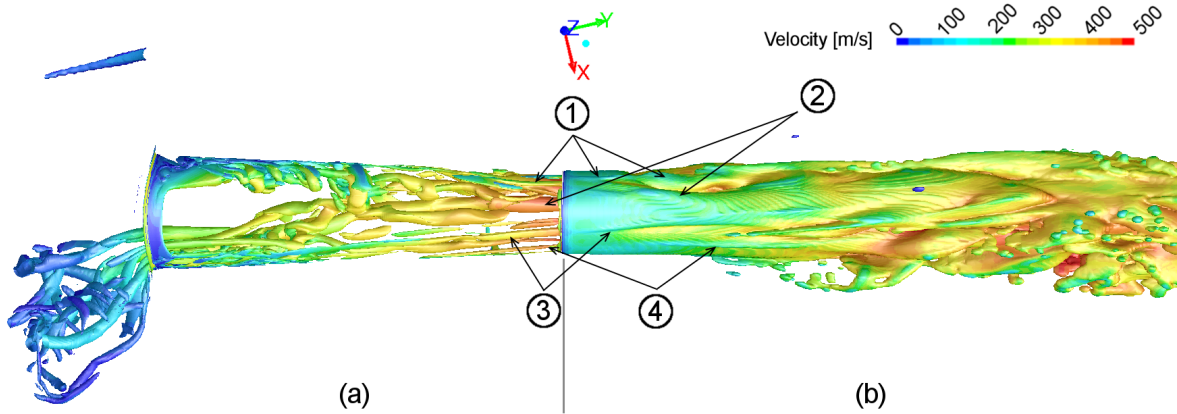


**Figure 7.6:** Instantaneous Q-criterion iso-surfaces of value  $10^{13} s^{-2}$  (a), liquid volume fraction iso-surfaces of value 0.1 (b). ① Side vortices and resulting interface deformation on the upper side, ② String vortices and resulting interface deformation in the middle, ③ large vortices formed inside the sac and resulting liquid streaks, ④ slender vortices at the bottom of the hole and resulting liquid filaments

### 7.3 Correlation between LES results and X-ray images

Figure 7.7 compares qualitatively instantaneous liquid-gas interface structures predicted by LES with X-ray. The liquid-gas interface shown corresponds to the breakup mechanism triggered when the string vortices are paired at the top (Figure 7.4b). The contrast between breakup initiation on the upper side and relatively unperturbed liquid extruding from the lower side of the hole can be seen both in the liquid iso-surfaces and in the X-ray image. The sequence of transverse ligaments growing on the upper side of the spray predicted by LES is relatively similar to the regular distribution of dark structures curving from the upper side toward the spray axis in X-ray. The resulting pattern resembles a dense cloud of small droplets surrounding the ligaments. The periodic instabilities on the upper side grow slower in the LES results, leading to significantly narrower spray dispersion angle. There are several factors that can contribute to such behavior, including the absence of a model for fuel viscosity variation and surface tension effects, and a model to take into account aerodynamic forces (note that the mixture model used assumes velocity equilibrium at the liquid-gas interface).

The iso-surfaces shown in Figure 7.8 appear when the string vortices are paired on the upper side of the hole at the front (combination of states presented in Figures 7.4b and 7.5c'). At this instant, liquid volume fraction iso-surfaces show what seems to be the hollowing out of the

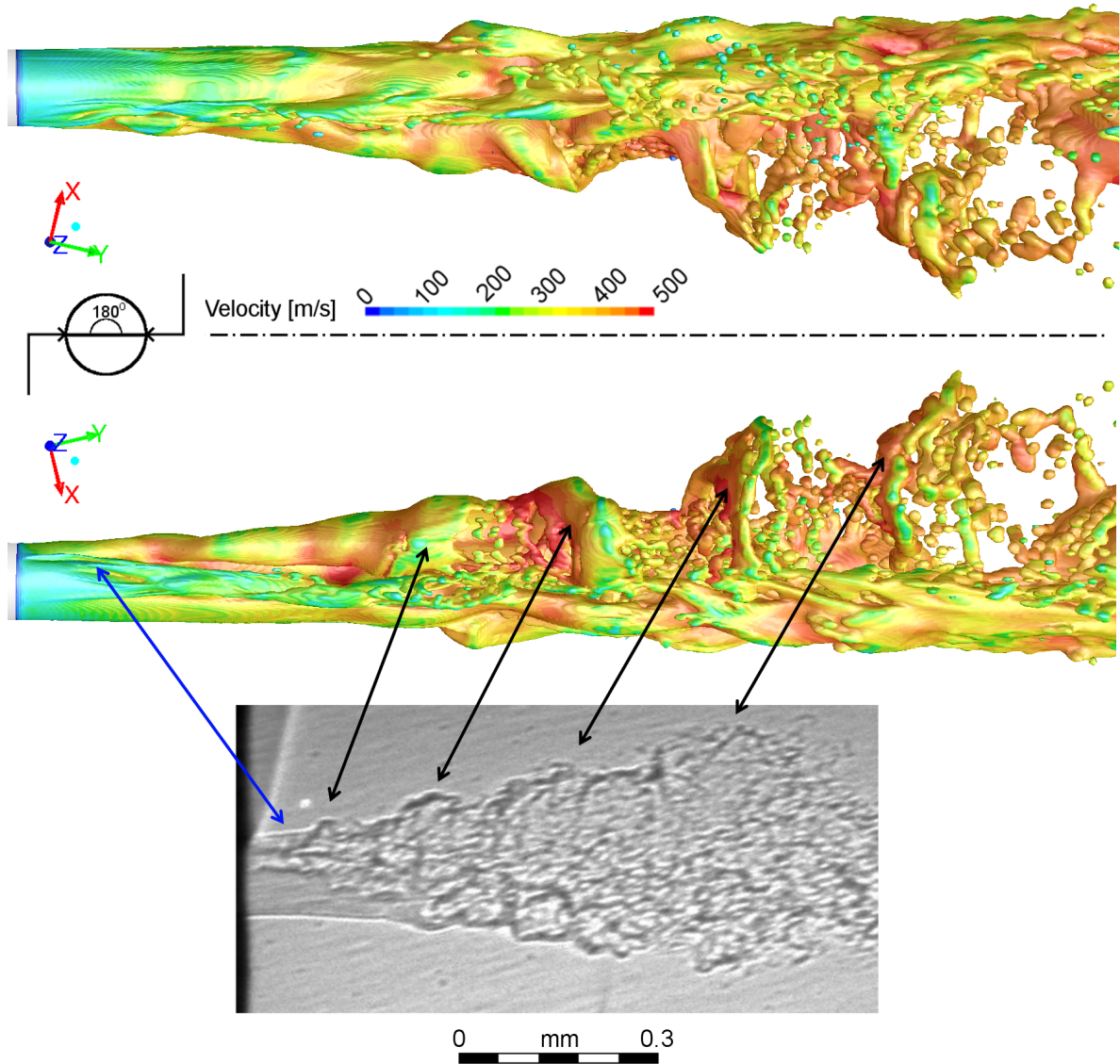


**Figure 7.7:** Instantaneous liquid volume fraction iso-surfaces of value 0.1, back view (top); front view (middle); and X-ray image (bottom). The blue arrow highlights similar breakup initiation on the upper side and the black arrows periodic ligament breakup on the upper side

liquid core, leading to a regular distribution of large, transverse liquid ligaments bending over the front side. Similarly, X-ray captures a regular distribution of transverse dark structures extending from the upper boundary to the lower boundary of the spray. Towards the end of the domain, these structures are replaced by small, isotropic scales that could be caused by a dense cloud of ligaments and droplets, which are observed in the LES results. Another interesting feature captured by X-ray is the spray initiation on the upper side close to the hole exit. The liquid column splits into two divergent edges, one parallel to the spray axis and the other tilted upwards, increasing the spray dispersion angle. Whereas the lower edge penetrates well inside the domain relatively undisturbed, the upper edge undergoes deformation, turning into a wavy line whose amplitude grows smoothly away from the hole exit. The LES results predict liquid-gas interface that is well correlated with this feature, showing a wave-like deformation on the upper side and a long streak parallel to the spray axis. Finally, the bottom of the spray is remarkably undisturbed both in LES and X-ray, especially compared to the upper side.



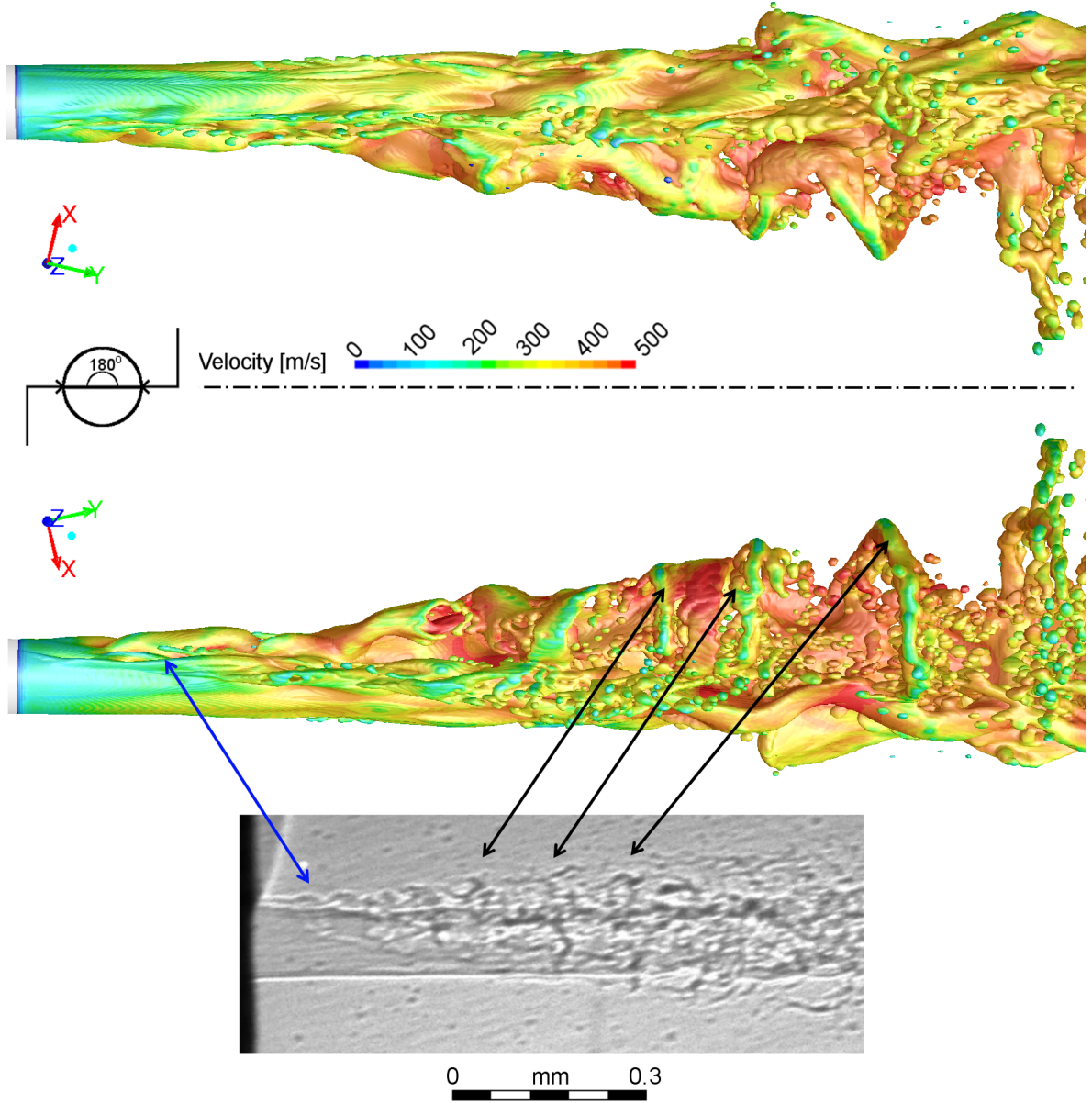


**Figure 7.8:** Instantaneous liquid volume fraction iso-surfaces of value 0.1, back view (top); front view (middle); and X-ray image (bottom). The blue arrow highlights interface split on the upper side and the black arrows transverse ligaments across the spray

The average distance between transverse structures predicted in LES is  $\sim 150 \mu\text{m}$ . This value is obtained by tracking surface vortices and liquid-gas interface structures along the spray. As for X-ray, the characteristic length of transverse structures can be estimated by applying 1D FFT to light intensity distribution along selected lines (see Section 5.2). Figure 7.9 shows the resulting probability density function of characteristic length scales obtained in this way. The mean value  $103.8 \mu\text{m}$  is smaller than the distance predicted in LES, in line with the findings discussed above. The pdf draws attention to the high variance, indicating that there is a relatively wide range of length scales that can occur with high degree of probability. One of the reasons that can explain these results is that the transverse structures appear only in some of the X-ray images, the rest typically showing smaller, isotropic scales. This is in agreement with the results discussed in Section 7.2, where it is shown that the generation of

### 7.3 Correlation between LES results and X-ray images

transverse ligaments depends not only on surface vortices but also on string vortices. Only when the strings are close to the walls the resulting surface vortices are sufficiently strong to induce separation of transverse ligaments.

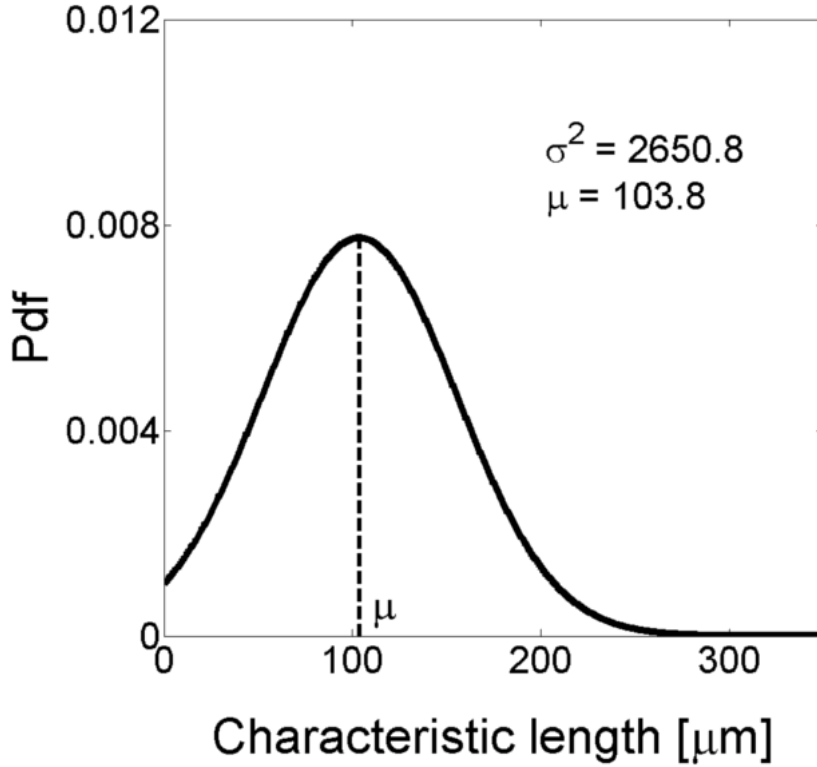


**Figure 7.9:** Probability density function of characteristic length scale. The statistical population consists of 88 samples obtained as described in Section 5.2

Figure 7.10 shows liquid-gas interface structures generated when the string vortices are paired in the middle of the hole very close to the front side (Figures 7.4a and 7.5c'). It correlates two additional features observed in X-ray images: the oblique streak crossing the spray toward the upper side and the transverse ligaments surrounded by a cloud of droplets on the lower side. The X-ray image exhibits a series of transverse, regular structures on the lower side of the spray clearly separated from one another, growing as they travel downstream. They appear as dark, vertical strokes surrounded by a cloud of smaller, brighter structures. Even though intense breakup on the lower side is seldom, LES predicts this phenomenon reasonably well, assuming that the dark strokes are ligaments separating from the liquid core and the bright structures are droplets undergoing further breakup. Regarding the oblique streak closer to the hole exit, it correlates well with the interface deformation caused by string and sac vortices (see Figure 7.6). The differences between the front and back views indicate that this deformation can be generated on either side of the spray, enhancing breakup on the side where it forms.

The breakup pattern shown in Figure 7.10 occurs when transverse instabilities, driven by the surface vortices, propagate from top to bottom. However, a less frequent breakup pattern can appear on the lower side as a consequence of the whip-like motion of one of the string vortices (separated strings shown in Figure 7.4d). Figure 7.11 shows this pattern, characterized by weak separation of large ligaments from the liquid core. Although initially they are relatively aligned with the spray axis, they start rotating with respect to the Z axis as they move

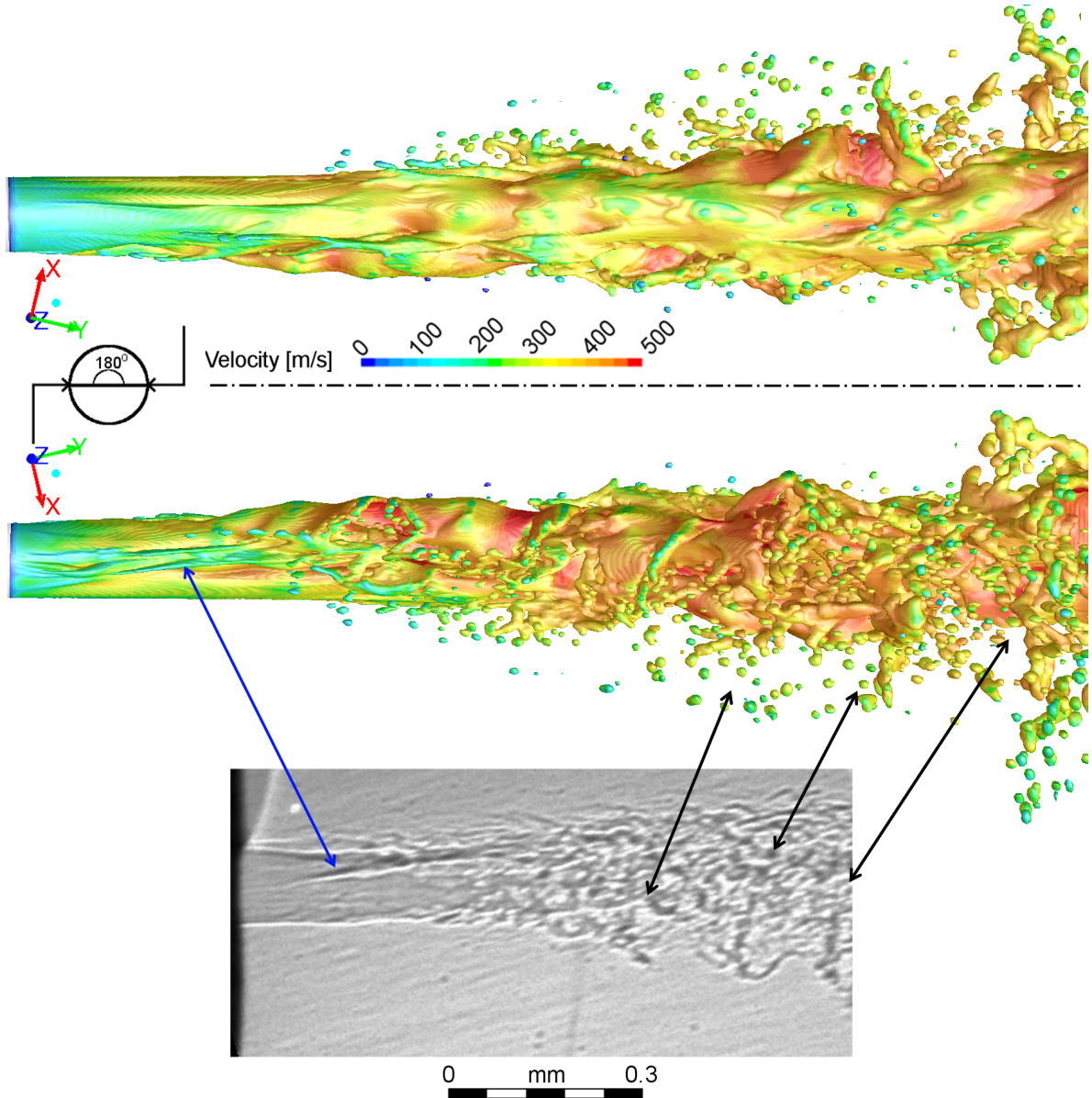


**Figure 7.10:** Instantaneous liquid volume fraction iso-surfaces of value 0.1, back view (top), front view (middle); X-ray image (bottom). The blue arrow highlights the oblique streak and the black arrows periodic ligament breakup on the lower side

downstream, impulsed by the momentum inherited from the string vortex. The structures captured by X-ray are compatible with these features, showing large dark areas smoothly detaching from the liquid core and smaller dark areas perpendicular to the spray axis further downstream. Since this breakup pattern occurs when one of the string vortices moves down, the upper side is less unperturbed and breakup is weak. In fact, side vortices are the main source of instability (see Figure 7.6), leading to long filaments developing on the upper side. X-ray also shows relatively weak breakup initiation, including absence of wave-like deformation.

The last X-ray visualization correlated with liquid iso-surfaces is shown in Figure 7.12, corresponding to the breakup mechanism induced by string vortices horizontally separated in the middle of the hole (Figures 7.4a and 7.5d'). It highlights a helical structure protruding

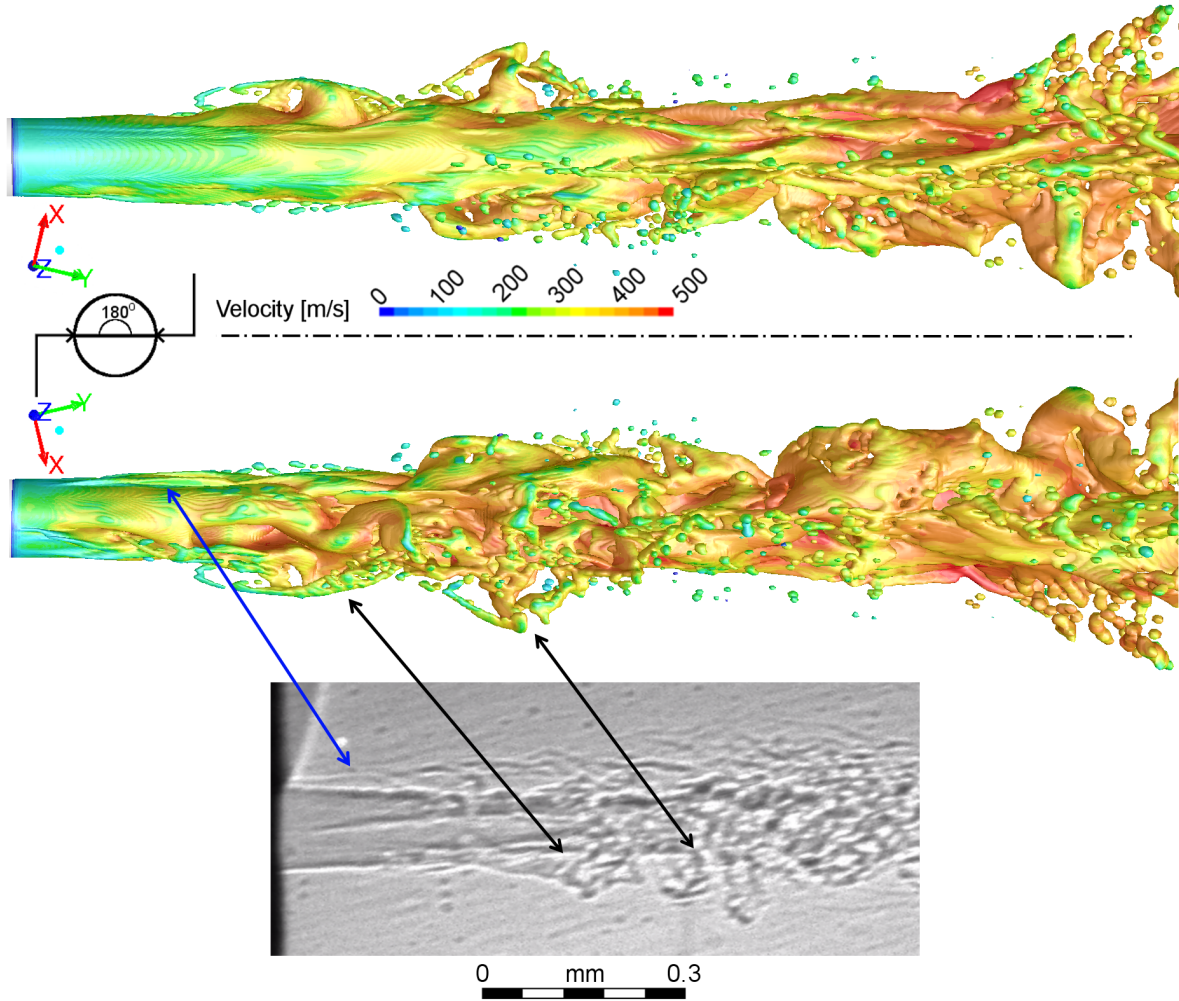


**Figure 7.11:** Instantaneous liquid volume fraction iso-surfaces of value 0.1, back view (top); front view (middle); and X-ray image (bottom). The blue arrow highlights weak breakup initiation on the upper side induced by side vortices and the black arrows smooth ligament breakup on the lower side

on both sides of the spray. As can be seen in the X-ray image, a braid-like structure appears on the upper side of the jet, consisting of relatively thick ligaments overlapping with each other parallel to the spray axis. A similar helical pattern is predicted by LES, caused by twisting of the interface as the liquid column penetrates into the discharge volume. Comparing the front and side views, it can be concluded that similar features can be generated on both sides of the spray independently from one another, the consequence being the formation of a high-velocity jet with relatively poor atomization.



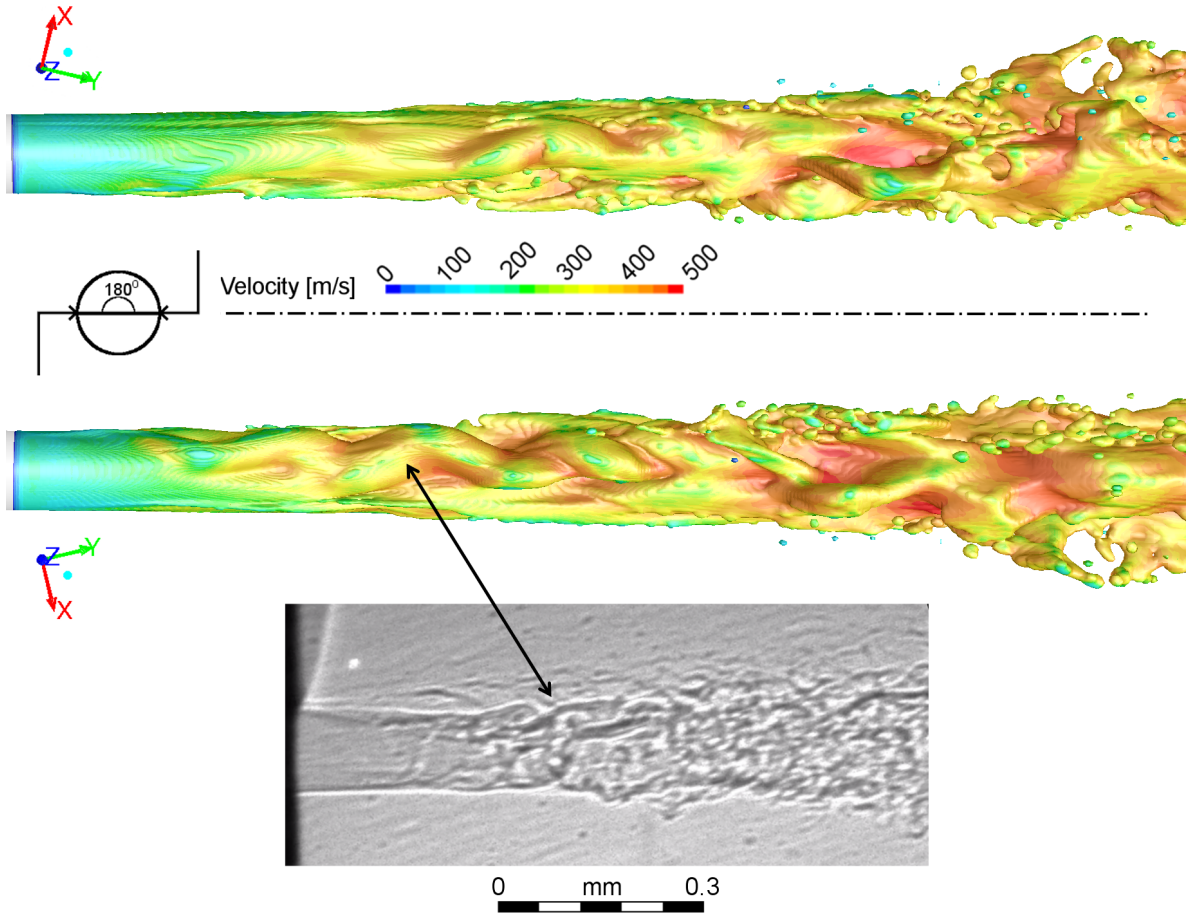


**Figure 7.12:** Instantaneous liquid volume fraction iso-surfaces of value 0.1, back view (top); front view (middle); and X-ray image (bottom). The black arrow highlights braid-like twisting of the liquid gas interface

## 7.4 Conclusions

Simultaneous simulation of in-nozzle and near-nozzle flow developing in the HP hole nozzle revealed that the main atomization mechanisms are driven by the interaction between shed vortices and string vortices close to the hole exit. More specifically, shed vortices introduced a regular pulsation in the flow that propagated downstream depending on the position of the string vortices, which could be paired near the walls, paired in the center of the hole or separated. Some of the resulting breakup patterns were correlated with X-ray images:

- If the string vortices are paired at the top, either in the middle of the hole, at the front or at the back, intense flow instabilities propagate outside the nozzle, generating strong surface vortices on the upper side that depart periodically from the hole outlet. These structures grow as they move downstream, deforming the liquid-gas interface until ligament separation occurs. Subsequently, the ligaments undergo further breakup driven by small eddies detached from the parent surface vortex. This breakup mechanism seems to correlate with X-ray images, where transverse strokes appear regularly distributed on the upper side of the jet surrounded by what could be a cloud of smaller droplets.



## 7.4 Conclusions

---

- If the string vortices and other large scales move horizontally to one side of the hole, the liquid-gas interface twists on that side of the spray, leading to a large, oblique streak crossing the spray toward the upper side. If they also move down, surface vortices propagate to the lower side, inducing separation of transverse ligaments and small droplets. X-ray images show very similar features, including an oblique streak in the first part of the jet and transverse structures regularly distributed further downstream on the lower side.
- If one of the string vortices moves down, whipping the bulk flow and transferring downward momentum to the liquid, large ligaments relatively aligned with the spray axis detach from the liquid core and rotate downstream until they lay perpendicular to the spray. X-ray images show large interface structures protruding from the lower side of the jet and transverse structures further downstream that could be triggered by the same phenomenon.
- If the string vortices are horizontally separated in the middle of the hole, one at the front and the other at the back, each vortex twists the interface on its side of the spray, leading to a braid-like structure along the liquid column. In this case, atomization is poor and spray dispersion angle very small. X-ray also shows a very small dispersion angle and a very similar braid-like structure on the upper side of the jet consisting of relatively thick ligaments overlapping with each other parallel to the axis.

The results suggested that string vortices and shed vortices drive spray atomization in the primary breakup region. However, it must be noted that many other structures such as side vortices, needle vortices, small scales generating on the lower inlet edge or slender vortices developing at the bottom of the hole also promote interface distortion and spray instability.

Although the study provided only qualitative information about primary breakup, the understanding of how in-nozzle vortex dynamics drive spray dynamics, ligament separation and breakup can be very useful for knowledge-base nozzle design. It can be concluded from this work that acting on the shed vortices and string vortices can help control atomization and spray stability (i.e. reduce flapping). Moreover, the string vortices can be used to promote atomization everywhere in the spray and not only on the upper side. Further investigation is needed to provide quantitative correlations between vortex size and droplet size distribution that could be used in reactive spray simulations.



## Part IV

# Conclusions



## Chapter 8

---

# Conclusions and future research

---

---

### 8.1 General conclusions

The work presented in this thesis provides a numerical framework for the study of Diesel engine injection and contributes to the understanding of nozzle geometry impact on primary breakup. A first part of the research work concerned the development of a 5-Equation model for compressible, two-phase, two-species flows. A second part was dedicated to the development of a simulation methodology based on LES and its application to the investigation of in-nozzle flow and primary breakup assuming flow incompressibility.

The 5-Equation model developed in the first part of the research work is valid for problems involving liquid-gas mixtures where the gas phase is composed of two species, one of them non-condensable. Heat and mass transfer are calculated based on temperature equilibrium and Gibbs free energy equilibrium, which are attained through relaxation processes. On the one hand, temperature equilibrium is attained through instantaneous heat transfer, assumed to be infinitely slower than pressure and velocity relaxation. On the other hand, Gibbs free energy equilibrium results from instantaneous mass transfer, assumed to be infinitely slower than heat transfer. In this case, the effects of mass fraction variation in the presence of a non-condensable species are taken into account when deriving energy and mass exchange coefficients. Under the assumption of different characteristic relaxation times, the calculation of heat and mass transfer can be decoupled from the homogeneous system.

The model was implemented in the IFP-C3D code using a phase-splitting method, decoupling the calculation of source terms, diffusion terms and convective terms. Explicit calculation of source terms is first performed, followed by an implicit calculation of diffusion terms. The implicit calculation of heat diffusion before temperature relaxation posed one particular difficulty: the need for a mixture temperature based on different phase temperatures. To overcome this problem, an expression for the mixture temperature compatible with ideal and stiffened gas equations of state was used. Finally, explicit calculation of convective terms is

carried out before heat and mass relaxation.

Three test cases were used to validate the model. The shock tube case showed the ability of the 5-Equation model to compute wave propagation in a stiff medium composed of liquid and dissolved, non-condensable gas. While the results were similar to those obtained with a 7-Equation model already available in the same code, the numerical robustness and efficiency were significantly improved, reducing the computational cost by as much as 20%. On the down side, the 5-Equation model was more sensitive to numerical errors than the 7-Equation model, predicting a pressure overshoot across the interface. The water cavitation tube and the two-phase expansion tube test cases indicated that the proposed model can successfully predict gas expansion and mass transfer in flows subject to intense pressure drop. Good agreement with experimental data was attained even at low temperatures, when the equation of state of the liquid is less accurate. The results are comparable to those obtained by other authors using a 7-Equation model.

The 5-Equation model was finally applied to a single hole injector for which experimental measurements of void fraction are available. The model reproduced cavitation onset at the hole inlet edge and its propagation along the walls. Furthermore, it captured gas expansion along the nozzle hole centerline, which is mainly caused by non-condensable gas, and its disconnection from the cavitation region near the walls. The absence of a turbulence model did not allow assessing whether some of the inaccuracies observed (i.e. overprediction of gas expansion) stem from this fact or from the 5-Equation model itself. Similar simulations reported in the literature suggest that turbulence can increase significantly cavitation and gas expansion in the center of the nozzle hole.

In the second part of the presented research, LES was used to study the impact of nozzle geometry on vortex dynamics, turbulence generation and primary breakup. The proposed investigation strategy consisted of using contrasting geometric features in order to isolate the effects of needle lift, hole inlet rounding, hole length, hole number and hole taper. In all the cases, the flow was assumed incompressible, justified by the fact that they concerned an injection pressure of 800 bar, leading to a maximum Mach number of 0.3. The numerical results were qualitatively correlated with X-ray PCI images of near-nozzle flow.

The simulations were performed with the commercial code ANSYS Fluent using a URANS-LES approach. This consists of applying URANS in the region of low turbulence above the needle seat sealing and LES in the sac and hole. The URANS region was resolved with coarse tetrahedral cells and the LES region with small hexahedral cells, which are better for resolving boundary and shear layers. An incompressible, two-phase, isothermal, mixture model was used in all the cases, sacrificing accuracy but increasing numerical efficiency and robustness. Mass transfer effects were accounted via a bubble dynamic based cavitation model, which was shown to affect cavitation formation but not vortex dynamics. The resulting simulation resolution satisfied  $y^+ < 1$  in all the walls of interest, maximum cell-based CFL number  $< 5$  and  $SGS < 1$ .

The main conclusion drawn from all the cases is that, among all the structures developing inside the nozzle, there are two type of vortices that play a key role in turbulence generation and cavitation formation: the string vortices and the shed vortices. The string vortices form inside the sac as a consequence of sac flow recirculation. When the flow coming from the seat moves along the housing walls instead of entering directly into the hole, it generates

## 8.1 General conclusions

---

two counter-rotating vortices before the hole inlet. These structures penetrate into the hole and can reach the exit if the interaction with the upper shear layer is weak. String vortex dynamics lead to a low frequency event whose characteristic frequency and intensity is largely affected by the nozzle geometry. For instance, dividing the hole length by half can reduce this frequency from 40 kHz to 20 kHz and increase significantly its power. As far as the shed vortices are concerned, they are periodically generated at the upper hole inlet edge when the flow turns into the hole. They generally propagate on the upper side and reach the nozzle exit if they are sufficiently intense, which in turn depends on the geometry. Shed vortex dynamics lead to a high frequency event whose intensity is affected by the nozzle geometry but whose characteristic frequency  $\sim 2$  MHz is remarkably insensitive to geometric variations. Overall, the impact of nozzle geometry on these structures can be summarized as follows:

- **Needle lift effect:** At high lift, strong flow acceleration at the hole inlet and intense sac flow recirculation trigger relatively strong shed and string vortices, leading to an intermittent in-nozzle flow pattern alternating between large, anisotropic vortices and small, isotropic scales. Significant flow pattern intermittency also appears in X-ray images, which show large, unperturbed interface structures in some of the images and small, isotropic structures in the others. At low lift, flow acceleration at the hole inlet is weak and sac flow recirculation is very intense, leading to a relatively constant flow pattern composed of small scales and cavitation pockets scattered all over the nozzle. Similarly, X-ray images show small, homogeneously distributed structures exiting the nozzle and spreading further downstream.
- **Hole inlet rounding effect:** Decreasing hole inlet rounding increases flow acceleration at the hole inlet and thus enhances the shed vortices. Their interaction with the string vortices is very intense and results in string vortex breakdown on the upper side of the hole, yielding small scales and cavitation on this side and large scales at the bottom. As a consequence, the high frequency event strengthens and the low frequency event weakens, leading to small temporal variation of in-nozzle flow pattern. X-ray images show very stable atomization pattern, consisting of small, homogeneously distributed scales exiting the nozzle on the upper side and small spray dispersion angle variation. Moreover, 2D FFT and 1D FFT applied to the X-ray images identify a characteristic length scale of the order of the distance between shed vortices at the hole outlet identified in the LES.
- **Hole length effect:** Decreasing hole length increases flow separation on the upper side of the hole and sac flow recirculation, which leads to intense string vortices reaching the nozzle exit. The resulting flow pattern is very stable and is dominated by large structures.
- **Hole number effect:** Increasing the number of holes reduces sac flow recirculation and increases the amount of flow that turns from the seat directly into the hole. As a consequence, the string vortices are much weaker and the shed vortices much stronger. The resulting flow pattern consists of shed vortices on the upper side of the hole, a region of negligible vorticity in the middle and large structures at the bottom.
- **Hole taper:** Increasing hole taper results in gradual acceleration along the hole rather than at the inlet, suppressing cavitation and weakening both the string and the shed

vortices. Although the flow pattern is relatively independent of the taper, the small vortices generate as much turbulence as the large ones in the High taper nozzle.

Simultaneous simulation of in-nozzle and near-nozzle flow was performed for the HP hole nozzle. Ligament breakup is governed by surface vortices departing from the hole outlet, which result from the interaction between string vortices and shed vortices. Depending on the location of the string vortices at the outlet, ligament separation can occur on the upper side, in the middle or on the lower side of the spray. This conclusion is supported by X-ray images, which show similar breakup patterns to those predicted by LES.

Although other structures such as needle vortices or side vortices were found to have non-negligible impact on atomization, it was concluded that acting on the shed and string vortices could help control atomization. On the one hand, shed vortices are a source of instability that promotes atomization but can trigger cavitation, reducing nozzle efficiency. Hence, a good design criterion could be to enhance these vortices while breaking them up before the hole exit to induce cavitation collapse. On the other hand, string vortices induce spray asymmetry, flapping and spray pattern variation. However, they can contribute significantly to break up the shed vortices and to mix the resulting scales. Furthermore, they induce non-axial flow rotation that help increase the spray dispersion angle. Therefore, it would be desirable not to suppress them but to keep them separated in order to promote atomization in all sides of the spray.

## 8.2 Recommendation for future work

The research presented in this thesis has opened up several areas for future work:

- Further developments of the 5-Equation model:

Coupling to a turbulence model is necessary to better predict the in-nozzle flow dynamics. Although the 5-Equation model per se is not restricted to any turbulence model in particular, the IFP-C3D code provides the numerical framework for the URANS  $k-\varepsilon$  model. A functional version including both models could be coupled with the already available Lagrangian spray and combustion solvers to provide a complete platform for simultaneous simulation of in-nozzle flow, atomization and combustion.

- Accounting for needle dynamics:

The LES study is limited to static needle lift when the flow structures are already developed. However, the present technological trend is towards strategies involving very short pilot injections preceding the main injection in order to decrease the ignition delay and improve engine performance. Pilot injections are relatively ballistic, meaning that needle opening and closing occupy most of the injection time. Hence, modeling needle motion is necessary to investigate the flow dynamics under such conditions. One of the main challenges associated with moving needle simulations is to ensure mesh quality even at very low needle lifts.



## 8.2 Recommendation for future work

---

Although some methods like re-layering or cell stretching can help increase the quality, there is still uncertainty in how much each one of them affects the numerical solution.

- Accounting for the impact of compressibility and variable fuel properties:

At high injection pressures (i.e.  $>2000$  bar) the flow can easily reach Mach numbers above 0.5 which are beyond the limits of incompressibility. In such a case, compressibility and variable fuel property effects need to be taken into account in order to capture, among others, wave propagation and variations of viscosity, specific heat capacity and surface tension. This is especially important for the study of erosion caused by strong pressure waves and for the study of sac filling and backflow during needle opening and closing, given the large amount of air remaining in the sac. The 5-Equation model proposed in this thesis could be a good candidate to perform this type of simulations.

- Improving cavitation modeling:

Predicting cavitation correctly is key to provide a reliable diagnostic tool for product development where precise description of integral magnitudes such as mass flow rate, discharge coefficient or spray momentum is necessary. Both bubble dynamic models and thermodynamic equilibrium models require some calibration that, in the best case scenario, is only accurate for a range of problems. Hence, further improvements in this area toward generalizing the models would be extremely useful.

- Towards LES of full injector operating under realistic conditions:

Increasing computational power enables more expensive simulations in terms of mesh size, mesh resolution and simulation time. This facilitates the study of full injection events lasting more than 100  $\mu$ s and the analysis of important phenomena such as hole-to-hole interaction, which requires using a full injector mesh instead of a single hole sector. As for spray atomization, higher computational power enables capturing smaller droplets in the near-nozzle field. This is particularly important when using high in-cylinder pressures that lead to very small droplets and the aim of the simulation is to feed another simulation (i.e. Lagrangian spray) with droplet size distribution. Furthermore, capturing smaller droplets and linking them to vortex structures is key to support the development of simplified models correlating atomization with nozzle geometry.

- Towards simultaneous simulation of in-nozzle and near-nozzle flows including cavitation

From a modeling standpoint, one of the biggest challenges is resolving the liquid-gas interface structures propagating outside the nozzle under cavitating conditions. The initial size of bubble nuclei makes their description by interface tracking methods very difficult. On the other hand, although VOF methods can deal with liquid, air and vapor simultaneously, they lead to unacceptable interface diffusion when aiming at capturing small droplets. Further improvements are required on this topic, either generalizing the use of interface tracking methods for cavitating flows or developing high resolution schemes for VOF to minimize interface diffusion.

- Towards coupling in-nozzle and near-nozzle flow simulations to reactive spray simulations

Performing simultaneous simulation of in-nozzle flow, near-nozzle flow, spray and combustion is not feasible in most industrial applications. Hence, it would be very useful if the results obtained in detailed in-nozzle and near-nozzle flow computations could be used to improve the accuracy of the boundary conditions applied to reactive spray simulations. As shown in this work, ligament breakup is correlated with shed vortices developing inside the nozzle and spray angle variation with the string vortices. This information could be further elaborated based on a quantitative analysis of LES results in order to formulate boundary conditions that take into account vortex dynamics and turbulence. Further work would be necessary in order to establish quantitative correlations between geometry, vortex dynamics and liquid atomization.

---

# Bibliography

---

- [1] Bohbot, J., Gillet, N., and Benkenida, A. (2009). IFP-C3D: An unstructured solver for reactive compressible gas flow with spray. *Oil Gas Sci. Technol.*, 65:309–335. [Cited on page 7]
- [2] Velghe, A., Gillet, N., and Bohbot, J. (2010). A high efficiency parallel unstructured solver dedicated to internal combustion engine simulation. *In 22nd International Conference on Parallel Computational Fluid Dynamics*. [Cited on page 7]
- [3] Gavaises, M., Arcoumanis, C., Roth, H., Choi, Y. S., and Theodorakakos, A. (2002). Nozzle flow and spray characteristics from VCO diesel injector nozzles. *THIESEL*. [Cited on page 12]
- [4] Chaves, H. and Ludwig, C. (2005). Characterization of cavitation in transparent nozzles depending on the nozzle geometry. *ILASS*. [Cited on page 12]
- [5] Bauer, D., Chaves, H., and Arcoumanis, C. (2012). Measurements of void fraction distribution in cavitating pipe flow using x-ray CT. *Meas. Sci. Technol*, 23. [Cited on page 12]
- [6] Mitroglou, N., McLorn, M., Gavaises, M., Soteriou, C., and Winterbourne, M. (2014). Instantaneous and ensemble average cavitation structures in Diesel micro-channel flow orifices. *Fuel*, 116:736–742. [Cited on pages 12, 13, and 71]
- [7] Arcoumanis, C., Flora, H., Gavaises, M., and Badami, M. (2000). Cavitation in real-size multi-hole Diesel injector nozzles. *SAE International*. [Cited on pages 12 and 14]
- [8] Mitroglou, N., Lorenzi, M., Santini, M., and Gavaises, M. (2016). Application of x-ray micro-computed tomography on high-speed cavitating diesel fuel flows. *Experiments in Fluids*, 57(175). [Cited on pages 13 and 14]
- [9] Duke, D. J., Kastengren, A. L., Zak Tilocco, F., Swantek, A. B., and Powell, C. F. (2013). X-ray radiography measurements of cavitation nozzle flow. *Atomization and Sprays*, 23(9):841–860. [Cited on pages 13, 15, 71, 79, 80, 82, and 83]
- [10] Chaves, H. (2008). Particle Image Velocimetry measurements of the cavitating flow in a real size transparent VCO nozzle. *ILASS*. [Cited on page 14]

- 
- [11] Mitroglou, N. and Gavaises, M. (2013). Mapping of cavitating flow regimes in injectors for medium-/heavy-duty diesel engines. *International Journal of Engine Research*. [Cited on pages 15 and 16]
- [12] Payri, F., Margot, X., Patouna, S., Ravet, F., and Funk, M. (2009). A CFD study of the effect of the needle movement on the cavitation pattern of Diesel injectors. *SAE International*, (2009-24-0025). [Cited on page 15]
- [13] Payri, R., Gimeno, J., Marti-Aldaravi, P., and Carreres, M. (2015). Assessment on internal nozzle flow initialization in Diesel spray simulations. *SAE Technical Paper*, (2015-01-0921). [Cited on page 15]
- [14] Gavaises, M., Papoulias, D., Andriotis, A., Giannadakis, E., and Theodorakakos, A. (2007). Link between cavitation development and erosion damage in diesel injector nozzles. *SAE Technical Papers*, (2007-01-0246). [Cited on pages 15 and 71]
- [15] Koukouvinis, P., Gavaises, M., Li, J., and Wang, L. (2016). Large Eddy Simulation of Diesel injector including cavitation effects and correlation to erosion damage. *Fuel*, 175:26–39. [Cited on page 15]
- [16] Orley, F., Hickel, S., Schmidt, S. J., and Adams, N. A. (2015). LES of cavitating flow inside a Diesel injector including dynamic needle movement. *J Phys: Conf Ser* 2015;656. [Cited on page 15]
- [17] Kolev, N. (2002). Multiphase Flow Dynamics 3: Turbulence, Gas, Absorption and Release, Diesel Fuel Properties. *Springer Verlag Berlin Heidelberg*, pages 275–308. [Cited on pages 16 and 29]
- [18] Strotos, G., Koukouvinis, P., Theodorakakos, A., Gavaises, M., and Bergeles, G. (2015). Transient heating effects in high pressure diesel injector nozzles. *International Journal of Heat and Fluid Flow*, 51:257–267. [Cited on page 16]
- [19] Shi, J. and Arafin, M. S. (2010). CFD investigation of fuel property effect on cavitating flow in generic nozzle geometries. *ILASS-Europe, Brno, Czech Republic*. [Cited on page 16]
- [20] Dernotte, J., Hespel, C., Houille, S., Foucher, F., and Mounaim-Rousselle, C. (2012). Influence of fuel properties on the Diesel injection process in nonvaporizing conditions. *Atomization and Sprays*, 22(6):461–492. [Cited on page 16]
- [21] Schaschke, C., Fletcher, I., and Glen, N. (2013). Density and viscosity measurement of Diesel fuels at combined high pressure and elevated temperatures. *Processes*, 1:30–48. [Cited on page 16]
- [22] Oefelein, J. C., Dahms, R. N., Lacaze, G., Manin, J. L., and Pickett, L. M. (2012). Effects of pressure on the fundamental physics of fuel injection in Diesel engines. *ICLASS*. [Cited on page 16]
- [23] Wensing, M., Vogel, T., and Gotz, G. (2016). Transition of Diesel spray to a supercritical state under engine conditions. *International Journal of Engine Research*, 17(1):108–119. [Cited on page 16]

- [24] Payri, R., Gimeno, J., Marti-Aldaravi, P., and Venegas, O. (2012). Study of the influence of internal flow on the spray behavior under cavitating conditions using a transparent nozzle. *ICLASS 2012*. [Cited on page 17]
- [25] Sou, A., Pratama, R. H., Tomisaka, T., and Kibayashi, Y. (2012). Cavitation flow in nozzle of liquid injector. *ICLASS*. [Cited on page 17]
- [26] Andriotis, A. and Gavaises, M. (2009). Influence of vortex flow and cavitation on near-nozzle diesel spray dispersion angle. *Atomization and Sprays*, 19(3):247–261. [Cited on pages 17 and 18]
- [27] Giannadakis, E., Gavaises, M., Roth, H., and Arcoumanis, C. (2004). Cavitation modelling in Single-Hole Diesel injector based on Eulerian-Lagrangian approach. *THIESEL 2004*. [Cited on page 17]
- [28] Heimgartner, C. and Leipertz, A. (2000). Investigation of the primary spray breakup close to the nozzle of a common-rail high pressure Diesel injection system. *SAE*, (2000-01-1799). [Cited on pages 17 and 19]
- [29] Eifler, W. (1990). Untersuchungen zur Struktur des instationären Deseleinspritzstrahls im Dusenabereich mit der Methode der Hochfrequenz-Kinematographie. *Dr.-Ing. Dissertation, Universität Kaiserslautern*. [Cited on page 17]
- [30] Berrocal, E., Kristensson, E., Richter, M., Linne, M., and Alden, M. (2008). Application of structured illumination for multiple scattering suppression in planar laser imaging of dense sprays. *Optics Express*, 16(22):17870–17881. [Cited on page 18]
- [31] Paciaroni, M., Linne, M. (2004). Single-shot, two-dimensional ballistic imaging through scattering media. *Applied Optics*, 43(26):5100–5109. [Cited on page 18]
- [32] Linne, M., Paciaroni, M., Hall, T., and Parker, T. (2006). Ballistic imaging of the near field in a diesel spray. *Experiments in Fluids*, 40(6):836–846. [Cited on pages 18 and 19]
- [33] Powell, C. F., Yue, Y., Poola, R., Wang, J., Lai, M., and Schaller, J. (2001). X-ray measurements of high pressure Diesel sprays. *SAE Technical Papers*, (2001-01-0531). [Cited on page 20]
- [34] Lai, M.-C., Zheng, Y., Xie, X.-B., Moon, S., Liu, Z., Gao, J., Zhang, X., Fezzaa, K., Wang, J., and Shi, J. (2011). Characterization of the near-field spray and internal flow of single-hole and multi-hole sac nozzles using phase contrast x-ray imaging and CFD. *SAE International*, (2011-01-0681). [Cited on pages 20 and 21]
- [35] Moon, S., Liu, Z., Gao, J., Dufresne, E., Fezzaa, K., Wang, J., Xie, X., and Lai, M. C. (2010). Ultrafast X-Ray Phase-Contrast Imaging of High-Speed Fuel Sprays from a Two-Hole Diesel Nozzle. *ILASS, Cincinnati*. [Cited on page 21]
- [36] Lai, M. C., Wang, F., Xie, X., Shi, J., Dober, G., Guerrassi, N., Meslem, Y., Gao, Y., Wang, J., Dufresne, E., and Moon, S. (2014). Correlating the nozzle flow to spray and primary breakup using visualization and multi-phase simulation. *SIA International Conference*. [Cited on pages 20 and 33]

- 
- [37] Linne, M. (2012). Analysis of X-ray Phase Contrast Imaging in atomizing sprays. *Exp. Fluids*, 52:1201–1218. [Cited on page 20]
- [38] Baer, M. R. and Nunziato, J. W. (1986). A two-phase mixture theory for the deflagration-to-detonation transition (DDT) in reactive granular materials. *International Journal of Multiphase Flow*, 12:861–889. [Cited on pages 22 and 39]
- [39] Saurel, R. and Lemetayer, O. (2001). A multiphase model for compressible flows with interfaces, shocks, detonation waves and cavitation. *Journal of Fluid Mechanics*, 431:239–271. [Cited on page 22]
- [40] Saurel, R. and Abgrall, R. (1999). A Multiphase Godunov Method for Compressible Multifluid and Multiphase Flows. *Journal of Computational Physics*, 150:425–467. [Cited on pages 22 and 39]
- [41] Abgrall, R. (1996). How to prevent pressure oscillations in multicomponent flow calculations: A quasi conservative approach. *Journal of Computational Physics*, 125:150–160. [Cited on page 22]
- [42] Zein, A., Hantke, M., and Warnecke, G. (2010). Modeling phase transition for compressible two-phase flows applied to metastable liquids. *Journal of Computational Physics*, 229:2964–2998. [Cited on pages 22, 44, 47, 49, 53, 54, 71, 75, 76, 77, 78, and 79]
- [43] Saurel, R. and Abgrall, R. (1999). A simple method for compressible multifluid flows. *SIAM J. Sci. Comput.*, 21(3):1115–1145. [Cited on page 22]
- [44] Saurel, R., Petitpas, F., and Berry, R. A. (2009). Simple and efficient relaxation methods for interfaces separating compressible fluids, cavitating flows and shocks in multiphase mixtures. *Journal of Computational Physics*, 228(5):1678–1712. [Cited on page 22]
- [45] Pelanti, M. and Shyue, K.-M. (2014). A mixture-energy-consistent six-equation two-phase numerical model for fluids with interfaces, cavitation and evaporation waves. *Journal of Computational Physics*, 259:331–357. [Cited on page 22]
- [46] Toro, E. F. (2009). Riemann solvers and numerical methods for fluid dynamics. *Springer Berlin Heidelberg*. [Cited on page 22]
- [47] LeVeque, R. J. (2002). Finite volume methods for hyperbolic problems. *Cambridge University Press*. [Cited on page 22]
- [48] Roe, P. L. (1981). Approximate Riemann solvers, parameter vectors, and difference schemes. *Journal of Computational Physics*, 43:357–372. [Cited on page 22]
- [49] Bore, S. L. (2014). Numerical solution of the six-equation two-phase single velocity model with finite relaxation. *Applied Physics*. [Cited on page 22]
- [50] Aursand, P., Evje, S., Flatten, T., Giljarhus, K. E. T., and Munkejord, S. T. (2014). An exponential time-differencing method for monotonic relaxation systems. *Applied Numerical Mathematics*, 80(0):1–21. [Cited on page 22]
- [51] Kapila, A. K., Menikoff, R., Bdzil, J. B., Son, S. F., and Stewart, D. S. (2001). Two-phase modeling of deflagration-to-detonation transition in granular materials: Reduced equations. *Physics of Fluids*, 13. [Cited on page 22]

## Bibliography

---

- [52] Kapila, A. K., Son, S. F., Bdzil, J. B., Menikoff, R., and Stewart, D. S. (1997). Two-phase modeling of DDT: Structure of the velocity-relaxation zone. *Phys. Fluids*, 9. [Cited on page 23]
- [53] Allaire, G., Clerc, S., and Kokh, S. (2002). A five-equation model for the simulation of interfaces between compressible flows. *Journal of Computational Physics*, 181:577–616. [Cited on page 23]
- [54] Allaire, G., Faccanoni, G., and Kokh, S. (2007). A strictly hyperbolic equilibrium phase transition model. *C. R. Acad. Sci. Paris, Ser. I*, 344:135–140. [Cited on page 23]
- [55] Faccanoni, G., Kokh, S., and Allaire, G. (2010). Approximation of liquid-vapor phase transition for compressible fluids with tabulated EOS. *C. R. Acad. Sci. Paris, Ser. I*, 348:473–478. [Cited on page 23]
- [56] Faccanoni, G., Kokh, S., and Allaire, G. (2012). Modelling and simulation of liquid-vapor phase transition in compressible flows based on thermodynamical equilibrium. *ESAIM: Mathematical Modelling and Numerical Analysis*, 46:1029–1054. [Cited on page 23]
- [57] Saurel, R., Petitpas, F., and Abgrall, R. (2008). Modelling phase transition in metastable liquids: application to cavitating and flashing flows. *Journal of Fluid Mechanics*, 607:313–350. [Cited on page 23]
- [58] Karni, S. (1993). Multicomponent flow calculations by consistent primitive algorithm. *Journal of Computational Physics*, 112:31–43. [Cited on page 23]
- [59] Morin, A. and Flatten, T. (2016). A two-fluid four-equation model with instantaneous thermodynamical equilibrium. *ESAIM: Mathematical Modelling and Numerical Analysis*, 50(4):1167–1192. [Cited on page 23]
- [60] Avva, R. K., Singhal, A. K., and Gibson, D. H. (1995). An enthalpy based model of cavitation. *ASME-PUBLICATIONS-FED*, 226:63–70. [Cited on page 23]
- [61] Bilicki, Z., Kwidzinski, R., and Mohammadein, S. A. (1996). An estimation of a relaxation time of heat and mass exchange in the liquid-vapour bubble flow. *International Journal of Heat and Mass Transfer*, 39(4). [Cited on page 23]
- [62] Bilicki, Z. and Kestin, J. (1990). Physical aspects of the relaxation model in two-phase flow. *Proceedings of the Royal Society*, 428(1875). [Cited on page 23]
- [63] Schmidt, D. P., Gopalakrishnan, S., and Jasak, H. (2010). Multi-dimensional simulation of thermal non-equilibrium channel flow. *International Journal of Multiphase Flow*, 36:284–292. [Cited on page 23]
- [64] Ning, W., Reitz, R. D., Diwakar, R., and Lippert, A. M. (2008). A numerical investigation of nozzle geometry and injection condition effects on Diesel fuel injection flow physics. *SAE International*, (2008-01-0936). [Cited on pages 23 and 27]
- [65] Guillard, H. and Labois, M. (2006). Numerical modeling of compressible two-phase flows. *European Conference on Computational Fluid Dynamics ECCOMAS CFD*. [Cited on page 24]

- 
- [66] Habchi, C. (2013). A Gibbs free energy relaxation model for cavitation simulation in diesel injectors. *ILASS Europe*. [Cited on page 24]
- [67] Rayleigh, L. (1917). On the pressure developed in a liquid during the collapse of a spherical cavity. *Philosophical Magazine*, 34(200):94–98. [Cited on page 24]
- [68] Plesset, M. S. (1949). The dynamics of cavitation bubbles. *Journal of Applied Mechanics*, 16:277–282. [Cited on page 24]
- [69] Plesset, M. S. and Prosperetti, A. (1977). Bubble dynamics and cavitation. *Annual review of fluid mechanics*, 9:145–185. [Cited on page 24]
- [70] Brennen, C. E. (1995). Cavitation and bubble dynamics. *Oxford University Press*. [Cited on pages 24 and 201]
- [71] Hinze, J. O. (1975). Turbulence. *McGraw-Hill Publishing Co., New York*. [Cited on pages 24, 30, and 204]
- [72] Giannadakis, E., Gavaises, M., and Arcoumanis, C. (2008). Modelling of cavitation in Diesel injector nozzles. *Journal of Fluid Mechanics*, 616:153–193. [Cited on pages 24 and 109]
- [73] Gavaises, M. and Giannadakis, E. (2004). Modelling of cavitation in large scale Diesel injector nozzles. *ILASS Europe*. [Cited on page 24]
- [74] Giannadakis, E., Papoulias, D., Theodorakakos, A., and Gavaises, M. (2008). Simulation of cavitation in outward-opening piezo-type pintle injector nozzles. *Proceedings of the Institution of Mechanical Engineers, Part D: Journal of Automobile Engineering*, 222:1895–1910. [Cited on page 24]
- [75] Koukouvinis, P., Gavaises, M., Supponen, O., and Farhat, M. (2016). Numerical simulation of a collapsing bubble subject to gravity. *Physics of Fluids*, 28. [Cited on page 24]
- [76] Battistoni, M., Som, S., and Longman, D. E. (2013). Comparison of mixture and multi-fluid models for in-nozzle cavitation prediction. *Proceedings of the ASME, ICEF2013-19093*. [Cited on pages 24, 71, 79, 80, 81, 82, 85, and 86]
- [77] Faeth, G. M. (1990). Structure and atomization properties of dense turbulent sprays. in *Twenty-Third Symposium on Combustion/The combustion Institute*. [Cited on pages 24, 25, and 26]
- [78] Reitz, R. D. and Bracco, F. V. (1982). Mechanism of atomization of a liquid jet. *Physic of Fluids*, 25:1730–1742. [Cited on pages 24 and 26]
- [79] Chehroudi, B., Chen, S.-H., Bracco, F. V., and Onuma, Y. (1985). On the intact core of full-cone sprays. *SAE international*. [Cited on page 25]
- [80] Reitz, R. D. and Bracco, F. V. (1979). On the dependence of spray angle and other spray parameters on nozzle design and operating conditions. *SAE International*. [Cited on page 25]



## Bibliography

---

- [81] Arai, M., Tabata, M., Hiroyasu, H., and Shimizu, M. (1984). Disintegrating process and spray characterization of fuel jet injected by a Diesel nozzle. *SAE International*. [Cited on page 25]
- [82] Siebers, D. L. (1999). Scaling liquid-phase fuel penetration in Diesel sprays based on mixing-limited vaporization. *SAE Technical Papers*, (1999-01-0528). [Cited on page 25]
- [83] Hiroyasu, H. and Arai, M. (1990). Structures of fuel sprays in Diesel engines. *SAE International*. [Cited on page 25]
- [84] Santos, F. D. and Moyne, L. L. (2011). Spray atomization models in engine applications, from correlations to Direct Numerical Simulations. *Oil and Gas Science and Technology - Rev. IFP Energies Nouvelles*, 66(5):801–822. [Cited on page 25]
- [85] Faeth, G. M., Hsiang, L. P., and Wu, P.-K. (1995). Structure and breakup properties of sprays. *International Journal of Multiphase Flow*, 21:99–127. [Cited on page 25]
- [86] Reitz, R. D. (1987). Modeling atomization processes in high-pressure vaporizing sprays. *Atomization and Spray Technology*, 3:309–337. [Cited on pages 26 and 28]
- [87] Kuensberg, S. C., Kong, S. C., and Reitz, R. D. (1999). Modeling the effects of injector nozzle geometry on Diesel sprays. *SAE Technical Paper*. [Cited on page 26]
- [88] Martinez, L., Benkenida, A., and Cuenot, B. (2010). A model for the injection boundary conditions in the context of 3D simulation of Diesel spray: Methodology and validation. *Fuel*, 89:219–228. [Cited on page 26]
- [89] Xue, Q., Battistoni, M., Som, S., and Quan, S. (2014). Eulerian CFD modeling of coupled nozzle flow and spray with validation against X-ray radiography data. *SAE International*, 2:1061–1072. [Cited on page 26]
- [90] O’Rourke, P. J. and Amsden, A. A. (1987). The TAB method for numerical calculation of spray droplet breakup. *SAE Technical Paper*, (872089). [Cited on pages 26 and 28]
- [91] Taylor, G. I. (1963). The shape and acceleration of a drop in a high speed air stream. *Technical report*, ed. G. K. Batchelor. [Cited on page 26]
- [92] Vallet, A. and Borghi, R. (1999). Modelisation eulerienne de l’atomisation d’un jet liquide. *C. R. Acad. Sci. Paris, Ser. II*, 327:1015–1020. [Cited on page 27]
- [93] Vallet, A., Burluka, A. A., and Borghi, R. (2001). Development of a Eulerian model for the atomization of a liquid jet. *Atomization and Sprays*, 11:619–642. [Cited on page 27]
- [94] Lebas, R., Menard, T., Beau, P. A., Berlemont, A., and Demoulin, F. X. (2009). Numerical simulation of primary break-up and atomization: DNS and modelling study. *International Journal of Multiphase Flow*, 35(3). [Cited on page 27]
- [95] Chesnel, J., Reveillon, J., Menard, T., and Demoulin, F. (2011). Large-Eddy Simulation of liquid jet atomization. *Atomization and Sprays*, 21(9):711–736. [Cited on page 27]
- [96] Hoyas, S., Gil, A., Margot, X., Khuong-Anh, D., and Ravet, F. (2013). Evaluation of the Eulerian-Lagrangian Spray Atomization (ELSA) model in spray simulations: 2D cases. *Mathematical and Computer Modelling*, 57(7-8):1686–1693. [Cited on page 27]

- 
- [97] Desportes, A., Zellat, M., Desoutter, G., Abouri, D., Liang, Y., and Ravet, F. (2010). Validation and application of the Eulerian-Lagrangian Spray Atomization (ELSA) model for the diesel injection simulation. *SAE*. [Cited on page 27]
- [98] Youngs, D. L. (1982). Time-dependent multi-material flow with large fluid distortion. *Numerical Methods for Fluid Dynamics*, pages 785–807. [Cited on pages 27 and 110]
- [99] Pilliod, J. E. and Puckett, E. G. (2003). Second-order accurate volume-of-fluid algorithms for tracking material interfaces. *Journal of Computational Physics*, 199(2):465–502. [Cited on page 27]
- [100] Dyadechko, V. and Shashkov, M. (2006). Moment-of-Fluid interface reconstruction. *Los Alamos National laboratory, LA-UR-05-7571*. [Cited on page 27]
- [101] Hirt, C. W. and Nichols, B. D. (1981). Volume of Fluid (VOF) method for the dynamics of free boundaries. *Journal of Computational Physics*, 39:201–225. [Cited on page 27]
- [102] Ubbink, O. (1997). Numerical prediction of two fluid systems with sharp interfaces. *PhD thesis, Imperial College of Science, Technology and Medicine, London, England*. [Cited on page 27]
- [103] Osher, S. and Sethian, J. A. (1988). Fronts propagating with curvature-dependent speed: Algorithms based on Hamilton-Jacobi formulations. *Journal of Computational Physics*, 79:12–49. [Cited on page 27]
- [104] Sussman, M., Fatemi, E., Smereka, P., and Osher, S. (1998). Improved level set method for incompressible two-phase flows. *Computers and Fluids*, 27(5-6):663–680. [Cited on page 28]
- [105] Sussman, M., Almgren, A. S., Bell, J. B., Colella, P., Howell, L. H., and Welcome, M. L. (1999). An adaptive level set approach for incompressible two-phase flows. *Journal of Computational Physics*, 148:81–124. [Cited on page 28]
- [106] Olsson, E., Kreiss, G., and Zahedi, S. (2007). A conservative Level-Set method for two phase flow II. *Journal of Computational Physics*, 225:785–807. [Cited on pages 28 and 109]
- [107] Enright, D., Fedkiw, R., Ferziger, J., and Mitchell, I. (2002). A hybrid particle level set method for improved interface capturing. *Journal of Computational Physics*, 183:83–116. [Cited on page 28]
- [108] Sussman, M. and Puckett, E. G. (2000). A coupled Level Set and Volume-of-Fluid method for computing 3D and axisymmetric incompressible two-phase flows. *Journal of Computational Physics*, 162(2):301–337. [Cited on page 28]
- [109] Menard, T., Tanguy, S., and Berlemont, A. (2007). Coupling level set/vof/ghost fluid methods: Validation and application to 3d simulation of the primary break-up of a liquid jet. *International Journal of Multiphase Flow*, pages 510–524. [Cited on page 28]
- [110] Befrui, B., Corbinelli, G., Spiekermann, P., Shost, M., and Lai, M.-C. (2012). Large-Eddy Simulation of GDI single-hole flow and near-field spray. *SAE International*, (2012-01-0392). [Cited on pages 28 and 33]

## Bibliography

---

- [111] Lai, M. C., Wang, T. C., Xie, X., Han, J., Henein, N. A., Schwarz, E., and Bryzik, W. (1999). Microscopic characterization of Diesel sprays at VCO nozzle exit. *Fuels Lubricants*, 107:1283–1293. [Cited on page 28]
- [112] Udaykumar, H. S. and Shyy, W. (1995). Grid-supported marker particle scheme for interface tracking. *Numerical Heat Transfer Part B (Fundamentals)*, 27(2):127–153. [Cited on page 28]
- [113] Morris, J. P. (2000). Simulating surface tension with smoothed particle hydrodynamics. *International Journal for Numerical Methods in Fluids*, 33:333–353. [Cited on page 28]
- [114] Unverdi, S. O. and Tryggvason, G. (1992). A front-tracking method for viscous, incompressible, multi-fluid flows. *Journal of Computational Physics*, 100:25–37. [Cited on page 28]
- [115] Welch, S. W. J. (1995). Local simulation of two-phase flows including interface tracking with mass transfer. *Journal of Computational Physics*, 121:142–154. [Cited on page 28]
- [116] Hu, H. H., Patankar, N. A., and Zhu, M. Y. (2001). Direct numerical simulations of fluid-solid systems using the arbitrary Lagrangian-Eulerian technique. *Journal of Computational Physics*, 169:427–462. [Cited on page 28]
- [117] Perot, B. and Nallapati, R. (2003). A moving unstructured staggered mesh method for the simulation of incompressible free-surface flows. *Journal of Computational Physics*, 184:192–214. [Cited on page 28]
- [118] O’Rourke, P. J. (1981). Collective drop effects on vaporizing liquid sprays. *PhD thesis, Princeton University, Princeton, New Jersey*. [Cited on page 28]
- [119] Schmidt, D. and Rutland, C. J. (2000). A new droplet collision algorithm. *Journal of Computational Physics*, 164:62–80. [Cited on page 28]
- [120] Schmidt, D. (2006). Theoretical analysis for achieving high-order spatial accuracy in lagrangian/eulerian source terms. *International Journal Numerical Methods Fluids*, 52:843–865. [Cited on page 28]
- [121] Stanton, D. W. and Rutland, C. J. (1996). Modeling fuel film formation and wall interaction in Diesel engines. *SAE Paper 960628*. [Cited on page 28]
- [122] O’Rourke, P. J. and Amsden, A. A. (2000). A spray/wall interaction submodel for the KIVA-3 wall film model. *SAE Paper*, (2000-01-0271). [Cited on page 28]
- [123] Wilcox, D. C. (2006). Turbulence modeling for CFD. *DCW Industries, Inc.* [Cited on page 29]
- [124] Smagorinsky, J. (1963). General circulation experiments with the primitive equations. *Monthly Weather Review*, 91(3):99–164. [Cited on pages 29 and 31]
- [125] Smith, A. M. O. and Cebeci, T. (1967). Numerical solution of the turbulent boundary layer equations. *Douglas aircraft division report DAC 33735*. [Cited on page 30]
- [126] Baldwin, B. S. and Lomax, H. (1978). Thin layer approximation and algebraic model for separated turbulent flows. *AIAA Paper*, pages 78–257. [Cited on page 30]

- 
- [127] Baldwin, B. S. and Barth, T. J. (1990). A one-equation turbulence transport model for high Reynolds number wall-bounded flows. *NASA TM 102847*. [Cited on page 30]
- [128] Spalart, P. R. and Allmaras, S. R. (1992). A one-equation turbulence model for aerodynamic flows. *AIAA Paper 92-0439*. [Cited on page 30]
- [129] Launder, B. E. and Sharma, B. I. (1974). Application of the energy dissipation model of turbulence to the calculation of flow near a spinning disc. *Letters in Heat and Mass Transfer*, 1(2):131–138. [Cited on page 30]
- [130] Wilcox, D. C. (1988). Re-assessment of the scale-determining equation for advanced turbulence models. *AIAA Journal*, 26(11):1299–1310. [Cited on page 30]
- [131] Menter, F. R. (1993). Zonal two equation k- $\omega$  turbulence models for aerodynamic flows. *AIAA Paper 93-2906*. [Cited on page 30]
- [132] Durbin, P. (1995). Separated flow computations with the k- $\epsilon$ -v2 model. *AIAA Journal*, 33:659–664. [Cited on page 30]
- [133] Launder, B. E., Reece, G. J., and Rodi, W. (1975). Progress in the development of a Reynolds-Stress turbulent closure. *Journal of Fluid Mechanics*, 68(3):537–566. [Cited on page 30]
- [134] Wallin, S. and Johansson, A. V. (2000). An Explicit Algebraic Reynolds Stress Model for Incompressible and Compressible Turbulent Flows. *Journal of Fluid Mechanics*, 403(2000):89–132. [Cited on page 30]
- [135] Salvador, F. J., Martinez-Lopez, J., Caballer, M., and De Alfonso, C. (2013). Study of the influence of the needle lift on the internal flow and cavitation phenomenon in diesel injector nozzles by CFD using RANS methods. *Energy Conversion and Management*, 66:246–256. [Cited on page 30]
- [136] Brusiani, F., Bianchi, G. M., and Falfari, S. (2014). Influence of cylindrical, k, and ks Diesel nozzle shape on the injector internal flow field and on the emerging spray characteristics. *SAE International*, (2014-01-1428). [Cited on page 30]
- [137] Shi, J., Aguado, P. L., Dober, G., Guerrassi, N., Bauer, W., and Lai, M.-C. (2016). Using LES and x-ray imaging to understand the influence of injection hole geometry on Diesel spray formation. *THIESEL*. [Cited on page 30]
- [138] Menter, F. R. (2015). Turbulence modeling for engineering flows. *ANSYS technical paper*. [Cited on page 30]
- [139] Menter, F. R. (1992). Influence of freestream values on k- $\omega$  turbulence model predictions. *AIAA Journal*, 30(6):1657–1659. [Cited on page 30]
- [140] Menter, F. R. (2015). Two-equation eddy-viscosity turbulence models for engineering applications. *AIAA*, 32(8):1598–1605. [Cited on page 30]
- [141] Langtry, R. and Menter, F. R. (2009). A correlation-based transition model using local variables for unstructured parallelized CFD codes. *AIAA Journal*, 47(12). [Cited on page 30]

## Bibliography

---

- [142] Macian, V., Payri, R., Margot, X., and Salvador, F. J. (2003). A CFD analysis of the influence of Diesel nozzle geometry on the inception of cavitation. *Atomization and Sprays*, 13:579–604. [Cited on page 30]
- [143] Arcoumanis, C., Gavaises, M., Nouri, J. M., and Abdul-Wahab, E. (1998). Analysis of the flow in the nozzle of a vertical multi-hole Diesel engine injector. *SAE Paper 980811*. [Cited on page 30]
- [144] Kampmann, S., Dittus, B., Mattes, P., and Kirner, M. (1996). The influence of hydro-grinding at VCO nozzle on the mixture preparation in a DI Diesel engine. *SAE Paper 960867*. [Cited on page 30]
- [145] Shi, J., Guerrassi, N., Dober, G., Karimi, K., and Meslem, Y. (2014). Complex physics modelling of diesel injector nozzle flow and spray supported by new experiments. *THIESEL*. [Cited on page 30]
- [146] Moon, S., Gao, Y., Park, S., Wang, J., Kurimoto, N., and Nishijima, Y. (2015). Effect of the number and position of nozzle holes on in- and near-nozzle dynamic characteristics of Diesel injection. *Fuel*, 150:112–122. [Cited on page 31]
- [147] Thornber, B. (2007). Implicit Large-Eddy Simulation for unsteady multi-component compressible turbulent flows. *PhD, School of Engineering, Cranfield University, UK*. [Cited on page 31]
- [148] Germano, M., Piomelli, U., Moin, P., and Cabot, W. H. (1991). A dynamic subgrid-scale eddy viscosity model. *Physics of Fluids A*, 3(7):1760–1765. [Cited on page 32]
- [149] Lilly, D. K. (1991). A proposed modification of the germano subgrid-scale closure method. *Physics of Fluids A*, 4(3):633–635. [Cited on page 32]
- [150] Nicoud, F. and Ducros, F. (1999). Subgrid-scale stress modelling based on the square of the velocity gradient tensor flow. *Turbulence and combustion*, 62(3):183–200. [Cited on pages 32, 98, and 204]
- [151] Wray, A. A. and Hunt, J. C. R. (1989). Algorithms for classification of turbulent structures. *Topological Fluid Mechanics, Proceedings of the IUTAM Symposium*, pages 95–104. [Cited on pages 32 and 204]
- [152] Kim, W. W. and Menon, S. (1997). Application of the localized dynamic subgrid-scale model to turbulent wall-bounded flows. *Technical Report AIAA-97-0210*. [Cited on page 32]
- [153] Strelets, M. (2001). Detached Eddy Simulation of massively separated flows. *AIAA Paper 2001-0879*. [Cited on page 32]
- [154] Spalart, P., Deck, S., Shur, M., Squires, K., Strelets, M., and Travin, A. (2006). A new version of Detached Eddy Simulation, resistant to ambiguous grid densities. *Journal of Theoretical and Computational Fluid Dynamics*, 20:181–195. [Cited on page 32]
- [155] Menter, F. R. and Egorov, Y. (2010). Scale-adaptive simulation method for unsteady flow predictions. part 1: Theory and model description. *Journal Flow Turbulence and Combustion*, 85(1):113–138. [Cited on page 32]

- 
- [156] Shi, J.-M., Wenzlawski, K., Helie, J., Nuglisch, H., and Cousin, J. (2010). URANS and SAS analysis of flow dynamics in a GDI nozzle. *ILASS Europe*. [Cited on page 33]
  - [157] Hunt, J. C. R., Wray, A., and Moin, P. (1988). Eddies, stream, and convergence zones in turbulent flows. *Center of Turbulence Research Report*, (CTR-S88). [Cited on page 33]
  - [158] Kolar, V. (2007). Vortex identification: New requirements and limitations. *International Journal of Heat and Fluid Flow*, pages 638–652. [Cited on page 33]
  - [159] Chong, M. S., Perry, A. E., and Cantwell, B. J. (1990). A general classification of threedimensional flow fields. *Physics of Fluids A*, 2(5):765–777. [Cited on page 33]
  - [160] Chakraborty, P., Balachandar, S., and Adrian, R. J. (2005). On the relationships between local vortex identification schemes. *Journal of Fluid Mechanics*, pages 189–214. [Cited on pages 33 and 34]
  - [161] Jeong, J. and Hussain, F. (1995). On the identification of a vortex. *Journal of Fluid Mechanics*, pages 69–94. [Cited on page 33]
  - [162] Zhou, J., Adrian, R. J., Balachandar, S., and Kendall, T. M. (1999). Mechanisms for generating coherent packets of hairpin vortices in channel flow. 387:353–396. [Cited on page 33]
  - [163] Haller, G. (2001). Distinguished material surfaces and coherent structures in 3d fluid flows. *Physica D*, 149:248–277. [Cited on page 34]
  - [164] Haller, G. (2005). An objective definition of a vortex. *Journal of Fluid Mechanics*, pages 1–26. [Cited on page 34]
  - [165] Perrin, R., Braza, M., Cid, E., Cazin, S., Barthet, A., Sevrain, A., Mockett, C., and Thiele, F. (2007). Obtaining phase averaged turbulence properties in the near wake of a circular cylinder at high Reynolds number using POD. *Experiments in Fluids*, 43:341–355. [Cited on page 35]
  - [166] Schmid, P., Meyer, K., and Pust, O. (2009). Dynamic Mode Decomposition and Proper Orthogonal Decomposition of flow in a lid-driven cylindrical cavity. *Proceedings of the 8th International Symposium on Particle Image Velocimetry*. [Cited on page 35]
  - [167] Schmid, P. (2010). Dynamic Mode Decomposition of numerical and experimental data. *Journal of Fluid Mechanics*, 656(1):5–28. [Cited on page 35]
  - [168] Muld, T. W., Efraimsson, G., and Henningson, D. S. (2012). Flow structures around a high-speed train extracted using Proper Orthogonal Decomposition and Dynamic Mode Decomposition. *Computers and Fluids*, 57:87–97. [Cited on page 35]
  - [169] Zhuang, H., Hung, D. L. S., Xu, M., and Chen, H. (2013). Analysis of spray structure and penetration variations using Proper Orthogonal Decomposition. *ILASS Asia*. [Cited on page 35]
  - [170] Chen, H., Hung, D. L. S., Xu, M., Zhuang, H., and Yang, J. (2014). Proper Orthogonal Decomposition analysis of fuel spray structure variation in a spark-ignition direct-injection optical engine. *Experiments in Fluids*, 55. [Cited on page 35]

## Bibliography

---

- [171] Fogleman, M., Lumley, J., Rempfer, D., and Haworth, D. (2004). Application of the proper orthogonal decomposition to datasets of internal combustion engine flows. *Journal of Turbulence*. [Cited on page 35]
- [172] Sakowitz, A. (2013). Computation and analysis of EGR mixing in Internal Combustion Engine manifolds. *Technical report, Royal Institute of Technology, Department of Mechanics, Stockholm, Sweden*, (2013:02). [Cited on page 35]
- [173] Tirunagari, S., Vuorinen, V., Kaario, O., and Larimi, M. (2012). Analysis of Proper Orthogonal Decomposition and Dynamic Mode Decomposition on LES of subsonic jets. *CSI Journal of Computing*, 1(3). [Cited on pages 35 and 36]
- [174] Himmelblau, D. M. (1964). Diffusion of dissolved gases in liquids. *Chem. Rev.*, 64(5):527–550. [Cited on page 39]
- [175] Baur, T., Kongeter, J., and Leucker, R. (1998). Effects of dissolved gas on cavitation inception in free surface flows. *Third Int. Symposium on Cavitation*. [Cited on page 39]
- [176] Arcoumanis, C., Gavaises, M., and Flora, H. (2001). Visualisation of cavitation in diesel engine injectors. *Mech. Ind.*, 2:375–381. [Cited on page 39]
- [177] Murrone, A. and Guillard, H. (2005). A five equation reduced model for compressible two phase flow problems. *Journal of Computational Physics*, 202:664–698. [Cited on pages 39, 42, and 47]
- [178] Saurel, R. and Gallouet, T. (1998). Modeles et methodes numeriques pour les ecoulements fluides. *Cours de DEA, Centre de Mathematique et d’Informatique*. [Cited on page 40]
- [179] Baer, M. R. (1992). A numerical study of shock wave reflections on low density foam. *Shock Waves*, 2:121–124. [Cited on page 40]
- [180] Stewart, H. B. and Wendroff, B. (1984). Two-phase flow: models and methods. *Journal of Computational Physics*, 56:363–409. [Cited on page 42]
- [181] Drew, D. A. and Passman, S. L. (1998). Theory of multicomponent fluids. *Applied Mathematical Sciences*, 135. [Cited on page 42]
- [182] Petitpas, F., Massoni, J., Saurel, R., Lapebie, E., and Munier, L. (2009). Diffuse interface models for high speed cavitating underwater systems. *Journal of Multiphase Flows*, 35(8):747–759. [Cited on page 44]
- [183] Le Metayer, O., Massoni, J., and Saurel, R. (2004). Elaborating equations of state of a liquid and its vapor for two-phase flow models. *International Journal of Thermal Sciences*, 43:265–276. [Cited on pages 45 and 191]
- [184] Lagarias, J. C., Reeds, J. A., Wright, M. H., and Wright, P. E. (1998). Convergence properties of the Nelder-Mead Simplex method in low dimensions. *SIAM Journal of Optimization*, 9(1):112–147. [Cited on pages 45 and 192]
- [185] Amsden, A. A., O’Rourke, P. J., and Butler, T. D. (1989). KIVA-II: A Computer Program for Chemically Reactive Flows with Sprays. *Los Alamos National Laboratory*. [Cited on pages 55, 60, 65, and 196]

- [186] v. Leer, B. (1979). Towards the ultimate conservative difference scheme. A second-order sequel to Godunov's method. *Journal of Computational Physics*, pages 101–136. [Cited on page 65]
- [187] Press, W. H., Flannery, B. P., Teukolsky, S. A., and Vetterling, W. T. (1992). Secant Method, False Position Method, and Ridders' Method. *Numerical Recipes in FORTRAN: The Art of Scientific Computing*, pages 347–352. [Cited on page 69]
- [188] Gavaises, M. and Arcoumanis, C. (2006). Cavitation inside multi-hole injectors for large Diesel engines and its effect on the near-nozzle spray structure. *SAE International*, (2006-01-1114). [Cited on page 71]
- [189] Payri, R., Salvador, F. J., Gimeno, J., and Venegas, O. (2013). Study of cavitation phenomenon using different fuels in a transparent nozzle by hydraulic characterization and visualization. *Experimental Thermal and Fluid Science*, 44:235–244. [Cited on page 71]
- [190] Sou, A., Minami, S., Prasetya, R., Pratama, R. H., Moon, S., Wada, Y., and Yokohata, H. (2015). X-ray visualization of cavitation in nozzles with various sizes. *ICLASS*. [Cited on page 71]
- [191] Simoes-Moreira, J. R., Massoni, J., and Saurel, R. (1999). Evaporation waves in superheated dodecane. *Journal of Fluid Mechanics*, 382:63–86. [Cited on page 77]
- [192] Perry, R. H. and Green, D. W. (1997). Perry's Chemicals Engineers' Handbook. *McGraw-Hill*. [Cited on page 82]
- [193] Blazek, J. (2001). Computational Fluid Dynamics: Principles and Applications. *Elsevier*. [Cited on page 82]
- [194] ANSYS, I. (2015). FLUENT Theory Guide. *Release 15.0*. [Cited on pages 98, 101, 102, 106, 108, 110, and 203]
- [195] Zwart, P. J., Gerber, A. G., and Belamri, T. (2004). A two-phase flow model for predicting cavitation dynamics. *Fifth International Conference on Multiphase Flow, Yokohama, Japan*. [Cited on pages 98 and 202]
- [196] Kraichnan, R. (1970). Diffusion by a random velocity field. *Physics of Fluids*, 11:21–31. [Cited on page 101]
- [197] Smirnov, R., Shi, S., and Celik, I. (2001). Random flow generation technique for Large-Eddy Simulations and Particle-Dynamics Modeling. *Journal of Fluids Engineering*, 123:359–371. [Cited on page 101]
- [198] Sergent, E. (2002). Vers une methodologie de couplage entre la simulation des grandes echelles et les modeles statistiques. *PhD thesis. Ecole Centrale de Lyon*. [Cited on page 101]
- [199] Mathey, F., Cokljat, D., Bertoglio, J. P., and Sergent, E. (2003). Specification of LES Inlet Boundary Condition Using Vortex Method. *International Symposium on Turbulence, Heat and Mass Transfer, Antalya, Turkey, Begell House, Inc*. [Cited on page 101]



## Bibliography

---

- [200] Vandoormaal, J. P. and Raithby, G. D. (1984). Enhancements of the simple method for predicting incompressible fluid flows. *Numer. Heat Transfer*, 7:147–163. [Cited on page 102]
- [201] Shi, J., Aguado, P. L., Guerrassi, N., and Dober, G. (2017). Understanding high pressure Diesel injection primary breakup by using Large-Eddy Simulation and x-ray spray imaging. *MTZ Worldwide, issue 3/2017*. [Cited on page 151]
- [202] Menter, F. (2015). Best Practice: Scale-Resolving Simulations in ANSYS CFD. *Version 2.0, ANSYS Inc.* [Cited on page 204]
- [203] Vasquez, S. A. and Ivanov, V. A. (2000). A phase coupled method for solving multiphase problems on unstructured meshes. *Proceedings of ASME*. [Cited on page 206]
- [204] Rhie, C. M. and Chow, W. L. (1983). Numerical study of the turbulent flow past an airfoil with trailing edge separation. *AIAA Journal*, 21(11):1525–1532. [Cited on page 207]
- [205] Leonard, B. P. (1991). The ULTIMATE conservative difference scheme applied to unsteady one-dimensional advection. *Comp. Methods Appl. Mech. Eng.*, 88:17–74. [Cited on page 208]
- [206] Gaskell, P. H. and Lau, A. K. C. (1988). Curvative-compensated convective transport: SMART, a new boundedness-preserving transport algorithm. *International Journal for Numerical Methods in Fluids*, 8(6):617–641. [Cited on page 208]
- [207] Chen, H., Reuss, D. L., and Sick, V. (2012). On the use and interpretation of proper orthogonal decomposition of in-cylinder engine flows. *Measurement Science and Technology*, 23(085302). [Cited on page 215]
- [208] Chen, H., Reuss, D. L., Hung, D. L. S., and Sick, V. (2013). A practical guide for using proper orthogonal decomposition in engine research. *International Journal of Engine Research*, 14(4):307–319. [Cited on page 215]
- [209] Golub, G. H. and Reinsch, C. (1970). Singular value decomposition and least squares solutions. *Numerische Mathematik*, 14(5):403–420. [Cited on page 217]



## Appendix A

---

# Calculation of SG-EOS parameters

---

The calculation of SG-EOS parameters  $\pi$ ,  $q$ ,  $C_{v_l}$ ,  $\gamma_l$  is done following the ideas of LeMetayer et al. [183] to approximate the thermodynamic curves of the liquid. In order to build the SG-EOS, one needs the experimental curves of specific enthalpy,  $h_{l_{exp}}(T)$ , specific volume at saturated conditions,  $v_{l_{exp}}(T)$ , and vapor pressure,  $p_{sat_{exp}}(T)$ . Using the constitutive equations of the liquid (3.46), (3.47) and the definition of specific enthalpy

$$h_l(T) = e_l + \frac{p}{\rho_l} = \frac{\gamma_l(p + \pi)}{\rho_l(\gamma_l - 1)} + q = \gamma_l C_{v_l} T + q = \gamma_l C_{v_l}(T - T_0) + h_{l_0} = C_{p_l}(T - T_0) + h_{l_0} \quad (\text{A.1})$$

$$q = h_{l_0} - C_{p_l} T_0 \quad (\text{A.2})$$

A first order approximation to the experimental curve  $h_{l_{exp}}(T)$  can be obtained by linear regression using the least squares method. Given  $M$  experimental points of the curve  $h_{l_{exp}}(T)$ , the parameters  $C_{p_l}$  and  $q$  are given by

$$C_{p_l} = \frac{\sum_{i=1}^M \{ (h_{l_{exp}}(T_i) - h_{l_{ext}}(T_0)) (T_i - T_0) \}}{\sum_{i=1}^M (T_i - T_0)^2} \quad (\text{A.3})$$

$$q = h_{l_{ext}}(T_0) - C_{p_l} T_0 \quad (\text{A.4})$$

$T_0$  is taken so that  $h_{l_{ext}}(T_0) = 0 \text{ J kg}^{-1}$ . Figure A.1 compares the experimental curve of specific enthalpy with the linear approximation for a high viscosity Diesel calibration fluid, Viscor 16BR.

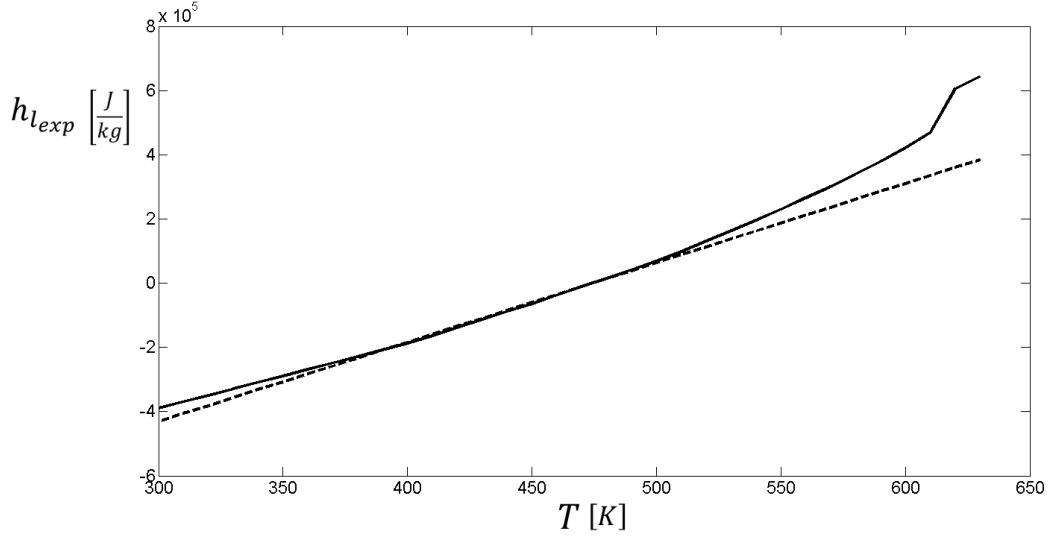


**Figure A.1:** Specific enthalpy of Viscor 16BR. Experimental (solid line) and approximated (dashed line)

Based on equation (3.47), the specific volume at saturated conditions can be written as

$$v_{l_{exp}}(T) = \frac{(\gamma_l - 1) C_{v_l} T}{p_{sat_{exp}}(T) + \pi} = \frac{(C_{p_l} - C_{v_l}) T}{p_{sat_{exp}}(T) + \pi} \quad (\text{A.5})$$

where the two parameters  $C_{v_l}$  and  $\pi$  are aimed. To calculate  $C_{v_l}$  and  $\pi$ , a multi-dimensional optimization is performed using the Nelder-Mead Simplex algorithm as described in [184]. The method minimizes the error

$$err(C_{v_l}, \pi) = \sum_{i=1}^M \left( v_{l_{exp}}(T_i) - \frac{(C_{p_l} - C_{v_l}) T_i}{p_{sat_{exp}}(T_i) + \pi} \right)^2 \quad (\text{A.6})$$

for a given range of temperatures. Noteworthy, the interval of temperatures  $[T_0, T_M]$  chosen has a significant impact on the curve approximation. Figure A.2 shows the optimization for three different temperature intervals, each one yielding different values of  $C_{v_l}$  and  $\pi$ . Once the parameters  $C_{p_l}$ ,  $q$ ,  $C_{v_l}$  and  $\pi$  are determined,  $\gamma_l$  is calculated from

$$\gamma_l = \frac{C_{p_l}}{C_{v_l}} \quad (\text{A.7})$$

The last parameter to be calculated is the entropy offset  $q'$  in the entropy equation of the liquid

$$s_l = C_{v_l} \ln \frac{T^{\gamma_l}}{(p + \pi)^{\gamma_l - 1}} + q' \quad (\text{A.8})$$

This parameter is calculated assuming that, at full thermodynamic equilibrium, the Gibbs free energies of the liquid and its vapor are equal

$$g_l = g_v \longrightarrow (\gamma_l C_{v_l} - q') T - T C_{v_l} \ln \frac{T^{\gamma_l}}{(p_{sat} + \pi)^{\gamma_l - 1}} + q = C_{p_v} T - T C_{v_v} \ln \frac{T^{\gamma_g}}{(p_{sat})^{\gamma_g - 1}} \quad (\text{A.9})$$

Equation (A.9) provides an implicit link between  $T$  and  $p_{sat}$  for a  $q'$  given. Using the

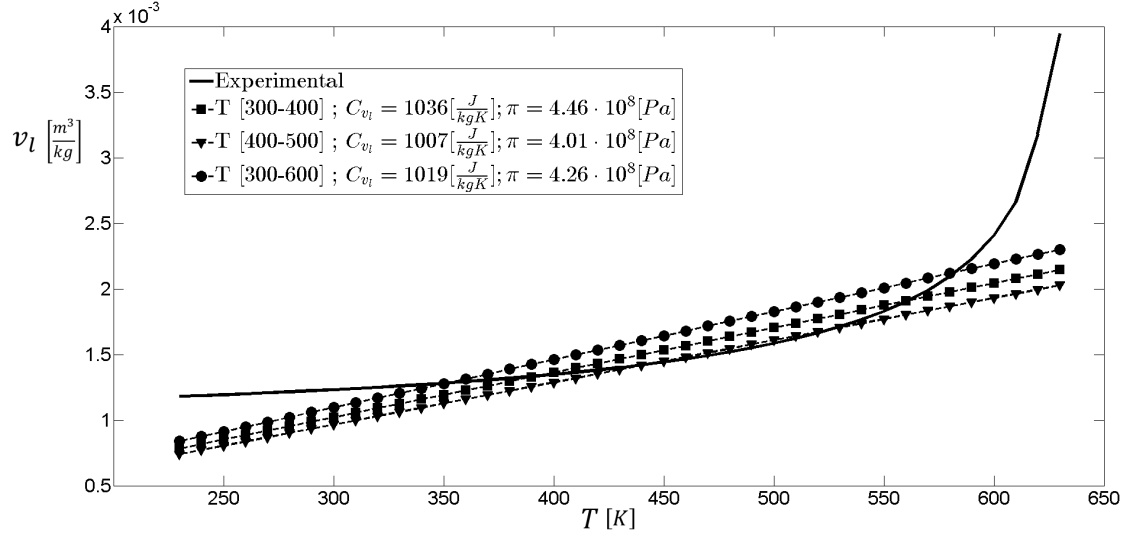


**Figure A.2:** Experimental and approximated curves of specific volume at saturation conditions of Viscor 16BR. Three different optimization intervals are displayed:  $[T_0 = 300 \text{ K}, T_M = 400 \text{ K}]$ ,  $[T_0 = 400 \text{ K}, T_M = 500 \text{ K}]$ ,  $[T_0 = 300 \text{ K}, T_M = 600 \text{ K}]$

experimental curve of the saturation pressure  $p_{sat_{exp}}(T)$ , it is possible to find the  $q'$  that minimizes the error between  $p_{sat}(T)$  from (A.9) and  $p_{sat_{exp}}(T)$ .



## Appendix B

---

# Derivation of the mixture energy equation coefficients

---

The mixture energy equation (3.35) solved in Stage B keeping only diffusion terms reads

$$\frac{\partial(\rho e)}{\partial t} = -p \nabla \cdot \mathbf{u} + \boldsymbol{\sigma} : \nabla \mathbf{u} + \nabla \cdot (K \nabla T) \quad (\text{B.1})$$

The aim is to integrate (B.1) over a control volume and discretize it in the form

$$T^{new} = T^* - C_T^* \Delta t \sum_{f=1}^{faces} K_f \nabla T^{new} \cdot \mathbf{A}_f^A \quad (\text{B.2})$$

providing  $T^*$  and  $C_T^*$ . Integration of the first term on the right hand side of (B.1) can be approximated as

$$- \int_{V^A} p \nabla \cdot \mathbf{u} dV \approx - \frac{p^B + p^A}{2} \int_{V^A} \nabla \cdot \mathbf{u} dV = - \frac{p^B + p^A}{2} \int_{A^A}^{A^B} \mathbf{u} \cdot \mathbf{n} dA \quad (\text{B.3})$$

where the divergence theorem has been applied to cell volumes  $V^A$ ,  $V^B$  enclosed by the external surfaces  $A^A$ ,  $A^B$ . Using the Reynolds transport theorem for a given property  $\phi$

$$\frac{D}{Dt} \int_V \phi dV = \int_V \frac{\partial \phi}{\partial t} dV + \int_A \phi \mathbf{u} \cdot \mathbf{n} dA \quad (\text{B.4})$$

and making  $\phi = 1$

$$\frac{D}{Dt} \int_V dV = \frac{DV}{Dt} = \int_V 0 dV + \int_A \mathbf{u} \cdot \mathbf{n} dA = \int_A \mathbf{u} \cdot \mathbf{n} dA \quad (\text{B.5})$$

This result can be used to integrate and discretize eq. (B.1) between Stage A and B as

$$M(e^B - e^A) = -\frac{p^B + p^A}{2} (V^B - V^A) + \underbrace{\Delta t V^A \boldsymbol{\sigma}(\mathbf{u}^B) : \nabla \mathbf{u}^B}_{VD} + \Delta t \sum_{f=1}^{faces} K_f \nabla T^B \cdot \mathbf{A}_f^A \quad (\text{B.6})$$

where it has been assumed that  $M^A = M^B = M$  with help of eq. (3.149). Eq. (B.6) needs to be fed with two expressions  $e = e(T, \dots)$  and  $V = V(T, \dots)$  in order to express all the terms as functions of the temperature of the mixture instead of partial temperatures. The relation  $V(T, \dots)$  for the mixture can be provided through the EOS of both liquid and gas phases. Using the EOS of each phase, eq. (3.45) and (3.47)

$$p = \rho_g R_g T_g \rightarrow V_g = \frac{M_g R_g T_g}{p} \quad (\text{B.7})$$

$$p = \rho_l C_{v_l} (\gamma_l - 1) T_g - \pi \rightarrow V_l = \frac{M_l C_{v_l} (\gamma_l - 1) T_l}{p + \pi} \quad (\text{B.8})$$

The mixture volume is

$$V = V_g + V_l = \frac{M_g R_g T_g}{p} + \frac{M_l C_{v_l} (\gamma_l - 1) T_l}{p + \pi} = \frac{M_g C_{v_g} (\gamma_g - 1) T_g}{p} + \frac{M_l C_{v_l} (\gamma_l - 1) T_l}{p + \pi} \quad (\text{B.9})$$

Assuming constant  $C_{v_g}$  between Stage A and B it can be written

$$\rho C_v T = \alpha_g \rho_g C_{v_g} T_g + \alpha_l \rho_l C_{v_l} T_l \xrightarrow{\cdot V} M C_v T = M_g C_{v_g} T_g + M_l C_{v_l} T_l \quad (\text{B.10})$$

The convergence of the implicit loop in Stage B is insensitive to the assumption of constant  $C_{v_g}$  for the calculation of the mixture coefficients, and therefore is used to simplify (B.6). Introducing eq. (B.10) into (B.9)

$$V = \frac{M_g C_{v_g} (\gamma_g - 1) T_g}{p} + \frac{(\gamma_l - 1) (M C_v T - M_g C_{v_g} T_g)}{p + \pi} \quad (\text{B.11})$$

and using the EOS of the gas phase

$$V = \frac{(\gamma_l - 1) M C_v T}{p + \pi} + \alpha_g V \frac{C_{v_g}}{R_g} \left( (\gamma_g - 1) - \frac{(\gamma_l - 1) p}{p + \pi} \right) \quad (\text{B.12})$$

$$V \left( p + \pi - \alpha_g \left( 1 - \frac{(\gamma_l - 1) p}{(\gamma_g - 1) (p + \pi)} \right) (p + \pi) \right) = (\gamma_l - 1) M C_v T \quad (\text{B.13})$$

$$V = V(T, p) = \frac{M C_v T}{\frac{\alpha_l}{(\gamma_l - 1)} (p + \pi) + \frac{\alpha_g}{(\gamma_g - 1)} p} \quad (\text{B.14})$$

Equation (B.14) yields the mixture volume for given  $T$  and  $p$ . Note that the asymptotic limits for  $\alpha_l$ ;  $\alpha_g \rightarrow 0$ ; 1 yield the same expression as pure gas and liquid phases provided in [185].

An expression for the mixture energy  $e = e(T, \dots)$  assuming constant  $C_{v_g}$  can be obtained from eqs. (3.43), (3.44) and (3.46)

$$\rho e = \alpha_g \rho_g e_g + \alpha_l \rho_l e_l \xrightarrow{\cdot V} M e = M_g C_{v_g} T_g + M_l C_{v_l} T_l + M_l q + V_l \pi =$$



## Appendix B

$$= MC_v T + M_l q + V_l \pi \quad (\text{B.15})$$

Using  $e$  in equation (B.6)

$$\begin{aligned} MC_v T^B + M_l q + V_l^B \pi - (MC_v T^A + M_l q + V_l^A \pi) = \\ = -\frac{p^B + p^A}{2} (V^B - V^A) + VD + \Delta t \sum_{f=1}^{faces} K_f \nabla T^B \cdot \mathbf{A}_f^A \end{aligned} \quad (\text{B.16})$$

$$MC_v (T^B - T^A) = -\left(\frac{p^B + p^A}{2} + \alpha_l \pi\right) (V^B - V^A) + VD + \Delta t \sum_{f=1}^{faces} K_f \nabla T^B \cdot \mathbf{A}_f^A \quad (\text{B.17})$$

where  $\alpha_l^B = \alpha_l^A = \alpha_l$  since there is no volume fraction change between Stage A and B (as inferred from equation (3.30) neglecting non-diffusion terms). Introducing the mixture volume  $V(T, p)$  in (B.17)

$$\begin{aligned} MC_v T^B \left( 1 + \frac{\frac{p^B + p^A}{2} + \alpha_l \pi}{\frac{\alpha_l}{(\gamma_l - 1)} (p^B + \pi) + \frac{\alpha_g}{(\gamma_g - 1)} p^B} \right) = \\ = MC_v T^A + \left( \frac{p^B + p^A}{2} + \alpha_l \pi \right) V^A + VD + \Delta t \sum_{f=1}^{faces} K_f \nabla T^B \cdot \mathbf{A}_f^A \end{aligned} \quad (\text{B.18})$$

and finally

$$T^B = \frac{T^A + \left( \frac{p^B + p^A}{2} + \alpha_l \pi \right) \frac{V^A}{MC_v} + \frac{VD}{MC_v} + \frac{\Delta t}{MC_v} \sum_{f=1}^{faces} K_f \nabla T^B \cdot \mathbf{A}_f^A}{1 + \frac{\frac{p^B + p^A}{2} + \alpha_l \pi}{\frac{\alpha_l}{(\gamma_l - 1)} (p^B + \pi) + \frac{\alpha_g}{(\gamma_g - 1)} p^B}} \quad (\text{B.19})$$

Comparing (B.19) with (B.2) leads to the definition of  $T^*$  and  $C_T^*$

$$T^* = \frac{T^A + \left( \frac{p^B + p^A}{2} + \alpha_l \pi \right) \frac{V^A}{MC_v} + \frac{VD}{MC_v}}{1 + \frac{\frac{p^B + p^A}{2} + \alpha_l \pi}{\frac{\alpha_l}{(\gamma_l - 1)} (p^B + \pi) + \frac{\alpha_g}{(\gamma_g - 1)} p^B}} \quad (\text{B.20})$$

$$C_T^* = \frac{1}{MC_v \left( 1 + \frac{\frac{p^B + p^A}{2} + \alpha_l \pi}{\frac{\alpha_l}{(\gamma_l - 1)} (p^B + \pi) + \frac{\alpha_g}{(\gamma_g - 1)} p^B} \right)} \quad (\text{B.21})$$



## Appendix C

---

### IFP-C3D solver

---

---

The mixture model defined in Section 3.3 is implemented in the code IFP-C3D following the steps described in Section 3.4. Figure C.1 sketches the solution strategy, indicating not only the calculation of source, diffusion and convective terms but also general processes such as meshing motion and remeshing, initialization and boundary condition definition. Figure C.1 also shows other capabilities of IFP-C3D that were not applied in the present research such as breakup, collapse, collision and evaporation of Lagrangian particles, turbulent transport and combustion.

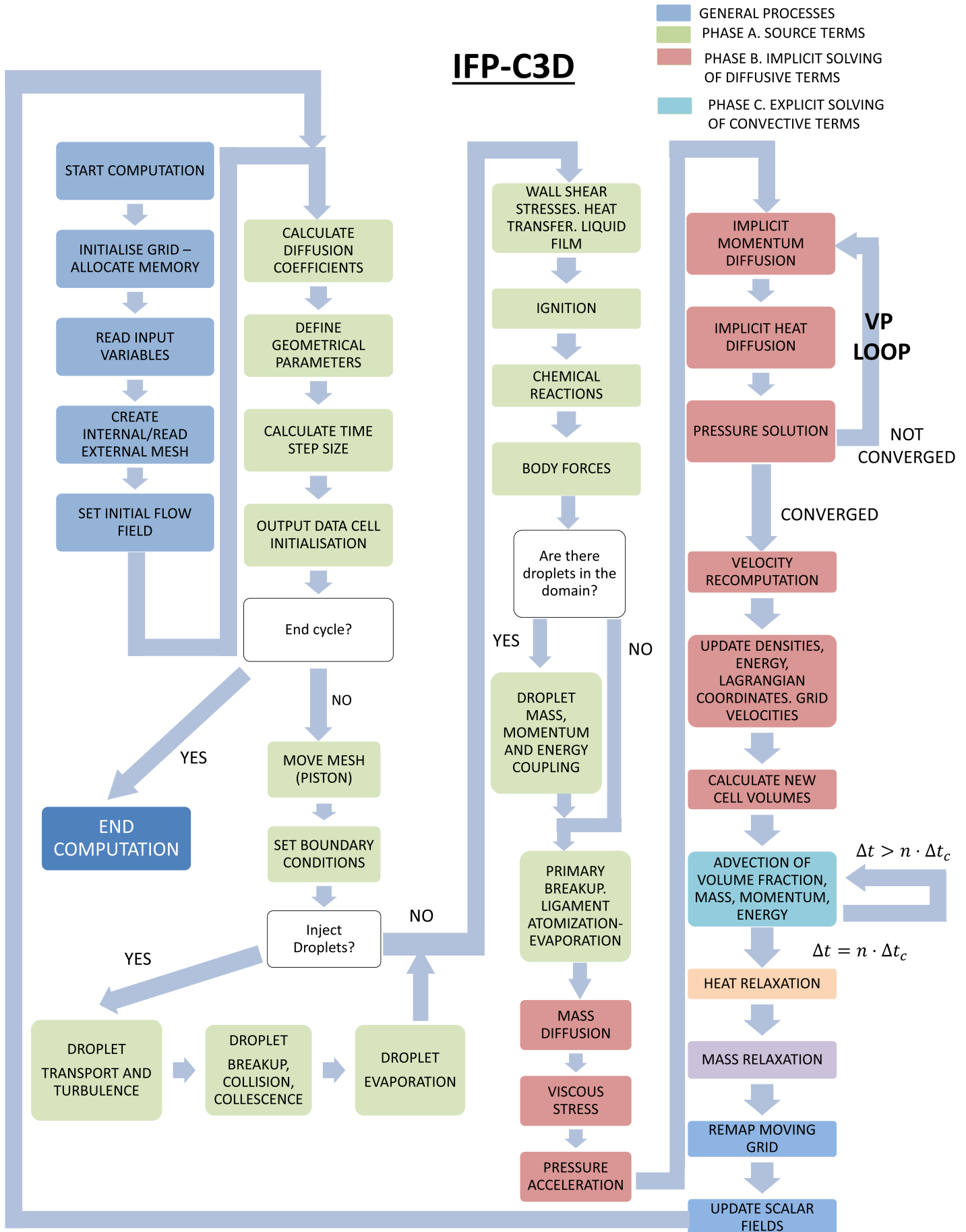


Figure C.1: IFP-C3D solver flowchart  
200

## Appendix D

---

# Mathematical model and numerical method for LES of in-nozzle flow

---

---

### D.1 Mixture model

The in-nozzle flow is solved using an incompressible, homogeneous, two-phase mixture model (fuel liquid and vapor) where both phases share same velocity and pressure. The model consists of a continuity and a momentum equation for the mixture plus a mass conservation equation for the vapor phase

- Continuity of the vapor phase

$$\frac{\partial (\alpha_v \rho_v)}{\partial t} + \nabla \cdot (\alpha_v \rho_v \mathbf{v}) = R_e - R_c \quad (\text{D.1})$$

- Continuity of the mixture

$$\frac{\partial \rho}{\partial t} + \nabla \cdot (\rho \mathbf{v}) = 0 \quad (\text{D.2})$$

- Momentum of the mixture

$$\frac{\partial (\rho \mathbf{v})}{\partial t} + \nabla \cdot (\rho \mathbf{v} \mathbf{v} + p) = \nabla \cdot \boldsymbol{\sigma} + \rho \mathbf{g} \quad (\text{D.3})$$

The viscous stress tensor  $\boldsymbol{\sigma}$  is defined in (3.36). The terms  $R_e$  and  $R_c$  represent mass transfer between phases due to bubble expansion and collapse respectively. These magnitudes are calculated based on the Rayleigh-Plesset equation (see for example Brennen [70])

$$R(t) \frac{d^2 R(t)}{dt^2} + \frac{3}{2} \left( \frac{dR(t)}{dt} \right)^2 = \frac{p_b(t) - p(t)}{\rho_l} - \frac{4v_l}{R} \frac{dR(t)}{dt} - \frac{2S_t}{\rho_l R(t)} \quad (\text{D.4})$$

where  $R(t)$  is the bubble radius as a function of time,  $p_b(t)$  is the static pressure inside the bubble, taken as uniform,  $p(t)$  is the far-field static pressure,  $\nu_l$  is the kinematic viscosity of the surrounding liquid and  $S_l$  is the liquid surface tension. If one assumes that the bubble growth is relatively constant during most of the expansion or collapse, Equation (D.4) can be simplified by neglecting the bubble inertia. In the same way, if one considers that the surface tension and the viscous contribution are small compared to the mechanical force induced by the pressure gradient, eq. (D.4) becomes

$$\frac{3}{2} \left( \frac{dR(t)}{dt} \right)^2 = \frac{p_b(t) - p(t)}{\rho_l} \quad (\text{D.5})$$

$$\frac{dR(t)}{dt} = \pm \sqrt{\frac{2}{3} \frac{p_b(t) - p(t)}{\rho_l}} \quad (\text{D.6})$$

Bubble radius variation due to bubble expansion and collapse can be linked to mass transfer between phases via the Zwart-Gerber-Belamri cavitation model. Initially proposed by Zwart et al. [195], this model assumes that all the bubbles in the system have the same size and therefore the mass transfer rate per unit volume can be calculated as

$$\begin{aligned} R_e &= \begin{cases} n4\pi R(t)^2 \rho_v \frac{dR(t)}{dt} & \text{if } \frac{dR(t)}{dt} > 0 \\ 0 & \text{if } \frac{dR(t)}{dt} < 0 \end{cases} \\ R_c &= \begin{cases} 0 & \text{if } \frac{dR(t)}{dt} > 0 \\ n4\pi R(t)^2 \rho_v \frac{dR(t)}{dt} & \text{if } \frac{dR(t)}{dt} < 0 \end{cases} \end{aligned} \quad (\text{D.7})$$

where  $n$  is the number of bubbles per unit volume. Considering spherical bubbles,  $n$  is related to the vapor volume fraction through

$$\alpha_v = n \frac{4}{3} \pi R(t)^3 \quad (\text{D.8})$$

Combining (D.7) and (D.8), mass transfer terms become

$$\begin{aligned} R_e &= \tilde{F}_{vap} \frac{3\alpha_v \rho_v}{R} \sqrt{\frac{2}{3} \frac{p_{vap}(t) - p(t)}{\rho_l}} \\ R_c &= F_{cond} \frac{3\alpha_v \rho_v}{R} \sqrt{\frac{2}{3} \frac{p(t) - p_{vap}(t)}{\rho_l}} \end{aligned} \quad (\text{D.9})$$

where  $F_{cond}$  is an empirical calibration coefficient. Expression (D.9) is suitable for the collapse process, but not for the bubble expansion mechanism. This stems from the assumption of negligible bubble-to-bubble interaction, which becomes realistic when the average bubble is small, but fails with larger bubbles. When a number of bubbles expand within a given volume, the bubble density number must decrease accordingly. This effect can be taken into account

## Appendix D

---

through the coefficient  $\tilde{F}_{vap}$

$$\tilde{F}_{vap} = F_{vap} \frac{\alpha_{nuc}(1 - \alpha_v)}{\alpha_v} \quad (D.10)$$

where  $\alpha_{nuc}$  is the volume fraction associated with the nuclei embedded in the liquid and  $F_{vap}$  is a empirical calibration coefficient. As the amount of vapor increases in a given volume, the domain becomes saturated, decreasing the amount of liquid vaporization. The mass transfer terms are therefore written as

$$\begin{aligned} R_e &= F_{vap} \frac{3\alpha_{nuc}(1 - \alpha_v)\rho_v}{R} \sqrt{\frac{2}{3} \frac{p_{vap}(t) - p(t)}{\rho_l}} & \text{if } p(t) < p_{vap}(t) \\ R_c &= F_{cond} \frac{3\alpha_v\rho_v}{R} \sqrt{\frac{2}{3} \frac{p(t) - p_{vap}(t)}{\rho_l}} & \text{if } p(t) > p_{vap}(t) \end{aligned} \quad (D.11)$$

The amount of mass transfer is highly dependent on  $F_{vap}$  and  $F_{cond}$ . According to [194], typical values of  $R$ ,  $\alpha_{nuc}$ ,  $F_{vap}$  and  $F_{cond}$  are  $R = 10^{-6}m$ ,  $\alpha_{nuc} = 5 \cdot 10^{-4}$ ,  $F_{vap} = 50$  and  $F_{cond} = 0.001$ . However, best practice studies concerning nozzle flow show that a good agreement with experimental measurements is achieved with  $F_{vap} = 500$  and  $F_{cond} = 0.05$ .

### D.2 LES model

System (D.1)-(D.3) can be spatially filtered to obtain

$$\frac{\partial (\overline{\alpha_v \rho_v})}{\partial t} + \nabla \cdot (\overline{\alpha_v \rho_v} \tilde{\mathbf{v}}) = R_e - R_c \quad (D.12)$$

$$\frac{\partial \bar{\rho}}{\partial t} + \nabla \cdot (\bar{\rho} \tilde{\mathbf{v}}) = 0 \quad (D.13)$$

$$\frac{\partial (\bar{\rho} \tilde{\mathbf{v}})}{\partial t} + \nabla \cdot (\bar{\rho} \tilde{\mathbf{v}} \tilde{\mathbf{v}} + \bar{\mathbf{p}}) = \nabla \cdot \bar{\boldsymbol{\sigma}} + \bar{\rho} \mathbf{g} - \nabla \cdot (\overline{\rho \mathbf{v} \mathbf{v}} - \bar{\rho} \tilde{\mathbf{v}} \tilde{\mathbf{v}}) \quad (D.14)$$

where

$$\tilde{\mathbf{v}} = \frac{\overline{\rho \mathbf{v}}}{\bar{\rho}} \quad (D.15)$$

is the so-called Favre filtered velocity and the filtered viscous tensor

$$\bar{\boldsymbol{\sigma}} = 2\bar{\mu} \left[ \nabla \bar{\mathbf{v}} + (\nabla \bar{\mathbf{v}})^T \right] + \left( \bar{\mu}_v - \frac{2}{3}\bar{\mu} \right) \mathbf{I} \nabla \cdot \bar{\mathbf{v}} \quad (D.16)$$

The last term in the right hand side of equation (D.14)

$$\boldsymbol{\tau} = -(\overline{\rho \mathbf{v} \mathbf{v}} - \bar{\rho} \tilde{\mathbf{v}} \tilde{\mathbf{v}}) \quad (D.17)$$

is the divergence of the SGS momentum resulting from the averaging process, and it is modeled using the Boussinesq approach as described in Hinze [71]

$$\boldsymbol{\tau} - \frac{1}{3} (\boldsymbol{\tau} : \mathbf{I}) \mathbf{I} = -2\mu_T \left[ \tilde{\mathbf{S}} - \frac{1}{3} (\tilde{\mathbf{S}} : \mathbf{I}) \mathbf{I} \right] \quad ; \quad \tilde{\mathbf{S}} = \frac{1}{2} [\nabla \tilde{\mathbf{v}} + (\nabla \tilde{\mathbf{v}})^T] \quad (\text{D.18})$$

with the matrix multiplication operator

$$\tilde{\mathbf{S}} : \mathbf{I} = \sum_i \sum_j S_{ij} \delta_{ij} \quad ; \quad \delta_{ij} = \begin{cases} 1 & \text{if } i = j \\ 0 & \text{if } i \neq j \end{cases} \quad (\text{D.19})$$

Expression (D.18) describes the deviatoric part of the SGS tensor  $\boldsymbol{\tau}$ . The isotropic part is added to the filtered pressure in (D.14). In order to close the model, a suitable definition of the SGS viscosity  $\mu_T$  must be provided. In this work, the Wall-Adapting Local Eddy-Viscosity (WALE) model is selected as described in Nicoud et al. [150]. First, the SGS viscosity is written as

$$\mu_T = -\bar{\rho} L_S^2 \overline{OP} \quad (\text{D.20})$$

where  $L_S$  is the mixing length for the subgrid scales and  $\overline{OP}$  is an operator that should satisfy the following conditions:

- Behave correctly near the wall, reproducing the  $\mu_T \propto o(y^3)$  behavior ( $y$  normal distance to the wall) and becoming 0 at  $y = 0$
- Take into account the contributions of both the strain rate and the flow rotation, which are necessary to predict partial laminarization, turbulence inception and transition, and turbulence generation in regions with high rotation rates (see Wray et al. [151])
- Be invariant to any coordinate translation or rotation

The mixing length  $L_S$  is defined as

$$L_S = \min \left( \kappa d, C_w V^{\frac{1}{3}} \right) \quad (\text{D.21})$$

$\kappa$  is the von Karman constant equal to 0.4,  $d$  is the normal distance to the nearest wall and  $C_w$  is the WALE constant taken as 0.325 following the suggestions in Menter [202]. The definition of  $L_S$  provided in (D.21) is consistent with the law of the wall. Very close to the wall, where

$$\kappa d < C_w V^{\frac{1}{3}}$$

the mixing length tends to 0. The operator  $\overline{OP}$  must be based on the invariants of a tensor  $\boldsymbol{\tau}$  that should be representative of the turbulence field, such as the velocity gradient tensor  $\nabla \mathbf{v}$ . Alternatively to the Smagorinsky model, where only the second invariant of the symmetric part of  $\nabla \mathbf{v}$  is considered

$$\overline{OP} = \sqrt{2\overline{\mathbf{S}} : \mathbf{S}}$$



## Appendix D

---

leading to a  $o(y)$  behavior near the wall and neglecting the influence of the rotational tensor, the WALE model builds the  $\overline{OP}$  operator starting from the traceless symmetric part of the square of the velocity gradient tensor

$$\mathbf{S}^d = \frac{1}{2} \left[ (\nabla \mathbf{v})^2 + \left( (\nabla \mathbf{v})^T \right)^2 \right] - \frac{1}{3} [\mathbf{I} : (\nabla \mathbf{v})]^2 \quad (\text{D.22})$$

Equation (D.22) can be recast in terms of the symmetric  $\mathbf{S}$  and anti-symmetric  $\mathbf{\Omega}$

$$\mathbf{\Omega} = \frac{1}{2} \left( \nabla \mathbf{v} - (\nabla \mathbf{v})^T \right) \quad (\text{D.23})$$

parts of the velocity tensor as

$$\mathbf{S}^d = \overline{\mathbf{S}} \overline{\mathbf{S}} + \overline{\mathbf{\Omega}} \overline{\mathbf{\Omega}} - \frac{1}{3} (\overline{\mathbf{S}} : \overline{\mathbf{S}} - \overline{\mathbf{\Omega}} : \overline{\mathbf{\Omega}}) \quad (\text{D.24})$$

The trace of  $\mathbf{S}^d$  is zero and the second invariant is always finite and proportional to  $\mathbf{S}^d : \mathbf{S}^d$ . Multiplying equation (D.24) by itself and using the Cayley-Hamilton theorem, one reaches

$$\begin{aligned} \mathbf{S}^d : \mathbf{S}^d &= \frac{1}{6} [(\overline{\mathbf{S}} : \overline{\mathbf{S}}) (\overline{\mathbf{S}} : \overline{\mathbf{S}}) + (\overline{\mathbf{\Omega}} : \overline{\mathbf{\Omega}}) (\overline{\mathbf{\Omega}} : \overline{\mathbf{\Omega}})] + \\ &\quad \frac{2}{3} (\overline{\mathbf{S}} : \overline{\mathbf{S}}) (\overline{\mathbf{\Omega}} : \overline{\mathbf{\Omega}}) + 2 (\overline{\mathbf{S}} \overline{\mathbf{S}}) : (\overline{\mathbf{\Omega}} \overline{\mathbf{\Omega}})^T \end{aligned} \quad (\text{D.25})$$

It is worth noting that, in the case of pure shear,

$$(\overline{\mathbf{S}} : \overline{\mathbf{S}}) = (\overline{\mathbf{\Omega}} : \overline{\mathbf{\Omega}}) \quad ; \quad (\overline{\mathbf{S}} \overline{\mathbf{S}}) : (\overline{\mathbf{\Omega}} \overline{\mathbf{\Omega}})^T = -\frac{1}{2} (\overline{\mathbf{S}} : \overline{\mathbf{S}}) (\overline{\mathbf{S}} : \overline{\mathbf{S}}) \quad (\text{D.26})$$

and the invariant (D.25) becomes zero. This means that in the case of wall-bounded flow, where the shear stresses dominate, almost no eddy viscosity will be introduced by the SGS model, allowing the development of linearly unstable waves. This last point represents a very important advantage with respect to the Smagorinsky model, which is unable to predict laminar to turbulent transition because the invariant considered to build the SGS viscosity is large in the case of pure shear. Another important feature of the invariant (D.25) is that it behaves  $o(y^2)$  near the wall. In order to model the  $o(y^3)$  behavior, the operator  $\overline{OP}$  can be taken as

$$\overline{OP} \propto \overline{OP}_1 = \left( \mathbf{S}^d : \mathbf{S}^d \right)^{\frac{3}{2}} \quad (\text{D.27})$$

The operator  $\overline{OP}_1$  has dimensions of frequency to the power 6, so it needs to be scaled before being used in (D.20). A good candidate for the scaling is

$$\overline{OP}_2 = \left( \mathbf{S}^d : \mathbf{S}^d \right)^{\frac{5}{2}} + \left( \mathbf{S}^d : \mathbf{S}^d \right)^{\frac{5}{4}} \quad (\text{D.28})$$

and therefore

$$\overline{OP} = \frac{\overline{OP}_1}{\overline{OP}_2} \quad (\text{D.29})$$

The operator  $\overline{OP}_2$  ensures that the  $o(y^3)$  behavior near the wall is respected, since  $y \rightarrow 0$ ,  $\overline{OP}_1 \propto o(y^3)$ ,  $\overline{OP}_2 \propto o(1)$ . In the definition of the  $\overline{OP}_2$ , eq. (D.28), the first term on the right hand side may locally tend to zero (i. e. inside the eddies) while the operator  $\overline{OP}_2$  remains finite. This would lead to numerical instabilities if the second term on the right hand side of (D.28) were not introduced. This term is negligible near the wall, but avoids numerical instability since it does not locally tend to zero. The final definition of the SGS turbulent viscosity reads

$$\begin{aligned}\mu_T &= -\bar{\rho} L_S^2 \overline{OP} = \mu_T = -\bar{\rho} \left[ \min \left( \kappa d, C_w V^{\frac{1}{3}} \right) \right]^2 \frac{\overline{OP}_1}{\overline{OP}_2} \\ &= -\bar{\rho} \left[ \min \left( \kappa d, C_w V^{\frac{1}{3}} \right) \right]^2 \frac{(\mathbf{S}^d : \mathbf{S}^d)^{\frac{3}{2}}}{(\mathbf{S}^d : \mathbf{S}^d)^{\frac{5}{2}} + (\mathbf{S}^d : \mathbf{S}^d)^{\frac{5}{4}}}\end{aligned}\quad (\text{D.30})$$

which is used in (D.18) to compute the SGS tensor  $\boldsymbol{\tau}$ .

### D.3 Numerical method

The mathematical system (D.12)-(D.14) can be integrated over a control volume  $V$  as

$$\frac{\partial (\overline{\alpha_v \rho_v})}{\partial t} V + \sum_{f=1}^{faces} (\overline{\alpha_v \rho_v} \tilde{\mathbf{v}})_f \cdot \mathbf{A}_f = R_e V - R_c V \quad (\text{D.31})$$

$$\frac{\partial \bar{\rho}}{\partial t} V + \sum_{f=1}^{faces} (\bar{\rho} \tilde{\mathbf{v}})_f \cdot \mathbf{A}_f = 0 \quad (\text{D.32})$$

$$\frac{\partial (\bar{\rho} \tilde{\mathbf{v}})}{\partial t} V + \sum_{f=1}^{faces} (\bar{\rho} \tilde{\mathbf{v}} \tilde{\mathbf{v}} + \bar{p})_f \cdot \mathbf{A}_f = \sum_{f=1}^{faces} (\bar{\boldsymbol{\sigma}} + \boldsymbol{\tau})_f \cdot \mathbf{A}_f + \bar{\rho} \mathbf{g} V \quad (\text{D.33})$$

where the sum extends to all the faces delimiting the control volume  $V$ . The three equations (D.31)-(D.33) can be expressed in the general form

$$\frac{\partial \bar{\rho} \tilde{\phi}}{\partial t} V + \sum_{f=1}^{faces} (\bar{\rho} \tilde{\phi} \tilde{\mathbf{v}})_f \cdot \mathbf{A}_f = \sum_{f=1}^{faces} \Gamma_\phi \nabla \phi_f \cdot \mathbf{A}_f + \sum_{f=1}^{faces} \bar{p}_f \cdot \mathbf{A}_f + B_\phi \quad (\text{D.34})$$

where

$$\text{Continuity of the vapor: } \tilde{\phi} = \frac{\overline{\alpha_v \rho_v}}{\bar{\rho}} \quad ; \quad \Gamma_\phi = 0 \quad ; \quad B_\phi = R_e V - R_c V$$

$$\text{Continuity of the mixture: } \tilde{\phi} = 1 \quad ; \quad \Gamma_\phi = 0 \quad ; \quad B_\phi = 0$$

$$\text{Momentum of the mixture: } \tilde{\phi} = \tilde{\mathbf{v}} \quad ; \quad \Gamma_\phi = f(\mu) \quad ; \quad B_\phi = \bar{\rho} \mathbf{g} V$$

Let consider (D.34) discretized in time using a first order implicit scheme. The system (D.31)-(D.33) is converged using the Semi-Implicit Method for Pressure Linked Equations-Consistent (SIMPLEC) algorithm for multiphase flows (PC-SIMPLEC) as described in Vasquez et al. [203]. The volume fraction equation and the momentum equation

## Appendix D

for the velocity component  $u^i$  become

$$\frac{(\overline{\alpha_v \rho_v})^{n+1} - (\overline{\alpha_v \rho_v})^n}{\Delta t} V + \sum_{f=1}^{faces} \left[ (\overline{\alpha_v \rho_v} \tilde{\mathbf{v}})_f^{n+1} \cdot \mathbf{A}_f \right] = (R_e - R_c)^{n+1} V \quad (\text{D.35})$$

$$\frac{(\overline{\rho u^i})^{n+1} - (\overline{\rho u^i})^n}{\Delta t} V + \sum_{f=1}^{faces} \left[ (\overline{\rho} \tilde{\mathbf{v}} \tilde{\mathbf{v}})_f^{n+1} \cdot \mathbf{A}_f \right]^i = \sum_{f=1}^{faces} \left[ (\Gamma_{u^i} \nabla \tilde{\mathbf{v}})_f^{n+1} \right]^i \cdot \mathbf{A}_f + B_{u^i}^{n+1} \quad (\text{D.36})$$

after some algebra, (D.35) and (D.36) can be written as

$$a_{P_v} \overline{\alpha_v} = \sum_{c=1}^{NB} a_{c_v} \overline{\alpha_{v_c}} + S_v \quad (\text{D.37})$$

$$a_{P \tilde{u}^i_P} = \sum_{c=1}^{NB} a_{c \tilde{u}^i_c} + \sum_{f=1}^{faces} \bar{p}_f \cdot \mathbf{A}_f \cdot \mathbf{i} + S_{u^i} \quad (\text{D.38})$$

The first sum in the right hand side of (D.37) and (D.38) extends to all the neighboring cells  $NB$  of the cell  $P$  with volume  $V$ . In (D.38), the coefficients  $a_c$  depend on the spatial discretization used for the velocity gradient, and the term  $S_{u^i}$  includes the fluxes as

$$S_{u^i} = \sum_{f=1}^{faces} \left[ (\overline{\rho} \tilde{\mathbf{v}} \tilde{\mathbf{v}})_f^{n+1} \cdot \mathbf{A}_f \right]^i + (\overline{\rho u^i})^n + B_{u^i}^{n+1} \quad (\text{D.39})$$

If the cell  $P$  is surrounded in the  $i$  direction by the cells  $P_{i-1}$  and  $P_{i+1}$ , the filtered pressure at the interface  $\bar{p}_f$  can be interpolated using the momentum equation coefficients as suggested by Rhie et al. [204]

$$\bar{p}_f = \frac{\frac{\bar{p}_{P_{i-1}}}{a_{P_{i-1}}} + \frac{\bar{p}_{P_{i+1}}}{a_{P_{i+1}}}}{\frac{1}{a_{P_{i-1}}} + \frac{1}{a_{P_{i+1}}}} \quad (\text{D.40})$$

Provided an initial pressure guess, the velocities and vapor volume fraction can be calculated through (D.37) and (D.38). Combining the continuity equations (D.12), (D.13), one can derive the pressure-correction relationship

$$\begin{aligned} & \frac{1}{\overline{\alpha_v \rho_v}} \left[ \frac{(\overline{\alpha_v \rho_v}) - (\overline{\alpha_v \rho_v})^n}{\Delta t} + \nabla \cdot (\overline{\alpha_v \rho_v} \tilde{\mathbf{v}}) + \nabla \cdot (\overline{\alpha_v \rho_v} \tilde{\mathbf{v}}^n) - (R_e - R_c) \right] + \\ & + \frac{1}{\overline{\alpha_l \rho_l}} \left[ \frac{(\overline{\alpha_l \rho_l}) - (\overline{\alpha_l \rho_l})^n}{\Delta t} + \nabla \cdot (\overline{\alpha_l \rho_l} \tilde{\mathbf{v}}) + \nabla \cdot (\overline{\alpha_l \rho_l} \tilde{\mathbf{v}}^n) - (R_e - R_c) \right] = 0 \end{aligned} \quad (\text{D.41})$$

For simplicity, the superscript at the new time instant  $n+1$  is not written. The velocity and volume fraction calculated in (D.37) and (D.38) are introduced in (D.41). If the equality is satisfied, the pressure, density and velocity fields are converged. Otherwise, a new pressure guess is formulated until the convergence is achieved. Figure (D.1) shows the solution procedure schematically. The commercial software ANSYS Fluent v16.0 is used to perform the LES study.

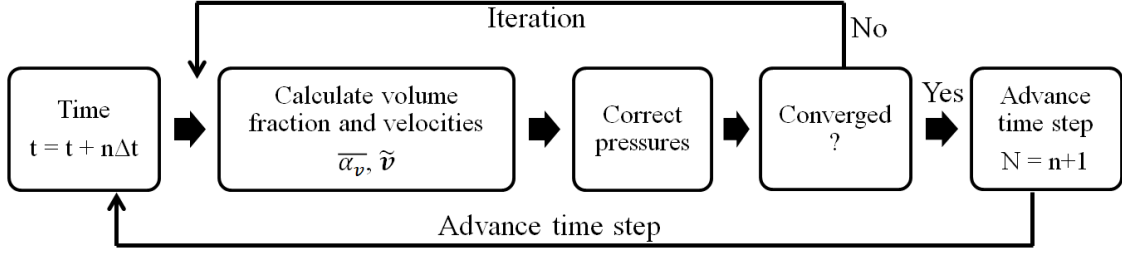


Figure D.1: Solver flow chart

### D.3.1 Interface reconstruction

The calculation of the fluxes through the control volume faces requires the reconstruction of the conserved magnitudes at the surrounding faces. The vapor volume fraction and momentum fluxes

$$(\overline{\alpha_v \rho_v \tilde{\mathbf{v}}})_f$$

$$(\bar{\rho} \tilde{\mathbf{v}} \tilde{\mathbf{v}})_f$$

are computed at the cell face  $f$  using a central differencing scheme

$$(\overline{\alpha_v \rho_v \tilde{\mathbf{v}}})_f = \frac{1}{2} \left[ (\overline{\alpha_v \rho_v \tilde{\mathbf{v}}})_{f-\frac{1}{2}} + (\overline{\alpha_v \rho_v \tilde{\mathbf{v}}})_{f+\frac{1}{2}} \right] + \frac{1}{2} \left[ \nabla (\overline{\alpha_v \rho_v \tilde{\mathbf{v}}})_{f-\frac{1}{2}} \cdot \mathbf{r}_{f-\frac{1}{2}} + \nabla (\overline{\alpha_v \rho_v \tilde{\mathbf{v}}})_{f+\frac{1}{2}} \cdot \mathbf{r}_{f+\frac{1}{2}} \right] \quad (\text{D.42})$$

$$(\bar{\rho} \tilde{\mathbf{v}} \tilde{\mathbf{v}})_f = \frac{1}{2} \left[ (\bar{\rho} \tilde{\mathbf{v}} \tilde{\mathbf{v}})_{f-\frac{1}{2}} + (\bar{\rho} \tilde{\mathbf{v}} \tilde{\mathbf{v}})_{f+\frac{1}{2}} \right] + \frac{1}{2} \left[ \nabla (\bar{\rho} \tilde{\mathbf{v}} \tilde{\mathbf{v}})_{f-\frac{1}{2}} \cdot \mathbf{r}_{f-\frac{1}{2}} + \nabla (\bar{\rho} \tilde{\mathbf{v}} \tilde{\mathbf{v}})_{f+\frac{1}{2}} \cdot \mathbf{r}_{f+\frac{1}{2}} \right] \quad (\text{D.43})$$

Subscripts  $f - \frac{1}{2}$  and  $f + \frac{1}{2}$  denote the left and right cells sharing the interface  $f$ , and the vectors  $\mathbf{r}_{f-\frac{1}{2}}$  and  $\mathbf{r}_{f+\frac{1}{2}}$  are the distances from the cell center to the face centroids. The central differencing scheme is a second-order discretization with low numerical diffusion. However, this scheme may induce spurious oscillatory behavior, which can lead to numerical instability and unphysical solutions. To circumvent this problem, the reconstruction is reformulated as

$$\mathcal{L}_f = \mathcal{L}_f^{CD} + (\mathcal{L}_f^{CD} - \mathcal{L}_f^{UP}) \quad (\text{D.44})$$

In equation (D.44),  $\mathcal{L}_f$  is any of  $(\overline{\alpha_v \rho_v \tilde{\mathbf{v}}})_f$ ,  $(\bar{\rho} \tilde{\mathbf{v}} \tilde{\mathbf{v}})_f$ , superscript  $CD$  refers to the central differencing scheme and the superscript  $UP$  to the upwind. The reconstruction (D.44) is based on the normalized variable diagram (NVD) approach, as described in Leonard [205], which applies the central differencing discretization when the solution is smooth, and switches to a second-order or first-order upwind scheme near high gradients. It is worth noting that the first-order upwind is only used for unbounded reconstructions, this is, when the convection boundedness criterion (CBC) is violated (see Gaskell et al. [206]).

## Appendix E

---

# Impact of URANS-LES interface on turbulence and vortex generation

---

The URANS-LES interface has a considerable influence on the flow behavior. The method used for transferring data from URANS to LES, in addition to the interface position, is of paramount importance. First, this Appendix is devoted to the analysis and comparison of two different methods, namely synthetic turbulence and vortex generation, assessing their impact on vortex dynamics. Later, the impact of interface position on vortex generation is addressed, highlighting the advantages and disadvantages of placing it inside or outside the sac.

### E.1 Turbulence generation method at the interface

Figure E.1 shows the mesh used for the analysis based on the Reference nozzle geometry. The URANS-LES interface is located close to the hole entrance to highlight its effect on vortex structures developed inside the hole. The LES region consists of approximately 4 million hexahedral cells with characteristic cell size  $\sim 1\mu m$ . The sac is meshed using tetrahedral elements of  $\sim 10\mu m$  characteristic size connected to the LES domain through the non-conformal URANS-LES interface (hexahedral and tetrahedral nodes do not necessarily merged). Along the needle and housing, a thin layer ( $\sim 30\mu m$ ) of pentahedral cells is defined parallel to the wall. Finally, the tetrahedral cells are refined by a factor of 2.5 downstream of the needle seat to better capture the flow detachment from the needle tip. The boundary conditions and numerical setups are the same as in Section 5.3.2 and 5.3.3.

Figures E.2a and E.2b compare mean velocity and TKE results yielded by the synthetic turbulence and the vortex generation methods. The mean velocity is calculated as the

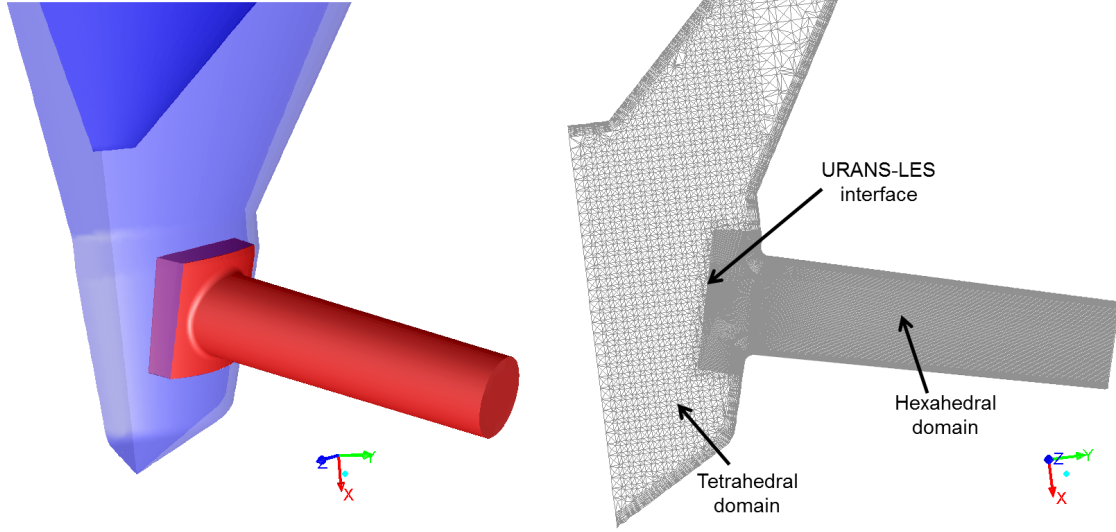


**Figure E.1:** Left: Reference nozzle geometry highlighting domain separation (URANS domain in blue; LES domain in red). Right: Mid-cut plane  $z = 0$  of the computational domain used for turbulence generation method evaluation

ensemble average of the velocity during the whole simulation

$$|\overline{V}| = \frac{1}{N} \sum_{n=1}^N \sqrt{(V_x^2 + V_y^2 + V_z^2)_n} \quad (\text{E.1})$$

where  $N$  is the number of time-steps and  $\overline{(\cdot)}$  is the ensemble average operator. TKE is computed using the root mean square of the velocity components

$$TKE = \frac{1}{2} \left( \frac{1}{N} \sum_{n=1}^N \left\{ [V_x|_n - \overline{V_x}]^2 + [V_y|_n - \overline{V_y}]^2 + [V_z|_n - \overline{V_z}]^2 \right\} \right) \quad (\text{E.2})$$

Although the results are qualitatively and quantitatively very similar, there are some discrepancies between both approaches. The mean velocity color iso-levels show similar velocity distribution in the sac and hole, but the upper separation region predicted by the synthetic turbulence method is slightly shorter and broader. This is in line with the TKE distribution observed in the separation region, which is shorter when the synthetic turbulence method is applied.

URANS-LES interface effects on turbulence generation can be assessed from TKE near the hole inlet. The vortex generation approach predicts higher homogeneously distributed turbulence intensity on the lower half of the hole. However, the synthetic turbulence method captures a stronger string vortex coming from the sac, feeding the upper shear layer with turbulence. This enhances the upper shear layer reattachment, decreasing the separation length as observed in Figure E.2a.

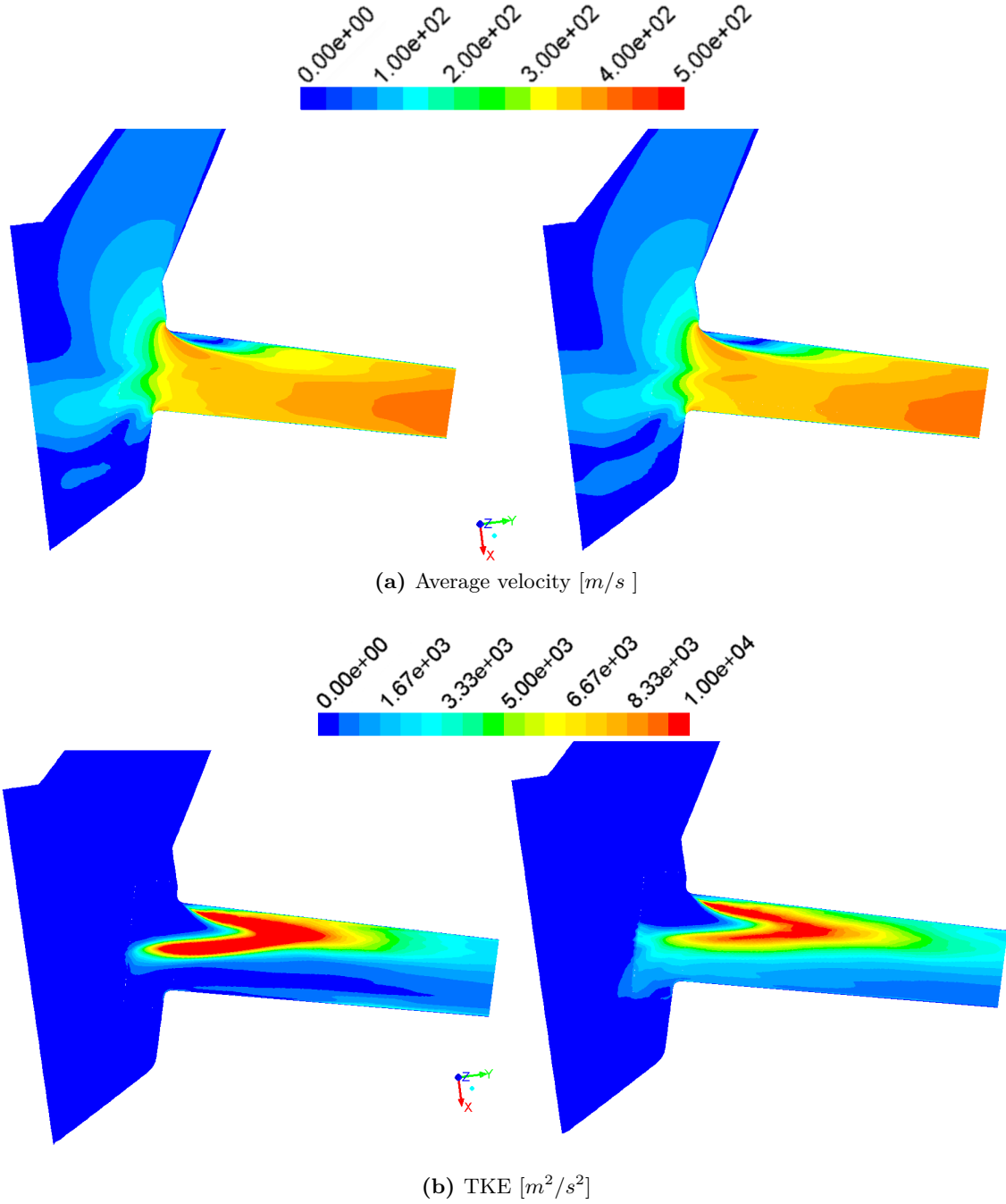


**Figure E.2:** Mean velocity and TKE color iso-levels on the mid-plane using the initial mesh. Synthetic turbulence (left) and vortex generation (right)

As far as the flow structure is concerned, the turbulence generation method can be evaluated using instantaneous iso-surfaces of normalized Q-criterion equal to 0.2. Figure E.3 shows these iso-surfaces colored by velocity. Although both methods introduce relatively small, weak turbulent structures at the interface, the synthetic turbulence approach preserves the string vortex integrity to a greater extent. In fact, the vortex generation method breaks down this structure at the URANS-LES interface, leading to smaller, better distributed scales along the hole centerline. This is in agreement with the TKE profiles shown in Figure E.2b, where turbulence intensity associated with the string vortex is higher with synthetic turbulence. In light of these results, it can be concluded that the turbulence generation method used at the

interface has an important impact not only on the statistical magnitudes but also on the flow structure coming from the URANS region such as the string vortices.

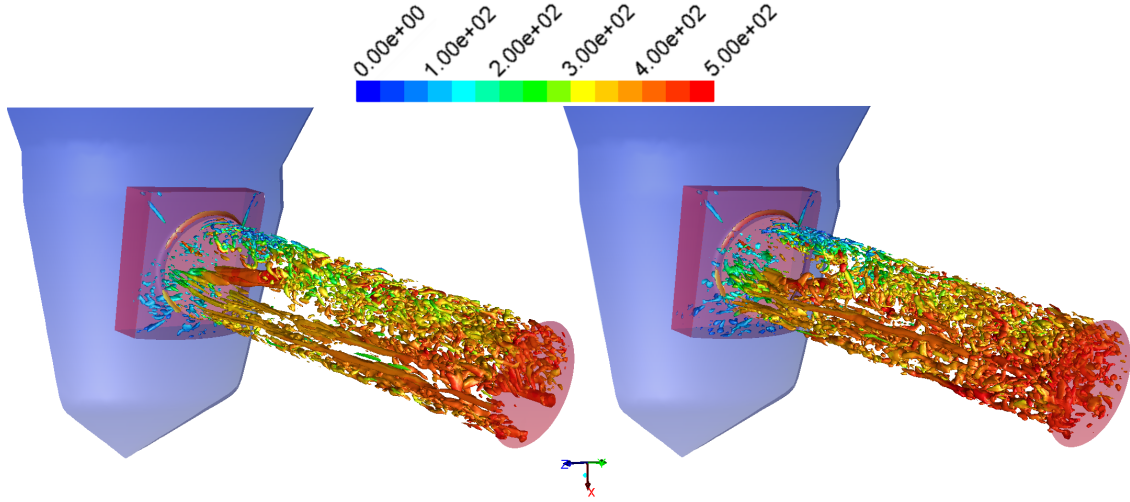


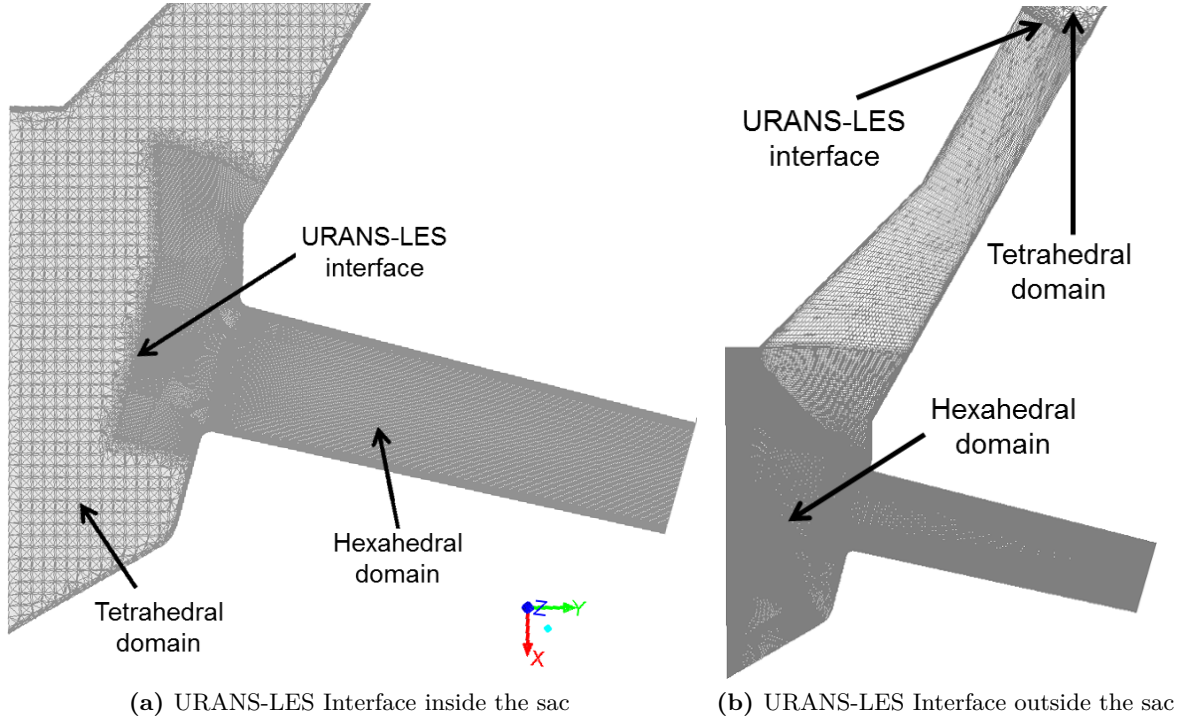
**Figure E.3:** Instantaneous normalized Q-criterion iso-surfaces of value 0.2 colored by velocity color iso-levels (units in  $m/s$ ). Synthetic turbulence (left) and vortex generation (right) methods

## E.2 Interface position

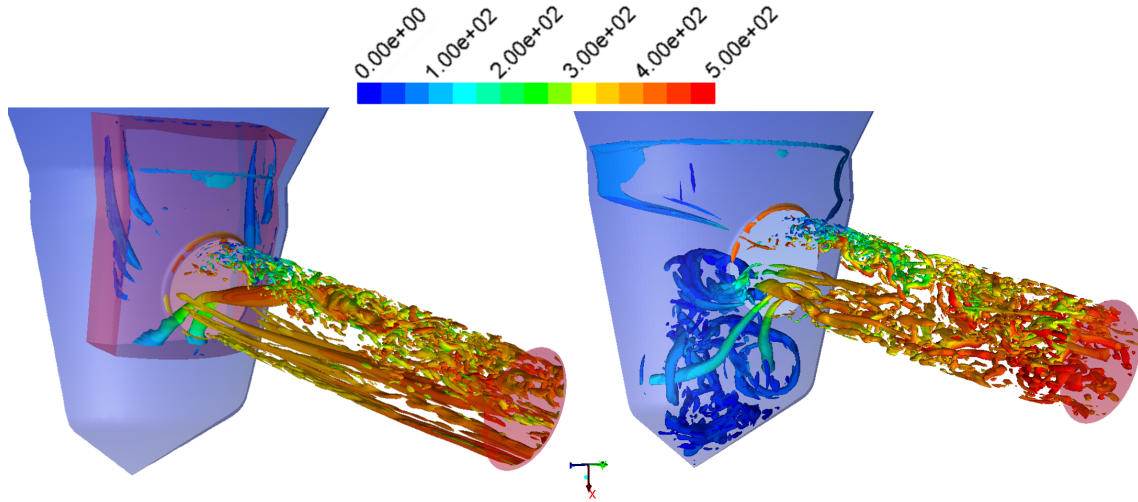
Figure E.4 shows the computational domains used to assess the impact of URANS-LES interface position on vortex dynamics. The URANS-LES interface in Figure E.4a is located inside the sac and in Figure E.4b is moved upstream of the needle seat. In order to capture the shear layer developing on the upper side of the hole entrance, the interface position in E.4a is chosen so that the hexahedral domain includes the two upper corners. As for the extended hexahedral domain in Figure E.4b, the position is the same as in Section 5.3.2. In both cases, mesh resolution and quality are chosen as close as possible to those specified in Section 5.3. Similarly, the numerical method and boundary conditions are those described in Section 5.3.

Figure E.5 depicts instantaneous vortex structures via Q-criterion iso-surfaces equal to 0.2 and velocity color iso-levels. Although the case with the URANS-LES interface inside the sac case preserves the integrity of the string vortices entering the hole, it does not capture the smaller scales shed from the center of the sac. Furthermore, it predicts long, weak vortices attached to the lateral faces of the URANS-LES interface that are not seen when the interface is moved out of the sac. These structures are artificially generated and can introduce unphysical phenomena.





**Figure E.4:** Computational mesh used for URANS-LES interface position evaluation based on Reference nozzle geometry. Side view of mid-cut plane  $z = 0$



**Figure E.5:** Instantaneous normalized Q-criterion iso-surfaces of value 0.2 colored by velocity color iso-levels (units in  $m/s$ ). Left: URANS-LES Interface inside the sac. Right: URANS-LES Interface outside the sac

Even though both cases predict the main structures, the vortices shed from the center of the sac cannot be accurately predicted if the interface is located close to the hole entrance. These vortices are important phenomena, since they represent secondary recirculation above the string vortices and rotating flow detached from the needle. Hence, as far as there are no quantitative or qualitative data available to evaluate the impact of such structures, it is preferable to place the interface as far as possible from the sac.



## Appendix F

---

# Implementation of Proper Orthogonal Decomposition (POD)

---

The fundamental idea behind POD is similar to the one behind FFT: identify coherent structures and isolate them from the seemingly stochastic flow. From the POD point of view, however, this task is more complex, since the concept is typically applied to multiple dimensions. In this work, the flow pattern at the nozzle hole exit plane is investigated using POD of the in-plane velocity components.

The concept behind POD is illustrated in Figure F.1. Provided a finite number of samples of the instantaneous velocity distribution (“snapshots”) collected over time, the POD algorithm looks for coherent patterns and classifies them based on their characteristic energy. In Figure F.1, the flow field represented by three snapshots taken at different time-instants (but with constant time interval between them) is decomposed into three coherent modes and classified according to the associated energy. This energy indicates how “present” the mode in question is contained within each snapshot. Although in this simple case it is relatively easy to infer in advance which modes are involved in the flow field, it is significantly more complex to determine which are the most energetic modes. POD mathematically decomposes the velocity and provides this information. For a more complex flow such as the one found at the nozzle hole outlet, POD becomes an essential tool to identify coherent features. In particular, this technique can provide substantial information regarding dominant vortices and spray stability.

POD used in this work is based on the method of snapshots described in Chen et al. [207, 208]. The method aims at building a spatial correlation matrix  $\mathbf{C}$ , using  $N$  flow snapshots, and decomposing it into eigenvalues and eigenvectors. Provided  $N$  two-dimensional sets of data, including the in-plane velocity components at  $P$  spatial locations

$$u_1^n = u^n(x_1, y_1) \quad ; \quad u_2^n = u^n(x_2, y_2) \quad ; \quad \dots \quad ; \quad u_P^n = u^n(x_P, y_P)$$

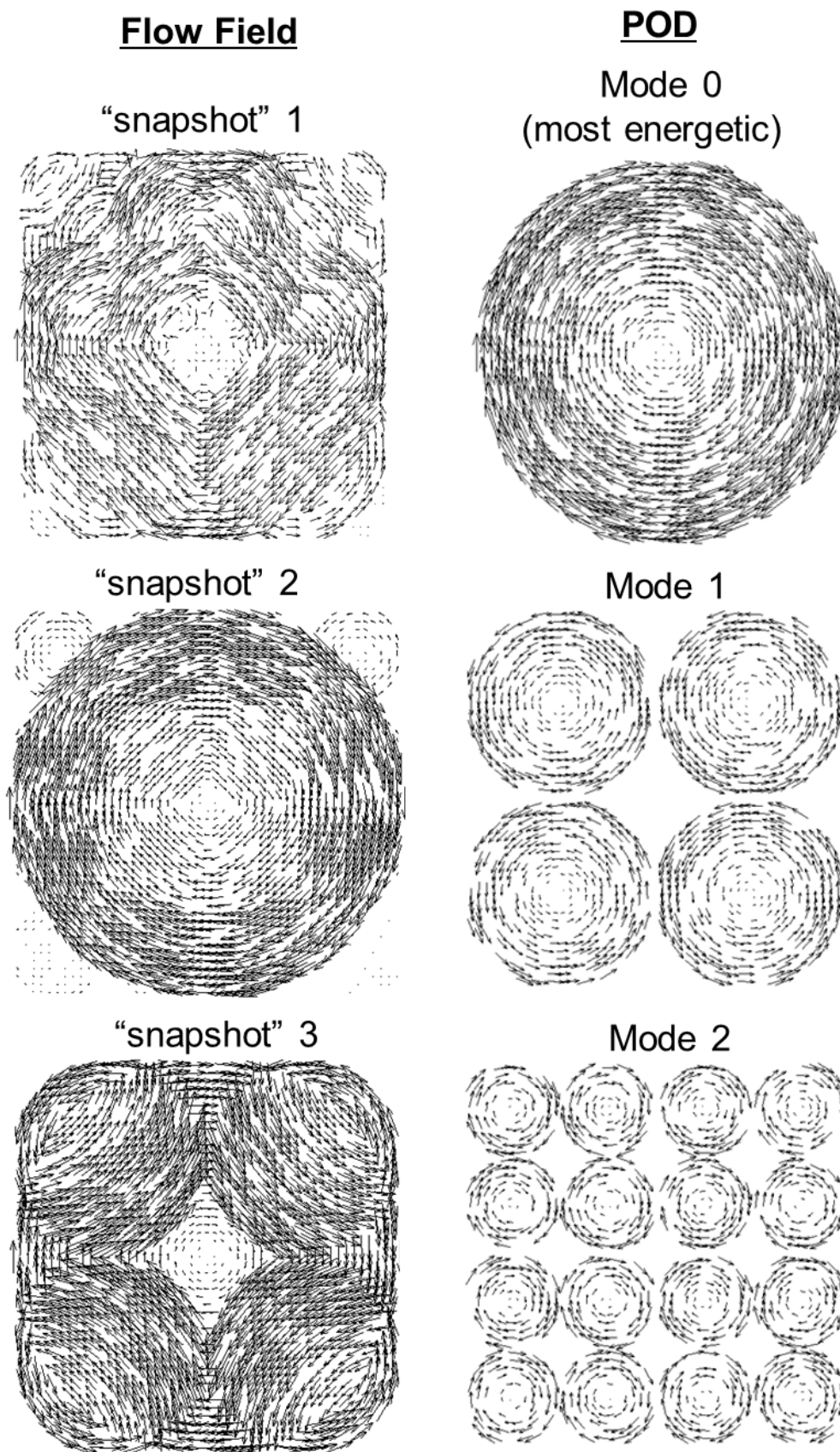


**Figure F.1:** Example of POD. Instantaneous flow fields (left) and coherent POD modes (right)

## Appendix F

---

$$v_1^n = v^n(x_1, y_1) \quad ; \quad v_2^n = v^n(x_2, y_2) \quad ; \quad \dots \quad ; \quad v_P^n = v^n(x_P, y_P)$$

where  $n = 1, N$ . The spatial correlation matrix can be constructed as

$$\mathbf{C} = \frac{\mathbf{C}_1 + \mathbf{C}_2}{N} \quad (\text{F.1})$$

where

$$\mathbf{C}_1 = \mathbf{u}\mathbf{u}^T \quad (\text{F.2})$$

$$\mathbf{C}_2 = \mathbf{v}\mathbf{v}^T \quad (\text{F.3})$$

and

$$\mathbf{u} = \begin{pmatrix} u_1^1 & u_2^1 & \dots & u_P^1 \\ u_1^2 & u_2^2 & \dots & u_P^2 \\ \vdots & \vdots & \ddots & \vdots \\ u_1^N & u_2^N & \dots & u_P^N \end{pmatrix} \quad ; \quad \mathbf{v} = \begin{pmatrix} v_1^1 & v_2^1 & \dots & v_P^1 \\ v_1^2 & v_2^2 & \dots & v_P^2 \\ \vdots & \vdots & \ddots & \vdots \\ v_1^N & v_2^N & \dots & v_P^N \end{pmatrix} \quad (\text{F.4})$$

are two matrix with dimensions  $N \times P$ . The eigenvalue problem posed in terms of  $\mathbf{C}$  reads

$$\mathbf{C} \mathbf{P} = \mathbf{P} \boldsymbol{\lambda} \quad (\text{F.5})$$

where  $\boldsymbol{\lambda}$  is a diagonal matrix composed of the eigenvalues in decreasing order and the columns of  $\mathbf{P}$  are their associated eigenvectors. The problem in eq. (F.5) can be solved by first computing the matrix singular value decomposition (Golub et al. [209])

$$\mathbf{C} = \mathbf{L} \boldsymbol{\Sigma} \mathbf{R}^T \quad (\text{F.6})$$

to obtain the left, singular and right matrix  $\mathbf{L}$ ,  $\boldsymbol{\Sigma}$  and  $\mathbf{R}$ , where  $\boldsymbol{\Sigma}$  is positive diagonal and the relations  $\mathbf{L}^T \mathbf{L} = \mathbf{I}$ ,  $\mathbf{R}^T \mathbf{R} = \mathbf{I}$  hold. By definition, for a data set of non-zero velocity components,  $\mathbf{C}$  is a  $N \times N$  normal, positive-definite matrix

$$\mathbf{C}^T = \left( \frac{\mathbf{u}\mathbf{u}^T + \mathbf{v}\mathbf{v}^T}{N} \right)^T = \frac{1}{N} \left[ (\mathbf{u}\mathbf{u}^T)^T + (\mathbf{v}\mathbf{v}^T)^T \right] = \frac{\mathbf{u}\mathbf{u}^T + \mathbf{v}\mathbf{v}^T}{N} = \mathbf{C} \quad (\text{F.7})$$

Thus, it is possible to write

$$\mathbf{C}^T \mathbf{C} = (\mathbf{L} \boldsymbol{\Sigma} \mathbf{R}^T)^T (\mathbf{L} \boldsymbol{\Sigma} \mathbf{R}^T) = \mathbf{R} \boldsymbol{\Sigma}^T \mathbf{L}^T \mathbf{L} \boldsymbol{\Sigma} \mathbf{R}^T = \mathbf{R} (\boldsymbol{\Sigma}^T \boldsymbol{\Sigma}) \mathbf{R}^T \quad (\text{F.8})$$

The eigenvalue problem (F.5) rewritten as

$$\mathbf{C} \mathbf{P} = \mathbf{P} \boldsymbol{\lambda} \rightarrow \mathbf{C} = \mathbf{P} \boldsymbol{\lambda} \mathbf{P}^{-1} \rightarrow \mathbf{C} \mathbf{C} = \mathbf{P} \boldsymbol{\lambda} \mathbf{P}^{-1} \mathbf{P} \boldsymbol{\lambda} \mathbf{P}^{-1} = \mathbf{P} \boldsymbol{\lambda}^2 \mathbf{P}^{-1} \quad (\text{F.9})$$

can be compared with (F.8) to deduce

$$\mathbf{C}^T \mathbf{C} = \mathbf{C} \mathbf{C} = \mathbf{R} (\boldsymbol{\Sigma}^T \boldsymbol{\Sigma}) \mathbf{R}^T \rightarrow \mathbf{R} = \mathbf{P} \quad ; \quad \boldsymbol{\Sigma}^T \boldsymbol{\Sigma} = \boldsymbol{\lambda}^2 \quad (\text{F.10})$$

which means that the right matrix  $\mathbf{R}$  is equal to the eigenvector matrix  $\mathbf{P}$  and the elements

of  $\Sigma$  are equal to the ordered eigenvalues. The normalized basis functions become

$$\phi_x = \frac{\mathbf{u}^T \mathbf{R}}{\sqrt{(\mathbf{u}^T \mathbf{R}) : (\mathbf{u}^T \mathbf{R}) + (\mathbf{v}^T \mathbf{R}) : (\mathbf{v}^T \mathbf{R})}} \quad (\text{F.11})$$

$$\phi_y = \frac{\mathbf{v}^T \mathbf{R}}{\sqrt{(\mathbf{u}^T \mathbf{R}) : (\mathbf{u}^T \mathbf{R}) + (\mathbf{v}^T \mathbf{R}) : (\mathbf{v}^T \mathbf{R})}} \quad (\text{F.12})$$

The normalized basis functions  $\phi_x$  and  $\phi_y$  are  $P \times N$  matrix that contain the same number of eigenmodes as snapshots. Finally, the basis coefficients are yielded by

$$\mathbf{C}_f = \mathbf{u}\phi_x + \mathbf{v}\phi_y \quad (\text{F.13})$$

The elements in  $\mathbf{C}_f$  are the linear combination coefficients to reconstruct a given snapshot  $n$  using the normalized basis functions  $\phi_x$  and  $\phi_y$ . In the example shown in Figure F.1, and taking  $x, y$  as the horizontal and vertical components respectively, each one of the  $N$  columns of  $\phi_x$  contains the horizontal velocity field for each mode (i.e. mode 0 in first column, mode 1 in second column, etc.). Alternatively, each column of  $\phi_y$  contains the vertical velocity field of each mode. The first snapshot shown could be reconstructed as

$$\begin{pmatrix} u_1 \\ u_2 \\ \vdots \\ u_P \end{pmatrix}^{Snapshot1} = \phi_x \mathbf{C}_f^1 ; \quad \begin{pmatrix} v_1 \\ v_2 \\ \vdots \\ v_P \end{pmatrix}^{Snapshot1} = \phi_y \mathbf{C}_f^1 \quad (\text{F.14})$$

where  $\mathbf{C}_f^1$  is the first column of  $\mathbf{C}_f$ . The eigenvalues  $\lambda$  calculated in (F.10) are used to classify the modes, so that  $\lambda_0 > \lambda_1 > \dots > \lambda_N$ .

---

# Résumé substantiel

---

Une étude numérique de l'écoulement dans la buse et de l'atomisation primaire en injection Diesel est conduite afin de comprendre le lien entre la géométrie interne de l'injecteur et l'atomisation du carburant. En raison de la complexité des phénomènes impliqués, les effets de compressibilité sont étudiés séparément de ceux liés à la turbulence et à la dynamique tourbillonnaire.

Dans une première partie, un modèle à 5 équations pour des écoulements diphasiques à deux espèces est développé et implémenté dans le code IFP-C3D pour analyser les effets de compressibilité sur l'écoulement. Il décrit des mélanges gaz-liquide dont la phase gazeuse est composée de deux espèces : vapeur et gaz non condensable. Il est le résultat de la réduction d'un modèle à 7 équations sous l'hypothèse d'un équilibre instantané entre vitesse et pression. Les transferts de chaleur et de masse sont pris en compte en supposant des équilibres entre températures et énergie libre de Gibbs.

Le modèle est validé à l'aide de trois cas test très répandus : tube à choc, tube à cavitation dans l'eau et tube d'expansion diphasique. Les résultats montrent la capacité du modèle à prédire les transitions de phase en présence de fortes ondes de détente. En outre, sa précision est comparable à celle du modèle à 7 équations, tout en permettant de réduire le temps de calcul de 20%. Enfin, le modèle à 5 équations est appliqué à un injecteur monotrou afin de valider sa capacité à traiter les écoulements cavitants et l'expansion de gaz non-condensables. Les résultats sont comparés à des données expérimentales, confirmant que le modèle est capable de reproduire la formation de vapeur et la détente de l'air. Le modèle à 5 équations développé est disponible pour étudier l'écoulement dans une buse d'injecteur dans des conditions opératoires réelles, à condition d'être couplé à un modèle de turbulence.

Dans une seconde partie, l'impact de la géométrie de la buse sur la génération de turbulence, sur la dynamique tourbillonnaire et sur l'atomisation primaire est étudié sous l'hypothèse d'un écoulement incompressible. La Simulation aux Grandes Échelles (ou LES pour Large-Eddy Simulation) est employée pour simuler l'écoulement dans la buse et proche de sa sortie. La méthodologie employée consiste à comparer des géométries de buse se distinguant par des paramètres de conception très tranchés afin d'en isoler l'impact sur l'écoulement. Dans certains cas, des corrélations qualitatives sont proposées entre les résultats numériques et les images expérimentales obtenues par rayon X au voisinage du nez d'injecteur.

Les résultats montrent que l'atomisation du carburant dans la zone d'atomisation primaire est le résultat de dynamiques tourbillonnaires. Deux phénomènes jouent ainsi un rôle primordial dans la formation de ligaments liquides et dans l'atomisation : un phénomène de haute fréquence engendré par des tourbillons détachés à l'entrée de la buse, et un phénomène de basse fréquence causé par des filaments tourbillonnaires formés dans le sac du fait de recirculations. Les interactions complexes entre ces deux types de tourbillons impactent non seulement le type d'atomisation et la stabilité du spray, mais aussi la taille des ligaments liquides et des gouttes. Il est conclu qu'en agissant sur ces deux types de tourbillons, il est envisageable de

contrôler dans certaines limites la dynamique du spray, en intensifiant l'atomisation et en augmentant la stabilité du spray.

En termes de perspectives futures, identifier des corrélations quantitatives entre les tourbillons générés à l'intérieur de la buse et la distribution en taille des gouttes dans le spray peut améliorer la prédiction des simulations numériques de spray réactif.





**Titre :** Etude numérique de l'impact de la géométrie de la buse de l'injecteur sur l'écoulement à l'intérieur de la buse et l'atomisation primaire

**Mots clés :** moteur Diesel, injecteur, simulation numérique, spray, atomisation primaire

**Résumé :** Une étude numérique de l'écoulement dans la buse et de l'atomisation primaire en injection Diesel est conduite afin de comprendre le lien entre la géométrie interne de l'injecteur et l'atomisation du carburant. En raison de la complexité des phénomènes impliqués, les effets de compressibilité sont étudiés séparément de ceux liés à la turbulence et à la dynamique tourbillonnaire.

Dans une première partie, un modèle à 5 équations pour des écoulements diphasiques à deux espèces est développé et implémenté dans le code IFP-C3D pour analyser les effets de compressibilité sur l'écoulement. Il décrit des mélanges gaz-liquide dont la phase gazeuse est composée de deux espèces : vapeur et gaz non condensable. Le modèle est validé à l'aide de trois cas test très répandus et est appliqué à un injecteur monotrou. Les résultats sont comparés à des données expérimentales, confirmant que le modèle est capable de reproduire la formation de vapeur et la détente de l'air.

Dans une seconde partie, l'impact de la géométrie de la buse sur la génération de turbulence, sur la dynamique tourbillonnaire et sur l'atomisation primaire est étudié sous l'hypothèse d'un écoulement incompressible. Large-Eddy Simulation est employée pour simuler l'écoulement dans la buse et proche de sa sortie.

La méthodologie employée consiste à comparer des géométries de buse se distinguant par des paramètres de conception très tranchés. Les résultats montrent que l'atomisation du carburant dans la zone d'atomisation primaire est le résultat de un phénomène de haute fréquence engendré par des tourbillons détachés, et un phénomène de basse fréquence causé par filaments tourbillonnaires. Les interactions complexes entre ces tourbillons impactent le type d'atomisation, la stabilité du spray et la taille des gouttes. Il est conclu qu'en agissant sur ces deux types de tourbillons, il est envisageable de contrôler dans certaines limites la dynamique du spray.

**Title :** Numerical study of nozzle geometry impact on in-nozzle flow and primary breakup

**Keywords :** Diesel engine, injector, numerical simulation, spray, primary breakup

**Abstract :** A numerical study of nozzle flow and primary breakup in Diesel injection is conducted in order to understand the link between injector geometry and fuel atomization. Owing to the complex physical processes involved, flow compressibility effects are studied separately from turbulence and vortex dynamics.

In a first part, a 5-Equation model for two-phase, two-species flows is developed and implemented in the IFP-C3D code to analyze the flow behavior under compressibility effects. It is intended for liquid-gas mixtures where the gas phase is composed of two species, vapor and non-condensable gas. The model is validated against three well-known test cases and is applied to a single hole injector. The results are compared with available experimental and numerical data, showing that it is able to successfully predict vapor formation and air expansion.

In a second part, the impact of nozzle geometry on turbulence generation, vortex dynamics and primary breakup is studied assuming incompressible flow. Large-Eddy Simulation is used to simulate the flow inside the nozzle and close to its exit.

The investigation strategy consists of comparing different geometries with contrasting design parameters. The results show that fuel atomization in the primary breakup region is driven by a high frequency event triggered by shed vortices, and a low frequency event caused by large string vortices. The complex interaction between them determines the breakup pattern, the spray stability and the size of ligaments and droplets. In view of the results, it is concluded that acting on these two structures makes it possible to control the dynamics of the spray to some extent.